INFLUENCE OF THE IMPLANT LOCATION ON THE HINGE AND LEAKAGE FLOW FIELDS THROUGH BILEAFLET MECHANICAL HEART VALVES

A Dissertation

Presented to

The Academic Faculty

By

Hélène A. Simon

In Partial Fulfillment

Of the Requirements for the Degree

Master of Science in Chemical Engineering

Georgia Institute of Technology

May, 2004

Influence of the Implant Location on the Hinge and Leakage Flow Fields Through Bileaflet Mechanical Heart Valves

Approved by:

Ajit P. Yoganathan

Fotis Sotiropoulos

Athanassios Sambanis

March 24. 2004

ACKNOWLEDGMENTS

There are many people whom I would like to acknowledge for their support in helping me complete my master's thesis. First, I would like to thank my advisor, Dr. Ajit Yoganathan, for giving me the opportunity to perform graduate research in such an interesting field. I would also like to thank Dr. Sambanis and Dr. Sotiropoulos for being part of my thesis committee.

The financial support given by Tom and Shirley Gurley and by the National Heart, Lung and Blood Institute (RO1-HL-07262) are also gratefully acknowledged.

I thank the administrative staff of Chemical Engineering and Biomedical Engineering, especially Chris Ruffin, for always being cheerful and helpful.

Special thanks go to Leo for teaching me all about LDV and for always being present and providing technical assistance in "crisis times". I really appreciated your help, encouragement, and particularly your optimism. Thanks for all the good laughs, the long and interesting conversations, and for introducing me to the English literature.

I am also very grateful for the support and especially for the fun times provided by all the members of the Cardiovascular Fluid Mechanics Lab: Hiroumi, Kartik, Jenni, Dennis, Steffan, Jorge, Diane, Zhaoming, James, Yun, Josie, Casey, Saul, Ashley, Dave, Diane, Leo, Kerem, Anna, Alyssa and Tommy.

Thanks to Caroline, Amon, Massimiliano, Tommaso and Violetta, for being awesome roommates and providing great “international” times outside the lab at 311 10th street.

I would like to thank my family for helping me to take the opportunity I was given at Georgia Tech. Finally, muchas gracias to Pedro for every time you were there to listen, inspire and bring fun times!

TABLE OF CONTENTS

LIST OF TABLES

LIST OF FIGURES

SUMMARY

Since the first successful heart valve replacement four decades ago, more than fifty valve designs have been developed. Bileaflet mechanical heart valves have been used for over two decades and today remain the most widely implanted valve design due to their great durability, good bulk forward flow hemodynamics, and large orifice area which generates small transvalvular pressure drops. Despite the widespread clinical use of mechanical heart valves, the function of these devices is far from perfect. The major complications that contribute to valve failure are hemolysis, platelet destruction, and thromboembolic events arising from the formation of clots and their subsequent detachment. Prevention of these complications requires lifelong anticoagulation therapy.

Recent studies have shown that the thrombogenic complication rates caused by bileaflet mechanical heart valves are related to the leakage flow. The stresses imposed on blood by mechanical heart valves during the closing phase was concluded to initiate hemolysis and the coagulation cascade. Additionally, animal and clinical studies have shown that the clinical performances of mechanical heart valves implanted in the aortic position were better than those in the mitral position due to a lower rate of thrombus formation and hemolysis. Therefore, there is a need for a better understanding of how the implant location influences the valve performance and the subsequent risk of blood damage. The present study tested the hypothesis that the hinge flow patterns as well as the leakage flow fields are different for a bileaflet mechanical heart valve placed under aortic or mitral conditions.

The goal of this study was to investigate the leakage, hinge, and near hinge flow fields of two bileaflet mechanical heart valves under simulated physiologic aortic flow

conditions. Two and three-component Laser Doppler Velocimetry techniques were used to quantify the velocity and turbulent shear stress fields in both the hinge flow region and the upstream leakage flow field. The study focused on the 23 mm St. Jude Medical Regent and the 23 mm CarboMedics valves, which are two of the most commonly implanted mechanical heart valves.

Even tested under similar physiologic conditions, shape and location of the leakage jets were dependent on valve design. Nevertheless, turbulent shear stress levels recorded within all jets were well above the threshold shear stress for the onset of blood element damage. Within the hinge region, the flow fields were complex and unsteady. However, the angled recess of the CM valve appeared to promote blood damage while the streamlined geometry of the SJM valve contributed to a better washout of the hinge region. Comparison of the present findings with results already published for the mitral position suggests that the superior clinical results of the mechanical valves located in the aortic position may be due to less severe leakage flow upon valve closure as well as an enhanced hinge washout during the forward flow phase.

This study imparts an improved understanding of the thrombogenecity associated with bileaflet mechanical heart valves by characterizing the blood damage potential of a valve depending on its position, aortic or mitral. The results provide a new insight into the importance of implant location on prosthesis design selection.

CHAPTER I

INTRODUCTION

According to the World Health Organization, cardiovascular disease contributes to nearly one third of global deaths. In 2001 7.2 million people died from cardiovascular disease worldwide, with over 4 million in Europe alone (AHA, 2003). Cardiovascular disease or congenital birth defects may compromise native heart valve function. Aortic stenosis occurs in approximately 5 out of every 10,000 people and represents 5% of the clinically apparent cardiac defects. The most common congenital heart abnormality is a bicuspid aortic valve occurring in 1 to 2% of the population. Valves with limited functionality are commonly replaced by prosthetic heart valves. Since the first heart valve replacement in 1960, more than three million valves have been implanted world wide. In 2001 alone, 94,000 patients underwent heart valve surgery in the United States.

Many of these malfunctioning valves are replaced with mechanical heart valves because of their durability. Several mechanical valve designs are currently available, but bileaflet valves are preferred due to their better bulk flow hemodynamics, larger orifice area, lower transvalvular pressure drop, and fewer regions of flow stasis compared to their counterparts such as the ball-and-cage and the tilting disc valves.

Nevertheless, bileaflet mechanical heart valves can still cause major complications including hemolysis, platelet destruction, and thromboembolic events. To avoid these complications patients with a mechanical valve must undergo lifelong anticoagulant therapy. However, this treatment increases the risk of hemorrhage, infection, and autoimmune responses.

Clinical reports and recent in vitro experiments suggest that the thrombogenic complication rates caused by bileaflet mechanical heart valves are not related to valve

materials or forward flow patterns, but are mainly associated with the leakage flow through the closed valve. Bileaflet valve designs have small gaps between the leaflet and the housing, and when they close a small amount of fluid can flow through these gaps. The valve design deliberately includes this leakage flow during valve closure to wash out critical regions and prevent flow stasis. However, because the leakage flow is driven through narrow regions by a large transvalvular pressure gradient, elevated turbulent shear stresses and high velocities are usually observed in these regions.

Previous investigations have concluded that the stresses imposed on blood by mechanical heart valves during the closing phase can initiate hemolysis and the coagulation cascade. These studies were mainly performed under mitral flow conditions and no studies of the micro flow fields of bileaflet mechanical heart valves in the aortic position have been performed.

The goal of this study was to investigate the leakage, hinge, and near hinge flow fields of two bileaflet mechanical heart valves under simulated physiologic aortic flow conditions. Two and three-component Laser Doppler Velocimetry techniques were used to quantify the velocity and turbulent shear stress fields in both the hinge flow region and the upstream leakage flow field. The study focused on the St. Jude Medical Regent and the CarboMedics valves, which are two of the most commonly implanted mechanical heart valves.

This study imparts an improved understanding of the thrombogenecity associated with bileaflet mechanical heart valves. The results characterize the blood damage potential of a valve depending on its aortic or mitral position. The data provides a new insight into the importance of implant location on prosthesis design selection.

CHAPTER II

BACKGROUND

2.1 The Heart

2.1.1 Anatomy of the Heart

The heart is a muscular pump consisting of two atria and two ventricles (Figure 2.1). The valves between adjacent chambers are passive devices that open and close in response to changes in pressure to maintain the unidirectional blood flow through the heart and then to the body. The heart has four valves, the tricuspid, mitral, aortic, and pulmonary valves described below (Figure 2.2).

- The *pulmonary valve* is the smallest of the valves and is located between the right ventricle and the pulmonary artery. This valve has two leaflets and a valvular ring which is attached to the base of the heart.

- The *tricuspid valve* is composed of three leaflets and is located between the right atrium and the right ventricle. This valve consists of an annulus and chords that connect the leaflets to the heart.

- The *mitral valve* has two leaflets and is located between the left atrium and the left ventricle. It is comprised of a valve annulus and chordae tendineae that connect the leaflets to the papillary muscles that are attached to the heart wall.

- The *aortic valve* is located between the left ventricle and the ascending aorta. It has three cusps, an annulus, and the Sinuses of Valsalva.

The pulmonary and tricuspid valves are located on the right side of the heart and drive deoxygenated blood through the lungs, whereas the aortic and mitral valves are

located on the left side of the heart and drive oxygenated blood through the capillaries of the systemic circulation.

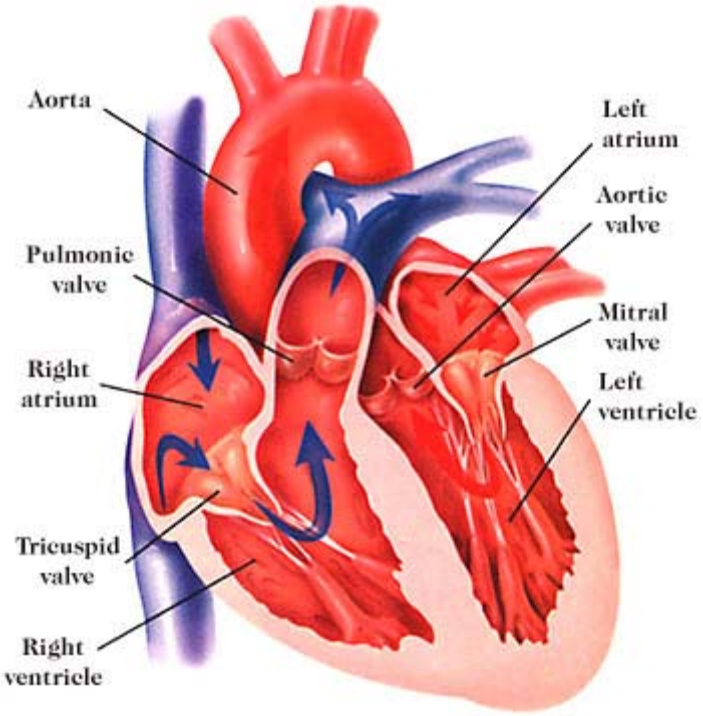

Figure 2.1: Cross-section of the heart

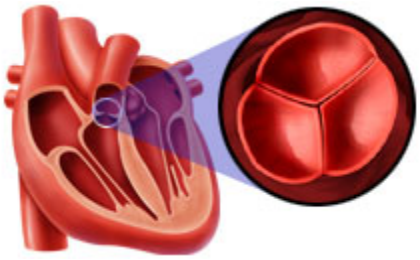

Pulmonary valve

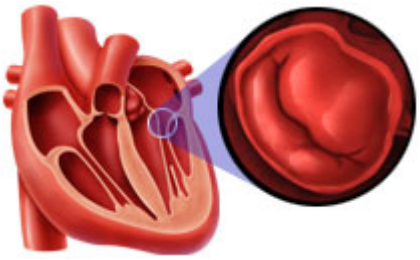

Biscupid valve

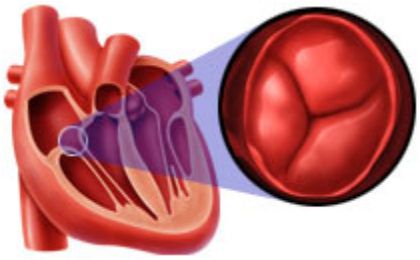

Tricuspid valve

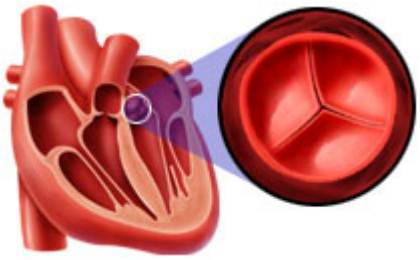

Aortic valve

Figure 2.2: Natural heart valves

2.1.2. Cardiac Cycle

The cardiac cycle includes alternating periods of contraction and relaxation. For each chamber of the heart, the cardiac cycle is divided into two phases, systole and diastole.

During systole, the ventricular chambers contract and the pressure within these chambers increases. The relatively high pressure within the ventricles causes the aortic and pulmonary valves to open while the mitral and tricuspid valves close. Ventricular contractions drive the blood from the ventricles to the pulmonary artery and the aorta.

During diastole, the heart muscle relaxes and the ventricles expand. The pressure within the ventricles decreases, and the mitral and tricuspid valves open while the aortic and pulmonary valves close. Thus the blood is driven from the body through the mitral and tricuspid valves to the ventricles.

2.1.3. Heart Valve Disorder

Heart valve function may be compromised by congenital birth defects or disease. One in 120 infants is born with a heart defect, many of which are not severe. In children with an affected first-degree relative, the risk of having a heart defect rises to 2 to 3 %. The most common congenital abnormality is a bicuspid aortic valve occurring in 1 to 2 % of people. This defect is the second most common reason for aortic valve surgery. Rheumatic fever and syphilis used to be the most common cause of valve malfunction; however, due to the widespread use of antibiotics these diseases are now rare in North America and Western Europe. Today heart valve disease mainly occurs in the elderly as a result of calcium build up around the valve tissue, which eventually restricts or limits the motion of the valve leaflets. Congenital abnormalities and calcification lead to valve stenosis or regurgitation. A heart attack may also damage the supporting structure of the mitral valve causing mitral regurgitation.

2.1.3.1. Valve Stenosis

A stenotic valve has stiffened leaflets which prevent the valve from fully opening and offer a significant resistance to the flow. Aortic stenosis occurs in approximately 5 out of every 10,000 people and accounts for about 5% of clinically apparent cardiac defects. Pulmonary valve stenosis constitutes about 10% of congenital heart disease. Valve stenosis is likely the most common cardiac abnormality, and mainly affects men. Symptomatic valvular stenosis may occur in infancy and produce severe left ventricle dysfunction or heart failure, but this is relatively uncommon. Typically, it appears later in childhood as a bicuspid aortic valve with stenosis and sometimes with insufficiency.

2.1.3.2. Valve Insuffiency

An insufficient valve does not close properly allowing regurgitation. When closed, the aortic and the mitral valves must withstand backpressures of up to 100 mmHg and 150 mmHg, respectively, and the pulmonic and tricuspid valves close against pressures of up to 30 mmHg. Because of this extreme loading, the valves located in the left side of the heart are predisposed to disease that can cause the valve to weaken, balloon and become insufficient. This results in excess pressure on the heart or lungs. As a result, the heart may enlarge, weaken and eventually fail. Aortic insufficiency affects approximately 5 out of every 10,000 people and is most common in men between the age of 30 and 60.

2.1.4. Valve Replacement

When a heart valve does not work properly and surgical repair is contraindicated, a natural heart valve may be replaced by a prosthetic one. The first heart valve replacement with an artificial cage ball valve took place in 1960. Since then valve design has improved considerably, and heart valve replacement has been remarkably

successful. More than 50 prosthetic heart valve designs have been developed, and over 182,000 heart valves are implanted in the world each year (Yoganathan, 1995; Piehler, 2000). In 2001 94,000 individuals underwent heart valve surgery in the United States. Nearly three million prosthetic heart valves have been implanted worldwide since the first heart valve replacement, and demand for these devices continues to expand at a rate of 10-12% per year (Black, 1994).

2.1.5. Prosthetic Heart Valves

Existing commercial heart valve prostheses can be divided into two categories: mechanical heart valves which are fabricated mainly from synthetic material, and bioprosthetic valves, made from a combination of chemically treated animal tissues and synthetic material. Further subdivisions are usually made within these two categories. Mechanical valve categories are caged-ball, tilting-disc, or bileaflet designs, and bioprosthetic valves are porcine or pericardial valves (Figure 2.3). The search for a nonthrombogenic prosthesis mimicking the natural valve function had led to the development of a third heart valve type, polymeric valves.

2.1.5.1. Mechanical Valves

The Starr Edward ball-and-cage valve developed in 1960 was composed of a ball retained in a sub-cage on the proximal side of the valve. One of the main drawbacks of this valve was the turbulence produced by the ball obstructing the flow. Today, caged-ball valves have been superseded by tilting disc and bileaflet valves.

The development of tilting disc valves in the late 1960s made a notable contribution to the advancement of valve replacement. These prostheses are based on the concept of a free-rotating disc, which in the open position tilts to a particular angle.

Carpentier-Edwards S.A.V.
Aortic Bioprosthesis

Aortech trileaflet
Aortic polymeric Valve

Starr-Edwards Silastic Ball
Valve Prosthesis

Medtronic Hall Valve

St Jude Medical
Regent Valve

CarboMedics Standard
Aortic Valve

Figure 2.3: Different types of prosthetic heart valves

The pressure drop across the tilting-disk valve is much lower than that across any caged-ball valves. Tilting disc valve improvements have focused mainly on disc geometry and disc-retaining mechanisms.

The bileaflet mechanical heart valve (MHV) has been used for almost two decades and remains the most widely implanted valve design (Black, 1994; Baudet, 1995), with more than 500,000 implants worldwide (Black, 1994). Seventy-five percent of defective valves are currently replaced by a bileaflet valve. The design consists of two semicircular, hinged pyrolytic carbon occluders, which regulate the flow. When the leaflets are open, the blood flows through three orifices. These valves offer the benefit of great durability, and provide better functional safety than the single leaflet of a tilting disc. They also provide a relatively large orifice area for a small valve size, and therefore have a smaller transvalvular pressure drop.

2.1.5.2. Bioprosthetic Valves

A major disadvantage associated with mechanical valves is the need for long-term anticoagulation therapy to prevent thrombosis and thromboembolic complications. Furthermore, the hemodynamics of prosthetic valves differs significantly from that of natural valves. An alternative approach in the development of prostheses is a valve that resembles a natural valve. The first tissue valve design consisted of antibiotic or cryotreated human valves. This valve was optimal from a functional, structural, and hemodynamic point of view. However, the supply of such valves is limited. A second generation of bioprosthetic valves was the Hancock porcine xenograft, which was first used in 1970. This valve was fashioned from a chemically treated porcine heart valve mounted in a rigid ring with three flexible stents. Another popular bioprosthetic valve, the Carpentier-Edwards valve, was first used in 1976. This valve consists of three pieces of bovine pericardium mounted in a completely flexible frame. Tissue valves provide an

unobstructed central orifice and deform with the surrounding anatomical structure; however, their durability is limited and they are prone to time-dependent structural changes such as calcification and leaflet wear resulting in valve failure (Black, 1994). The main benefits of tissue valves are that lifelong anticoagulant therapy is usually not required and that they offer natural form and function, thus reducing blood damage. Implanted tissue valves often fail in less than ten years, at which time reoperation is necessary.

2.1.5.3. Polymeric Valves

Polymeric valves utilize synthetic materials to mimic the natural valve function. They are commonly made of polyurethane material, which is known to be an excellent non-thrombogenic material. Conceptually, these valves combine the best features of both tissue and mechanical heart valves. This valve type is still in development, and clinical trials have not yet been performed.

2.1.6. Related Valve Complications

Despite the widespread clinical use of mechanical heart valves, the function of these devices is far from perfect. Five years after surgery, the survival rate is approximately 80%, 60% after ten years, and only to 50% after fifteen years. Heart valve complications are divided into six categories: structural valvular deterioration, non-structural dysfunction, valve thrombosis, embolism, bleeding, and endocarditis (Grunkemeier, 1998).

The major complications that contribute to valve failure are hemolysis, platelet destruction, and thromboembolic events arising from the formation of clots and their subsequent detachment. Prevention of these complications requires lifelong anticoagulation therapy. However, such treatment increases the risk of hemorrhage,

infection, and autoimmune response (Walker, 1992). Prosthetic heart valve failure may also occur due to tissue overgrowth, paravalvular leaks associated with healing defects, material fatigue, or chemical change. Additionally, mechanical heart valves obstruct blood flow and decrease the effective valvular orifice area. Their non-physiological geometries may generate abnormal velocity profiles and high shear rates, which may cause blood cell damage. Despite improvement in valve design and development of new drug therapies, blood damage leading to chronic hemolysis and anemia remains a problem. Another main concern is platelet destruction, which causes the release of platelet factors that can stimulate platelet aggregation resulting in thrombus formation. These events can have disastrous consequences for the patient since thrombi can detach from the valve and become lodged in blood vessels downstream, thus reducing and potentially stopping the blood supply to vital tissues.

2.1.7. Ideal Valve Characteristics

Over the years there have been many improvements in valve design, but there is still no perfect artificial valve. Ideally, an artificial valve should be efficient in terms of minimal flow obstruction and minimal reverse flow. It should not be prone to time-dependent changes and should not damage blood cells or stimulate thrombosis. Moreover, it should be easy to insert in the heart, quiet, and affordable.

2.2. Blood Damage

2.2.2. Blood

In order to understand some of the valve-related complications associated with prosthetic heart valves, it is necessary to consider the biological origins of thromboembolic events.

2.2.2.1. Red Blood Cells and Hemolysis

Red blood cells, or erythrocytes are the most abundant cell type in the blood, and their primary function is to carry oxygen and carbon dioxide between the lungs and the tissues. They are a simple, membranous “bag” filled with enzymes and hemoglobin. The permeable membrane is composed of a lipid bilayer in association with protein molecules. Red blood cells have a biconcave discoid shape with a diameter of 7.6 μm and a thickness of 2.8μm. Despite their complex cytoskeleton, which holds the membrane in place, the red blood cells have an extraordinary ability to deform. Because they have an excess of membrane in relation to their volume, the membrane can tolerate large uniaxial strain without hemolysis. However, the physical properties of the membrane are not isotropic, and the membrane cannot tolerate areal strain. The red blood cell membrane is a non-homogeneous material, especially in the direction normal to the surface. When the membrane is subjected to shear, initially the membrane is viscoelastic, but after a transition region, it becomes viscoplastic (Chien, 1977). The typical life span of a red blood cell is about 120 days.

During normally occurring hemolysis, the fragile older red cells rupture and many components of hemoglobin are recycled. Hemolysis is the consequence of cumulative or instantaneous damage to the red cell membrane and corresponds to the release of hemoglobin from the red cells. When a red blood cell is stretched, the membrane develops ‘holes’ large enough for the diffusion of hemoglobin into the extracellular fluid. Once the pores are open, the protein molecules may pass through. If a large enough stretch is applied and the stretch required for lysis is exceeded, the membrane tears spilling the cell contents and leaving the membrane fragments.

2.2.2.2. Platelets and Coagulation Cascade

Another important blood cell type is the platelet. Platelets are produced in the bone marrow by megakaryotes. Platelets are colorless cell fragment without a nucleus that contain a cytoskeleton consisting of microtubules, actin filaments, and other binding proteins. They are smaller than red blood cells with a diameter of approximately 2.5 μm. They have a typical life span of about 10 days. Inactive platelets are small disk-like cells that are extremely responsive to alterations in the surrounding medium. Platelets constitute the principal line of defense against bleeding, and therefore become active in response to stimuli like a vessel wall injury. Active platelets lose their discoid form and extend long pseudopods in response to a change in their cytoskeleton. They also release a great number of vasoactive substances and adhere to any exposed collagen. This liberation of chemicals attracts additional platelets, which aggregate thus enlarging the forming plug. A series of reactions initiated by exposed collagen and tissue factor, occurs corresponding to the coagulation cascade during which inactive plasma proteins are converted into active enzymes. This cascade converts fibrinogen into fibrin fibers which are the major structural component of blood clots (Martini, 2000).

2.2.3. Shear Stress and Blood Damage

2.2.3.1. Red Blood Cell and Shear Stress

In 1968 Nevaril used a modified Couette viscometer to investigate the effects of a nearly uniform laminar stress field on hemolysis. For a 2-min exposure time, the threshold shear stress for the onset of red blood cell lysis was about 1,500 dyn/cm^2. When the shear stress exceeded 3,000 dyn/cm^2, many cells were lysed. Nevaril also demonstrated that the normal stress, which corresponds to pressure, was of secondary importance; which implied shear stress effects were the primary mechanism of

hemolysis (Nevaril, 1968). The instrument of choice to investigate blood damage by shear stress was a rotational viscometer, as it allowed a known shear stress to be applied to certain fluid regions. However, the secondary physical effects such as cell-solid surface interaction appeared to induce major errors. Nevertheless, the threshold value of 1,500 dyn/cm^2 was considered to be a realistic estimation and correlated well with Nevaril's results (Leverett, 1972). It was also concluded that under low shear stress conditions hemolysis was directly proportional to cell-solid surface interactions. Leverett emphasized the importance of exposure time and established that disagreements between previous results were due to the investigation of different regimes of the exposure time-stress domain (Leverett, 1972). Blackshear noticed that mechanical hemolysis could be divided into three classes: hemolysis induced by surface interaction, hemolysis occurring in the bulk fluid at medium stress (1000-2000 dyn/cm^2 applied for several seconds), and hemolysis occurring in the bulk fluid at high stress (about 40,000 dyn/cm^2 applied for milliseconds). According to Blackshear, a medium shear dependent on the exposure time induced a gradual fragmentation of the cells, whereas the third class seemed to be associated with an instantaneous rupture of the cell membrane (Blackshear, 1972). In order to study the changes in cell shape under bulk stress condition, Sutera fixed red cells directly in the fluid by adding glutaraldehyde (Sutera, 1975). At 37°C after 4 minutes of turbulent conditions at 100 dyn/cm^2, the cells had a bulbous shape. At around 1,500 dyn/cm^2, cells began to lose their concavity and exhibited an ellipsoidal shape. At about 2,500 dyn/cm^2, fragmentation became apparent. At 4,500 dyn/cm^2, more fragmentation was visible. The degree to which the reversibility of the damage varied with shear stress was investigated using a fixed recovery period of one minute. Cells sheared at 2,000 dyn/cm^2 could almost recover their normal shape, but cells sheared at 3,500 dyn/cm^2 were fragmented irreversibly. At high shear stress, the deformation through the entire population seemed to be uniform. According to

Sutera, the shear flow, and hence the turbulent characteristics of the flow, must be completely determined in order to obtain realistic data describing the relationship between shear stress and hemolysis. Hellums carried out studies on the effect of pressure changes, impact due to the crushing of red cells between solid surfaces, and shear stress. The hemolysis rate was found to be approximately linear with time at low hemolysis rates with an increase in morphological changes with time. The concept of threshold shear stress was therefore justified. Hellums concluded that the time-shear stress plane could be divided into two regimes. In the first regime with low shear stress and short exposure time, there was little damage, and this damage was influenced by surface interaction effects. In the second regime corresponding to high shear stress and long exposure time, very high hemolysis occurred and shear stress was the dominant factor of hemolysis (Hellums, 1977).

In 1984 Sallam used a submerged axisymmetric jet flow field to investigate the effect of shear on red blood cells. A technique was developed to allow the collection of samples directly in the jet flow field at locations corresponding to known values of mean velocity, turbulence intensity, and shear stress. Using this technique, local shear stress and blood cell damage could be related. The incipient hemolysis was associated with a shear stress of 400 N/m^2 for an exposure time of 1 ms. Below this level, no free hemoglobin was detectable. Beyond the threshold level, hemolysis increased with increasing shear stress. Sallam and Sutera investigated the additional effect of turbulence on red blood cell tolerance to shear flow. They found that a laminar shear stress and a fluctuating turbulent shear stress may not have the same impact on the cells (Sallam, 1984; Sutera, 1975). Lu reevaluated the threshold limit for hemolysis in a turbulent shear flow and showed that the values found by Sallam were an underestimation due to experimental methodology and calculations. The value determined by Lu was 800 N/m^2 with an exposure time of 1 ms (Lu, 2001).

2.2.3.2. Platelets and Shear Stress

Before 1960 there was no intensive research activity in the field of thrombosis, and the mechanism of coagulation was not well understood. Born developed a method measuring platelet aggregation in order to characterize the influence of shear stress on platelet-platelet interaction, but the applied shear stress was not uniform (Born, 1962). In 1975 Brown et al. hypothesized that shear stress may have hemolytic effects on blood as a result of its thrombogenic effect on platelet activation. They performed controlled shear stress experiments where platelet rich plasma was exposed to shear stresses from 5 to 900 dyn/cm^2. The platelets exhibited biochemical and morphological changes when subjected to shear stress as low as 50 dyn/cm^2. In addition it was shown that platelet function was altered when a shear stress exceeding 100 dyn/cm^2 was applied for five minutes (Brown, 1975). These experiments demonstrated that shear stress could induce platelet aggregation; however no attempt was made to establish a relation between platelet aggregation and exposure time.

In 1977, Bernstein attempted to separate the blood damage resulting from shear stress within the bulk fluid from that related to surface interaction by using two devices to selectively impose different forms of damage. He showed that high wall impact had no real influence on activation or aggregation of the platelets as evidenced by a moderate decrease in serotonin uptake, which might indicate cellular destruction. However, experiments demonstrated that high shear forces applied for a few milliseconds within the bulk flow partially affected platelet function. No significant change in platelet adhesion and aggregation was observed for shear stresses below 10^5 dyn/cm^2; however, structural and functional changes as well as serotonin release were detected at a shear stress of 10^6 dyn/cm^2. No abnormal platelet aggregation was observed. Following these observations, Hellums undertook a study of platelet ultrastructure to determine a correlation between morphologic changes and functional abnormalities. He observed

that platelet aggregates began to form at low shear stress. However the level of aggregates decreased after a period of 2 to 4 hours indicating that low shear stress could biochemically alter platelet function. At higher shear stresses, some platelets were fragmented and distorted but did not aggregate. Despite the discrepancies observed between these findings and previous experiments, it can be seen that factors such as exposure time and cell-solid surface interactions may contribute to blood damage (Hellums, 1977). In another study Anderson demonstrated that platelet surface interaction had no real influence on platelet aggregation or lysis since shear stress of 50-75 dyn/cm^2 applied for a duration of five minutes resulted only in reversible swelling and aggregation of platelets. Some aggregation and fragmentation occurred under a shear stress of 100 dyn/cm^2, but when a shear stress of 150 dyn/cm^2 was applied the platelet count was dropped greatly. Thus, this was considered to be the threshold for incipient lysis. Anderson showed that for platelet damage threshold shear stress increased with decreasing exposure time. He also underlined the fact that laminar and turbulent flows might not have the same impact on cell damage.

2.2.3.3. Comparison of Shear Stress Effects on Red Cells and on Platelets

A good agreement between studies supports the findings that shear stress does not have the same effect on red blood cells and platelets. Platelets are much more fragile than red cells when subjected to long exposure times. Bernstein's results indicate that for a 2-min exposure time, the threshold shear stress for hemolysis was around 1500 dyn/cm^2; whereas the threshold shear stress for lysis of platelets is tenfold lower (Bernstein, 1977; Hellums, 1977). However, it seems that the reverse is true at very short exposure times when platelets are observed to be more resistant to stress than the red blood cells (Anderson, 1978). Red blood cells and platelets also have different reactions to stress, which may be due to structural differences. One major difference

between red blood cells and platelets is in the deformability properties of erythrocytes, which platelets do not have. These properties may reduce their susceptibility to shear stress induced modification, as evidenced by Brown's study which showed that the leakage of hemoglobin by red cells was not significant compared to the leakage of ADP by sheared platelets (Brown, 1975).

2.3. Bileaflet Mechanical Heart Valves

2.3.1 Basic Design

The bileaflet mechanical heart valve is composed of two semi-circular occluders called leaflets. Within the annular housing, each leaflet pivots about two hinges (Figure 2.4). Contraction and relaxation of the heart generate pressure variations within the heart chambers, and these pressures control the opening and closing of the leaflets to regulate the blood flow.

A sewing cuff made of Dacron cloth is attached to the valve housing to facilitate the suturing of the prosthetic heart valve to the surrounding tissue. The leaflets and housing are made of pyrolytic carbon, which is both biocompatible and wear resistant.

When the leaflets are open the blood flows through the valve, which has a central rectangular orifice and two semi-circular lateral orifices. The open occluders form an angle with respect to the plane of the valve housing. Opening angles greater than 80° are preferable in order to minimize flow disturbances. When the leaflets are fully closed, small gaps at the B-datum line between the leaflets and between the leaflets and housing allow reverse leakage flow. These gaps are incorporated into the design to washout critical areas, such as the pivot regions, preventing blood element buildup.

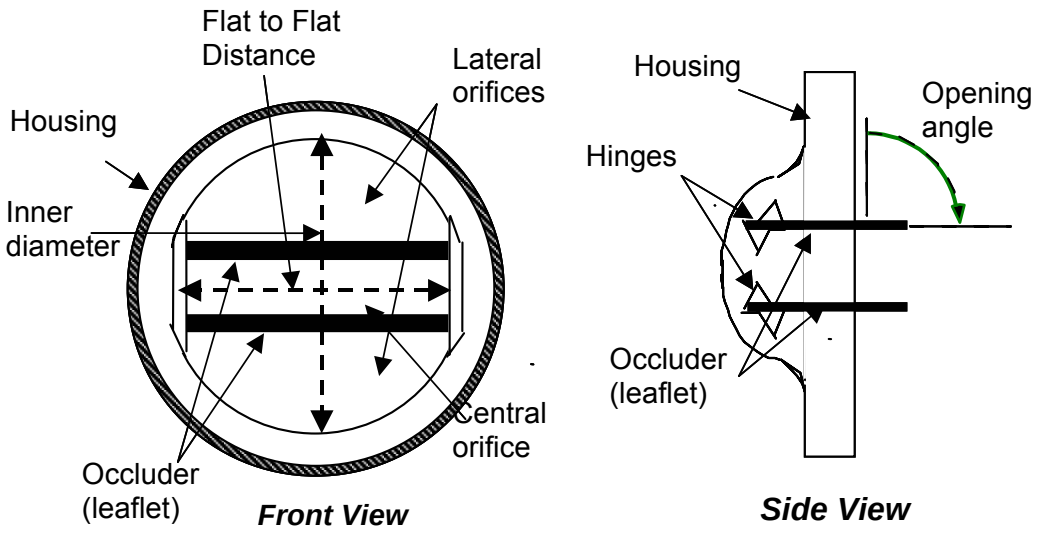

Figure 2.4: Characteristics of a bileaflet mechanical prosthesis

The obstruction of blood flow due to the valve is a critical design consideration and is characterized by the Effective Orifice Area (EOA). Typically a large EOA is preferable as this corresponds to a small pressure drop, and consequently a small energy loss. The Effective Orifice Area can be obtained from the following Gorlin-type equation

$$EOA\ (cm^2) = \frac{Q_{rms}}{51.6\sqrt{\Delta P}} \qquad \text{Equation 2.1}$$

With EOA in cm^2

Q_{rms} is the root mean square flow rate during forward flow phase in cm^3/s

ΔP is the mean pressure drop during forward flow phase in mmHg

For a common 27 mm sewing ring diameter, the EOA of different valve designs are given in table 2.1 (Yoganathan, 1995). The St. Jude Medical Standard valve EOA (4.05 cm^2) is larger than any other valve design of the same size.

Table 2.1: EOAs of different valve designs for a common 27 mm sewing ring

Valve	EOA (cm^2)
SJM Standard	4.05
CarboMedics bileaflet	3.75
Medtronic Hall tilting disk	3.64
Hancock I Porcine	2.14
Starr Edwards 1260 ball	1.75

2.3.2. St. Jude Medical Regent Mechanical Heart Valve

2.3.2.1. St. Jude Medical (SJM) Valve

To date the most recent enhanced configuration of the SJM mechanical heart valve is the SJM Regent valve. The main feature of this valve is a decrease in the wall thickness of the housing and a corresponding increase in the EOA for a given valve annulus diameter. This improvement was achieved by moving the SJM regent valve sewing cuff-retaining rims to a supra annular position. This valve offers up to an 84% orifice to annulus ratio, which is the largest of any other SJM mechanical heart valve. The hemodynamic performance of the SJM Regent valve, especially total energy losses, have been shown to be similar to those of the SJM Hemodynamic Plus of the next larger size, which is equivalent to a two-size increment improvement over the Standard valve (Walker, 1999). Aside from the increase in the geometric orifice area and the effective orifice area, the SJM Regent valve retains the same design features (geometric shapes of the housing and leaflets) as the other SJM valves (Figures 2.5 and 2.6). To increase ease of implantation the SJM Regent valve has a rotatable sewing cuff.

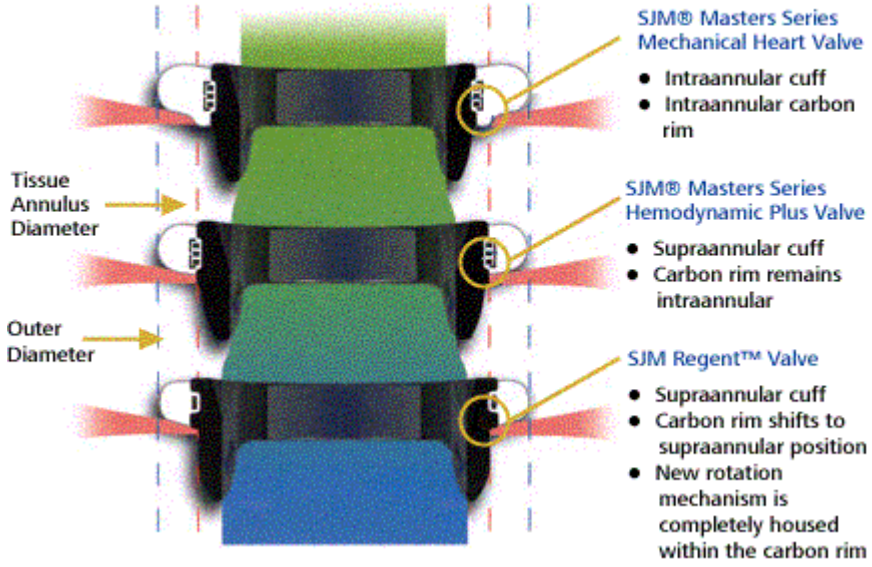

Figure 2.5: Evolutionary improvement of the SJM valves

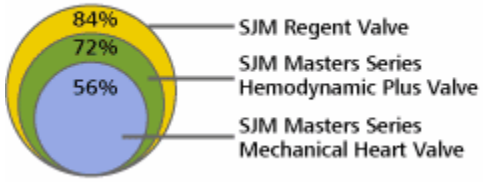

Figure 2.6: Orifice to annulus ratio of a 19 mm SJM valve.
The SJM regent valve offers up to an 84% orifice to annulus ratio.

2.3.2.2. Material

St. Jude Medical Inc. developed the first bileaflet mechanical heart valve with leaflets and orifice housing fabricated completely from pyrolytic carbon. The leaflets and orifice of the St. Jude Medical Regent MHV are constructed with Pyrolytic carbon using a graphite substrate containing tungsten. Pyrolytic carbon is biocompatible, wear resistant over the patient lifetime, and holds a high polished finish for increased thromboresistance.

2.3.2.3. Leaflets, Orifice, and Pivot Design

The design of the SJM valve exhibits two semicircular protrusions called pivot guards (Figure 2.7). The four hinges are machined within these two pivot guards, which are designed to protect the pivot mechanism from intrusion by sutures or calcium extension. The hinge design consists of a semicircular projection of the leaflet, called an ear, which mates to a recess of similar shape in the valve housing. During opening and closing, flat areas of leaflets contact flat areas of the orifice. This flat-to-flat contact is designed to evenly distribute pyrolytic carbon load and wear. Moreover, the mated-sphere pivot design allows the leaflet appendage to sweep all areas of the pivot depression (Figures 2.8 and 2.9). The opening angle of the leaflet relative to the plane of the valve housing is 84°, and the closing angle of the leaflet is 29°. The St. Jude Medical valve features an expansion region, called the thumbnail, located downstream of the hinge mechanism. The thumbnail is a small region of slight expansion machined into the housing to further increase the orifice area.

2.3.2.4. Clinical Results

The SJM valve and the Medtronic Hall valve are the most commonly implanted mechanical valves in the United States due to their superior and well documented hemodynamic performances and their low rates of valve related complications. The SJM valve achieves good results in terms of long-term rates of thrombogenicity, and has a lower reoperation rate than the Medtronic Hall. However, occasional loss of structural integrity, albeit a low percentage, have been reported (Akins, 1995).

A separate study by Zellner et al. showed, using 17 years of data, that the SJM valve had excellent clinical results and concluded that these valves were reliable prosthesis with low valve-related complications (Zellner, 1999).

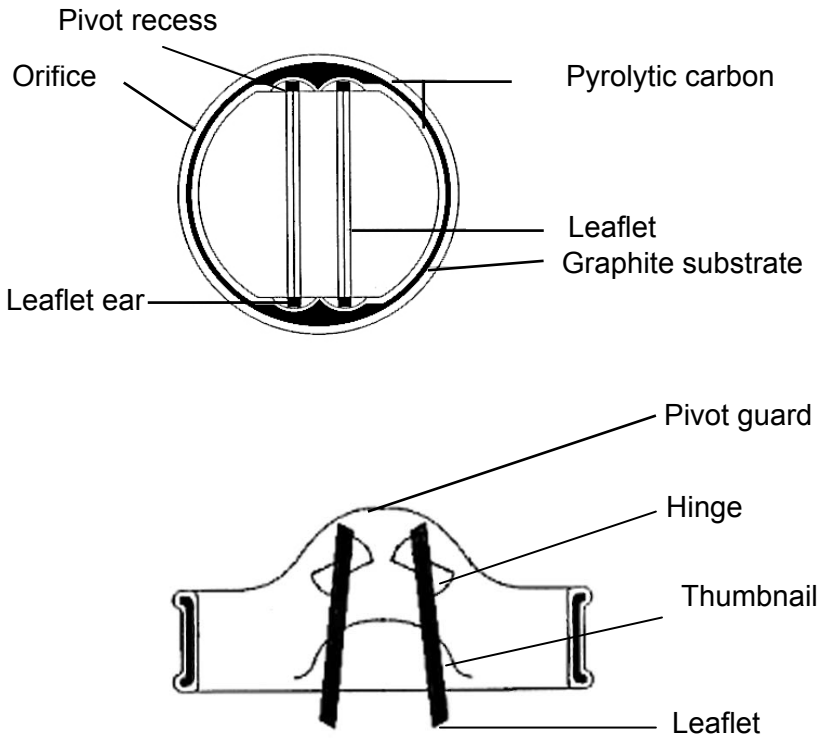

Figure 2.7: Upstream and top view of SJM Standard valve

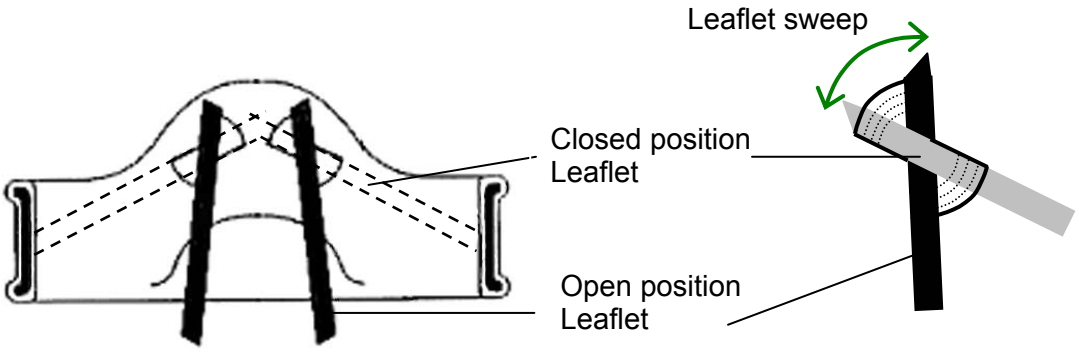

Figure 2.8: Pivot mechanism of the SJM valve

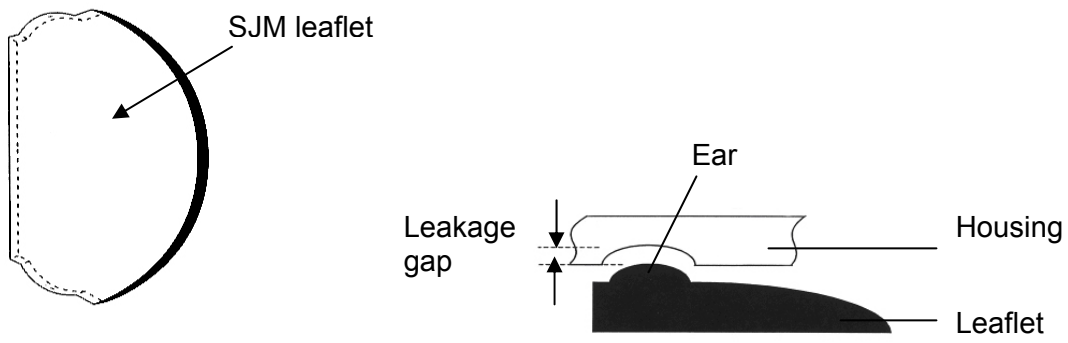

Figure 2.9: Leaflet design and close-up pivot of a SJM valve

2.3.3. CarboMedics Mechanical Heart Valve

2.3.3.1. CarboMedics (CM) Valve

The first CarboMedics bileaflet mechanical heart valve was implanted in 1986 and is today the second most widely used valve in the world. The CM valve shares many design features with the SJM bileaflet mechanical valve (Figure 2.10).

2.3.3.2. Material

The leaflets of the CarboMedics heart valve are constructed from pyrolytic carbon with a graphite substrate containing tungsten. The orifice is also constructed from pyrolytic carbon, but is reinforced with a titanium stiffening ring.

2.3.3.3. Leaflets, Orifice, and Pivot Design

The CarboMedics valve has a maximum opening angle of 78°. When the valve is fully open the flat angular leaflet ear rests on the curved profile in the pivot recess. This point of contact has the potential to generate increased stress, thus creating pyrolytic

carbon wear. Also, the pivot recess of the CM valve does not allow complete sweeping by the leaflet appendage, leaving an unswept area (Figures 2.11 and 2.12). The CM valve design does not have a pivot guard, but it is also able to rotate within the sewing ring.

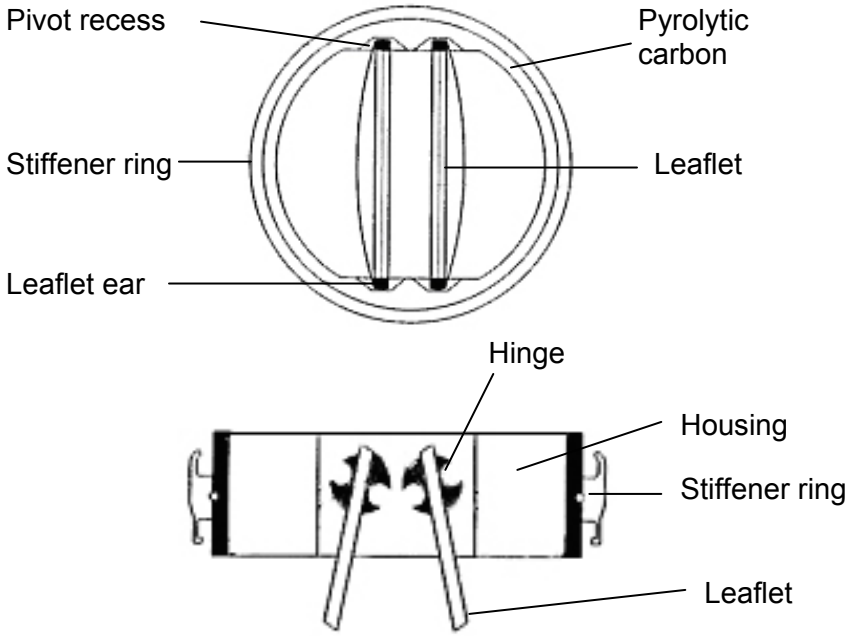

Figure 2.10: Upstream and top view of CM valve

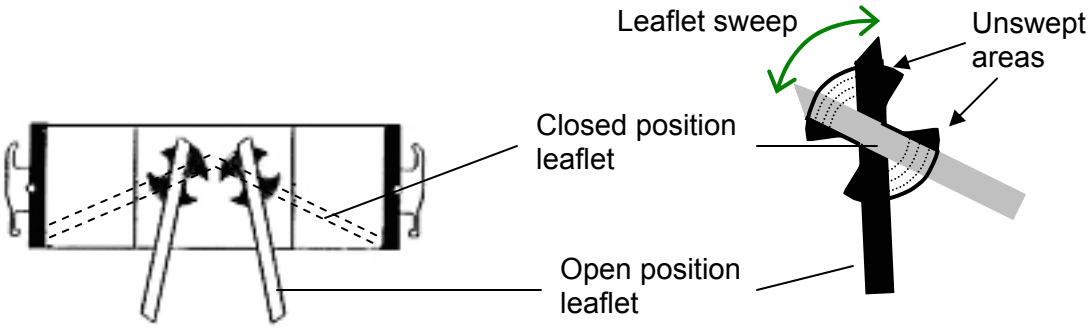

Figure 2.11: Pivot mechanism of the CM valve

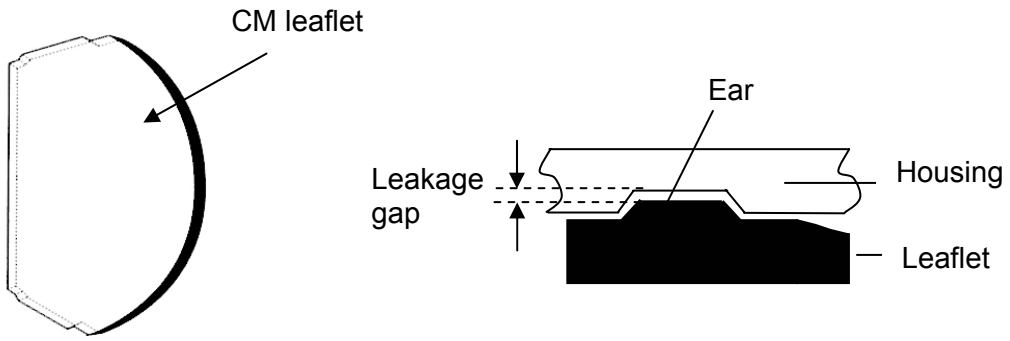

Figure 2.12: Leaflet design and close-up pivot of a CM valve

2.3.3.4. Clinical Results

The clinical performance of the CarboMedics valve based on transvavular pressure and incidence of thromboembolism is just behind the St. Jude Medical valve and the Medtronic Hall valve (Akins, 1995). However, a study performed by Dalrymple-Hay demonstrated that the rate of operative mortality and valve-related complications for the CarboMedics valve compares favorably with that of other mechanical prostheses (Dalrymple-Hay, 2000). In another study, Jamieson and coworkers showed that the CarboMedics valve, implanted in multiple positions, has satisfactory overall clinical performance (Jamieson, 2000). In a study performed over 14 years, Aagaard et al. showed that the CarboMedics valve was highly reliable as evidenced by no mechanical failure, valve dysfunction, or structural deterioration and a low incidence of valve related complications. Implantation of the CarboMedics valve was shown to be an excellent solution for aortic valve replacement in young adults with aortic valve disease (Aagaard, 2003). Minakata and coworkers found that in early and intermediate follow-ups with patients using CarboMedics prostheses the valve demonstrated satisfactory clinical performance early on and acceptable mid-term performance (Minakata, 2002).

2.3.4. Valve Comparison

2.3.4.1. Design

Both the SJM and the CM valves are low-profile bileaflet prosthesis. However, they exhibit some design differences. The leaflets of the SJM valve open to 85^{o} with a travel arc of 55^{o} to 60^{o}, while the leaflets of the CM valve open to 78^{o} with a travel arc of 53^{o}. The hinge design of the CM valve is very similar to that of the SJM valve, but its geometric profile has sharper corners (Figure 2.13). Both valves are made with pyrolytic carbon and can rotate within the sewing ring, but only the CarboMedics valve has a titanium stiffening ring.

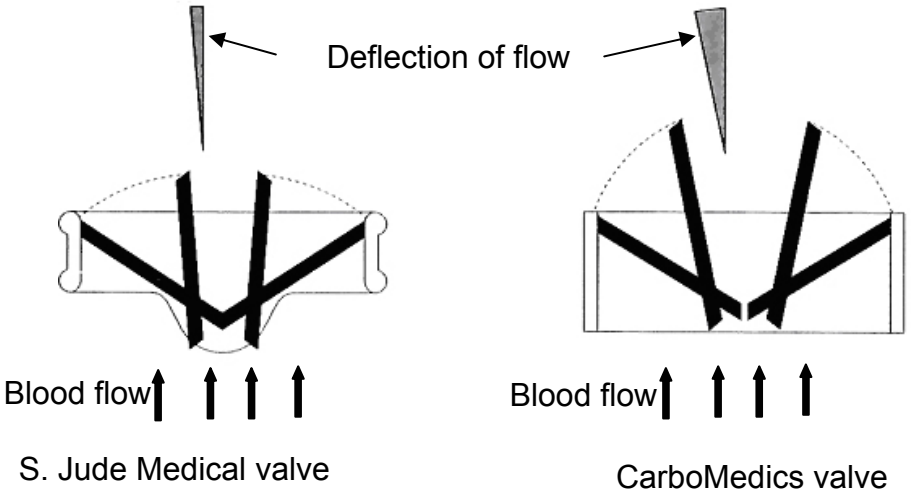

Figure 2.13: Opening angle and travel arc of CM and SJM valves

2.3.4.2. Clinical Results

Some structural failures of the St. Jude Medical valve, such as leaflet fracture or dislocation have been reported (Akins, 1995), but no failure of the CarboMedics valve has been reported (Aagaard, 2003). This structural integrity may be attributable to the titanium stiffening ring of the CM valve. A study done by Chang et al. showed that SJM

and CM valves have no discernible differences in clinical performances over 10 years (Chang, 2001). It should be noted, however, that compared to the CM valve, the SJM valves have been more extensively used and, consequently, have more follow up data.

2.4. Previous Investigations

2.4.2. Hinge Flows

Occasional leaflet embolization and pivot rupture have revealed that the pivot region is a crucial point where shear stress and wear are concentrated. Additionally, the bileaflet mechanical valve is usually preferred to the tilting disk valve because of its lower pressure gradient. However, this advantage may be lost due to greater regurgitation, especially through the hinges. Therefore, the hinge region appears to be one of the most critical components of a bileaflet mechanical heart valve since it directly affects valve durability, fluid dynamics, functionality, and thrombus formation (Vallana, 1992).

Studies by Shipkowtiz et al. showed that leaflet position, pivot location, and orifice height influence the pressure distribution across the valve and therefore the opening angle (Shipkowtiz, 2002). They observed that the leaflets of the ATS valve did not open completely while those of the SJM leaflets did. It is generally agreed that valves with large opening angles have better hemodynamics, a less perturbed flow pattern, and less turbulence. Thus, leaflet motion and consequently, the pivot region are important parameters of valve design.

The constricted region of the hinge geometry coupled with the high cross-valvular pressure gradients during closure produce elevated flow velocities and high turbulent shear stresses. Investigation of flow structures within the hinge of a Medtronic Parallel (MP) valve in the mitral position revealed a vortex in the inflow channel, disturbed flow, and multiple stagnation zones (Gross, 1996). These flow conditions may inhibit washing

in the MP pivot and thus contribute to the thrombosis formation. These findings were supported by clinical results which revealed high early thrombus formation within the MP hinge pocket. These flow phenomena were also observed by Ellis et al. and were found to correspond to regions of elevated shear stress (Ellis, 1996). Reynolds shear stresses near the inflow channel wall were greater than 6,000 dyn/cm^2, which is significantly greater than the accepted threshold level of blood damage of 4,000 dyn/cm^2 (Sallam 1984).

Undesirable flow phenomena such as vortex formation and stagnation regions were observed in the Medtronic Parallel (MP) hinge region but not in the SJM hinge region (Gao, 1999). The differences in flow patterns may be caused by variations in pivot geometry, since the Medtronic Parallel hinge exhibits abrupt changes in geometry while the SJM pivot has relatively smooth contours. The active leaflet motion of the SJM valve and streamlined hinge design may restrict the persistence of separation zones and regions of flow stagnation leading to reduced levels of mechanically induced tromboembolic events. Ellis investigated the influence of the hinge dimension. He suggested that the hinge flow dynamics of the 23 mm SJM Regent were superior to those of the 25 mm SJM Standard in studies with both valves placed in mitral position (Ellis, 1999). The highest peak leakage velocity and turbulent shear stress recorded in the 25 mm SJM Standard valve were 3.42 m/s and 7,400 dyn/cm^2, while the 23 mm SJM Regent valve achieved lower leakage velocity and turbulent shear stress of 1.52 m/s and 2,600 dyn/cm^2.

Studies of the SJM valve hinge recess are usually completed by an investigation of the thumbnail region. The thumbnail region is characterized by two recirculation zones, which bound a skewed forward flow. This complex and unsteady flow field may reduce the residence time of stagnant flow and clear any forming clots from the region (Ellis and Travis, 2000; Ellis 2000).

The comparative study of Leo et al. measured the velocity magnitudes and the turbulent shear stress levels within the hinge design of different hinge designs in the mitral position (Leo, 2002). Velocity and turbulent shear stress magnitudes up to 3.17 m/s and 5,640 dyn/cm^2 were recorded within the CarboMedics hinge, while corresponding values of 1.5 m/s and 2,600 dyn/cm^2, respectively, were found in the SJM Regent hinge. The abrupt changes in the hinge geometry of the Medtronic Parallel valve lead to even higher leakage velocities and turbulent shear stresses of 4 m/s and 8,000 dyn/cm^2, respectively. Leo concluded that the hemodynamic performance within the 23 mm CarboMedics hinge is between that of a 27 mm Medtronic Parallel and a 23 mm SJM Regent hinge.

Travis et al. studied different aspects of pivot geometry that could influence thrombogenic valve potential (Travis, 2001). He found that the leakage gap width of the bileaflet valve hinge had a significant effect on platelet secretion and anionic phospholipid expression. He also concluded that valve size and pivot geometry had, in comparison, only limited impact on platelet disruption.

2.4.3. Leakage Jets

Retrograde flow through mechanical heart valves can be divided into two fluid phenomena. At the beginning of the closing phase, a large spike in regurgitant flow, called squeeze flow, occurs. The second regurgitant flow category corresponds to a velocity regurgitant flow that persists after valve closure.

2.4.3.1. Squeeze Flow

Squeeze flow is observed in bileaflet and tilting disc prosthetic heart valve designs. It is a result of rising pressure between the leaflet and the valve housing, and its velocity exceeds valve closing velocity. This flow is usually associated with cavitation

phenomenon (Graf, 1991) and is therefore important for MHV function. Cavitation is characterized by local vaporization of fluid when the pressure drops below the vapor pressure. In regions of higher pressure, the vapor bubbles collapse violently generating a pressure wave, fluid jet, and subsequent blood and valve material damage. Graf showed that smaller valves have a greater tendency for cavitation since valves with low leakage rates typically have very tight sealing at valve closure, which promotes the generation of high negative pressures and consequently lowers the cavitation threshold (Graf, 1991). High negative pressures of approximately 15 MPa can lead to velocities as high as 30-40 m/s within a gap width of approximately 50 μm (Bluestein, 1994; Graf, 1991).

2.4.3.2. Sustained Regurgitant Flow

Sustained regurgitant flow can be observed at the perimeter of closed occluders, i.e. between the leaflet and the valve body. For the case of the bileaflet mechanical valve, it also occurs at the B-datum line, between the two closed leaflets.

Meyer observed a sustained leakage flow of with a maximum velocity of 3.7 m/s and a maximum Reynolds shear stress of 10,000 dyn/cm^2 in the vicinity of a Bjork-Shiley Monostrut mitral valve (Meyer, 1997). Under identical aortic flow and pressure conditions, Ellis showed that the peak velocity magnitude in the SJM leakage jet was 0.8 m/s while that in the MP leakage jet was over twice as high at 1.9 m/s. Similarly, the maximum turbulent shear stress levels in the SJM and in the MP valves were 1,800 dyn/cm^2 and 3,690 dyn/cm^2, respectively. Similar results were found by Meyer with three different valve designs: CarboMedics, St. Jude Medical and Medtronic Hall (Meyer, 2001). Regurgitant flow velocities ranged from 0.7 to 2.6 m/s, while the maximum Reynolds shear stress varied between 450 and 3,600 dyn/cm^2. The St. Jude Medical valve displayed the lowest level of regurgitant velocities and stress. Another study by

Steegers et al. investigated the blood damage potential of turbulent shear stresses within the leakage jets of four mechanical valves in the mitral position (Steegers, 1999). All four valve designs exhibit characteristic leakage flow patterns. The maximum velocity and TSS obtained with the CarboMedics valve were 1.7 m/s and 80 Pa (800 dyn/cm^2), respectively. However, Blood Damage Index (BDI) within these leakage jets revealed significant differences, with the lower BDI occurring in the Sorin Bicarbon valve. Asymmetry in the leakage jets was also observed indicating that the jets could be influenced by differences in the leakage orifice width within manufacturing tolerances. This is consistent with the results of previous studies that have shown that axisymmetric jet assumption is not valid in the case of flow through a slot-like orifice. The shape of a leakage jet was shown to have a major impact on turbulence, and consequently on Kolmogorov length scale and blood damage. Rounded and wall leakage jets appear to cause less damage than free planar jets (Travis, 2002).

CHAPTER III

HYPOTHESIS AND AIMS

Animal and clinical studies have shown that the clinical performances of mechanical heart valves implanted in the aortic position were better than those in the mitral position due to a lower rate of thrombus formation and hemolysis (Krautzberger, 1978; Skoularigis, 1993; Minakata, 2002). Increased blood damage in the mitral position is believed to be predominantly influenced by leakage flow rather than valve material or forward flow. Valve designs deliberately include a degree of leakage flow upon valve closure to wash out critical regions and prevent flow stasis. However, this leakage flow, which is driven through narrow regions by a large cross-valvular pressure, also leads to elevated turbulent shear stresses and high velocities in the hinge regions. The superior results of the mechanical valves located in the aortic position may be due to less leakage flow upon valve closure as well as a more favorable forward flow pattern.

The specific aims of this study were structured to address the hypothesis that:

The hinge and near-hinge flow fields of a bileaflet mechanical heart valve are different under aortic or under mitral conditions. Similarly, the leakage jets emanating from a closed bileaflet mechanical heart valve differ depending on the valve position.

This hypothesis was addressed by the following specific aims.

Specific Aim1: ***Characterize the hinge and near-hinge flow fields of the 23 mm St. Jude Medical Regent and the 23 m CarboMedics bileaflet mechanical heart valves in the aortic position***

To accomplish this goal, two-component Laser Doppler Velocimetry was used to characterize the hinge and near-hinge velocity and turbulent shear stress fields of two bileaflet mechanical heart valves. Detailed flow maps were constructed and animated in time to reveal the spatial and temporal variation of the hinge and near-hinge flow fields. The study mainly focused on four instances of the cardiac cycle, namely mid systolic acceleration, peak systole, valve closure, and mid diastole. Regions of high shear stress where blood damage could occur were identified as well as stagnation sites where damaged blood element could accumulate and clot. These maps provide the first measurements conducted within the hinge region of bileaflet mechanical heart valves under aortic conditions. This study presents both qualitative and quantitative assessments of the hinge washout during diastole and the flow structures formed during systole.

Specific Aim 2: ***Identify the upstream leakage flow structures of the 23 mm St. Jude Medical Regent and the 23 mm CarboMedics bileaflet mechanical heart valves in the aortic position***

To accomplish this goal, three-component Laser Doppler Velocimetry was used to characterize the velocity and turbulent shear stress fields immediately upstream of two bileaflet mechanical heart valves. Detailed flow maps were constructed and animated in time to reveal the spatial and temporal variation of the leakage jet fields. These maps provide the first measurements conducted within the leakage jet regions of bileaflet mechanical heart valve under aortic conditions. This study presents both qualitative and

quantitative assessment of the leakage jet formation, persistence and dissipation during valve closure.

Specific Aim 3: ***Compare the clinically significant flow characteristics of the 23 mm St. Jude Medical Regent and 23 mm CarboMedics bileaflet mechanical heart valves in the aortic position with previous findings in the mitral position.***

Peak velocity magnitudes and turbulent shear stress levels during the forward flow phase and the closed phase were extracted from the data gathered to accomplish specific aims 1 and 2. These peak velocity magnitudes and TSS levels were compared to those previously published for the mitral position.

CHAPTER IV

EQUIPMENT AND MATERIAL

4.1 Prosthetic Heart Valves

4.1.1 St. Jude Medical Regent Mechanical Heart Valve

In this study the leakage jets and the hinge flow fields of a 23 mm St. Jude Medical (SJM) Regent valve in the aortic position were studied. In order to gain optical assess into the hinge region of this valve, a clinical-quality clear housing model was used. The leaflets were manufactured from pyrolytic carbon. Tolerances of the clear valve were identical to those of a clinical quality SJM Regent valve.

4.1.2 CarboMedics Mechanical Heart Valve

In this study the leakage jets and the hinge flow fields of a 23 mm CarboMedics (CM) valve in the aortic position were studied. A reverse engineered casted housing of a clinical 23 mm CM bileaflet mechanical heart valve was used to gain optical assess into the hinge region. The clear valve housing was a high quality reproduction of the clinical valve to ensure accurate representation of the hinge flow field to be studied. Leaflets were manufactured from pyrolytic carbon.

A clinical quality 23 mm CarboMedics bileaflet mechanical heart valve was used for the leakage jet experiments.

4.2 Flow Loop

4.2.1 Static Leakage Circuit

A static leakage flow circuit was designed as illustrated in Figure 4.1. A plastic bucket was used as a fluid reservoir. The valve chamber and the reservoir were linked

by ¾" PVC tubing connected by rubber tubing and hose clamps. Because the solution of glycerin and water used in this experiment had a density of 1.09 g/cm^3, the valve chamber was positioned 1.49 m below the reservoir level to ensure that the pressure head upstream of the closed prosthetic valve was 120 mmHg.

Both the 23 mm SJM Regent and 23 mm CM valves were mounted in the closed position under a 120 mmHg glycerin/water column to determine the static leakage flow rates. Subsequently, the valves were mounted in the closed position under 120 mmHg water column to capture the leakage jet sprays with a digital camera.

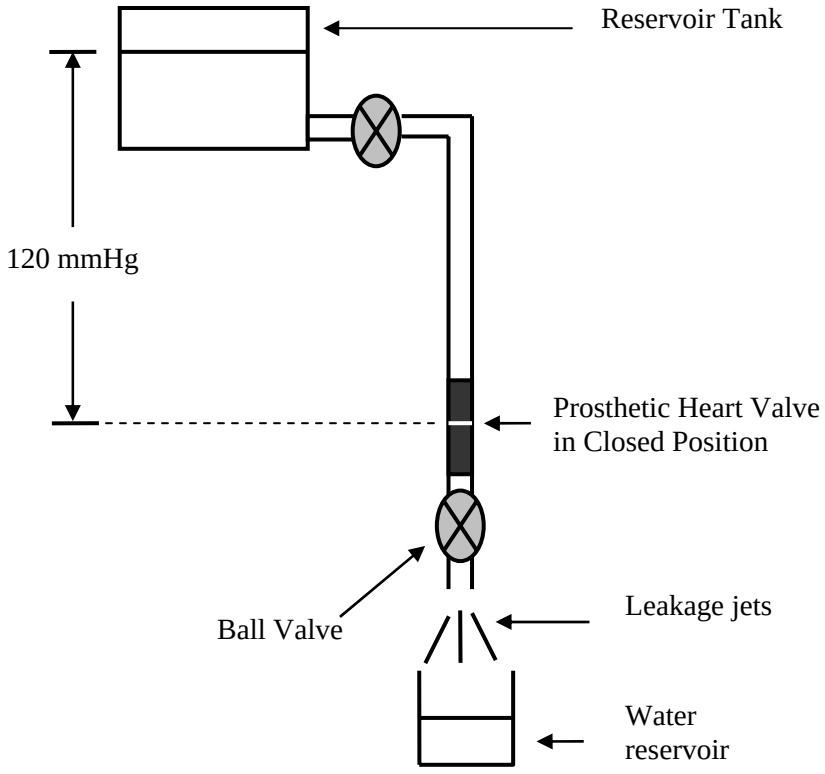

Figure 4.1: Static Leakage Circuit

4.2.2 Pulsatile Flow Loop

4.2.2.1 General Description

The experiments were conducted with the Georgia Tech left heart simulator. The flow loop consisted of a pneumatic pulsatile system, a reservoir, an aortic valve mounting chamber, a mitral valve mounting chamber, and resistance and compliance sections. The circuit was constructed with ¾" PVC tubing connected by rubber tubing and hose clamps.

A plastic bucket was used as a fluid reservoir. A pneumatic pulsatile pump drove the fluid through the loop. The pneumatic pulsatile system consisted of an air compressor (Ultra AirPac T-2820P, Rietschle Thomas, Sheboygan, WI), a throttle valve (R18-04-GOGO, Wilkerson Corporation, Englewood, CO), three pneumatic solenoid valves (model 130B-111CAAA, Mac Valves Inc., Wixon, MI), a computer interfaced with a custom made controller, and a flexible bladder sealed within an acrylic chamber. The intensity of bulb compression was regulated by the air pressure regulating valve, or throttle valve, while the frequency of bulb compression was controlled by the computer. During the systolic phase of the cycle the solenoid valve connecting the air compressor and the acrylic chamber was opened, the pressure within the acrylic chamber increased, compressing the flexible bulb and driving the fluid through the aortic valve while the mitral valve was closed. During the diastolic phase of the cycle the bulb relaxed, the aortic valve closed, and the fluid was driven through the open mitral valve into the bulb. Bulb relaxation was achieved by opening the two remaining solenoid valves. The air within the acrylic chamber was then in contact with the atmosphere, and the pressure within the chamber decreased allowing the bulb to refill. The computer controlled the opening and closing of the pneumatic solenoid valve with an accuracy of 1 ms.

To maintain physiologic conditions and generate physiologic flow and pressure waveforms, a series of clamps on the flexible rubber tubing were adjusted, and a vertical cylinder and a highly flexible rubber tubing section were used as compliance.

Pressure and flow were recorded as close as possible to the test section. Aortic pressure was recorded downstream of the valve mounting chamber while the ventricular pressure was recorded upstream.

4.2.2.2 Physiologic Conditions

The flow system was adjusted to maintain the following conditions: Cardiac cycle duration of 860 ms, systolic duration of 300 ms, heart rate of 70 beats/min, peak systolic flow rate of 25 L/min, cardiac output of 5 L/min, and aortic pressure of 90-100 mmHg. Wave forms obtained for both valves are shown in the results section.

4.2.2.3 Flow Loop for Hinge and Leakage Jet Studies

The flow loop set up for the CM valve was similar to the one for the SJM valve but with a bigger compliance section. The same flow loop was used to conduct both hinge and leakage jet investigations (Figure 4.2).

4.3 Working Fluid Description

4.3.1 Static Leakage Experiments

The composition of the working fluid was 40 % glycerin and 60% water by volume. The kinematic viscosity of 3.5 cSt was close to the blood viscosity. The density of this solution was 1.09 g/cm^3.

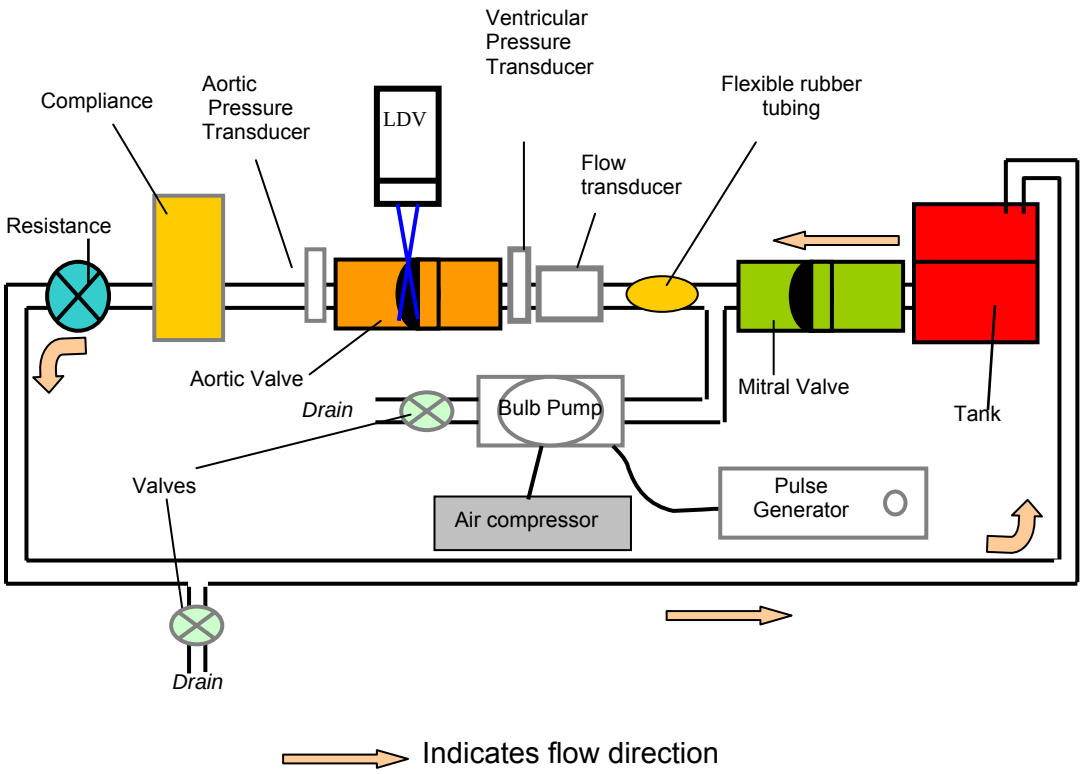

Figure 4.2: Pulsatile flow loop

4.3.2 Laser Doppler Velocimetry Experiments

4.3.2.1 Refractive Index and Viscosity

A solution of glycerin, water, and saturated aqueous sodium iodide was used as a blood analog fluid. The composition by volume of the working fluid was 79% saturated aqueous sodium iodide solution, 20% glycerin, 1% water. Although the density of blood (1.05 g/cm^3) could not be matched with such a solution (1.69 g/cm^3), the kinematic viscosity of the solution was close to that of blood at high shear rates (3.5 cSt). The solution was adjusted to have a refractive index of 1.49, which is the same as that of the Plexiglas valve mounting chamber.

Matching the kinematic viscosity of blood enforced the dynamic similarity between the blood flow through the prosthetic valve within the human aorta and the fluid flow through the same prosthetic valve within the mounting chamber. The kinematic

viscosity was measured using a calibrated viscometer (Cannon-Fenske Routine, Size 75, Cat # 9721-B56, Cannon Instrument Company, State College, PA).

Matching the refractive index eliminated lens effects and optical distortion of the laser beams. The refractive index of the solution was measured using a hand-held refractometer (Model 2192, Extech, Japan).

4.3.2.2 Flow Seeding

The flow was seeded with neutrally buoyant silicon carbide particles (Model 10081, TSI Inc, St Paul, MN) with a nominal diameter of 1.5 μm. The diameter of these particles was comparable to that of human platelets. The solution was filtered regularly through a 5 μm filter cartridge (Model C1, US Filter Plymouth Product, Warrendale, PA) to remove any contaminants.

4.4 Measurement Techniques

4.4.1 Flow Rate

Flow rate was measured with a 24 mm in-line ultrasonic flow probe (model T108, Transonic Inc, Ithaca NY) interfaced with a Medical Volume Flow Meter (CardioMed CM-4008, Medi-Stim AS, Norway) using a custom made adapter cable. The flow probe was calibrated using a calibrated rotameter (Precision bore tube flowrator tube No. B8-27-10/77, F&P Co). A steady pump was used to drive water through a closed flow loop (Figure 4.3). For each pump speed, the rotameter value, the reading on the CardioMed display, and the voltage output of the flow meter were recorded. The flow rate given by the rotameter was plotted against the voltage output and against the flow rate value given by the CardioMed. A linear regression equation was calculated for both calibration curves (Figure 4.4).

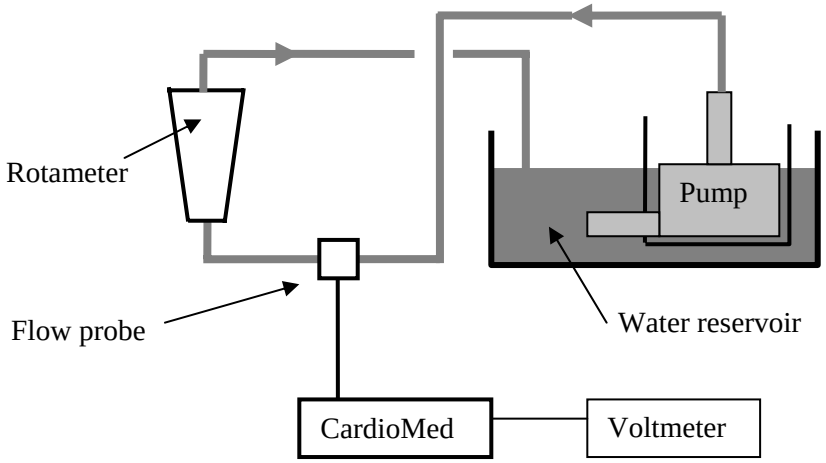

Figure 4.3: Flow loop used to calibrate flow probe

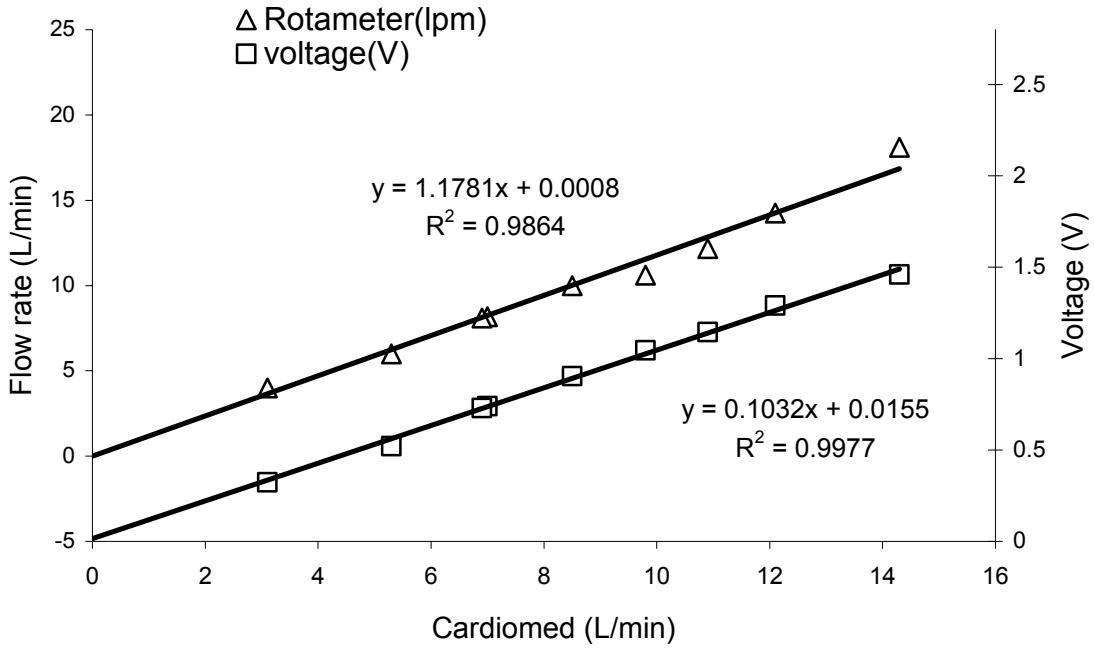

Figure 4.4: Calibration curve for flow meter

4.4.2 Pressure

Aortic and ventricular pressures were measured by two pressure transducers (Model 43-272, Baxter Healthcare Corporation, Irvine, CA) interfaced with a Physiological TraCe System (CardioMed CM-4008, Medi-Stim AS, Norway). The voltage signal from the pressure transducer and the reading on the CardioMed display were calibrated by connecting the pressure transducer to a water column of varying height. For each water height the voltage output of the transducer, the reading on the CardioMed display, and the water column height were recorded. Water column height was plotted against the voltage output and against the pressure value given by the CardioMed. A linear regression equation was calculated for both calibration curves (Figure 4.5).

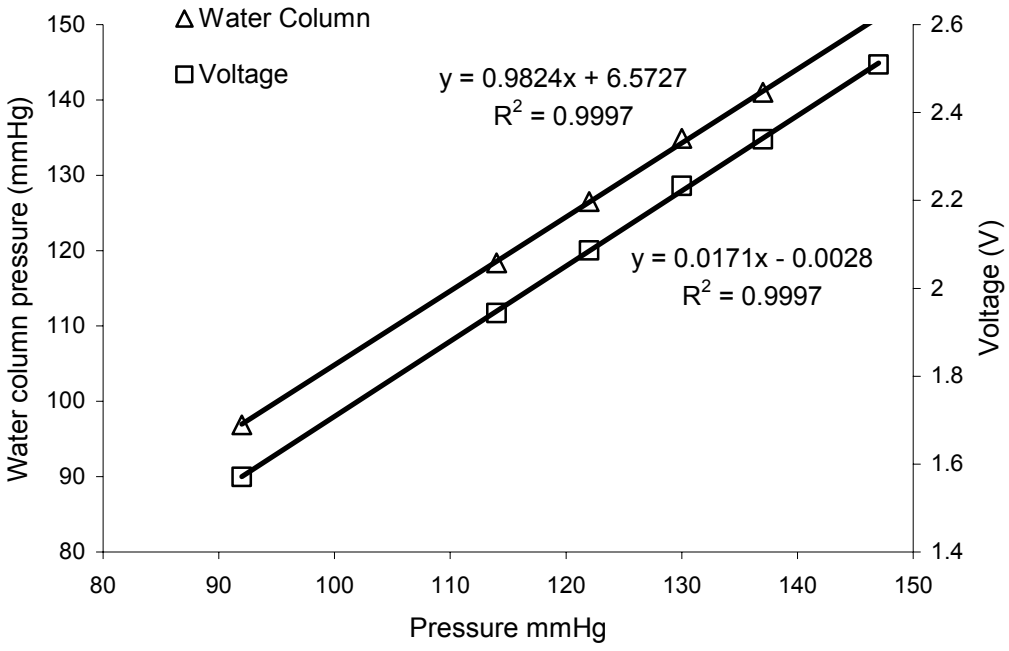

Figure 4.5: Calibration curve for pressure transducer

4.4.3 Velocity

Laser Doppler Velocimetry (LDV) is a technique used to measure fluid velocity accurately by detecting the Doppler frequency shift of laser light that has been scattered by small particles moving with the fluid. It provides velocity data at a single point. Using a traverse system to move the laser probe volume point-by-point it is possible to perform an area investigation. Since laser light is used as a measuring tool, the technique is non-invasive and can reach difficult measurement locations without disturbing the flow (Figure 4. 6).

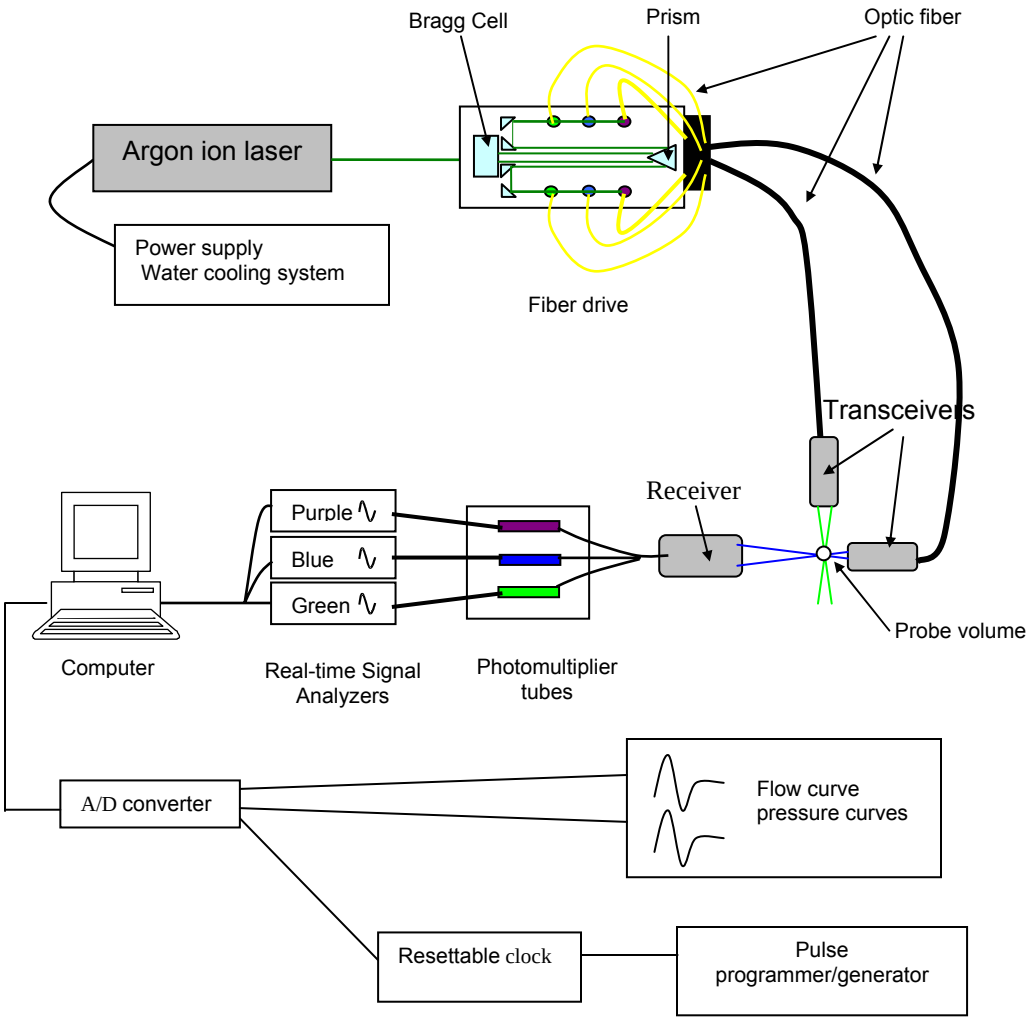

Figure 4.6: Laser Doppler Velocimetry system setup

4.4.3.1 Beam Specifications

A 5 W multi-line argon-ion gas laser (Innova 70, Coherent, Santa Clara, CA) was used to produce the primary laser beam. The intense primary laser beam was then directed towards a fiber drive (Model FBD 1340, TSI Inc, Shoreview, MN). A Bragg Cell within the fiber drive splitted the incoming laser into two parallel beams of equal intensity but of different frequency. A frequency shift was added to one beam of each focal pair; one beam (called the zero order beam) had the frequency of the incident beam while the other (called the first order beam) was shifted 40 MHz in frequency. The two beams were then manipulated by two dispersion prisms that separated the beams into individual colors. The six more powerful beams were directed into six fiber optic couplers, two green beams (with a wavelength of 514.5 nm), two blue beams (488 nm), and two violet beams (476.5 nm). This process created two beams for each color, for a total of six beams. The couplers linked the fiber drive with two transceivers (Models XRV 1104 and XRV 1204, TSI Inc, Shoreview, MN) via a series of fiber optic cable. A 100 mm focal length lens was used to transmit the beams towards the interrogation region of the model.

4.4.3.2 Probe Volume Specifications

The intersection of two coherent beams created a probe volume with the shape of an ellipsoid of revolution. Because the beams are coherent sources, the intersection of a pair of beams created interference fringes (pattern of bright and dark bands of light). Figure 4.7 shows the intersection of two coherent beams. l_m represents the larger dimension of the probe volume, d_m is the smaller dimension, d_f is the fringe spacing, α is the half-angle of the beam intersection, d is the beam spacing, and f is the beam focal length.

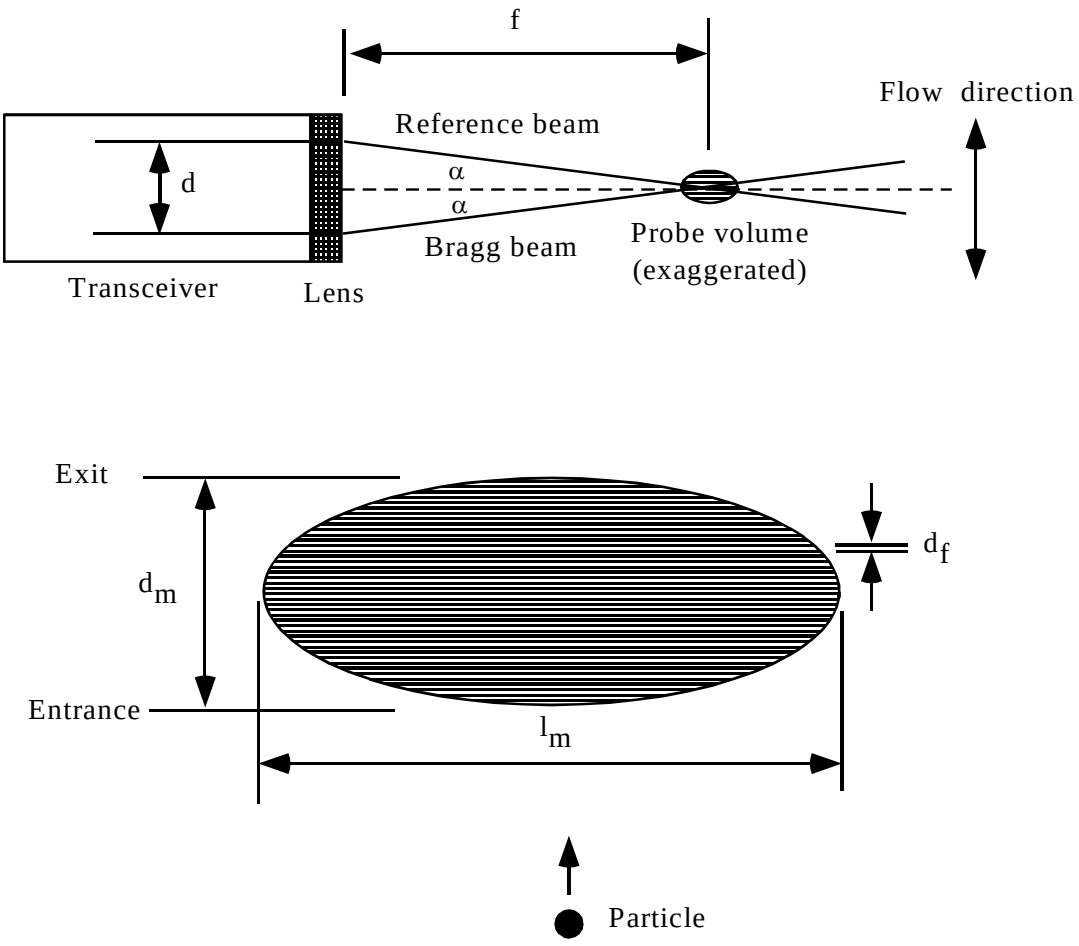

Figure 4.7: Probe volume formed by the intersection of a laser beam pair

Calculation of Probe Volume Dimensions

Supposing that the beams are intersecting in air, α can be calculated from d and f with the following equation.

$$\tan\alpha = \frac{d/2}{f}$$ Equation 3.1

The dimensions of the ellipsoidal probe volume formed by a couple of beams intersecting in air are given by

$$d_m = \frac{4\lambda f}{\pi D_e E} \quad \text{and} \quad l_m = \frac{d_m}{\tan\alpha}$$ Equations 3.2-3.3

Where λ is the wavelength of the beam in air

f is the focal length of the transceiver lens

D_e is the initial beam diameter

E is the beam expansion ratio

If the fluid of interest is not air, optical corrections have to be added. Indeed when the beams cross they will be refracted according to Snell's Law, and the resulting probe volume dimensions will be different than those just calculated (Figure 4.8).

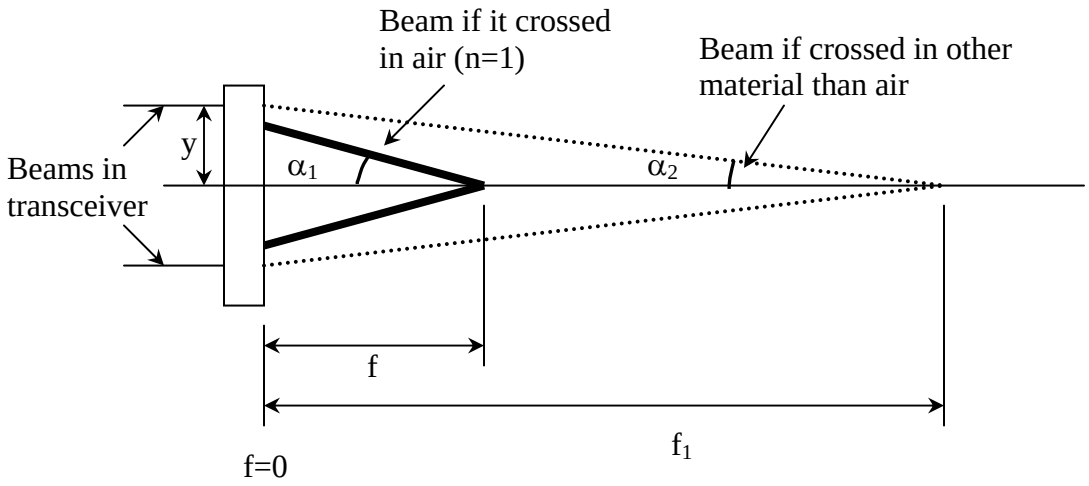

Figure 4.8: Calculation of laser beam crossing in different working mediums

By Snell's law, the half angle changes as the beams go from air into another material by:

$$n_1 \sin\alpha_1 = n \sin\alpha \qquad \text{Equation 3.4}$$

Where n is the refractive index of air

n_1 is the refractive index of liquid

α is the beam intersection angle in air

α_1 is the beam intersection angle in liquid

The change in wavelength of the beam is calculated in a similar fashion:

$$n_1\lambda_1 = n\lambda \qquad \text{Equation 3.5}$$

Where $\lambda$is the wavelength of the laser light in air

λ_1 is the wavelength of the laser light in liquid

$$\tan\alpha_1 = \frac{y}{f_1} \text{ and } \tan\alpha = \frac{y}{f} \qquad \text{Equations 3.6 -3.7}$$

so that $$f_1 \tan\alpha_1 = f \tan\alpha \qquad \text{Equation 3.8}$$

which gives

$$f_1 = \frac{f \tan\alpha}{\tan\alpha_1} = f \frac{\sin\alpha}{\sin\alpha_1}\frac{\cos\alpha_1}{\cos\alpha} = f \frac{\frac{n_1}{n}\sin\alpha_1}{\sin\alpha_1}\frac{\cos\alpha_1}{\cos\alpha} \qquad \text{Equation 3.9}$$

and finally

$$\therefore f_1 = f \frac{n_1}{n}\frac{\cos\alpha_1}{\cos\alpha} \qquad \text{Equation 3.10}$$

The probe volume dimensions in a material other than air can then be obtained with equations 3.2 and 3.3. The probe volume dimensions actually differ for the different color beams since the dimensions depend on wavelength. The overall resultant probe volume is the region formed by the intersection of the one, two, or three ellipsoid volumes. The major axis of the ellipsoid was 137.7 $\pm$ 5.3 μm and the minor axis was 18.3 $\pm$ 0.7 μm.

Fringe Patterns

Because the beams were coherent sources, the probe volume was a stable interference pattern characterized by alternating light and dark fringes. When a particle

passed through the probe volume formed by the intersection of all beam pairs, it scattered the light from within the probe volume, generating a light signal called a Doppler Burst. When a particle crossed a destructive (dark) fringe, the light intensity was zero. When the particles crossed a constructive (bright) fringe, a peak in the light signal was observed. The light intensity varied in a Gaussian fashion from the probe volume entrance to the exit. Thus, the signal amplitude modulated as the particle alternated between dark and bright fringes. A maximum light signal was recorded when the particle crossed the central light fringe of the probe volume. The crossing of the particle through the alternate light and dark fringes results in a characteristic “on-off intensity” Doppler burst as illustrated in Figure 4.9.

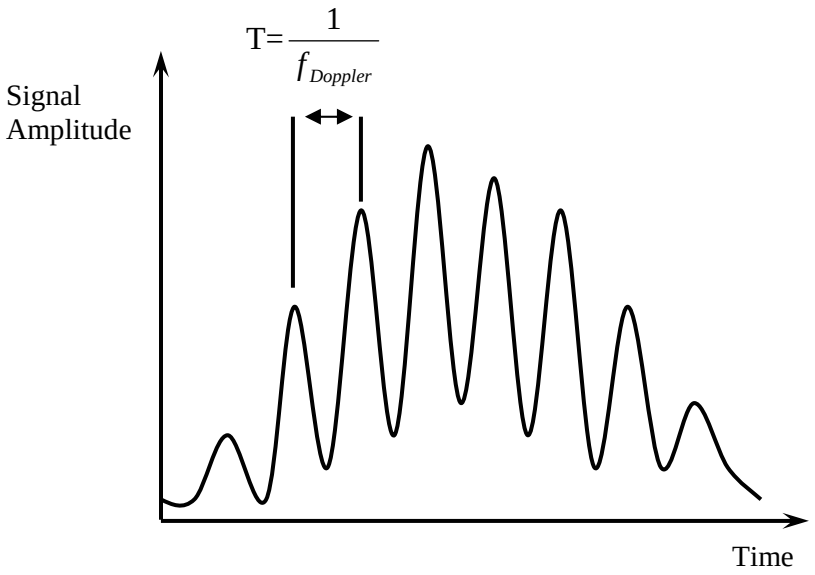

Figure 4.9: Doppler pulse obtained from light scattered by particle

The frequency shift introduced by the Bragg Cell to the input beams acted to offset the Doppler frequency, thereby moving the zero velocity away from the zero frequency and allowing particles of near-zero velocity to generate Doppler burst. The

frequency shift was also necessary to distinguish between positive and negative velocity fluctuations that occurred in each of the measured directions.

The time required for a particle to traverse the probe volume, called its gate time, was recorded for each valid particle. In order to measure multiple velocity components of a given particle, the probe volumes formed by each beam pair were aligned so that they intersected at the same spatial location and were positioned orthogonal to each other.

4.4.3.3 Photomultiplier Tubes

Particles moving through the measurement volume scattered light of varying intensity. However, the light signals were usually too weak to be analyzed and photomultipliers (PM) were needed to amplify and convert the input to a voltage output for analysis. A fiber optic receiver (Model RCV 2308 L, TSI Inc, Shoreview, MN) focused on the probe volume captured the Doppler burst from particles and transmitted them to three photomultiplier tubes (Model RCM 2300 L S, TSI Inc, Shoreview, MN) via a series of fiber optic cables. The PM tubes reproduced the light as a voltage at a gain determined by the software-controlled PMT high voltage. The advantage of using PMT over photodiodes was the high gain and low noise levels, which allowed the system to operate with a light signal of low intensity. The light signal picked up by the photodetectors contained the Doppler signal as well as the frequency shift from the Bragg Cell.

4.4.3.4 Signal Processors

The signal was then processed by three Real-Time Signal Analyzers (Model RSA1000 L, TSI Inc, Shoreview, MN) using the fast Fourier transform method. The signal was then downmixed, which is a process that removes the 40 MHz shift and leaves the Doppler frequency. After downmixing the signal was passed through a low

pass filter, which eliminated high frequency noise. The velocity components of each particle were calculated from the spacing between adjacent fringes and from the frequency with which the particle crossed the fringes. The spacing between fringes in the probe volume, which was dependent upon the laser wavelength and the angle between beams, could be obtained from optical theory. Since the velocities were calculated from properties of light no calibration of the Laser Doppler Velocimetry system was required.

4.4.3.5 Resettable Clock

For pulsatile flow measurements, data acquisition had to be synchronized with the cycle time. A 16 bit resettable clock (TSI Inc, Shoreview, MN) was interfaced with the pulse duplicator. A 64 kHz sampling frequency was selected for a cardiac cycle time of 860 ms. A total of 55,255 time points could be recorded during an entire cardiac cycle. This clock was also used to restrict measurements to only part of the cycle for the leakage jet measurements.

4.4.3.6 A/D Converter

A three channel, 12-bit analog/digital converter (Model External Input Model Ext1000, TSI Inc, Shoreview, MN) was used for the analog to digital conversion. The three channels were connected to the resettable clock, the flow meter, and the pressure transducer, respectively.

4.4.3.7 Software

The Real-Time Signal Processors were interfaced with a computer. Data were recorded via Aerometrics System Software, Particle Acquisition and Analysis, Version 0.80.

CHAPTER V

EXPERIMENTAL PROTOCOL

5.1 Static Leakage Experiments

A valve chamber with the mechanical valve of interest in the closed position was placed within the open flow circuit shown in Figure 4.1. The lowest ball valve was closed and the circuit was filled with fluid. Once the circuit was full, the ball valve was opened, and air was drained from the system. When the air was removed, the leakage volume was collected over a 30 second interval. Three to five runs were performed to ensure accuracy. Between each run, the valve chamber was removed from the circuit and the mechanical valve opened and closed again to allow possible leaflet alignment variation upon closure.

This experiment was performed with the 23 mm St. Jude Medical Regent clear housing valve, 23 mm CarboMedics clear housing valve, and 23 mm CarboMedics clinical valve.

5.2 Laser Doppler Velocimetry

5.2.1 General

In each experiment the receiver and transceivers were positioned about the valve chamber as shown in Figure 5.1. The violet laser beams were coupled to the one component transceiver. Because the violet beams were the weakest, the transceiver was placed in the forward scatter position with respect to the receiver to maximize the data acquisition rate. The blue and green laser beams were coupled with the two component transceiver. This transceiver was placed in the side scatter position with

respect to the receiver. The green laser beams, which were the most powerful, were used to measure axial velocity.

In all of the experiments, measurements were acquired in coincident mode. In order for a Doppler burst to be recorded as a valid data point in coincident mode, it must be received by all three channels at the same time for three-component data, and by both channels for two-component data. The minimum signal to noise ratio was set to 65% to ensure a good velocity signal. The gate scale was set at 1 to ensure that all velocity components were acquired simultaneously for each measurement. The sampling rate was set at 5 MHz if velocities above 2.45 m/s were not expected or to 10 MHz if higher velocity were expected.

At each location 21500 measurements were randomly acquired. The number of measurements was chosen to ensure an average of 500 measurements within the 20 ms cycle phase windows used for data analysis. If the data acquisition rate was too slow at a particular location, a minimum number of 8600 measurements were acquired to ensure an average of 200 measurements per cycle phase window.

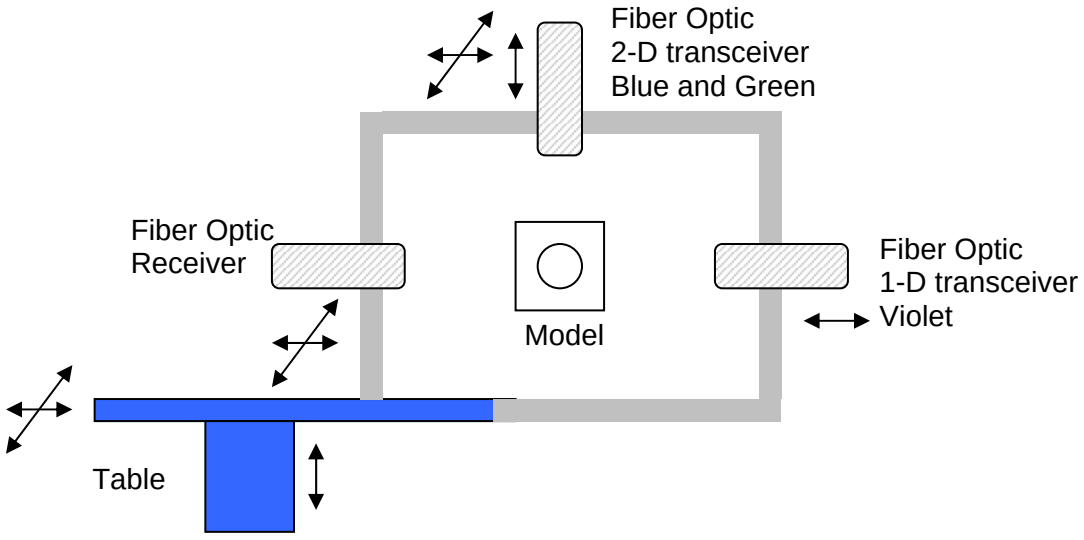

Figure 5.1: Transceiver and receiver orientation around flow model

The receiver and transceivers were bolted to a traversing stage. This apparatus allowed manual positioning of the probe volume with an accuracy of 0.001 inch.

5.2.2 Hinge Study

5.2.2.1 LDV System Setup

Hinge measurements were taken within the hinge and in the near hinge region. Due to the proximity of the hinges to the outer surface of the valve chamber and to the motion of the leaflets within the hinge region, the use of the receiver appeared to be unfeasible, and three-component Laser Doppler Velocimetry was not possible. The hinge study was therefore conducted with two-component Laser Doppler Velocimetry in backscatter mode so that a single optic fiber probe acted as a transmitter as well as a receiver.

The backscatter arrangement of the LDV setup is shown in Figures 5.2, 5.3 and 5.4. The green beams were used to measure the axial velocity component, V_1. The blue beams were used to acquire the V_2 velocity component.

5.2.2.2 Interrogation Sites

The flat inside surface of the housing wall, called the flat level, was chosen as the reference plane. Each investigation plane was located at a determined distance from the flat level. The flat level was found by traversing the probe volume through the housing towards the central region of the valve. The first appearance of particle Doppler bursts corresponded to the limit between flow and the housing, and was considered to be the flat level.

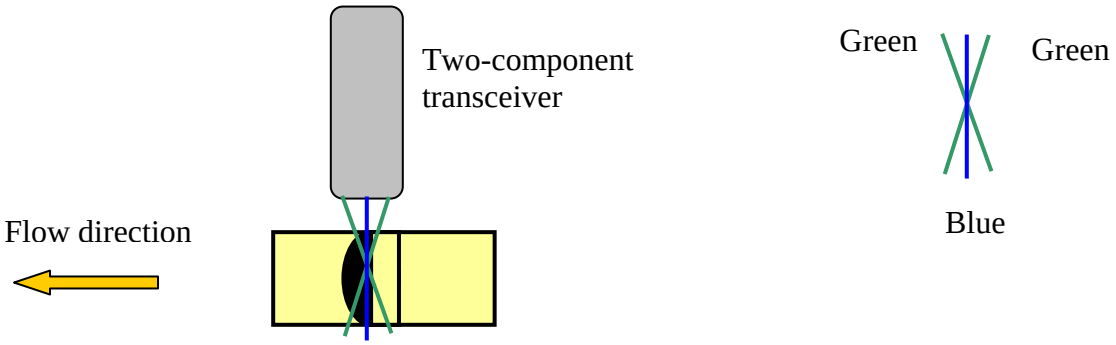

Figure 5.2: Front view of two-component Laser Doppler Velocimetry hinge flow m easurements, in back scatter mode

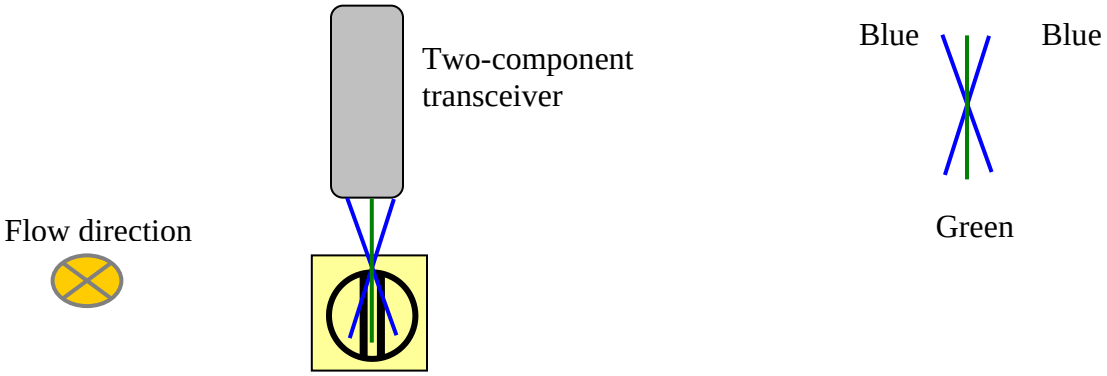

Figure 5.3: Side view of two-component Laser Doppler Velocimetry hinge flow measurements, in back scatter mode

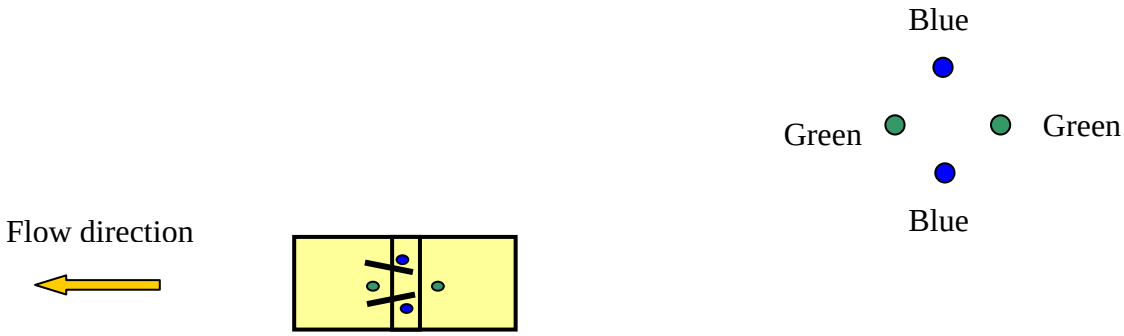

Figure 5.4: Top view of two-component Laser Doppler Velocimetry hinge flow measurements, in back scatter mode

CarboMedics Valve

Measurements were conducted along four planes shown in Figures 5.5 and 5.6. Table 5.1 shows the number of locations investigated at each level of interest within the hinge and thumbnail regions.

Table 5.1: Number of LDV measurement locations at each level of interest

Plane of Interest	Number of locations
390 μm above the flat	101
195 μm above the flat	138
level with the flat	156
1 mm below the flat	90

Incremental resolution was 0.203 mm in the x and y directions at and above the flat level. Incremental resolution was 1.06 mm and 0.406 mm in the x and y directions below the flat level. At each measurement site, between 10,000 and 21,500 coincident velocity measurements were acquired.

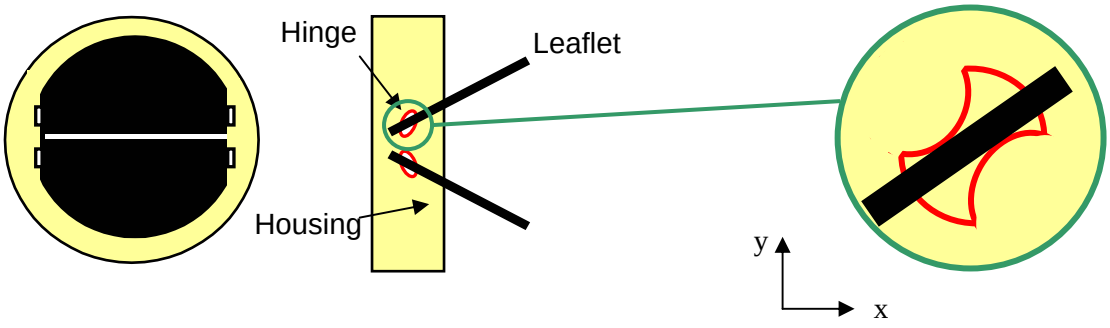

Figure 5.5: Schematic of a CM bileaflet mechanical heart valve showing the housing, the hinges and the leaflets

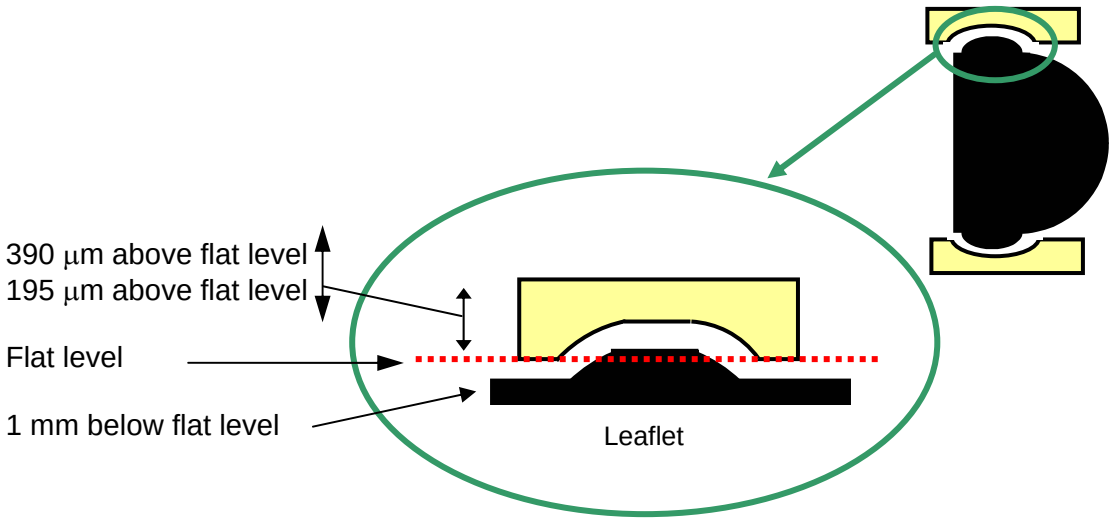

Figure 5.6: Measurement sites at four different levels within the hinge of the CM valve

St. Jude Medical Regent Valve

Measurements were conducted along seven planes shown in Figures 5.7 and 5.8. Table 4.2 shows the number of locations investigated at each level of interest within the hinge and thumbnail regions.

Table 5.2: Number of LDV measurement locations at each level of interest

Plane of Interest	Number of locations
585 μm above the flat	3
390 μm above the flat	64
195 μm above the flat	64
level with the flat	130
500 μm below the flat	92
1 mm below the flat	90
3 mm below the flat	80

Incremental resolution was 0.203 mm in the x and y directions at and above the flat level. Incremental resolution was 0.635 mm in the x and y directions below the flat level. At each measurement site, between 10,000 and 21,500 coincident velocity measurements were acquired.

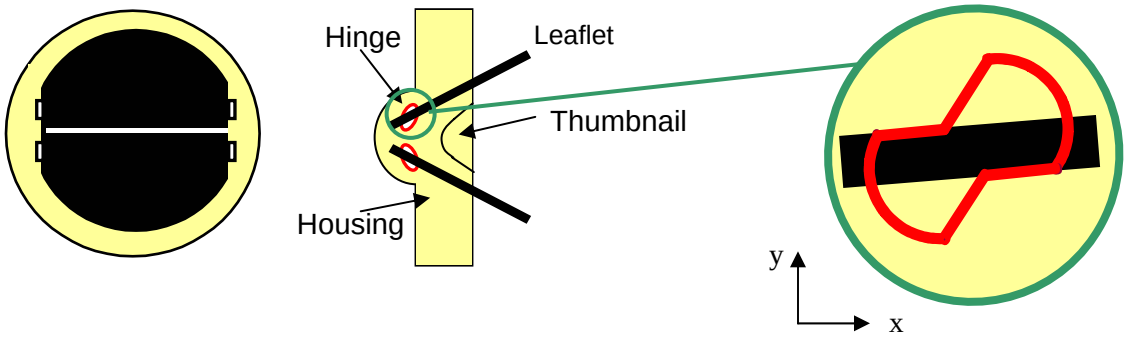

Figure 5.7: Schematic of a SJM Regent bileaflet mechanical heart valve showing the housing, the hinges and the leaflets

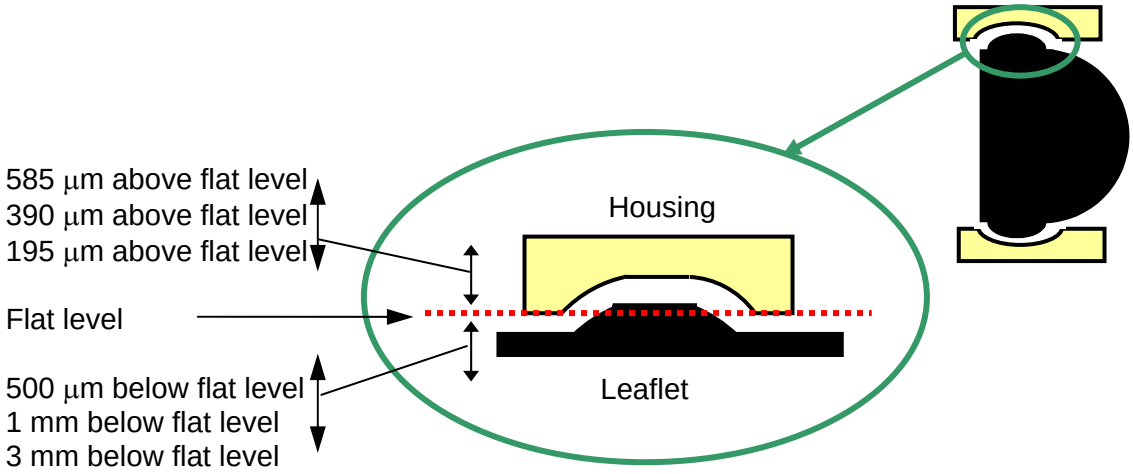

Figure 5.8: Measurement sites at seven different levels within the hinge of the SJM Regent valve

5.2.3 Leakage Jet Study

5.2.3.1 LDV System Setup

The measurements were conducted upstream of the valve, and three-component Laser Doppler Velocimetry was possible. A two/three-component measurement entailed the crossing of four/six laser beams. Since a single transceiver was used for two-component measurement, a three-component investigation required the use of two transceivers placed at a right angle to each other (Figure 5.1). In the backscattering mode, a single optic fiber probe acts as a transmitter as well as a receiver. An additional receiver was required in the forward and side scattering modes for three-component investigation.

A combination of forward and side-scatter mode was used as shown in Figures 5.9, 5.10 and 5.11. Because the violet beams were the weakest, they were coupled to the one component transceiver placed in the forward scatter position with respect to the receiver. The two component transceiver was placed in the side scatter position with respect to the receiver. The green beams were used to measure the V_1 velocity component, and the blue beams the V_2 velocity component.

5.2.3.2 Interrogation Sites

CarboMedics Valve

Due to optical limitations, the investigation plane could not be at 1 mm proximal to the outermost part of the valve housing. Thus, the measurement plane was located 65/1000 in (1.65 mm) from the outermost part of the valve housing. Only half of the cross sectional area of the aortic model was investigated. The grid was chosen so that it encompassed two hinges, part of the valve housing, and part of the b-datum line between the valve leaflets. The location of the interrogation grid is illustrated in Figure 5.12. Sampling was performed at spatial intervals of 0.381 mm in the x and y directions.

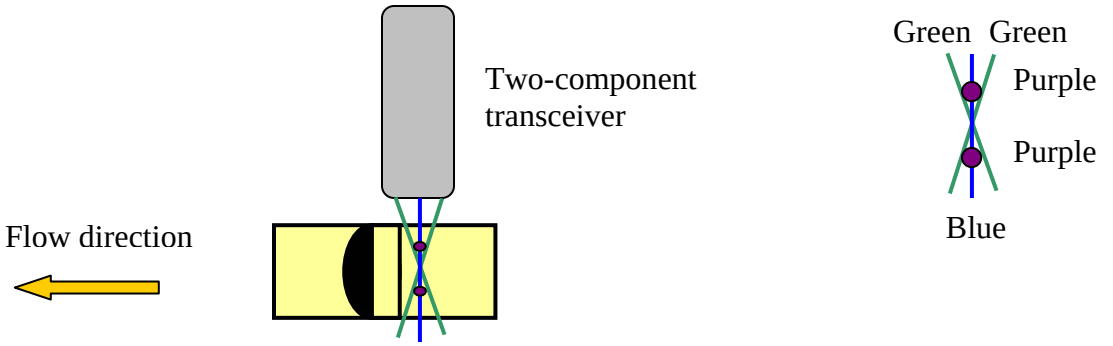

Figure 5.9: Front view of three-component Laser Doppler Velocimetry leakage jet flow measurements, in forward and side scatter modes

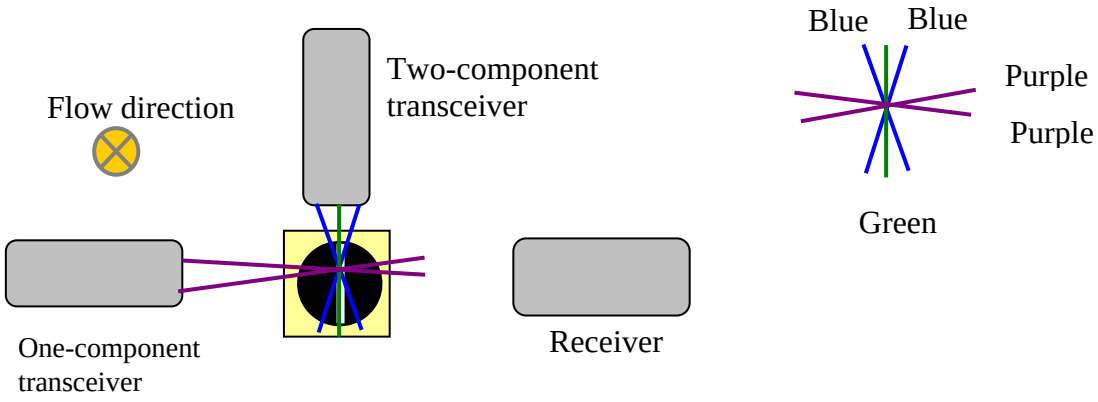

Figure 5.10: Side view of three-component Laser Doppler Velocimetry leakage jet flow measurements, in forward and side scatter modes

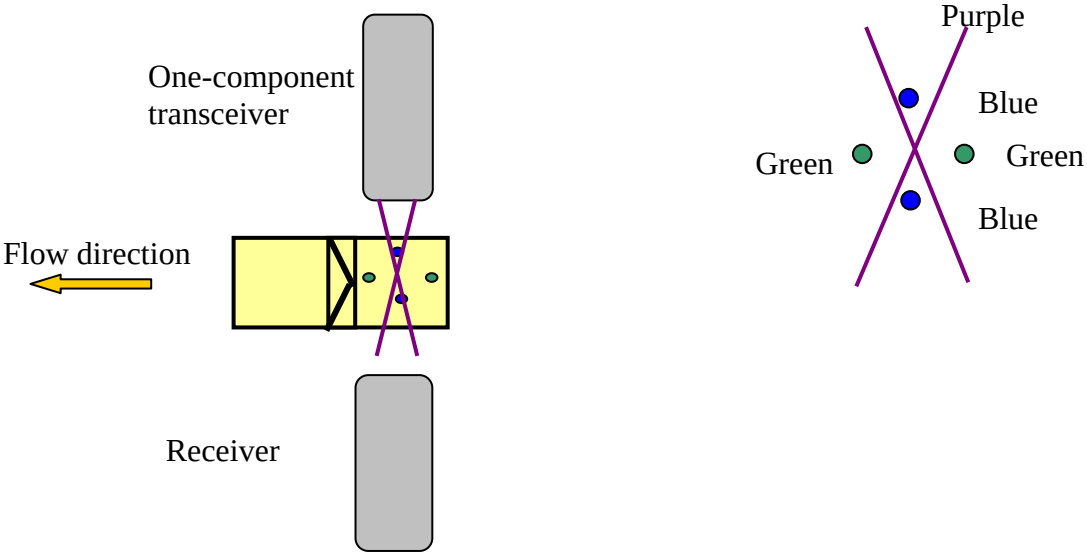

Figure 5.11: Top view of three-component Laser Doppler Velocimetry leakage jet flow measurements, in forward and side scatter modes

When a sampling revealed that the velocity magnitude at a given location was higher than 0.2 m/s during diastole, the sampling point was considered as part of leakage jet, and measurements were recorded. Once a leakage jet was located, the spatial interval was reduced to 0.190 mm in the y direction. At each measurement site, between 10,000 and 21,500 coincident velocity measurements were acquired.

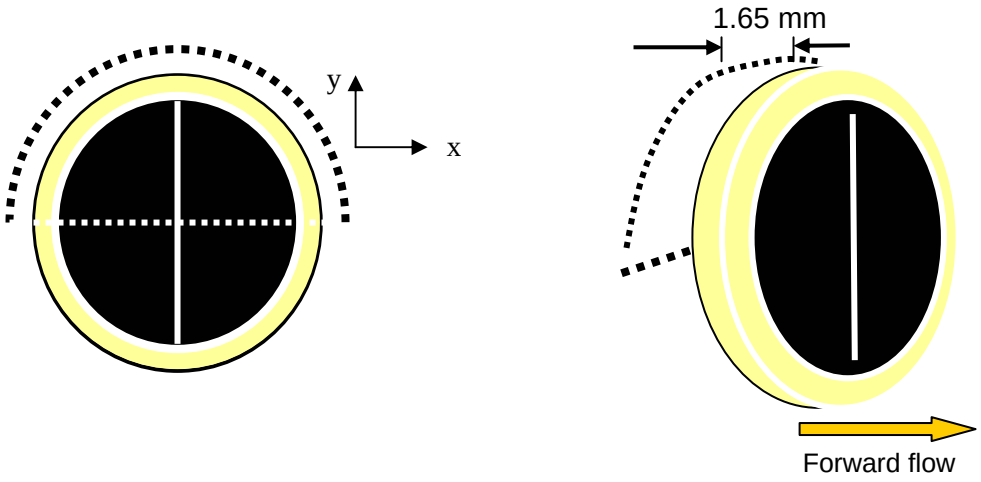

Figure 5.12: Location of leakage jet measurement grid for CM study

St. Jude Medical Regent Valve

The investigation plane was located 1 mm proximal to the outermost part of the valve housing, the pivot guards. Only half of the cross sectional area of the aortic model was investigated. The grid was chosen so that it encompassed two hinges, part of the valve housing, and part of the b-datum line between the valve leaflets. The location of the interrogation grid is illustrated in Figure 5.13. Sampling was performed at spatial intervals of 0.381 mm in the x and y directions. When a sampling revealed that the velocity magnitude at a given location was higher than 0.2 m/s during diastole, the

sampling point was considered as part of a leakage jet, and measurements were recorded. Once a leakage jet was located, the spatial interval was reduced to 0.127 mm in the y direction. At each measurement site, between 10,000 and 20,000 coincident velocity measurements were acquired.

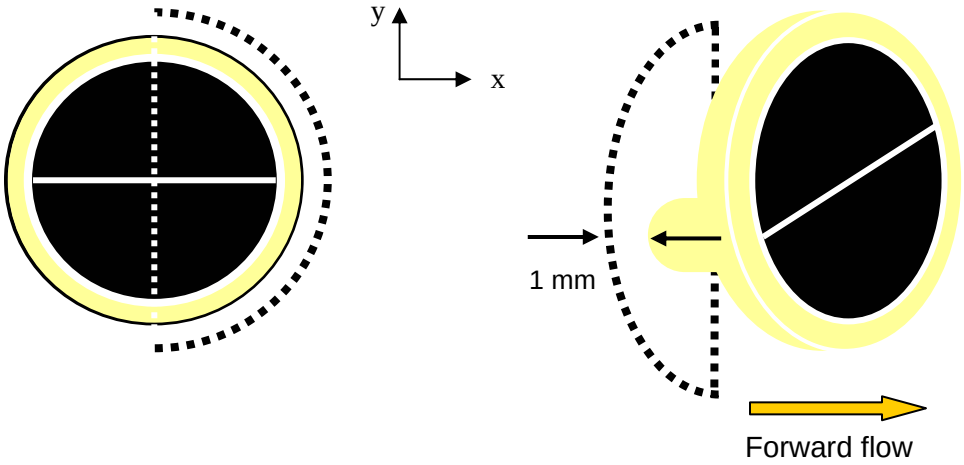

Figure 5.13: Location of leakage jet measurement grid for SJM study

5.2.4 Data Processing

5.2.4.1 Phase Window Averaging

The first step in processing Laser Doppler Velocimetry measurements made in pulsatile flow is to divide the prosthetic heart valve cycle into discreet intervals, called phase windows (Figure 5.14). Within these phase windows, the flow was assumed to be steady. In choosing the size of the phase windows, there is a tradeoff between temporal resolution and statistical accuracy. The choice of a relatively small phase window allows a fine definition of the temporal characteristics of the flow and increases the strength of the steady flow assumption. However, a relatively small phase window also contains a relatively small number of discreet velocity samples and limits statistical accuracy.

Conversely, choosing a large phase window size limits the temporal definition of the flow and decreases the strength of the steady flow assumption but increases statistical accuracy of the velocity measurements. Here velocities were phase-averaged within 20 ms time windows. A total of approximately 21500 measurements were taken at each location. An average of 500 measurements within each time bin was therefore used for data reduction, ensuring statistical validity of the results.

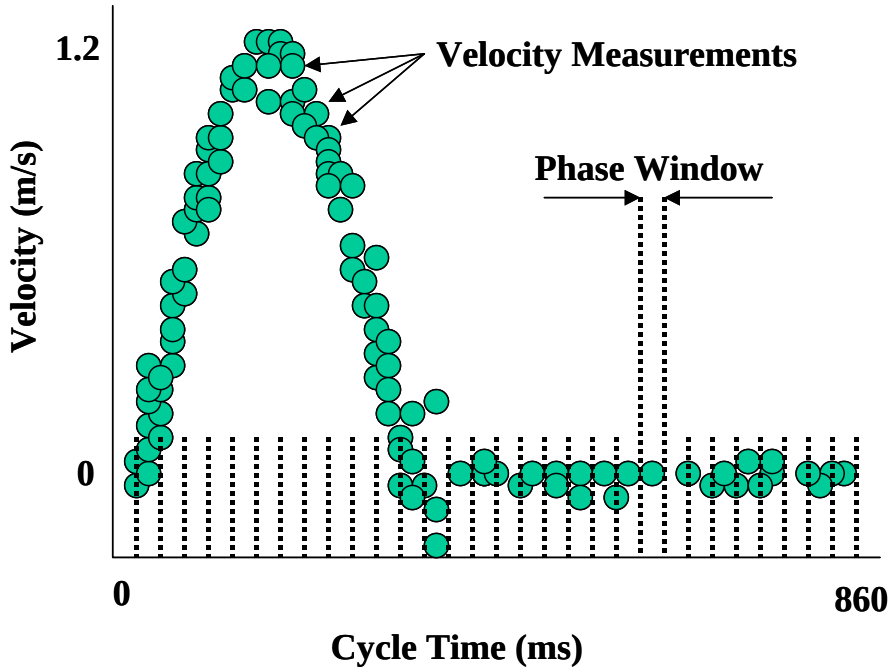

Figure 5.14: Phase window averaging

5.2.4.2 Ensemble Averaging

An ensemble averaging method was used to process the data. This method involved weighting individual measurements, calculating the statistics of the measurement population, filtering outliers, and calculating the mean velocity, fluctuating velocity, and Reynolds stresses.

Velocity Bias and Mean Velocity

Individual velocity measurements were weighted by the time a particle took in crossing the probe volume, called the gate time. This weighted technique was used to remove velocity bias which could lead to erroneous values of calculations. Velocity bias occurs because the probability for measuring a velocity higher than the mean is greater than the probability of measuring a velocity slower than the mean (Figure 5.15) (McLaughlin, 1973).

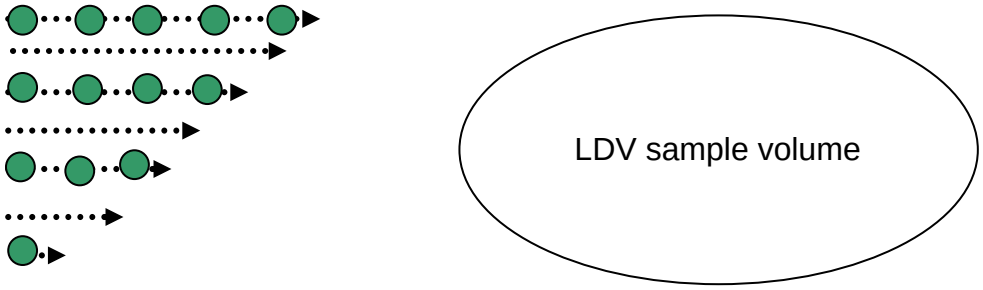

Figure 5.15 Velocity bias in LDV measurements. Arrows indicate velocity magnitude. Less seed particles will traverse the low velocity area towards the bottom of the LDV sample volume than the high velocity of the top for a given sampling time.

Mean velocity and standard deviation of the measurements at a specific time bin T, and a specific location L were obtained with the following equations.

$$\text{mean} = \frac{\sum_{j=1}^{a}\sum_{i=1}^{N} u_{ij} G_{ij}}{\sum_{j=1}^{a}\sum_{i=1}^{N} G_{ij}} \qquad \text{Equation 5.1}$$

$$\text{standard deviation} = \sqrt{\frac{\sum_{j=1}^{a}\sum_{i=1}^{N}(u_{ij} - mean)^2 G_{ij}}{\sum_{j=1}^{a}\sum_{i=1}^{N} G_{ij}}} \qquad \text{Equation 5.2}$$

Where a is the number of cycles during which measurements were recorded at the location L

N is the number of points acquired during the time bin T

G_{ij} is the gate time associated with velocity u_{ij}

u_{ij} is the instantaneous velocity

Statistical Filtering

Statistical filtering was then applied and measurements more than five standard deviations away from the mean were removed. After outlier removals, the mean velocity of each velocity component was calculated.

$$mean = \overline{u_{oo}} = \left(\frac{\sum_{i=1}^{a}\sum_{j=1}^{N} u_{ij} G_{ij}}{\sum_{i=1}^{a}\sum_{j=1}^{N} G_{ij}} \right)_{filtered} \qquad \text{Equation 5.3}$$

Mean velocity magnitude within each time bin, at each location could be obtained from the filtered mean velocity components.

$$Vmag = \sqrt{(\overline{u_{oo}})^2 + (\overline{v_{oo}})^2 + (\overline{w_{oo}})^2} \qquad \text{Equation 5.4}$$

Reynolds stress

Once mean and instantaneous velocities were both known, it was possible to calculate Reynolds shear stress and Reynolds normal stress according to the following respective equations.

$$\tau_{uv} = RSS(to) = \rho\overline{uv} = \rho\left(\frac{\sum_{i=1}^{a}\sum_{j=1}^{N}(u_{ij} - \overline{u_{oo}})(v_{ij} - \overline{v_{oo}})G_{ij}}{\sum_{i=1}^{a}\sum_{j=1}^{N}G_{ij}}\right)_{filtered} \quad \text{Equation 5.5}$$

$$\tau_{uu} = RNS(to) = \rho\overline{uu} = \rho\left(\frac{\sum_{i=1}^{a}\sum_{j=1}^{N}(u_{ij} - \overline{u_{oo}})^2 G_{ij}}{\sum_{i=1}^{a}\sum_{j=1}^{N}G_{ij}}\right)_{filtered} \quad \text{Equation 5.6}$$

Similarly, all the stress tensor components could be calculated.

Principal Stress Calculation

The magnitude of the Reynolds stress is dependent upon the coordinate system. The previous equations defined the Reynolds stress tensor in the coordinate system chosen for data acquisition. Nevertheless, the Reynolds stress obtained was not necessarily the peak stress value. Coordinate rotation was therefore applied to calculate the largest shear component of the Reynolds stress tensor $\tau_{pt.}$ The principal stress analysis is described in detail by Travis (Travis, 2001). The key point in this method was to solve the following equation:

$$\tau_{pp}^3 - (\tau_{uu} + \tau_{vv} + \tau_{ww})\tau_{pp}^2 + (\tau_{uu}\tau_{vv} + \tau_{uu}\tau_{ww} + \tau_{ww}\tau_{vv} - \tau_{uv}^2 - \tau_{uw}^2 - \tau_{vw}^2)\tau_{pp}$$

$$- (\tau_{uuu}\tau_{vvv}\tau_{www} - \tau_{uu}\tau_{vw}^2 - \tau_{vv}\tau_{uw}^2 - \tau_{ww}\tau_{uv}^2 + 2\tau_{uv}\tau_{vw}\tau_{uw}) = 0 \quad \text{Equation 5.7}$$

The solution of this equation gave three solutions, namely τ_{ii}, τ_{jj} and τ_{kk}. Each solution corresponded to the magnitude of the Reynolds normal stress acting along a plane normal to one of the three principal stress axes.

The maximum shear component tensor was obtained by taking the largest value of the following τ_{max} values.

$$\tau_{\max} = \left| \frac{\tau_{ii} - \tau_{jj}}{2} \right| \qquad \tau_{\max} = \left| \frac{\tau_{ii} - \tau_{kk}}{2} \right| \qquad \tau_{\max} = \left| \frac{\tau_{jj} - \tau_{kk}}{2} \right| \qquad \text{Equations 5.8-5.11}$$

Principal stress analysis was performed at each measurement location, and within every time bin.

5.2.4.3 Spatial and Time Averaged Standard Deviation

The standard deviation of the velocity magnitude for a particular location and time bin was estimated with equation 5.12.

$$\sigma_{Vmag|L,T} = \sqrt{\sum_{i=1}^{c} \frac{\overline{u_{i|L,T}^2}\ \sigma_{i|L,T}^2}{\sum_{i=1}^{c} \overline{u_{i|L,T}^2}}} \qquad \text{Equation 5.12}$$

Where $\sigma_{Vmag|L,T}$ is the standard deviation of the velocity magnitude for a particular measurement location, L, and time bin, T

$\overline{u_i^2}$ is the average value of the i^{th} velocity component in m/s

σi is the standard deviation of i^{th} velocity component in m/s

c is the number of acquired velocity components

The calculation was performed at each measurement location and within each time bin.

The average standard deviation of the velocity magnitude was estimated with the following equation:

$$\sigma_{avg} = \frac{\sum_{L=1}^{A}\sum_{T=1}^{B}\sigma_{Vmag|L,T}}{A*B} \qquad \text{Equation 5.13}$$

Where $\sigma_{Vmag|L,T}$ is the standard deviation of the velocity magnitude at location L and within time bin T

A is the total number of locations investigated

B is the total number of time bins

CHAPTER VI

RESULTS

This chapter is divided into three primary sections: the static leakage experiments, the hinge studies, and the leakage jet studies.

6.1 Static Leakage Experiment

Table 6.1 shows the number of leakage flow rate experiments performed and the averages and standard deviations of the leakage flow rates obtained for each of the bileaflet mechanical valves used in the leakage jet studies.

Table 6.1: Results of static leakage flow rate experiments

Valve	n	Average Flow rate (ml/min)	Standard deviation (ml/min)
23 mm SJM Regent clear housing valve	4	430	25.8
23 mm CM clinical valve	10	327	21.9

Pictures of the static water leakage jets were acquired to illustrate the leakage jet pattern of the two valves. The jet patterns observed with mechanical valves with horizontal B-datum line and with vertical B-datum line were compared to check the influence of the valve orientation. No discernable differences were found in the flow pattern.

Figure 6.1 shows the static water leakage jets through the closed 23 mm CM clinical valve. Distinct jets emanated from the hinge areas. Jets emanating from the same hinge region did not merge together. A small jet emanating from a gap between

leaflet and housing was observed. The leakage flow rate of the CM valve was 0.327 ± 0.22 L/min under a 120 mmHg static glycerin-water column.

Figure 6.2 shows the static water leakage jets through the closed 23 mm SJM Regent clear housing valve. One distinct jet emanated from the gap between the leaflets, as evidenced by the sheet of leakage flow emerging from the B-datum line. This jet expanded over the complete B-datum line. The remaining jets were confined to the hinge region. The small jets from the two pockets of the hinge merged together within the pivot guard, and then impinged the upper chamber few millimeters after the pivot guard. In some cases, the hinge jets angulated sharply impinging the pivot guard and thus were not visible upstream of the valve. The leakage flow rate of the SJM clear housing valve was 0.430 ± 0.026 L/min under a 120 mmHg static glycerin-water column.

6.2 Hinge Study

Velocity vector fields are presented at four times of interest during the cardiac cycle, which are mid acceleration, peak systole, valve closure and mid diastole. In each velocity vector field, the arrows point in the direction of the mean velocity vectors and are color-coded by the velocity magnitude (m/s) as given in the figure legends. A color printout of the velocity field is displayed when relevant.

Side View

Side View

Front View

Top View

Figure 6.1: Static leakage jets through the 23 mm CM clinical valve with the B-datum line positioned vertically

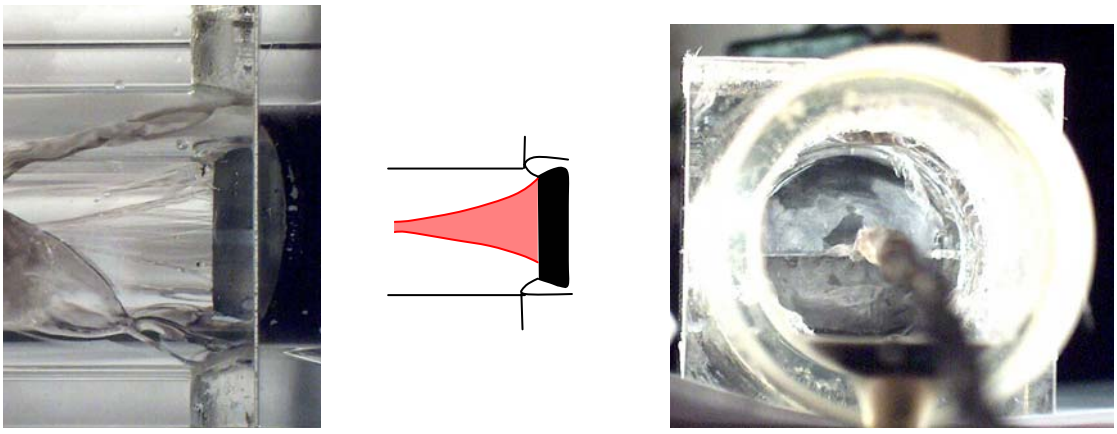

Top View

Front View

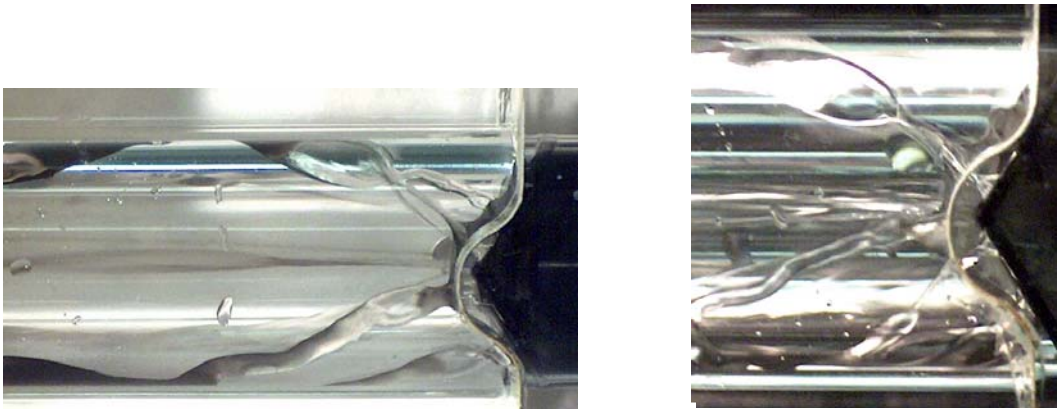

Side view

Side view

Figure 6.2: Static leakage jets through the 23 mm SJM Regent clear housing valve with the B-datum line positioned horizontally

6.2.1 23 mm CarboMedics Valve

6.2.1.1 Flow and Pressure Curves

Figure 6.3 represents the waveforms obtained in the vicinity of the 23 mm CM valve. The flow waveform was phase-window averaged according to the procedure outlined in the experimental protocol section. The time bins corresponding to mid acceleration, peak systole, valve closure, and mid diastole are indicated in Figure 6.3.

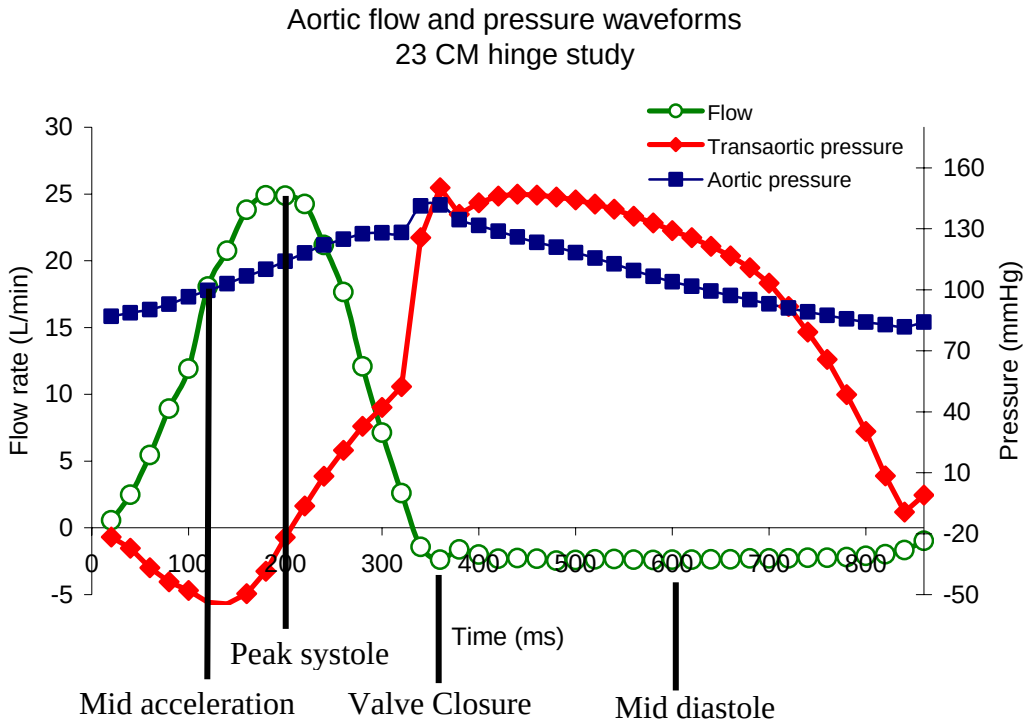

Figure 6.3: Aortic flow and pressure waveforms

6.2.1.2 Leaflet Positions

Figure 6.4 shows the leaflet positions at mid acceleration, peak systole as well as valve closure and mid diastole within the CM clear valve hinge. These leaflet positions correspond to those in the vector fields presented later. For clarity the leaflets are not shown on the color printouts of the velocity field. Terminology pertinent to the hinge design is shown in Figure 6.5 for orientation purposes.

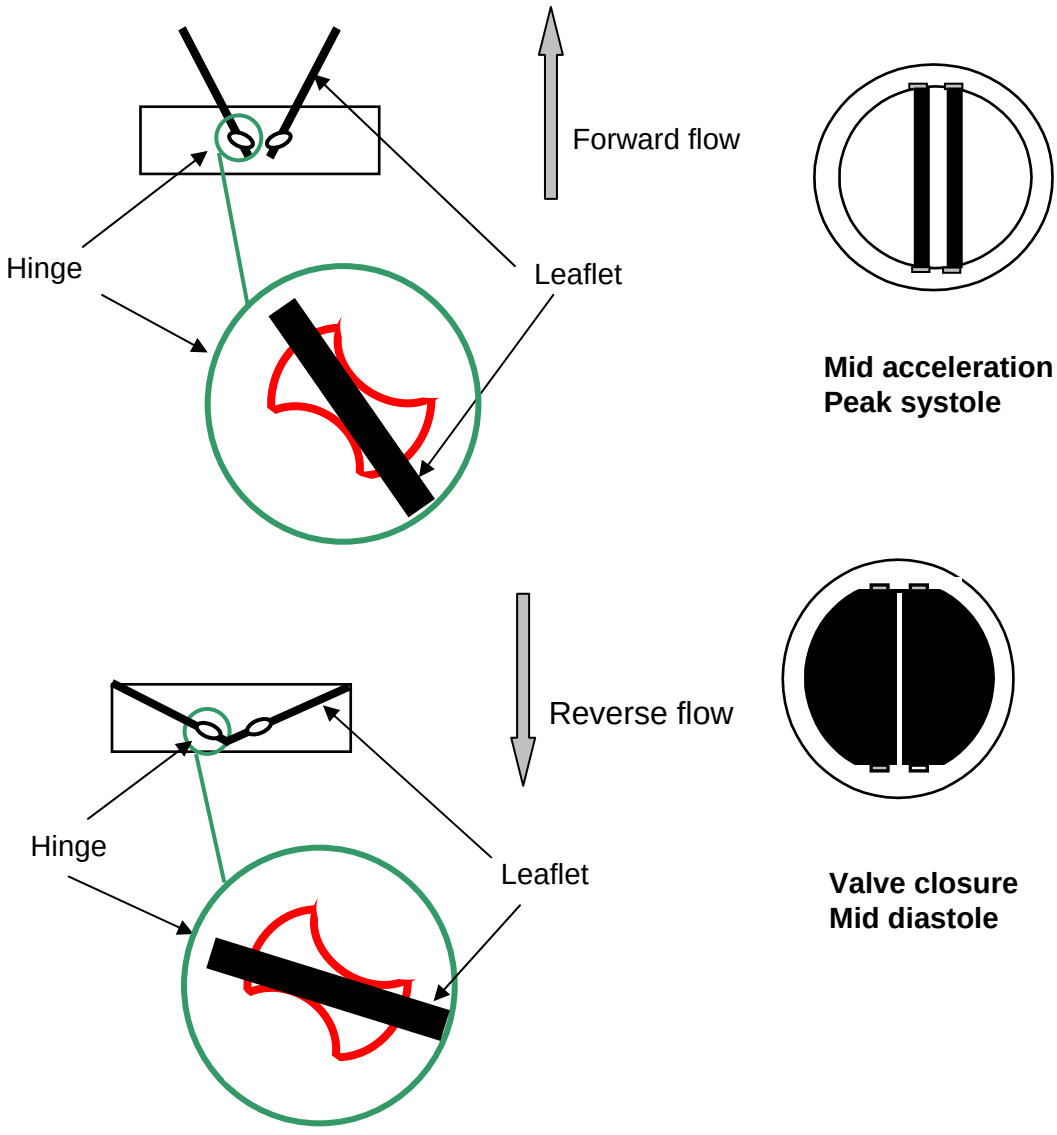

Figure 6.4: Leaflet position at mid acceleration, peak systole, valve closure, and mid diastole within the 23 mm CM clear housing valve.

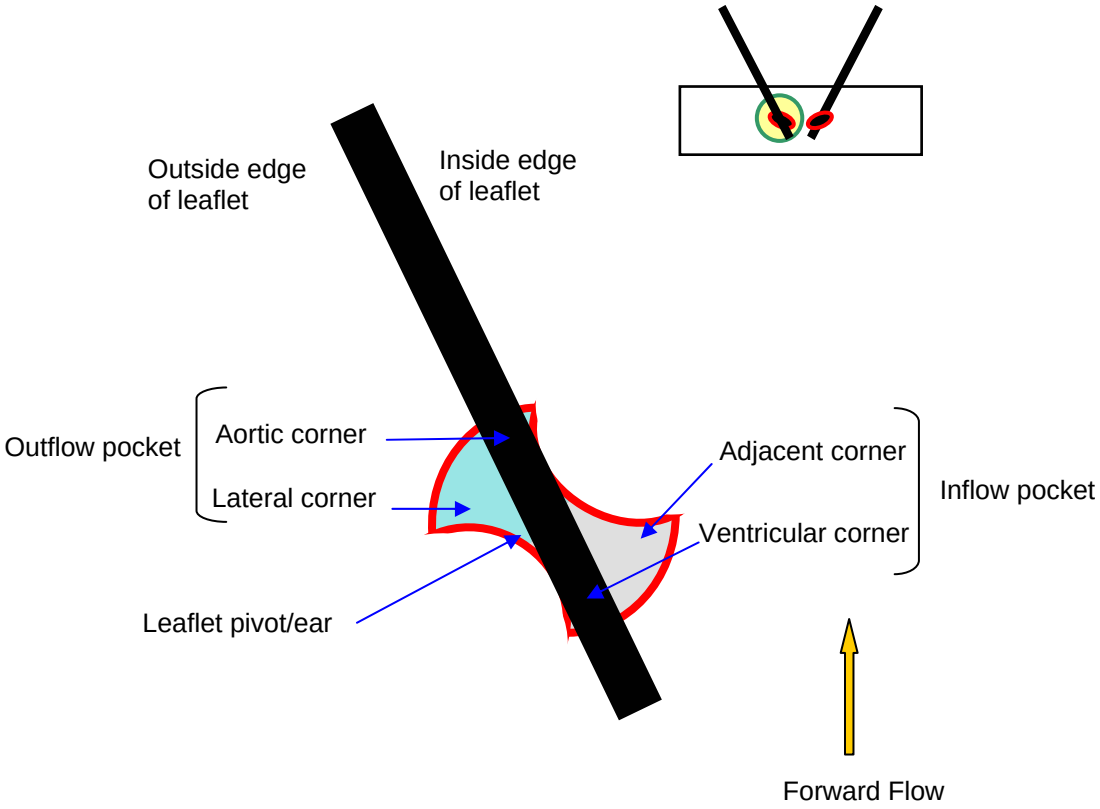

Figure 6.5: Pertinent terminology of the 23 mm CM hinge design.

6.2.1.3 Overview of the 23 mm CM Hinge Results

Animations (AVI format) of the velocity flow fields obtained at each elevation within the CM hinge region are given in appendix A. During systole significant forward flow was seen in the adjacent inflow corner at all elevations within the hinge recess. The flat level was the only elevation where a forward flow jet was observed in the lateral outflow corner. The peak velocities during systole were 2.31 m/s, 1.55 m/s, and 0.73 m/s at the flat, 195-μm, and 390-μm levels, respectively. The maximum TSS levels were 6,902 dyn/cm^2, 2,331 dyn/cm^2, and 4,379 dyn/cm^2 at the flat, 195-μm, and 390-μm levels, respectively.

During diastole, two leakage jets were observed within the hinge recess. The jet in the ventricular corner expanded throughout the entire area of the sharp corner, while the jet in the lateral corner was more localized. Flow vector distribution along the inner surface of the closed leaflet suggests that the flow was three-dimensional and the fluid may have flowed over the leaflet ear. The maximum velocities were 3.08 m/s, 2.57 m/s, and 1.37 m/s at the flat, 195-μm, and 390-μm levels respectively. The peak TSS levels were 5,440 dyn/cm^2, 6,192 dyn/cm^2, and 4,339 dyn/cm^2 at the flat, 195-μm, and 390-μm levels respectively.

Below the flat level, elevated velocities up to 2.98 m/s were recorded during systole as the forward flow developed between the hinges. The highest TSS levels were recorded at the edge of the central forward flow jet, and the peak TSS level was 5,881 dyn/cm^2. During diastole, the flow was almost stagnant, and the TSS levels were less than 842 dyn/cm^2.

For comparison the peak bulk velocity of a 23 mm CM valve implanted in the aortic position reaches approximately 2.15 m/s for a mean velocity of 1.44 m/s (Carbomedics Inc., 2003). The peak velocity magnitude recorded using LDV in the present study was 2.1 m/s. The spatial and time averaged standard deviation was 0.07 at 1 mm below the flat. Above the flat, the standard deviations of the velocity magnitude were 0.10 m/s, 0.11 m/s, 0.11 m/s and 0.11 m/s at the flat, 195-μm, 390-μm levels, respectively.

6.2.1.4 Detailed Description of the Hinge and Near-hinge Flow Fields of the 23mm CM Clear Housing Valve.

Flat Level

Mid Acceleration

Figure 6.6 shows the velocity field inside the CM hinge region at the flat level during mid acceleration. The location and angulation of the velocity vectors in the inflow pocket as well as the high velocity magnitude of up to 2.24 m/s suggested that the flow may have been squeezed between the leaflet ear surface and the inflow hinge wall. The flow then curved anticlockwise before turning clockwise, imparting a wavy shape to the flow field inside the adjacent corner. The TSS reached 2,550 dyn/cm^2 along the hinge wall as the flow entered the hinge inflow corner. Near the hinge inflow wall, a peak TSS of 6,902 dyn/cm^2 was observed at one measurement point during one time bin (20 ms).

Slightly higher velocity magnitudes were observed in the outflow hinge pocket as a forward flow jet began to develop in the lateral corner traveling nearly parallel to the main flow direction. The velocity magnitude in this region reached 2.31m/s, and within the jet, the TSS levels were less than 2,138 dyn/cm^2. Where the flow impinged the outflow hinge wall the TSS reached 5,690 dyn/cm^2.

Near zero velocity vectors were observed in the central region of the hinge due to the presence of the leaflet ear. A single measurement point located along the wall of the ventricular corner was associated with a velocity magnitude of up to 0.41 m/s.

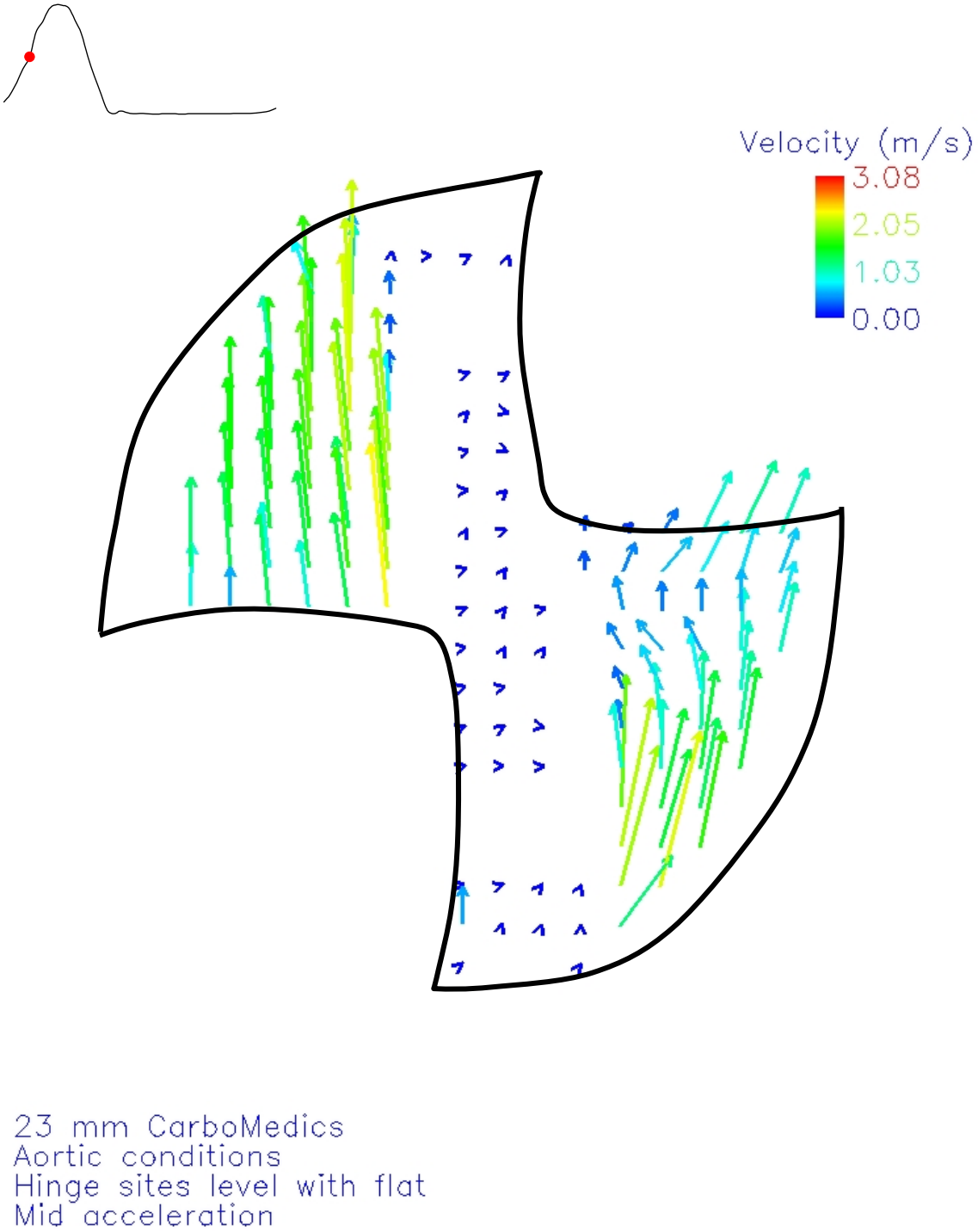

Figure 6.6: 23 mm CM clear valve hinge flow field
at the flat level at mid acceleration

Peak Systole

Figure 6.7 shows the velocity field inside the CM hinge region at the flat level at peak systole. At this instant of the cardiac cycle, the forward flow jet that developed in the lateral corner during mid acceleration was still present, but the velocity magnitudes were lower with a maximum velocity magnitude of 1.39 m/s. The TSS levels throughout the lateral corner were approximately 700 dyn/cm^2, except along the outflow wall where the TSS reached 2,772 dyn/cm^2. The squeeze flow in the adjacent corner was slower at peak systole than during mid acceleration. The velocity reached 1.45 m/s and the TSS reached 2,494 dyn/cm^2. The wavy flow structure seen during mid acceleration in the adjacent corner was still present at peak systole.

Near zero velocity vectors were seen in the central region of the hinge due to the presence of the leaflet ear. Two measurement points located along the wall of the ventricular corner were associated with a velocity magnitude of up to 0.41 m/s and TSS levels up to 2880 dyn/cm^2.

Valve Closure

Figure 6.8 shows the velocity field inside the hinge region at the flat level at valve closure. 280 ms after the beginning of systole, the forward flow jet and the wavy flow structure that were present during the forward flow phase of the cardiac cycle vanished and the velocity magnitude throughout the hinge was less than 0.22 m/s. At valve closure, a small isolated squeeze flow region was observed in the outflow lateral corner. The velocity reached 0.71 m/s and the TSS reached 2,030 dyn/cm^2.

Near zero velocity were observed near the inner surface of the closed leaflet. Downstream of the closed leaflet, reverse flow was present. The velocity magnitudes in the adjacent corners did not exceed 0.46 m/s, while in the aortic corner, the velocity magnitudes were on the order of 0.25 m/s. However, along the aortic hinge wall higher

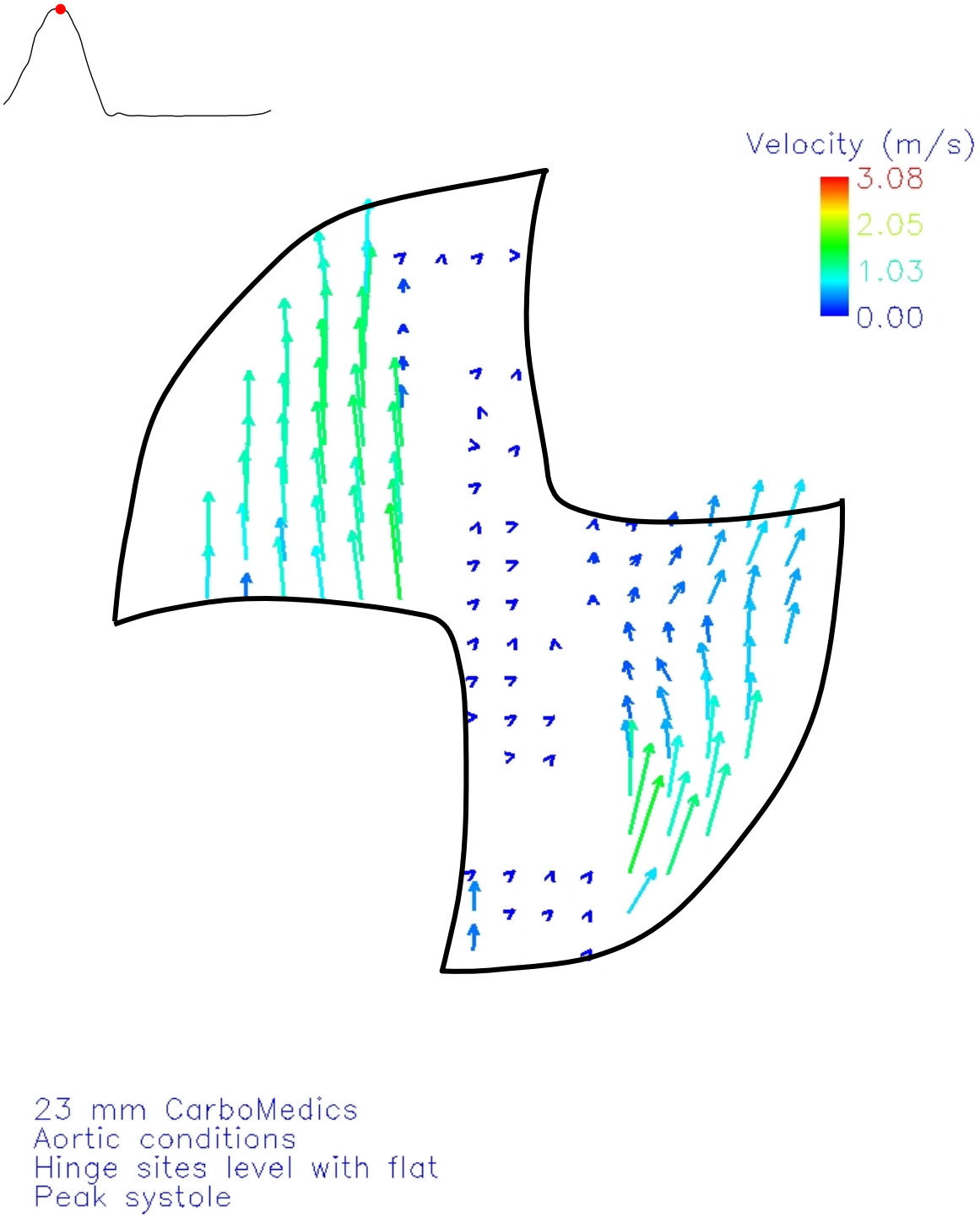

Figure 6.7: 23 mm CM clear valve hinge flow field
at the flat level at peak systole

velocities up to 0.66 m/s were detected as the fluid was directed towards the small gap between the leaflet ear and the hinge wall.

Within the ventricular corner slow velocity vectors flowed nearly parallel to the outer surface of the leaflet ear before forming a counterclockwise rotating structure. Velocity magnitudes in this region were less than 0.2 m/s. A squeeze reverse flow region was observed at the tip of the ventricular corner, with velocity magnitudes up to 3.02 m/s. This region of leakage flow was subjected to TSS levels up to 2,400 dyn/cm^2.

Mid Diastole

Figure 6.9 shows the velocity field inside the hinge region at the flat level during mid diastole. The flow pattern observed at mid diastole was similar to that at valve closure. During mid diastole the velocities in the squeeze flow region located in the outflow lateral corner reached a maximum value of 1.42 m/s, and the TSS levels were above 1500 dyn/cm^2, with a peak level at 4,312 dyn/cm^2. The velocity magnitudes in the aortic and adjacent corners did not exceed 0.29 m/s and 0.42 m/s, respectively.

The flow vector distribution within the ventricular corner at mid diastole was identical to that at valve closure. The velocities in the counterclockwise rotating structure were less than 0.15 m/s. Within the squeeze flow at the tip of the ventricular corner, a peak velocity of 3.08 m/s was recorded 80 ms after valve closure. Throughout diastole reverse flow velocities on the order of 3 m/s were recorded at the tip of the ventricular corner. This region of leakage flow was subjected to TSS levels less than 2700 dyn/cm^2, but one measurement point was associated with a TSS as high as 5,440 dyn/cm^2.

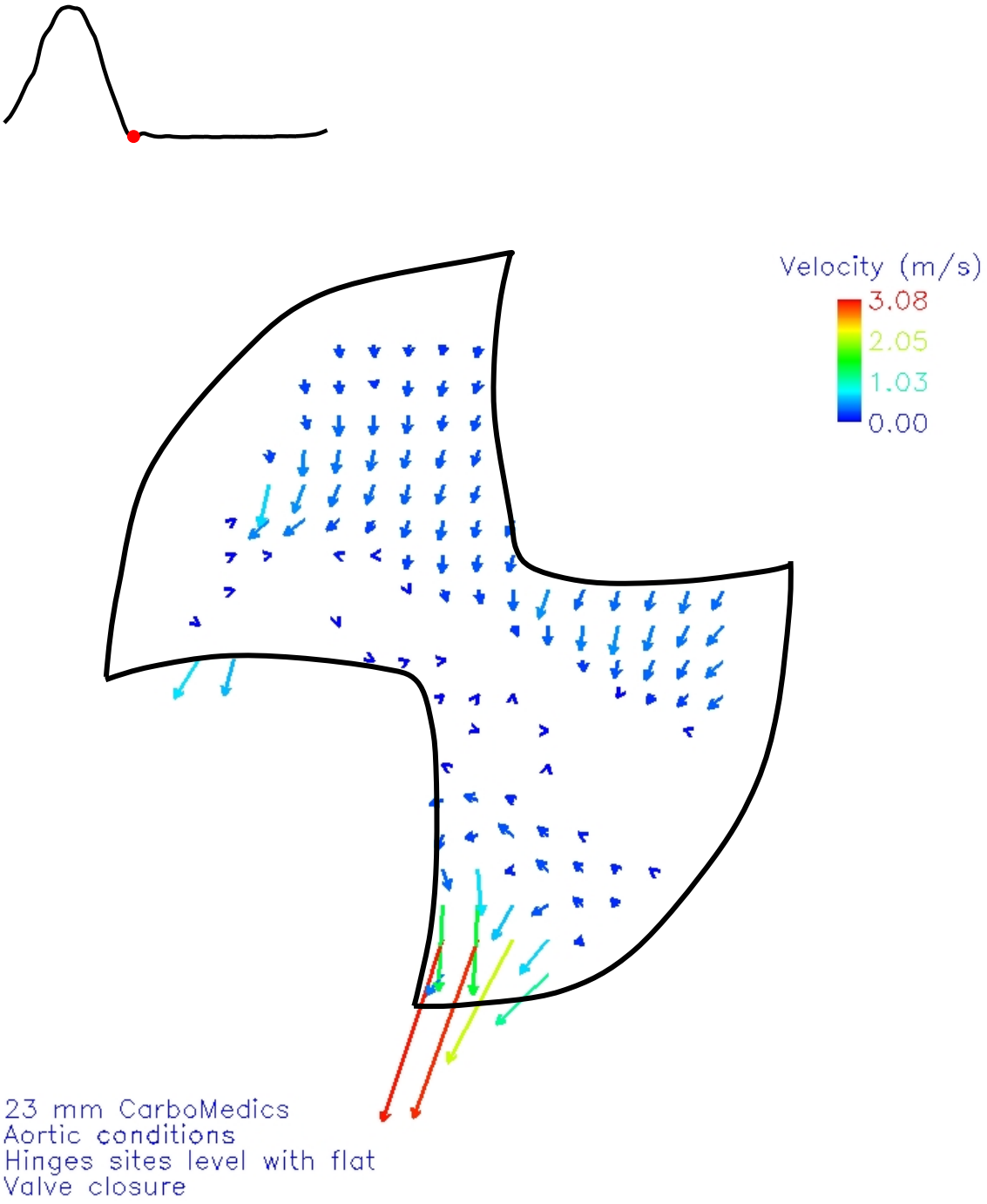

Figure 6.8: 23 mm CM clear valve hinge flow field
at the flat level at valve closure

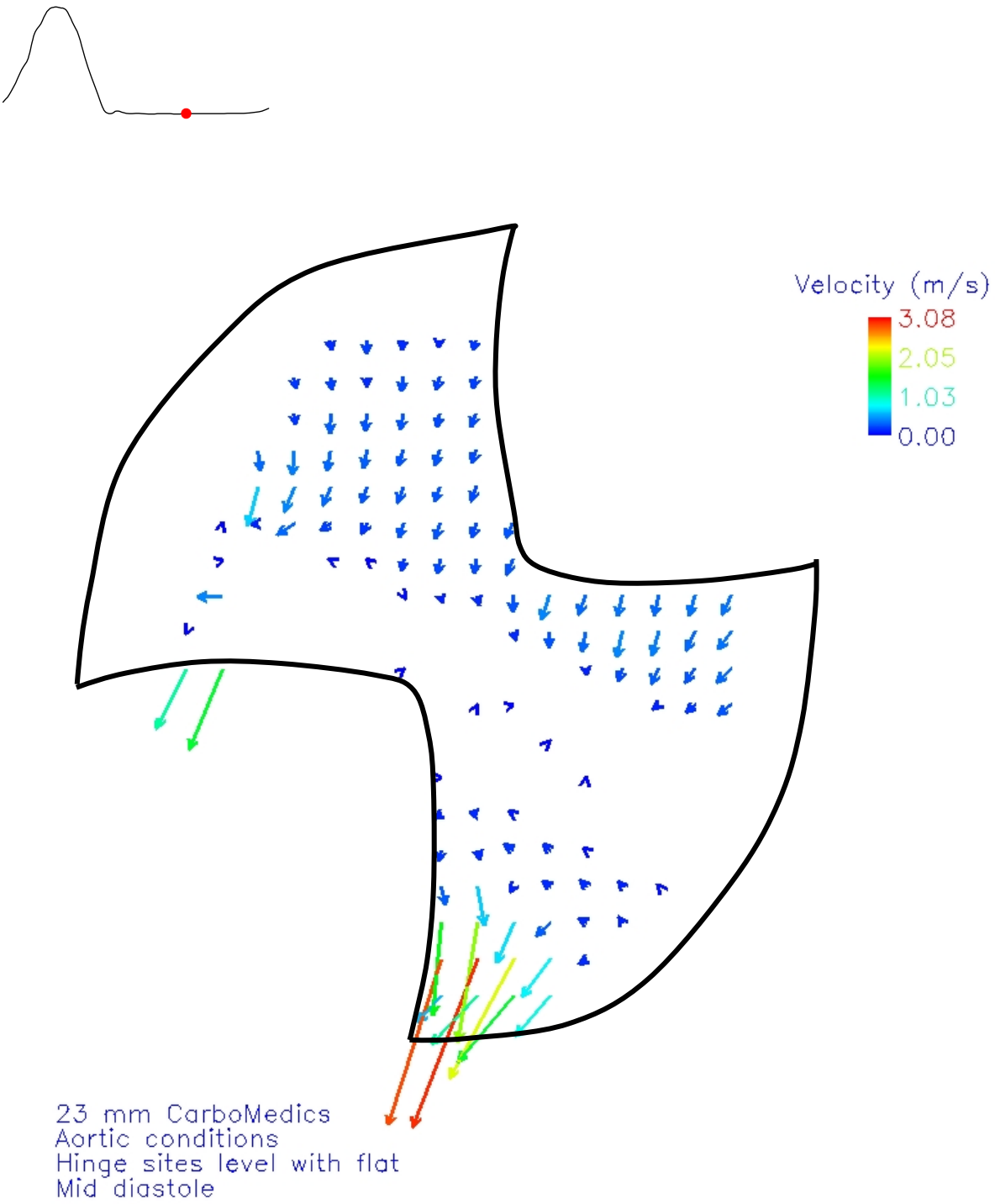

Figure 6.9: 23 mm CM clear valve hinge flow field
at the flat level at mid diastole

195 μm Above Flat Level

Mid Acceleration

Figure 6.10 shows the velocity field inside the hinge region 195 μm above the flat level during mid acceleration. The forward flow jet observed in the outflow pocket at the flat level was not seen at this elevation. Slow reverse flow was observed in the outflow pocket with velocity magnitudes less than 0.47 m/s, and the reverse flow within the lateral corner was skewed towards the central region of the hinge. The TSS levels within the outflow pocket ranged from nearly zero to 332 dyn/cm^2.

The location and angulation of the velocity vectors within the inflow hinge pocket suggested that the fluid flowed around the leaflet ear before exiting the hinge region through the tip of the adjacent corner. The velocity vectors in the adjacent corner had strong circumferential components, and the jet was almost perpendicular to the forward flow direction. The velocity reached 0.96 m/s in this region. A peak velocity of 1.55 m/s was recorded near the inner leaflet surface at early systole but was sustained for only 20ms. A small recirculation region was located beneath this jet. The velocity magnitudes did not exceed 0.20 m/s in this rotating structure. In the adjacent corner, the TSS levels did not exceed 483 dyn/cm^2, except at the lower edge of the leaflet ear where the TSS reached 980 dyn/cm^2. Localized high velocity vectors were also seen along the hinge wall of the ventricular corner near the outer surface of the leaflet ear. Flow may have been squeezed between the leaflet and the housing reaching velocity magnitudes of 1.06 m/s, and TSS levels of 1,718 dyn/cm^2.

The flow adjacent to the outer surface of the closed leaflet in the outflow pocket was almost stagnant as evidenced by near zero velocity magnitudes. The flow was also stagnant in the region where the leaflet ear was located.

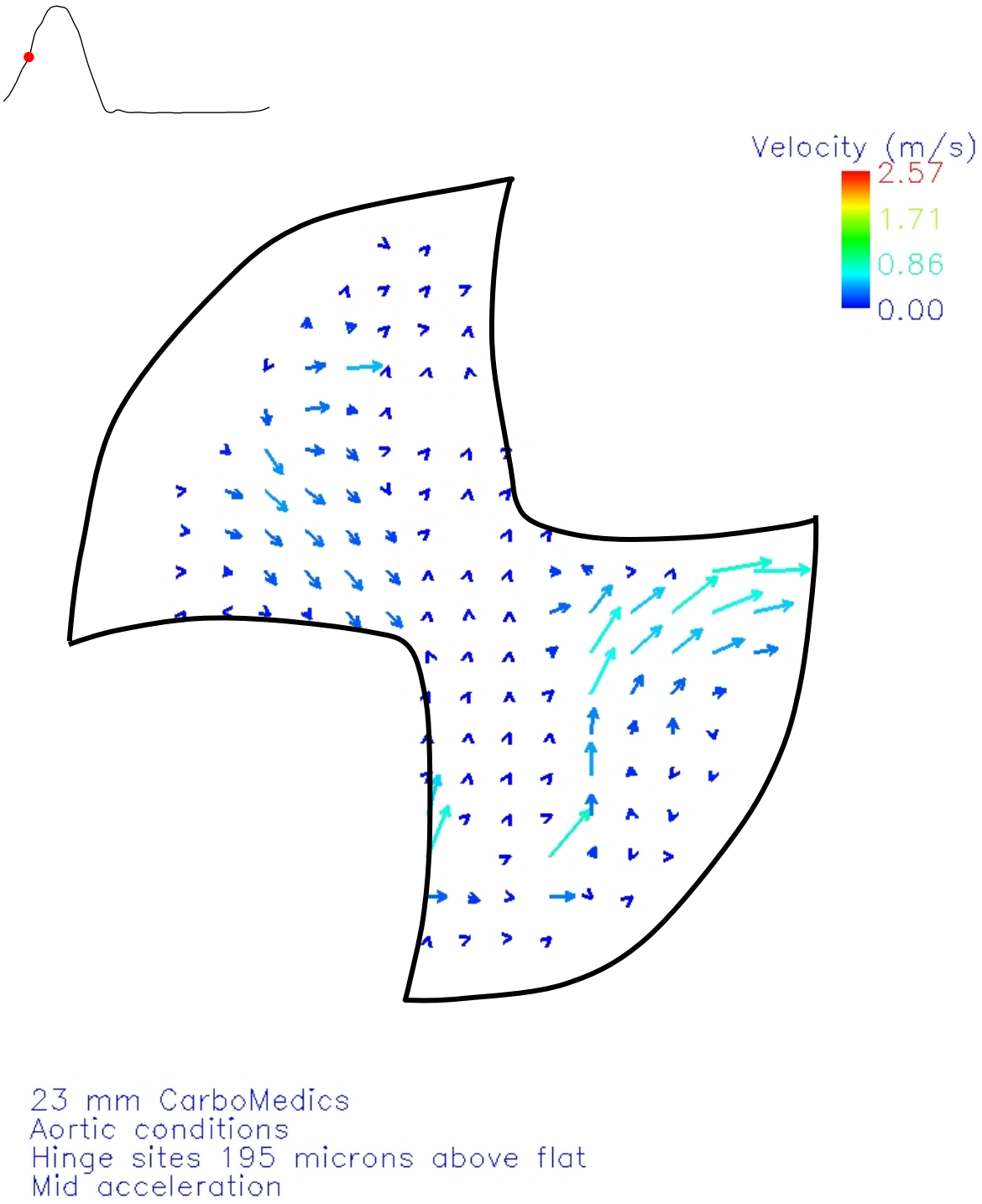

Figure 6.10: 23 mm CM clear valve hinge flow field
195 μm above the flat at mid acceleration

Peak Systole

Throughout the hinge velocity vectors at peak systole were directed similarly to those seen at this elevation during mid acceleration, therefore, no color coded velocity field is given. Velocity magnitudes in the outflow pocket were on the order of 0.2 m/s. The TSS levels throughout the outflow pocket were less than 166 dyn/cm^2, except along the outflow hinge wall where the TSS reached 304 dyn/cm^2.

The jet in the adjacent corner was slightly slower than it was during mid acceleration, with velocity magnitudes reaching 0.64 m/s. At the lower edge of the leaflet ear, the velocity and the TSS reached 0.75 m/s and 795 dyn/cm^2, respectively. Throughout the adjacent corner, the maximum TSS was 446 dyn/cm^2. In the recirculation region, velocity magnitudes were less than 0.38 m/s, and the TSS levels were less than 106 dyn/cm^2. Near the outer surface of the leaflet ear, the velocity along the ventricular wall reached 0.56m/s, and the TSS reached 585 dyn/cm^2.

Valve Closure

Figure 6.11 shows the velocity field inside the hinge region 195 μm above the flat level at valve closure. Throughout the hinge, velocity vectors pointed nearly in the same directions as those seen at the flat level at valve closure, and a squeeze flow was observed in the outflow lateral corner. This squeeze flow region was more localized at the flat level, but the velocities were higher than at flat level with a peak velocity of 1.68 m/s. The TSS reached 3,578 dyn/cm^2.

The vectors within the aortic corner indicated reverse flow towards the central region of the leaflet with velocity magnitudes on the order of 0.35 m/s. The highest velocities were seen along the inner surface of the leaflet ear, near the aortic hinge wall, with velocities up to reaching 0.87 m/s. The vectors through the adjacent corner were also retrograde with velocity magnitudes up to 0.72 m/s.

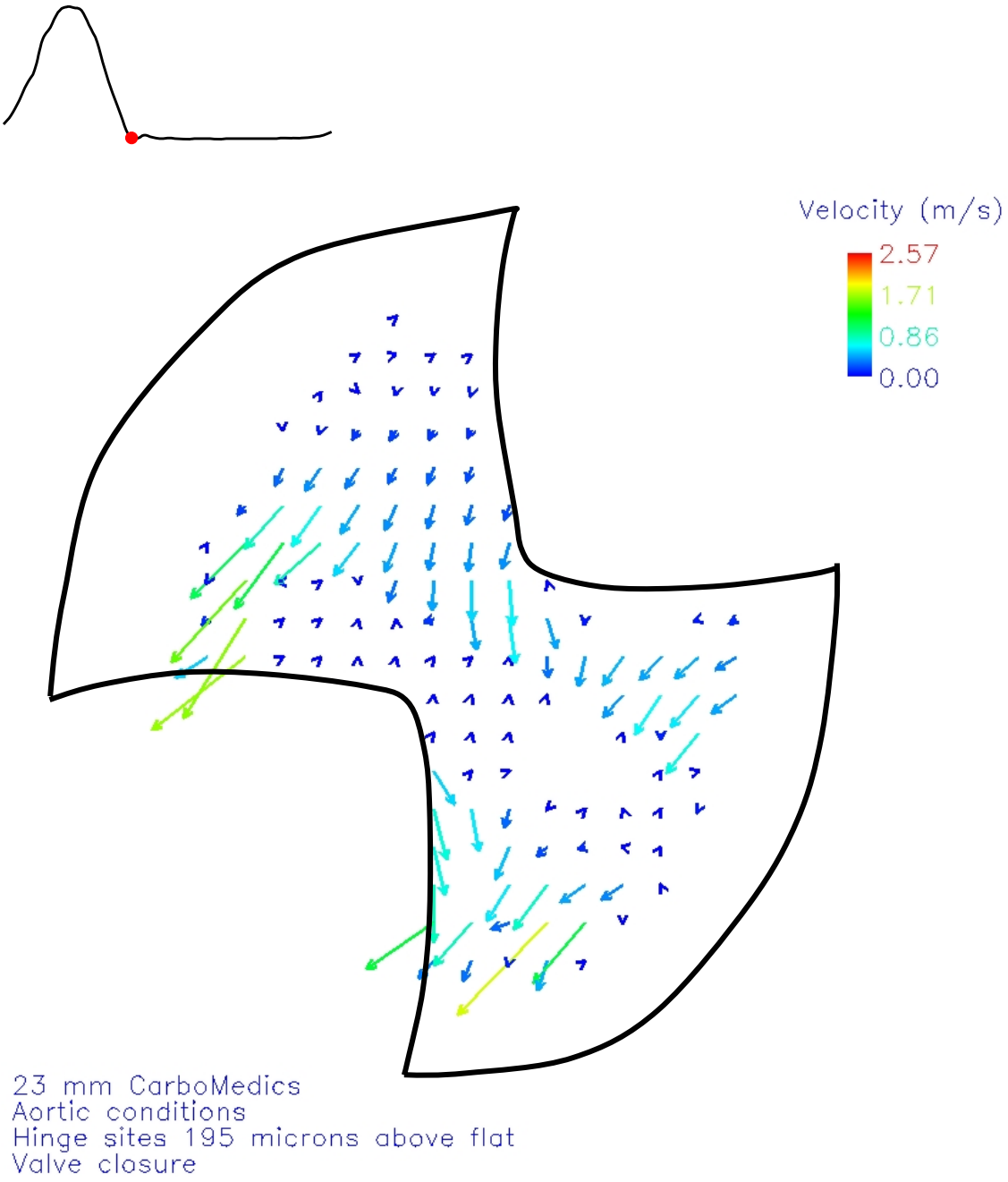

Figure 6.11: 23 mm CM clear valve hinge flow field
195 μm above the flat at valve closure

High velocity reverse flow was observed at the tip of the ventricular corner, with a maximum velocity of 1.84 m/s. A peak TSS level of 6,192 dyn/m^2 was recorded at one location. However, throughout the ventricular corner, the TSS levels were on the order of 2,000 dyn/cm^2.

Mid Diastole

Figure 6.12 shows the velocity field inside the hinge region 195 μm above the flat level during mid diastole. The flow pattern was similar to that seen at valve closure. The squeeze flow seen at valve closure in the outflow lateral corner was present throughout diastole, and was associated with velocities on the order of 1.9 m/s. A peak velocity of 2.07 m/s was recorded at mid diastole. The TSS levels in this region reached 4,633 dyn/cm2.

Within the aortic and adjacent corner, the reverse flow was slower than at valve closure. The velocities reached 0.53 m/s in the aortic corner and 0.56 m/s in the adjacent corner.

At 195-μm level the rotating structure seen at the flat level in the ventricular corner had disappeared, while the reverse jet seen at the tip of the ventricular corner at the flat level had expanded through the entire ventricular corner. Throughout diastole, the maximum velocities in the ventricular corner were above 2 m/s, with a peak at 2.57 m/s recorded at mid diastole. The TSS levels were on the order of 2,500 dyn/cm^2.

At late diastole, the velocity magnitude throughout the hinge region did not exceed 0.7 m/s and the flow pattern was disturbed with no apparent flow structure. However, at the end of diastole, a forward flow jet began to develop in the inflow lateral pocket as the leaflet began to reopen.

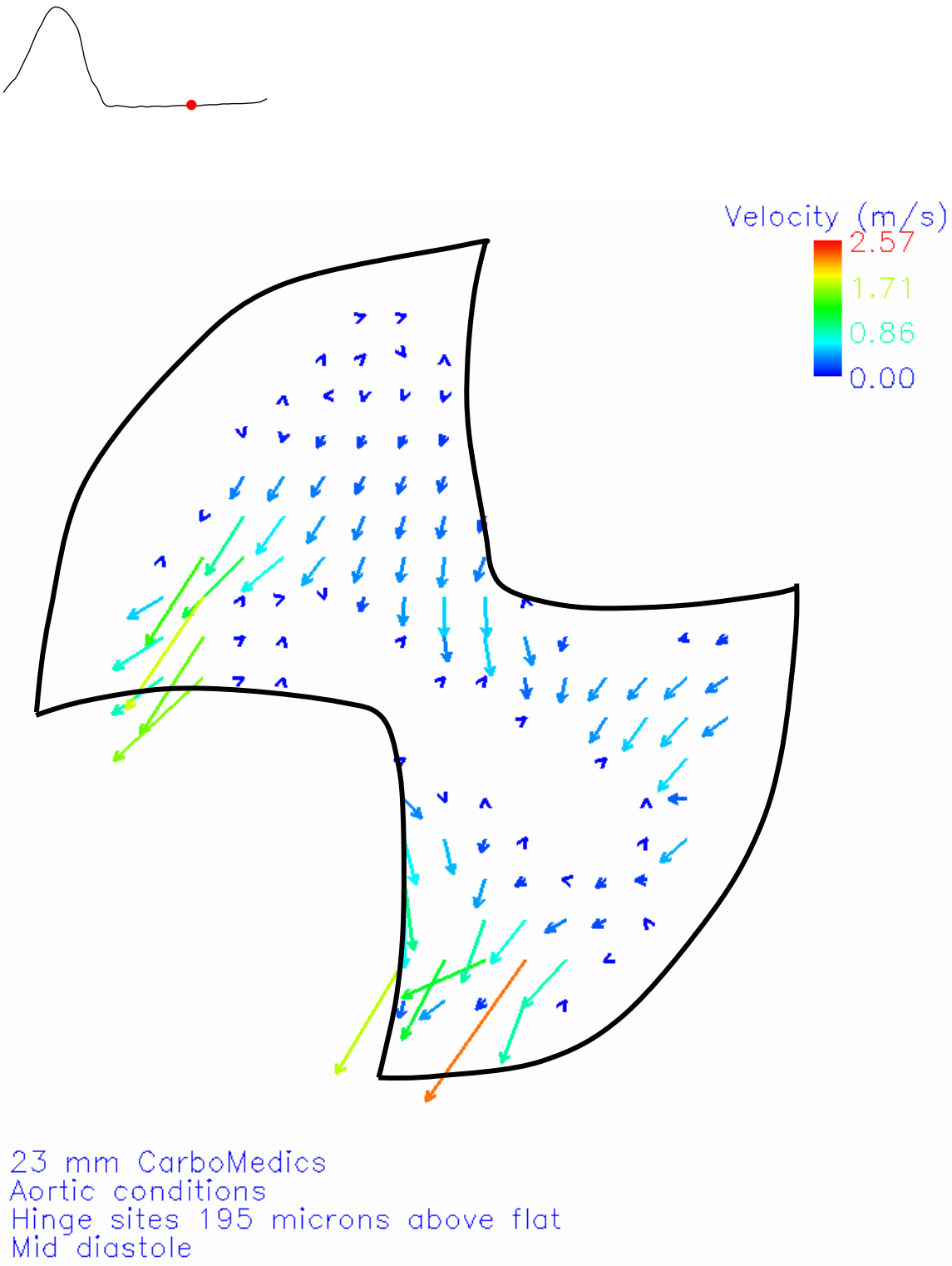

Figure 6.12: 23 mm CM clear valve hinge flow field
195 μm above the flat at mid diastole

390 μm Above Flat Level

Mid Acceleration

Figure 6.13 shows the velocity field inside the hinge region 390 μm above the flat level during mid acceleration. Disturbed flow was seen in the inflow adjacent corner, and a closer look at the location and angulation of the velocity vectors suggested that the flow field had a similar pattern to the one observed at the flat level and 195 μm above flat. The velocity magnitude in this region reached 0.73 m/s at early systole but were less than 0.39 m/s at mid acceleration. The TSS levels were up to 2482 dyn/cm^2 except for one measurement point where the TSS reached 4379 dyn/cm^2. Flow was almost stagnant in the region where the leaflet was located.

The reverse flow seen in the outflow pocket at 195 μm above flat was still visible at this elevation. Velocity magnitudes were lower than 0.21 m/s in this region, and the TSS levels were less than 141 dyn/cm^2 except for two measurement points where TSS levels were up to 519 dyn/cm^2.

Peak Systole

During this phase the flow pattern was similar to the one observed at mid acceleration, and therefore, the color-coded velocity field image is not displayed. The velocity magnitudes of the reverse flow in the outflow pocket were less than 0.22 m/s, and the TSS levels were less than 176 dyn/cm^2, except at one location where the TSS reached 770 dyn/cm^2. The velocity magnitudes in the inflow pocket were less than 0.35 m/s, and the maximum TSS, seen in the wavy flow pattern, was 2,200 dyn/cm^2. Throughout the rest of the inflow region, the TSS levels were less than 80 dyn/cm^2.

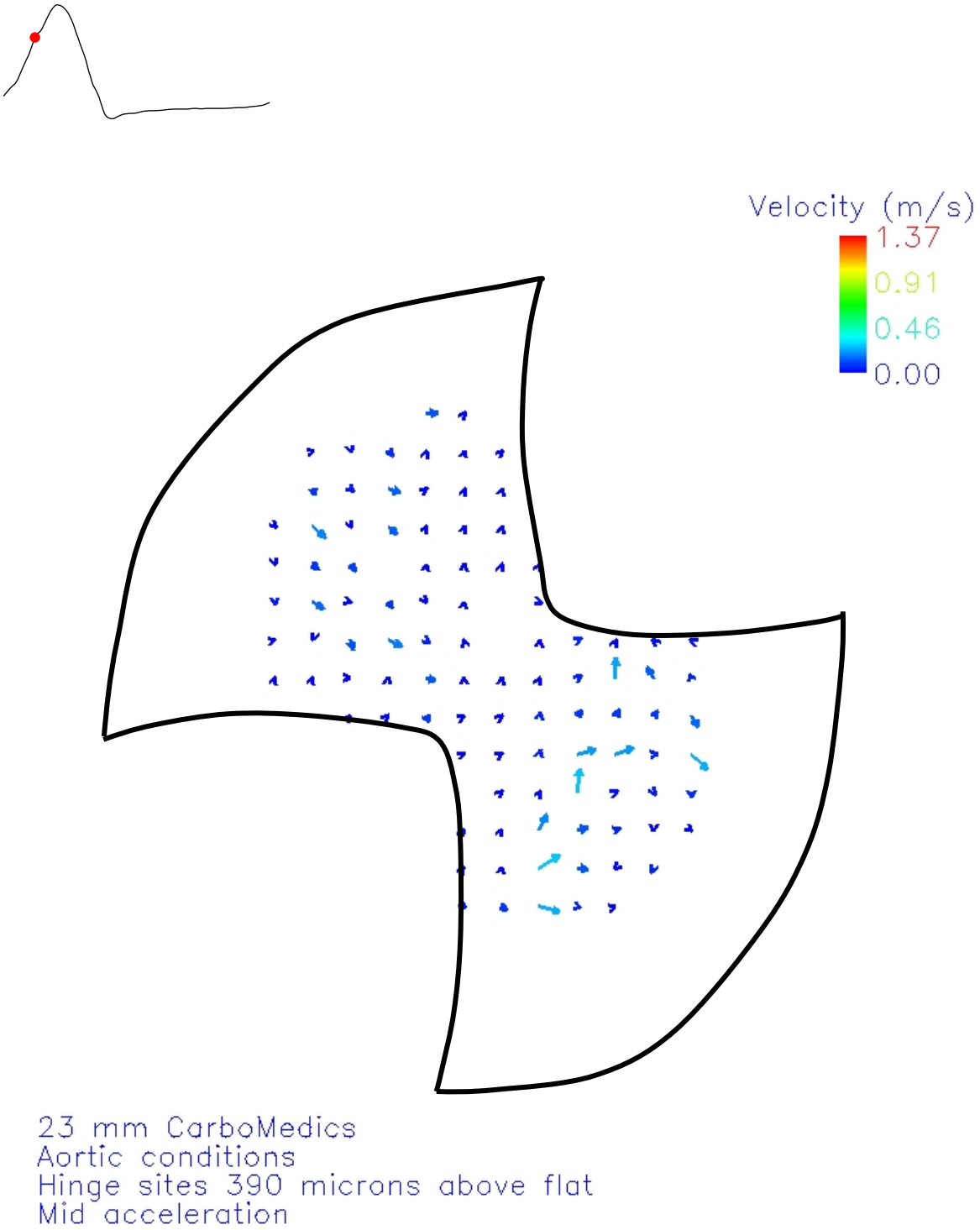

Figure 6.13: 23 mm CM clear valve hinge flow field
390 μm above the flat at mid acceleration

Valve Closure

Figure 6.14 shows the velocity field inside the hinge region 390 μm above the flat level at valve closure. The squeeze flow seen in the outflow lateral corner at 195 μm above the flat level was barely visible at this elevation. Velocity magnitudes reached 0.48 m/s where the flow was squeezed between the leaflet ear and the hinge wall. The TSS levels were less than 429 dyn/cm^2 along the hinge wall. The flow throughout the outflow aortic corner was almost stagnant as evidenced by near zero velocity magnitudes, except at two measurement locations where the velocity magnitude reached 0.33 m/s and the TSS levels reached 3,200 dyn/cm^2.

Localized high velocity reverse flow was seen along the inflow hinge wall suggesting that the fluid may have flowed around the leaflet ear. Peak velocity magnitudes of 0.91 m/s and peak TSS of 1,747 dyn/cm2 were recorded along the hinge wall. Angulation and location of the velocity vectors in the adjacent corner showed that the fluid may have flowed over the leaflet ear. The velocity magnitudes in this region reached 0.44 m/s.

Mid Diastole

Figure 6.15 shows the velocity field inside the hinge region 390 μm above the flat level during mid diastole. The flow pattern was similar than that observed at valve closure, but higher velocities were recorded downstream of the closed leaflet. Angulation and location of the velocity vectors located along the inner surface of the closed leaflet suggested the presence of three-dimensional flow. The velocity vectors in this region were directed towards the closed leaflets, and the fluid may have flowed over the leaflet ear. The velocity reached 0.92 m/s in this region of the flow field. The TSS levels were on the order of 1000 dyn/cm^2, with a peak TSS at 4,094 dyn/cm^2.

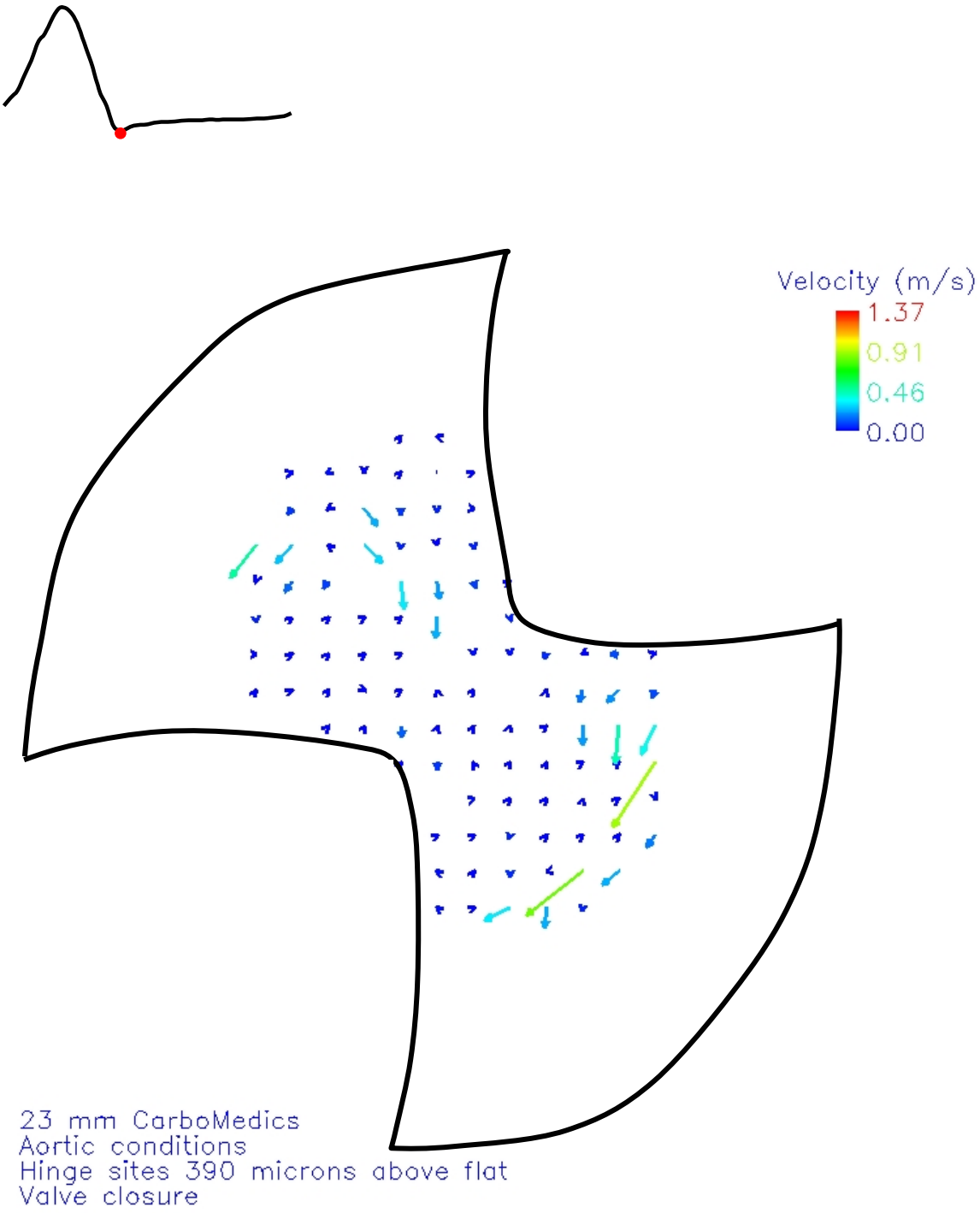

Figure 6.14: 23 mm CM clear valve hinge flow field
390 μm above the flat at valve closure

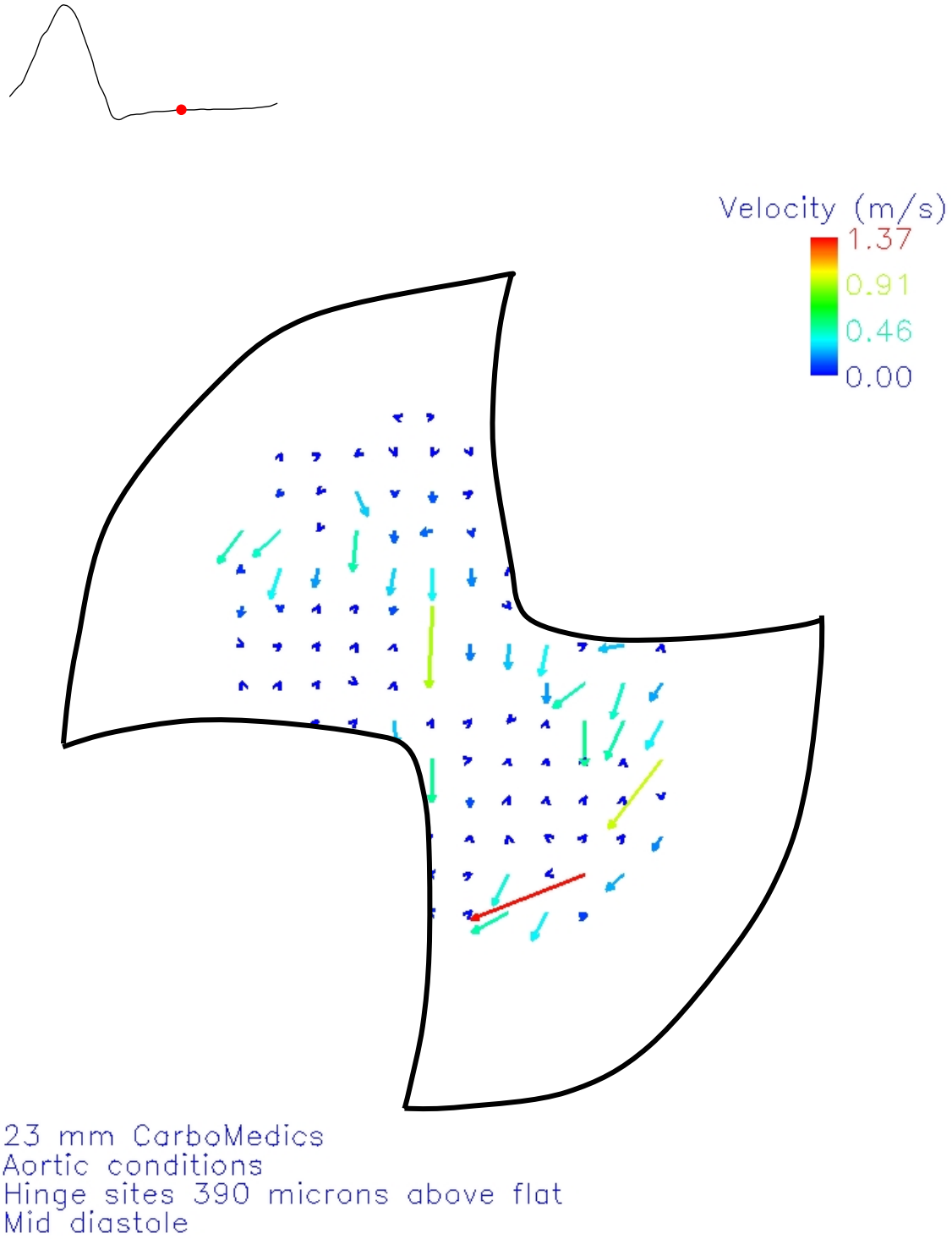

Figure 6.15: 23 mm CM clear valve hinge flow field
390 μm above the flat at mid diastole

The squeeze flow in the outflow lateral corner was slightly faster than at valve closure, with velocity magnitudes up to 0.6 m/s. In this region, the TSS levels were less than 735 dyn/cm^2. High velocity reverse flow was seen along the inflow hinge wall with a peak velocity of 1.37 m/s. The TSS reached 2,185 dyn/cm^2 within this reverse flow. High velocity magnitudes were also seen in the central region along the outer leaflet surface. The fluid may have flowed over the leaflet ear and, therefore, may have had a strong third velocity component. The velocity magnitudes were on the order of 0.5 m/s and the TSS reached 4,339 dyn/cm^2.

At late diastole, the flow decelerated and the velocities throughout the hinge region were less than 0.42 m/s. A low velocity forward flow pattern began to appear in the adjacent corner during the last 40 ms of diastole.

1 mm Below Flat Level

Mid Acceleration

Figure 6.16 shows the velocity field along the hinge inflow and outflow regions 1 mm below the flat level during the mid acceleration phase. In the inflow region the flow converged towards the center of the valve, and velocity magnitudes reached 2.47 m/s. Lower velocity flow, reaching 2.28 m/s, was observed at the outer edges of the open leaflets. The central forward jet accelerated to 2.98 m/s as the forward flow jet developed between the leaflets. The central jet velocity decreased to 2.78 m/s in the outflow region. The side jets were slower than the central jet, with velocity magnitudes of less than 2.67 m/s. The TSS levels were on the order of 20 dyn/cm^2 over the entire region of interest. A peak TSS level of 5881 dyn/cm^2 was seen at the edge of the central jet between the hinge pockets, but was sustained for only one time bin (20 ms). However, a second maximum of 2,136 dyn/cm^2 was seen at the edge of the central jet in the outflow region, and this peak value was sustained for seven time bins (140 ms).

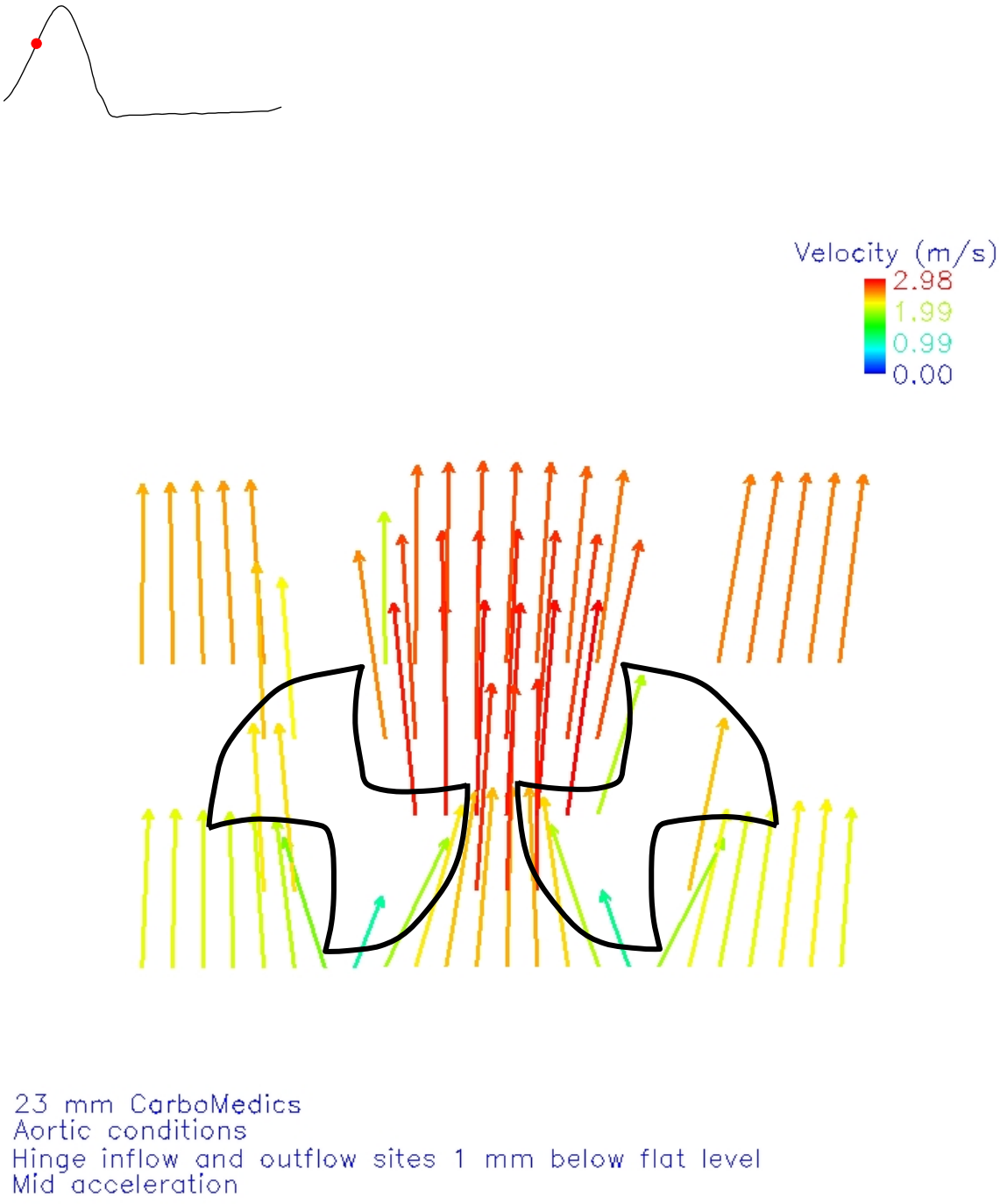

Figure 6.16: 23 mm CM clear valve hinge inflow, outflow flow field 1 mm below the flat at mid acceleration

Peak Systole

Figure 6.17 shows the velocity field along the hinge inflow and outflow regions 1 mm below the flat level at peak systole. The flow field observed at peak systole was similar to that at mid acceleration, but the velocity magnitudes were smaller. In the inflow region the velocity magnitudes of the central jet were up to 1.89 m/s, while the velocities of the jets at the outside edge of the leaflets reached 1.80 m/s. Between the open leaflets, the velocity magnitudes were less than they were during mid acceleration with a maximum velocity of 2.50 m/s.

Throughout the entire region, the TSS levels were on the order of 100 dyn/cm^2. However, the TSS reached 1829 dyn/cm^2 at the edge of the central jet in the outflow region.

Valve Closure

Figures 6.18 and 6.19 show the velocity field along the hinge inflow and outflow regions 1 mm below the flat level immediately before valve closure and at valve closure, respectively. The forward flow seen at early and peak systole was still observed 80 ms after peak systole. However 100 ms after peak systole, the forward flow pattern vanished and the vector distribution revealed the presence of a reverse flow with a preferential skewing towards the B-datum line. Immediately before valve closure, the flow between the hinges accelerated towards the leaflet seam and the peak velocity reached 1.2 m/s. At valve closure the high velocity flow observed before valve closure between the hinges was abolished. A reverse flow was present throughout the investigated region and the velocities were lower than 0.3 m/s, except in the inflow region where velocities up to 0.5 m/s were recorded.

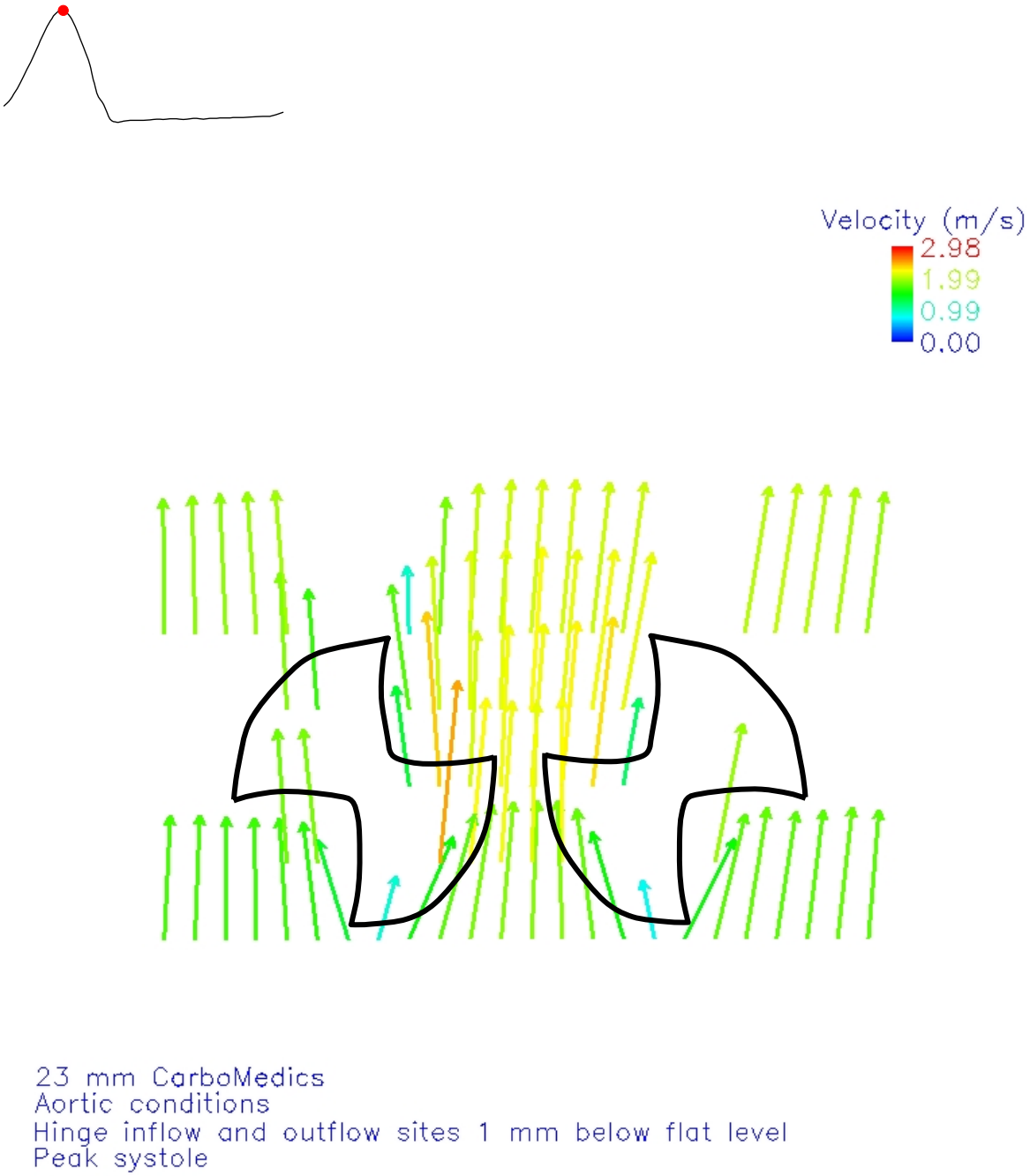

Figure 6.17: 23 mm CM clear valve hinge inflow, outflow field
1 mm below the flat at peak systole

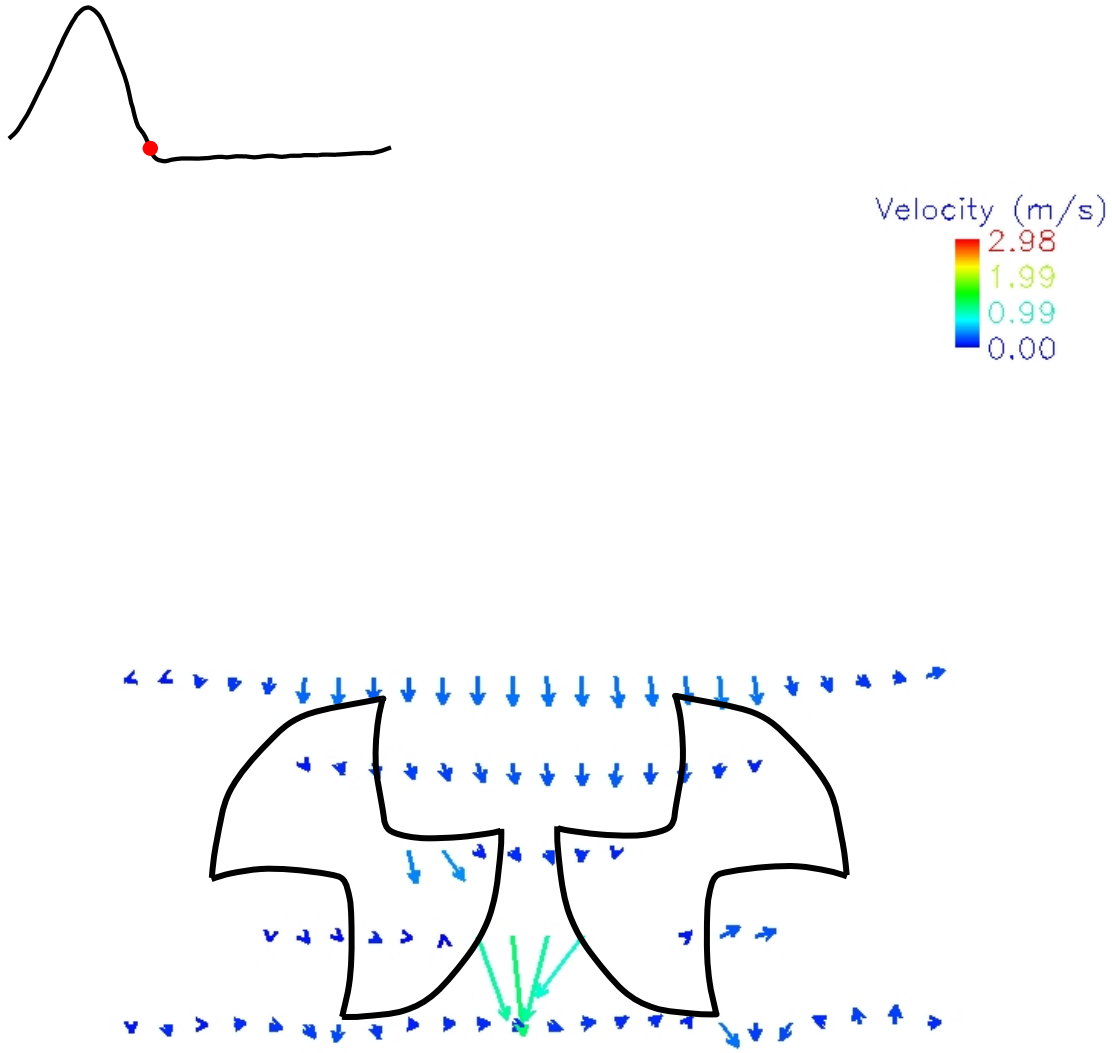

Figure 6.18: 23 mm CM clear valve hinge inflow, outflow flow field 1 mm below the flat immediately before valve closure

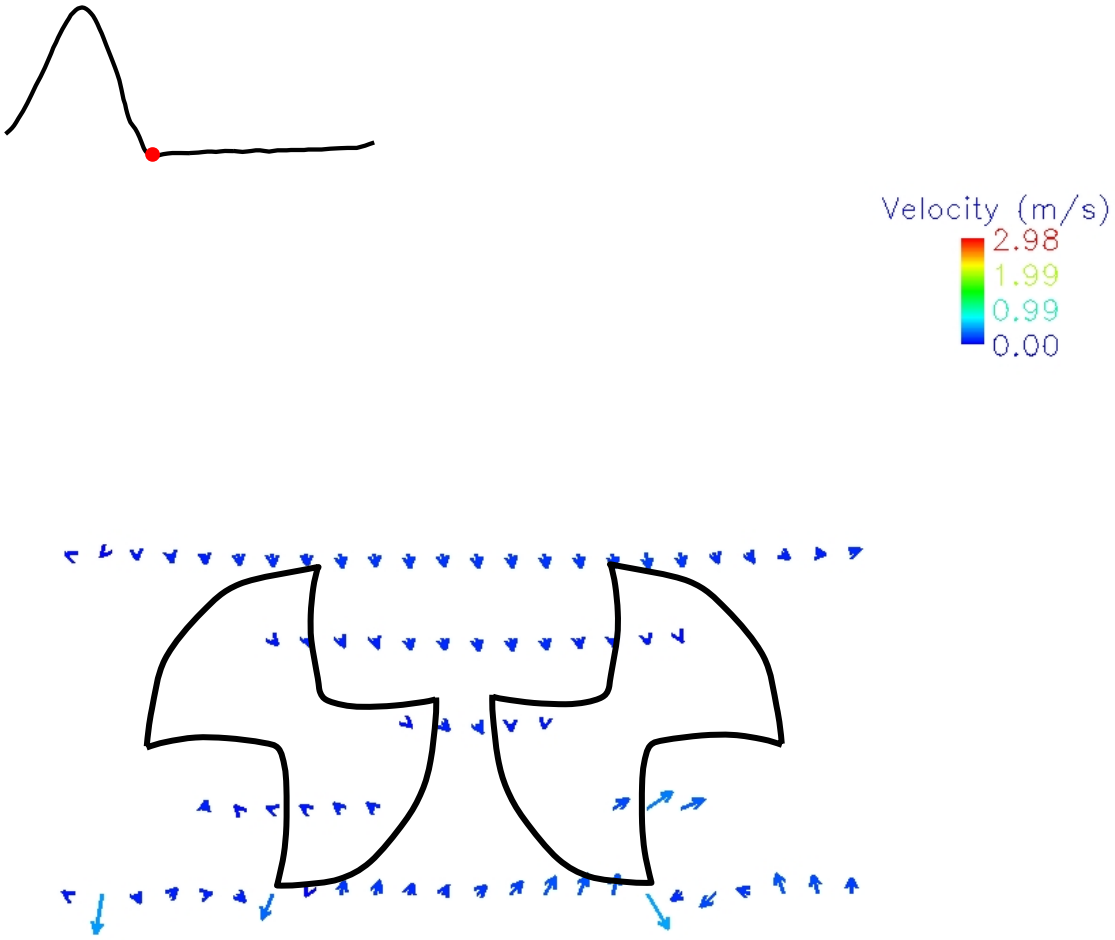

Figure 6.19: 23 mm CM clear valve hinge inflow, outflow flow field 1 mm below the flat at valve closure

Mid Diastole

Figure 6.20 shows the velocity field along the hinge inflow and outflow regions 1 mm below the flat level during mid diastole. The flow field throughout the entire region of interest was characterized by a reverse flow of near zero velocity magnitudes at mid diastole. However, at early diastole, a peak velocity at 0.82 m/s was recorded at the tip of the inflow pocket of the right hinge, and was sustained for 80 ms. High velocities were also recorded at the tip of the left hinge but the velocities were on the order of 0.5 m/s. These elevated velocities were associated with TSS levels up to 421 dyn/cm^2. The relatively high velocity magnitudes at the edge of the hinges were present throughout diastole. The velocities in the outflow region were lower than in the inflow region with velocity magnitudes on the order of 0.1 m/s. Between the hinges and in the outflow region, the TSS levels were near zero.

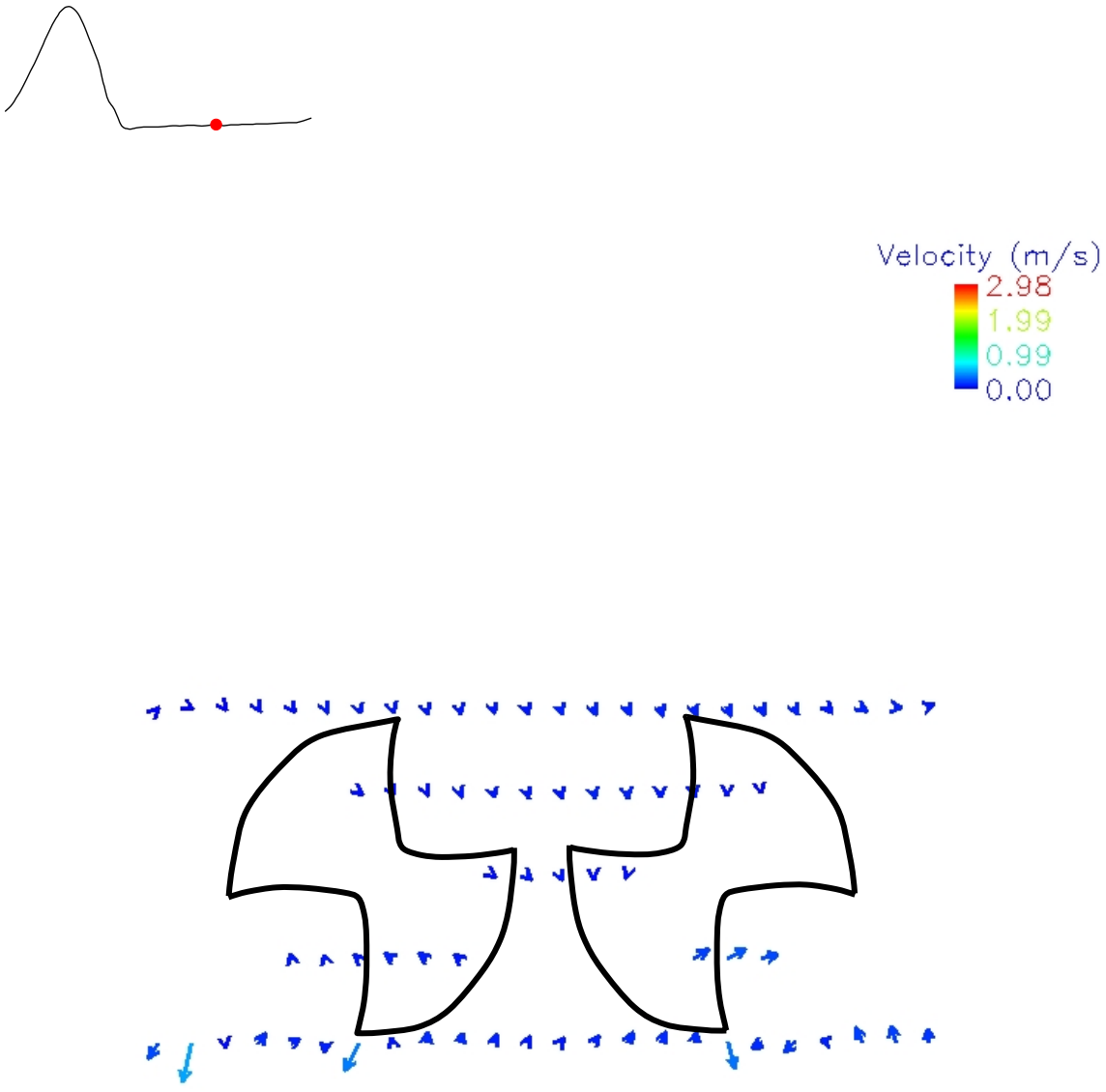

Figure 6.20: 23 mm CM clear valve hinge inflow, outflow flow field 1 mm below the flat at mid acceleration

6.2.2. 23 mm St. Jude Medical Regent Valve

6.2.2.1 Flow and Pressure Curves

Figure 6.21 represents aortic flow and pressure waveforms obtained in the vicinity of the 23 mm SJM Regent valve. The flow waveform was phase window averaged according to the procedure outlined in the experimental protocol section. The time bins corresponding to mid-acceleration, peak systole, valve closure and mid-diastole are also indicated in Figure 6.21.

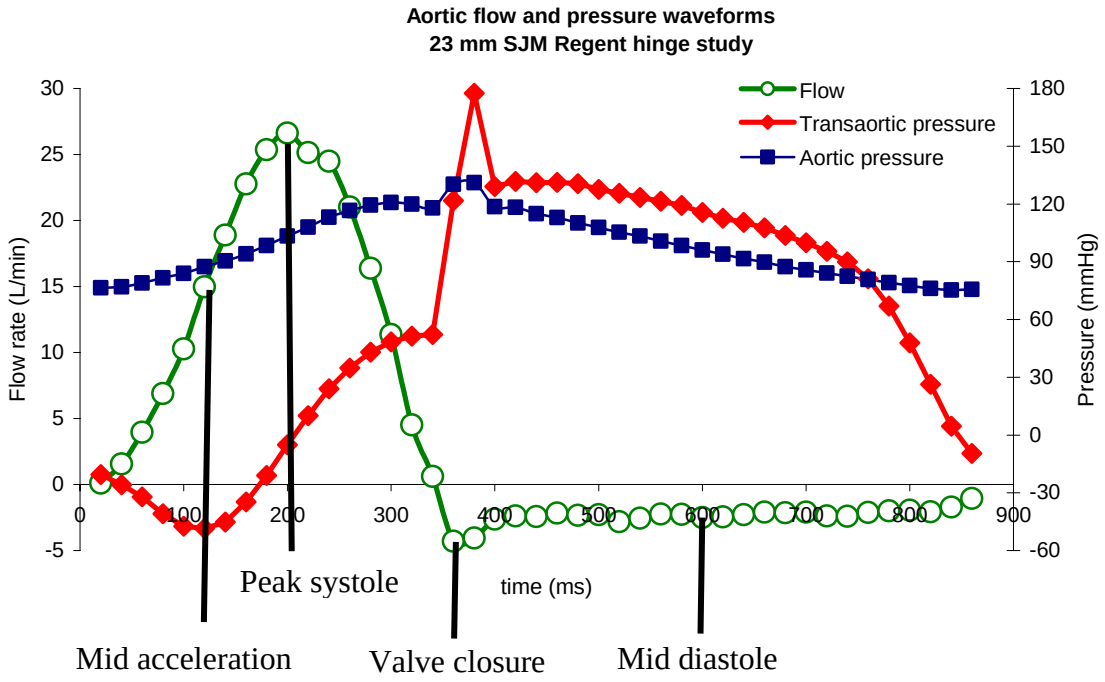

Figure 6.21: Aortic flow and aortic pressure waveforms

6.2.2.2 Leaflet Positions

Figure 6.22 shows the leaflet positions at mid acceleration, peak systole as well as valve closure and mid diastole within the 23 mm SJM clear valve hinge. These leaflet positions correspond to those in the images presented later. For clarity the leaflets are

not shown on the color printouts of the velocity field. Terminology pertinent to the hinge design is shown in Figure 6.23 for orientation purposes.

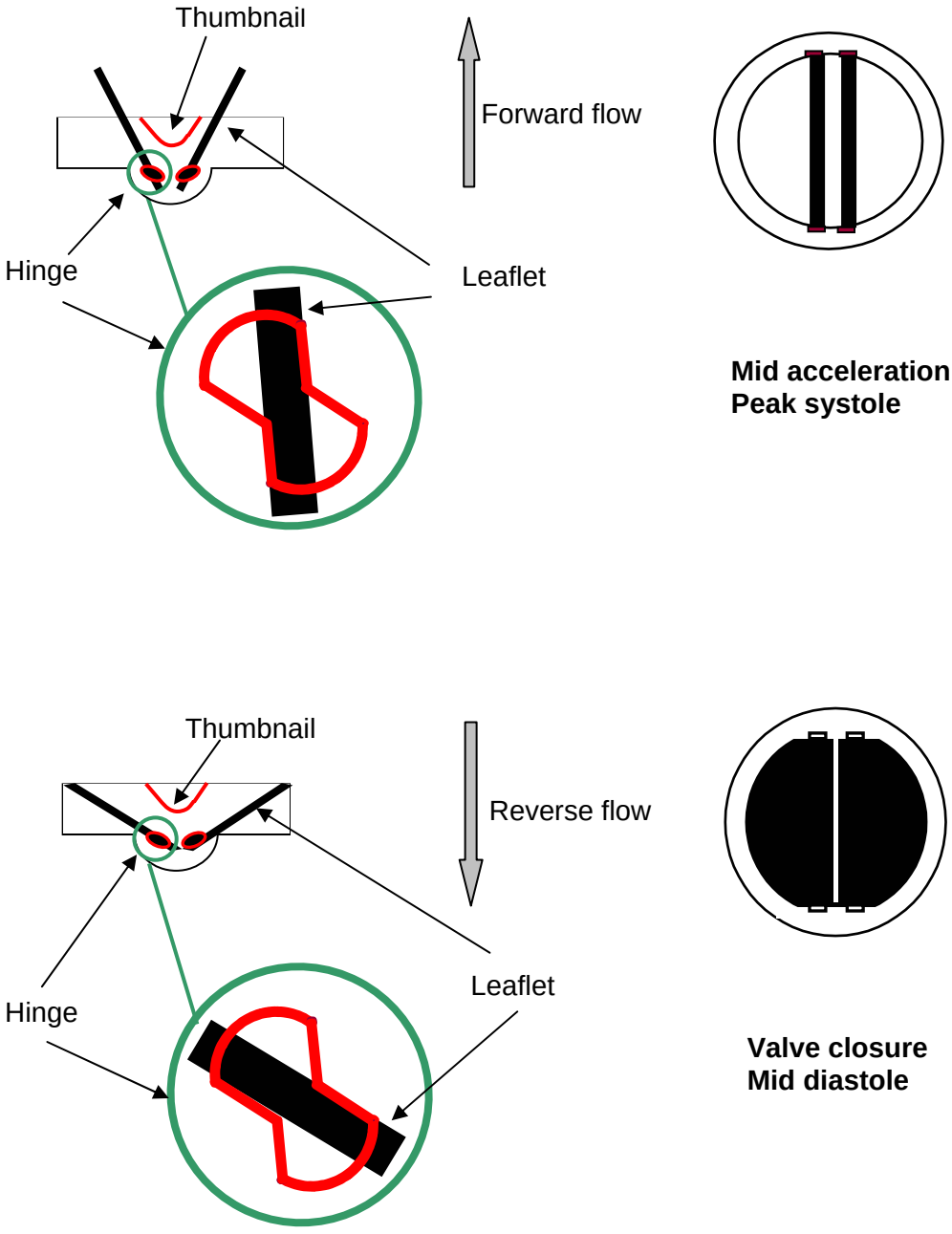

Figure 6.22: Leaflet position at mid acceleration, peak systole, valve closure, and mid diastole within the 23 mm SJM Regent clear housing valve

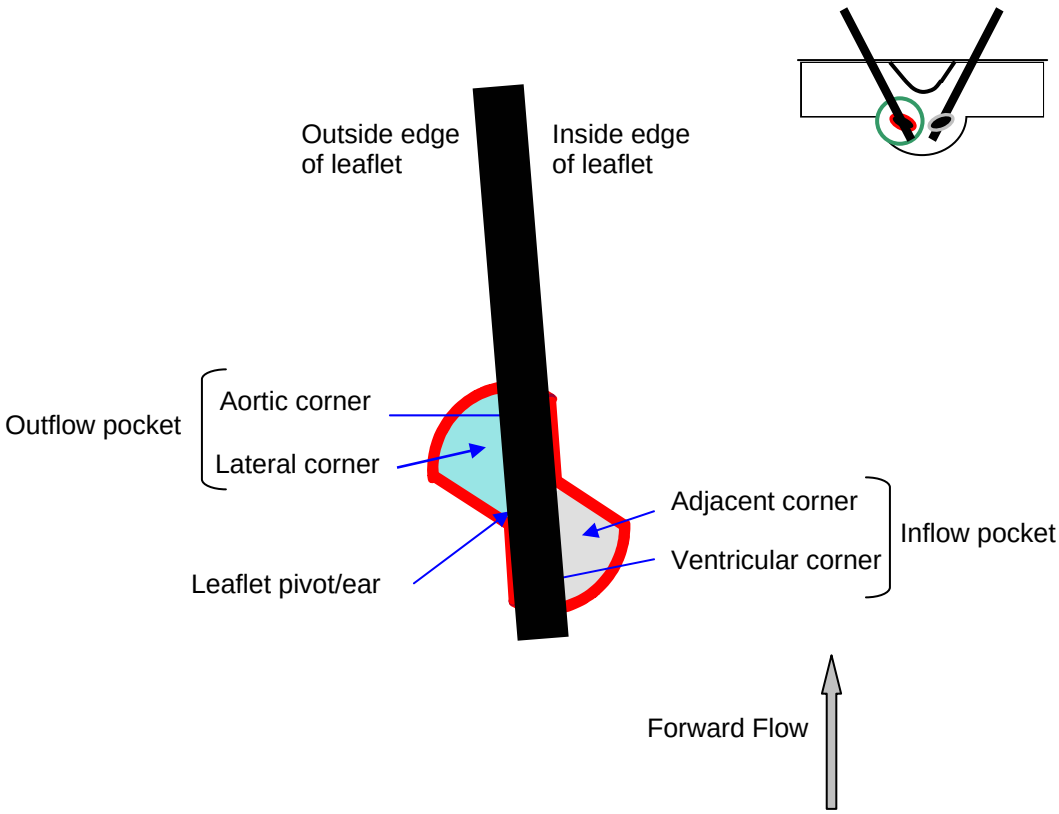

Figure 6.23: Pertinent terminology of 23 mm SJM Regent clear hinge design

6.2.2.3 Overview of the 23mm SJM Regent Hinge Results

Animations (AVI format) of the velocity flow fields obtained at each elevation within the SJM hinge region are given in appendix A. During systole a forward flow jet and a rotating structure were observed at the flat level in the lateral and adjacent corners, respectively. At the 195-μm and 390-μm levels, the forward flow jet vanished, and the rotating structure in the adjacent corner was disturbed. The peak velocities reached 1.75 m/s, 1.06 m/s, 1.07 m/s, and 0.32 m/s at the flat, 195-μm, 390-μm, and 585-μm levels, respectively. The maximum TSS levels were 1,327 dyn/cm^2, 936

dyn/cm^2, 779 dyn/cm^2, and 260 dyn/cm^2 at the flat, 195-μm, 390-μm, and 585-μm levels, respectively.

During diastole a localized leakage jet was observed in the lateral corner. The fluid in the adjacent corner flowed around the leaflet ear, was squeezed against the hinge wall, and redirected towards the ventricular corner. At the 195-μm level and at the 390-μm level, the leakage flow from the adjacent corner expanded throughout the ventricular corner as the fluid may have flowed over the leaflet ear. However, at flat level a recirculation region was observed in the ventricular corner but a localized leakage jet was present in the adjacent corner. The peak velocities were 1.64 m/s, 1.96 m/s, 2.27 m/s, and 0.49 m/s at the flat level, 195-μm, 390-μm, and 585-μm levels, respectively. The maximum TSS levels were 2,657 dyn/cm^2, 5,460 dyn/cm^2, 7,903 dyn/cm^2, and 647 dyn/cm^2 at the flat, 195-μm, 390-μm, and 585-μm levels, respectively.

At all elevations below the flat, the central systolic jet was skewed as it entered the thumbnail region and was surrounded by two recirculation regions of low velocity. The peak velocities were 2.49 m/s, 2.43 m/s, and 2.62 m/s at 500 μm, 1 mm, and 3 mm below the flat level, respectively. The maximum TSS levels were 3,189 dyn/cm^2, 3,192 dyn/cm^2, 4,544 dyn/cm^2 at 500 μm, 1 mm, and 3 mm below the flat level, respectively. During diastole the peak velocities were approximately 0.15 m/s at all elevations below the flat level, while the maximum TSS levels were 1,236 dyn/cm^2, 864 dyn/cm^2, and 48 dyn/cm^2 at 500 μm, 1 mm, and 3 mm below the flat level..

For comparison Doppler Echocardiography showed that the maximum bulk velocity of a normally functioning 23 mm SJM valve placed under aortic conditions reaches 2.5 ± 0.4 m/, for a mean velocity of 1.7 m/s ± 0.3 (Perin, 1991). The peak bulk velocity magnitude recorded using LDV in the present study was 1.8 m/s.

The spatial and time averaged standard deviations of the velocity magnitude were 0.09 m/s, 0.08 m/s and 0.07 m/s at 500 μm, 1 mm and 3 mm below the flat level, respectively. Above the flat level, the average standard deviations of the velocity magnitude were 0.04 m/s, 0.12 m/s, 0.19 m/s and 0.13 m/s at the flat, 195-μm, 390-μm and 585 -μm levels, respectively.

6.2.2.4 Detailed Description of the Hinge and Near-hinge Flow Fields of the 23mm SJM Regent Clear Housing Valve

Flat Level

Mid Acceleration

Figure 6.24 shows the velocity field inside the hinge region at the flat level during mid acceleration. In the adjacent corner a counterclockwise rotating structure developed due to the confining effect of the leaflet ear upon the entering flow. In the rotating structure the velocity magnitude was on the order of 0.3 m/s and the TSS reached 90 dyn/cm^2. Some flow from the rotating structure may have been squeezed against the hinge wall, as evidenced by the magnitude of the velocity vectors, which reached 1.45 m/s. In the squeeze flow, the TSS reached 675 dyn/cm^2 near the hinge wall.

Higher velocity magnitudes were observed in the inflow hinge pocket as a forward flow jet developed in the lateral corner. The velocity in this slightly skewed jet reached 1.75 m/s. In the outflow hinge pocket, the TSS levels were less than 60 dyn/cm^2, except along the hinge wall where the TSS reached 1,113 dyn/cm^2.

The lack of measurements in the central region was attributed to the obstruction of the probe volume by the leaflet ear.

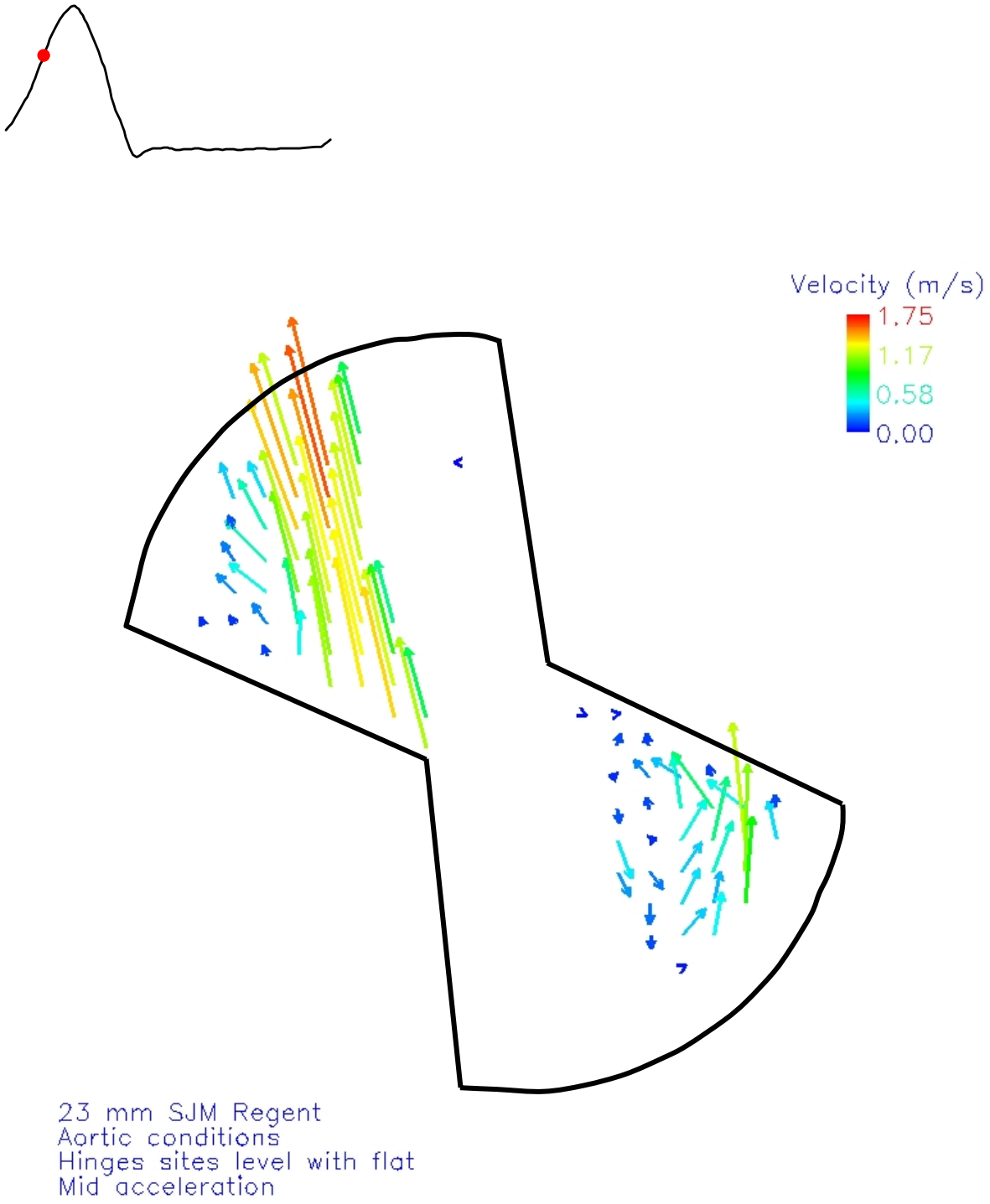

Figure 6.24: 23 mm SJM Regent clear valve hinge flow field at the flat level at mid acceleration

Peak Systole

Figure 6.25 shows the velocity field inside the hinge region at the flat level at peak systole. The forward flow jet that developed in the lateral corner during mid acceleration was still present at peak systole, but the velocity magnitudes were lower. The maximum velocity observed in this region was 1.27 m/s, while the maximum TSS was 425 dyn/cm^2. The squeeze flow in the adjacent corner was slower at peak systole than at mid acceleration, with a velocity of 0.94 m/s and a TSS of 478 dyn/cm^2.

Valve Closure

Figure 6.26 shows the velocity field inside the hinge region at the flat level at valve closure. The rotating structure and the forward flow jet present at mid acceleration and peak systole were abolished 60 ms after peak systole. The flow became nearly stagnant 80 ms after peak systole, except in the central region of the hinge where a reverse flow with velocities up to 0.29 m/s was observed. Immediately before valve closure, a reverse flow parallel to the leaflet ear, with velocities up to 0.32 m/s, was seen in the outflow aortic corner. At valve closure, the velocities decreased to 0.21 m/s in the aortic corner. Within the lateral corner, the velocity was less than 0.2 m/s and the maximum TSS level reached 484 dyn/cm2.

High velocities up to 1.08 m/s were recorded in the inflow adjacent corner as the leakage flow was squeezed between the hinge wall and the surface of the leaflet ear. Location and angulation of these vectors suggested that this leakage flow began nearly parallel to the surface of the leaflet ear, was redirected by the hinge wall, and was subsequently directed back towards the inflow ventricular corner. The TSS levels in the squeeze flow reached 949 dyn/cm^2. Additionally, a slow clockwise rotating structure was observed in the ventricular corner with velocity magnitudes up to 0.21 m/s, and TSS levels less than 65 dyn/cm^2. However, immediately before valve closure, slightly higher

velocities and TSS levels were recorded in this region with peak values of 0.27 m/s and 364 dyn/cm^2, respectively.

Mid Diastole

Figure 6.27 shows the velocity field inside the hinge region at the flat level during mid diastole. Throughout the hinge velocity vectors pointed nearly in the same directions as those seen at the same elevation at valve closure. A reverse flow was observed throughout the aortic corner but the velocity magnitudes were lower than at valve closure with velocity magnitudes on the order of 0.1 m/s. The squeeze flow seen at the tip of the outflow lateral corner at valve closure was present at mid diastole. Velocities up to 0.9 m/s were seen in this region. The squeeze flow in the inflow adjacent corner seen at valve closure was present at mid diastole. The velocities in this squeeze flow reached 1.64 m/s, and the TSS levels in the adjacent corner were less than 900 dyn/cm^2. However, within the squeeze flow the TSS reached 2,657 dyn/cm^2. Additionally, velocities in the ventricular corner were on the same order of magnitude as those recorded at valve closure. However, the rotating structure in this region changed orientation, as it was counterclockwise at mid diastole.

Throughout diastole, the hinge flow filed remained similar. At the end of diastole, the leakage flow pattern vanished as a forward flow began to develop in the lateral corner with velocities up to 0.23 m/s and a rotating structure appeared in the adjacent corner.

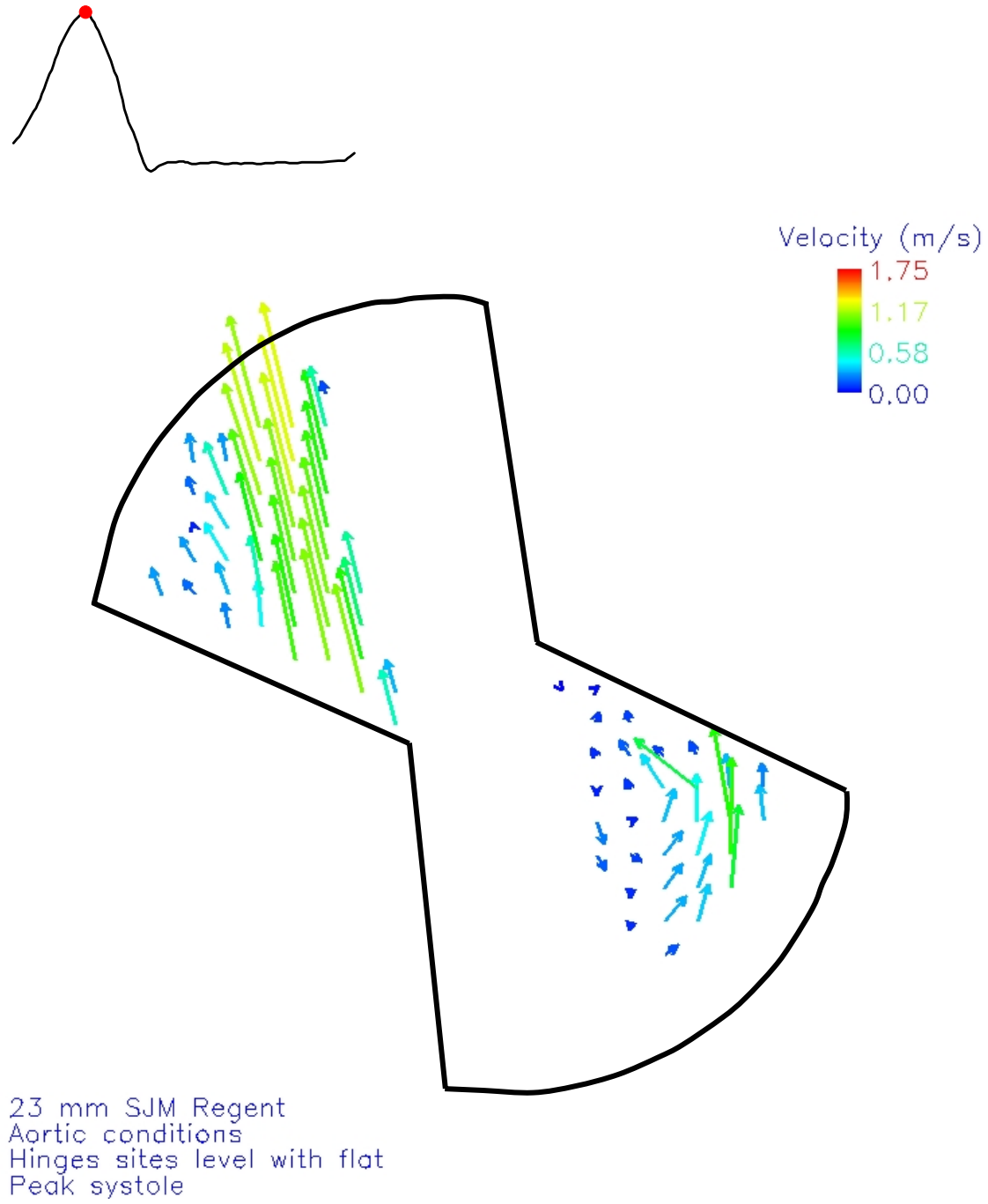

Figure 6.25: 23 mm SJM Regent clear valve hinge flow field at the flat level at peak systole

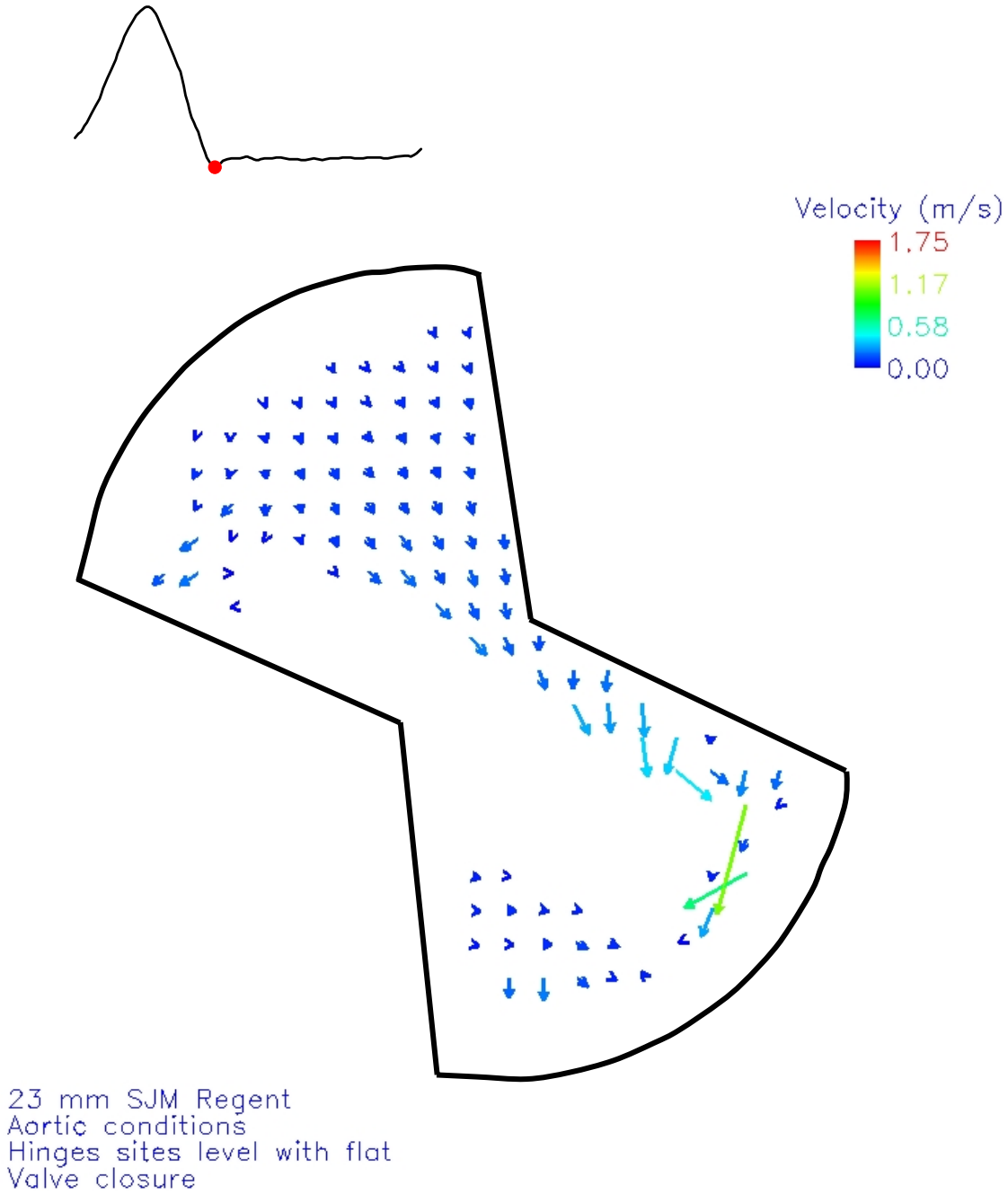

Figure 6.26: 23 mm SJM Regent clear valve hinge flow field at the flat level at valve closure

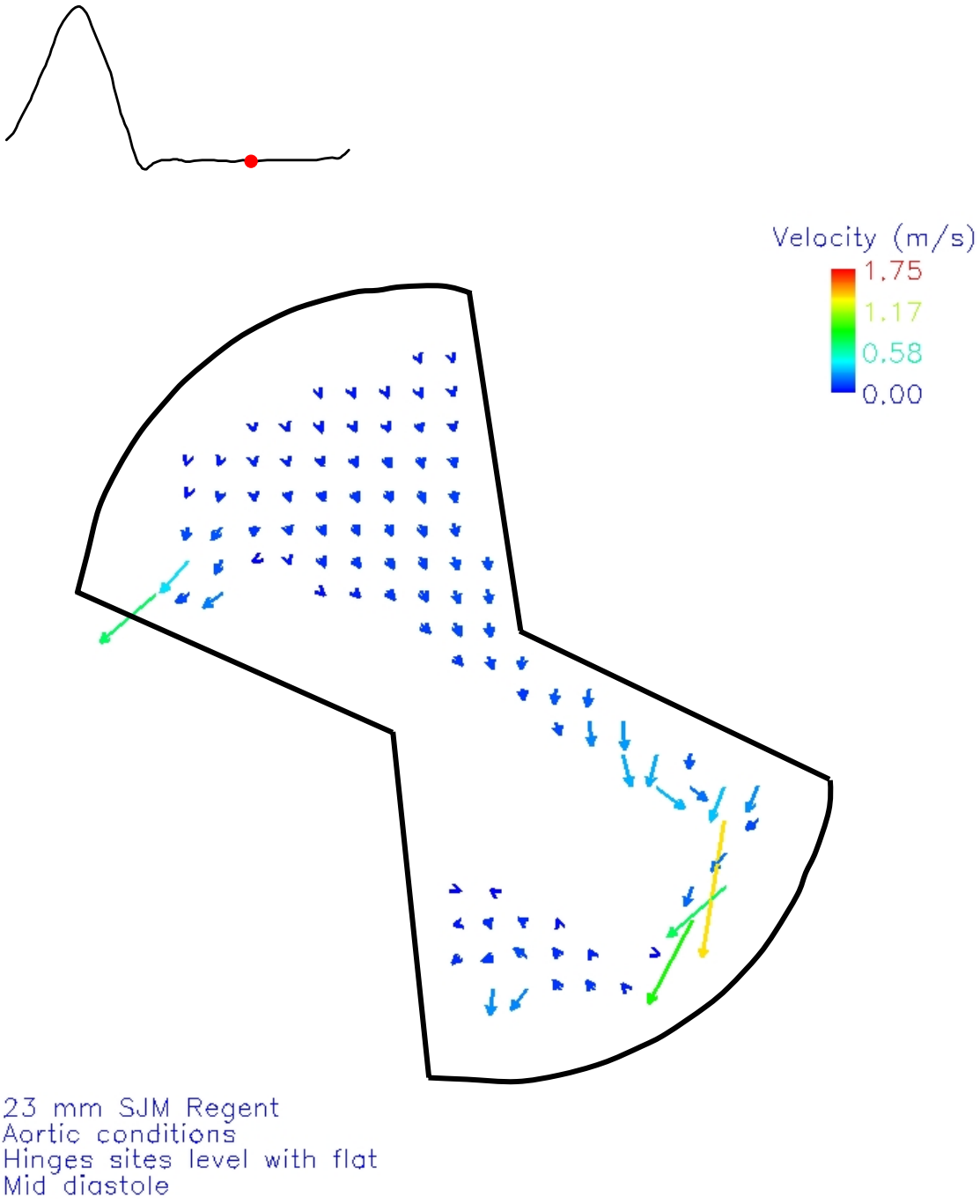

Figure 6.27: 23 mm SJM Regent clear valve hinge flow field at the flat level at mid diastole

195 μm Above Flat Level

Mid Acceleration

Figure 6.28 shows the velocity field inside the hinge region 195 μm above the flat level during mid acceleration. The forward flow jet observed at the flat level was not seen at this elevation. A disturbed rotating structure was present in the adjacent corner. Velocity magnitudes in this region ranged from 0.10 to 0.86 m/s, and in the lateral outflow corner, backward velocity vectors flowed nearly parallel to the lateral outflow hinge wall, with a velocity magnitude of 0.25 m/s. The TSS levels did not exceed 100 dyn/cm^2 in the outflow hinge pocket, but in the inflow adjacent hinge corner they ranged from nearly zero to 345 dyn/cm^2.

Peak Systole

Throughout the hinge, velocity vectors pointed nearly in the same directions as those seen at this elevation during mid acceleration. Therefore no color-coded velocity field image is displayed. Velocity magnitudes in the perturbed rotating structure in the inflow pocket were on the order of 0.4 m/s. However, velocity magnitudes up to 1.04 m/s were observed at one location. The TSS levels in the inflow hinge pocket ranged from nearly zero to 165 dyn/cm^2. The reverse flow parallel to the lateral hinge wall was slightly slower than at mid acceleration. Velocity magnitudes reached 0.2 m/s, and the TSS levels were less than 35 dyn/cm^2.

Valve Closure

Figure 6.29 shows the velocity field inside the hinge region 195 μm above the flat level at valve closure. A reverse flow pattern was first seen in the outflow region 100 ms after peak systole with a maximum velocity of 0.27 m/s and a peak TSS level of 436

dyn/cm2. At valve closure, a leakage flow appeared in the inflow pocket with a maximum velocity of 1.13 m/s, and a peak TSS at 2,227 dyn/cm^2. The velocities in the outflow pocket were on the order of 0.1 m/s.

Mid Diastole

Figure 6.30 shows the velocity field inside the hinge region 195 μm above the flat level during mid diastole. The flow vector distribution was similar to that seen at valve closure. The velocity magnitudes were near zero along the surface of the leaflet ear in the outflow hinge pocket. The vectors through the outflow pocket were reverse. In this region, the velocity magnitudes and the TSS levels were less than 0.25 m/s and 40 dyn/cm^2, respectively. A peak velocity at 0.70 m/s was recorded along the aortic wall corner 20 ms after valve closure. In the adjacent corner a region of backflow larger than that present at valve closure was observed. Velocity magnitudes reached up to 1.96 m/s in this region. As seen at the flat level, this reverse jet was skewed towards the ventricular hinge corner. The highest TSS levels were seen in the inflow hinge pocket with a maximum TSS of 5,460 dyn/cm^2. The reverse flow pattern in the inflow pocket vanished 40 ms before the end of diastole. Leakage flow was visible throughout diastole in the outflow pocket, except during the last 20 ms of diastole when a forward flow up to 0.15 m/s began to develop.

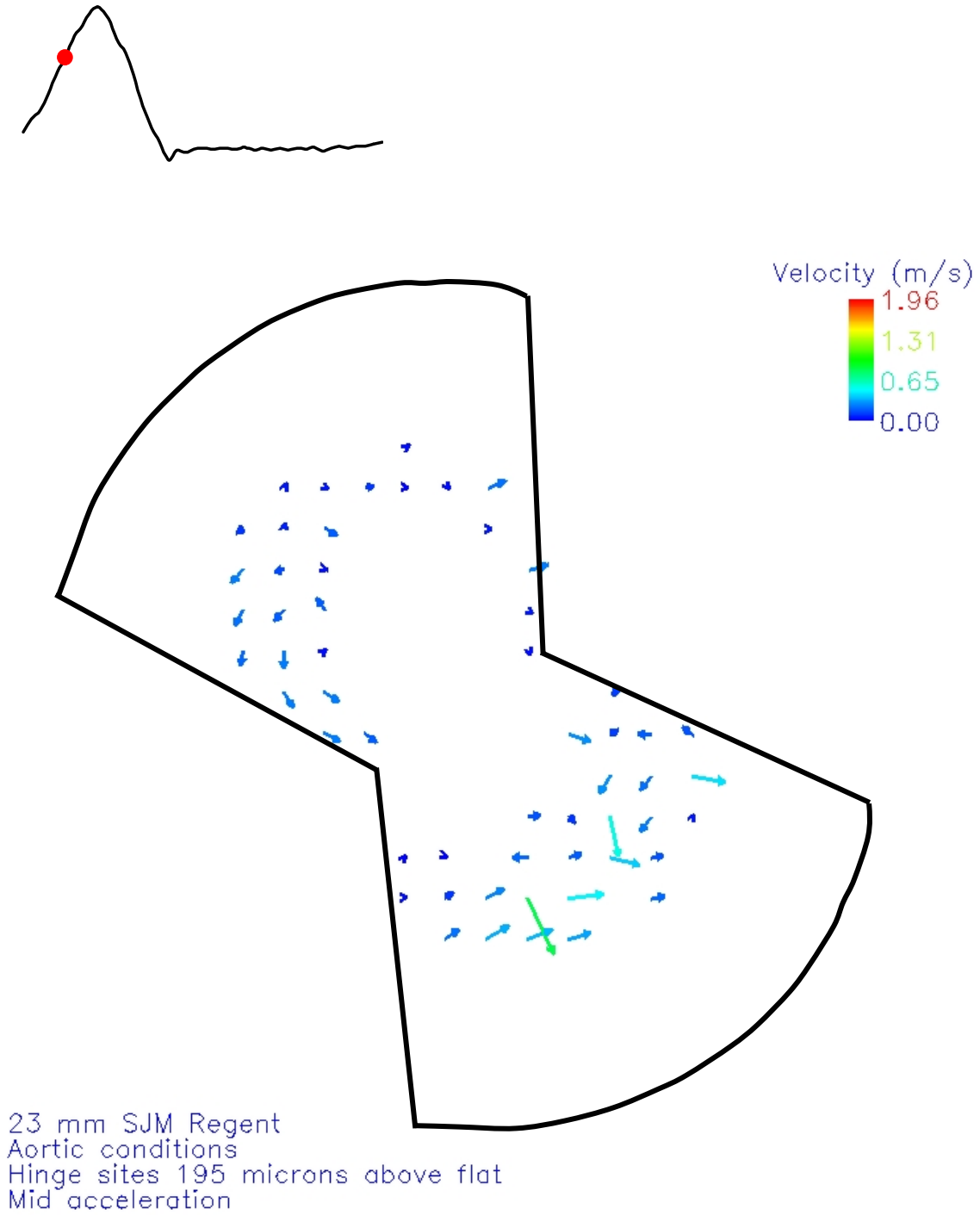

Figure 6.28: 23 mm SJM Regent clear valve hinge flow field
195 μm above the flat at mid acceleration

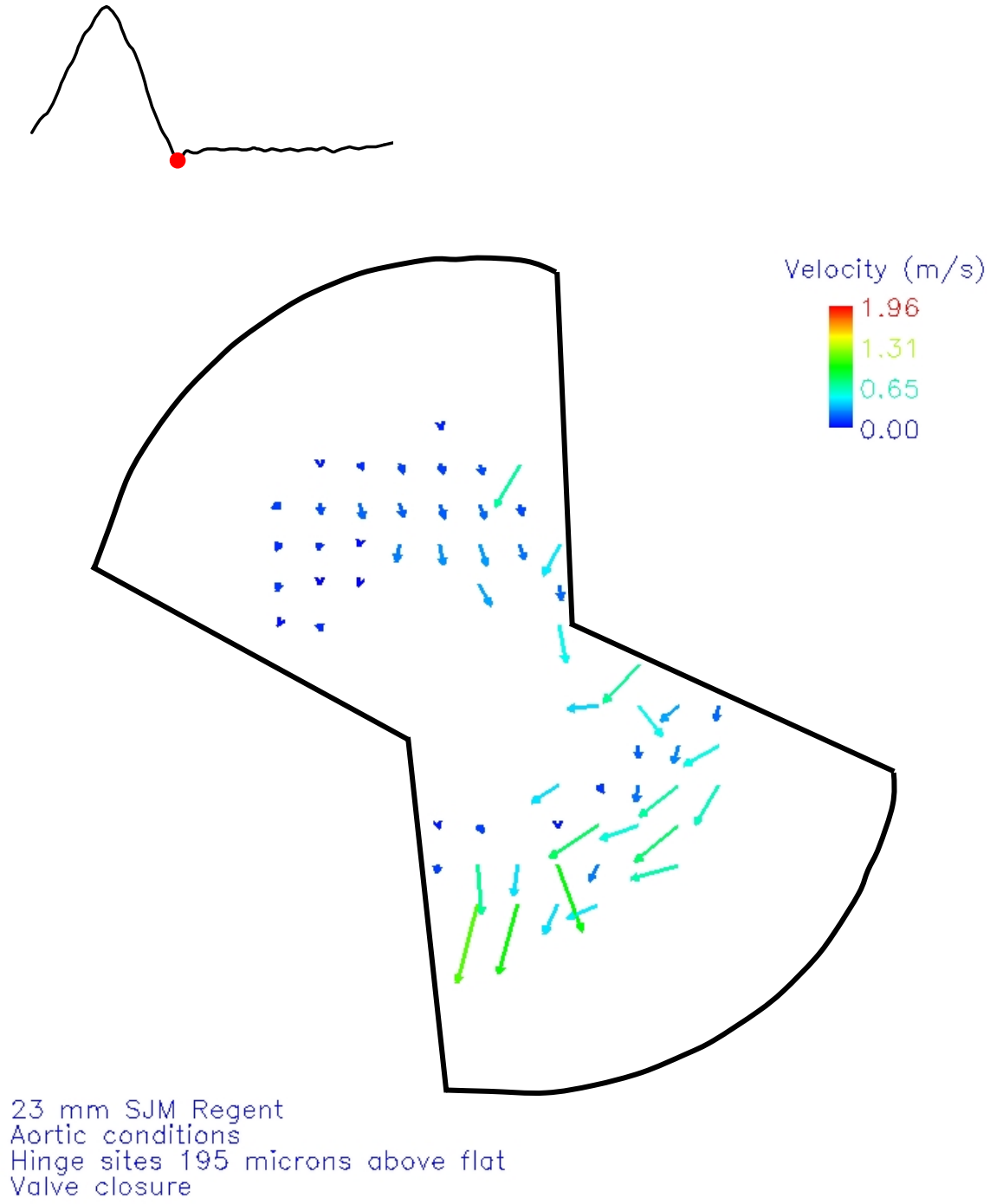

Figure 6.29: 23 mm SJM Regent clear valve hinge flow field
195 μm above the flat at valve closure

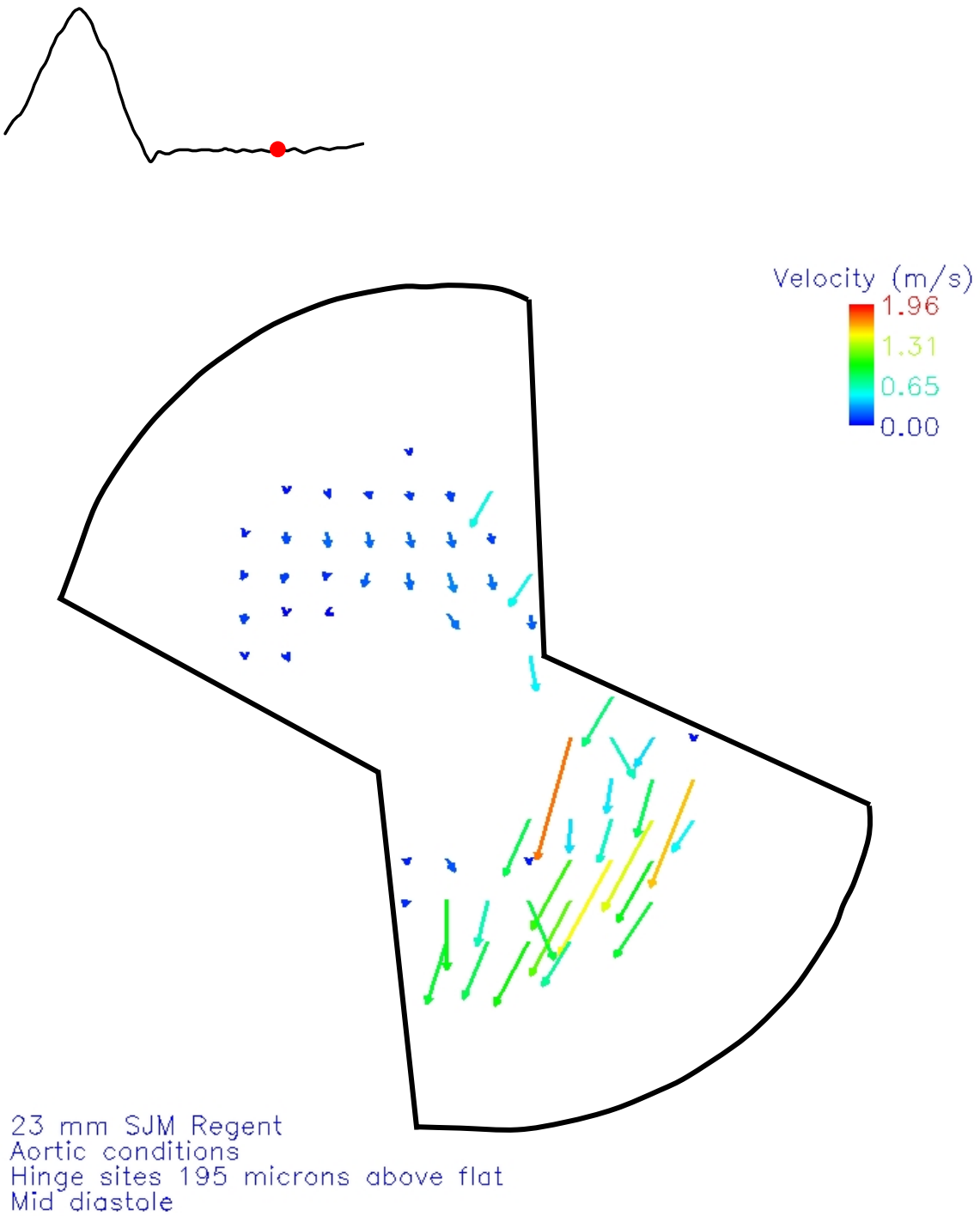

Figure 6.30: 23 mm SJM Regent clear valve hinge flow field
195 μm above the flat at mid diastole

390 μm Above Flat Level

Mid Acceleration

Figure 6.31 shows the velocity field inside the hinge region 390 μm above the flat level during mid acceleration. During this phase a rotating structure was observed in the adjacent inflow corner. In this rotating structure velocity magnitudes reached 1.07 m/s. The outflow region was characterized by low velocity flow with velocity magnitudes ranging from near zero to 0.40 m/s. Velocity vectors adjacent to the surface of the leaflet ear approached zero. The peak TSS levels in both inflow and outflow pockets were on the same order of magnitude, as the TSS levels reached 675 dyn/cm^2 in the outflow pocket and 632 dyn/cm^2 in the inflow pocket.

Peak Systole

Figure 6.32 shows the velocity field inside the hinge region 390 μm above the flat level at peak systole. During this phase the flow pattern was similar to the one observed at mid acceleration. However, the velocity magnitudes recorded in the rotating structure in the adjacent corner were slower, reaching a peak value of 0.67 m/s. The velocity field inside the outflow hinge pocket was nearly stagnant. At peak diastole, the velocity magnitudes were less than 0.21 m/s, except one measurement point that was associated with a velocity magnitude of 0.41 m/s. Throughout the hinge the TSS levels were less than 300 dyn/cm^2.

Valve Closure

Figure 6.33 shows the velocity field inside the hinge region 390 μm above the flat level at valve closure. Reverse flow in the aortic corner was first seen 40 ms before valve closure, while the reverse flow in the inflow pocket appeared immediately before

valve closure. At valve closure, the velocity vectors in the outflow pocket pointed towards the central region of the valve. In this region, the velocity magnitudes were on the order of 0.4 m/s with a peak velocity at 0.66 m/s. The TSS levels were on the order of 300 dyn/cm^2 with a peak value at 1,080 dyn/cm^2.

Velocity magnitudes up to 1.54 m/s were recorded at the tip of the ventricular corner where a large leakage flow was observed. High velocities were also recorded in the adjacent corner. Reverse flow from the outflow region flowed around the leaflet ear before impacting the adjacent inflow region and being redirected towards the ventricular corner. Velocities in this region reached 0.99 m/s. In the adjacent corner, the peak TSS reached 2,984 dyn/cm^2, while in the ventricular corner, the peak TSS level was 2,416 dyn/cm^2.

Mid Diastole

Figure 6.34 shows the velocity field inside the hinge region 390 μm above the flat level during mid diastole. The flow pattern was similar to that seen at valve closure. The flow throughout the hinge region was retrograde and nearly parallel to the surface of the leaflet ear. Velocity magnitudes within the leakage jet in the inflow pocket reached 2.27 m/s at mid diastole, while the velocity magnitudes in the outflow region reached 1.08 m/s. The highest TSS were recorded in the inflow pocket, with levels on the order of 3,000 dyn/cm^2. A peak TSS level of 7,903 dyn/cm2 was recorded at mid diastole but this elevated TSS level was associated with a single measurement site. In the outflow pocket, the TSS levels did not exceed 1,000 dyn/cm^2.

At late diastole, the reverse flow pattern was still visible but the velocities were less than 0.38 m/s, and the TSS levels less than 210 dyn/cm^2. At the end of diastole the maximum velocity decreased to 0.25 m/s, and the vectors distribution revealed the presence of a forward flow pattern.

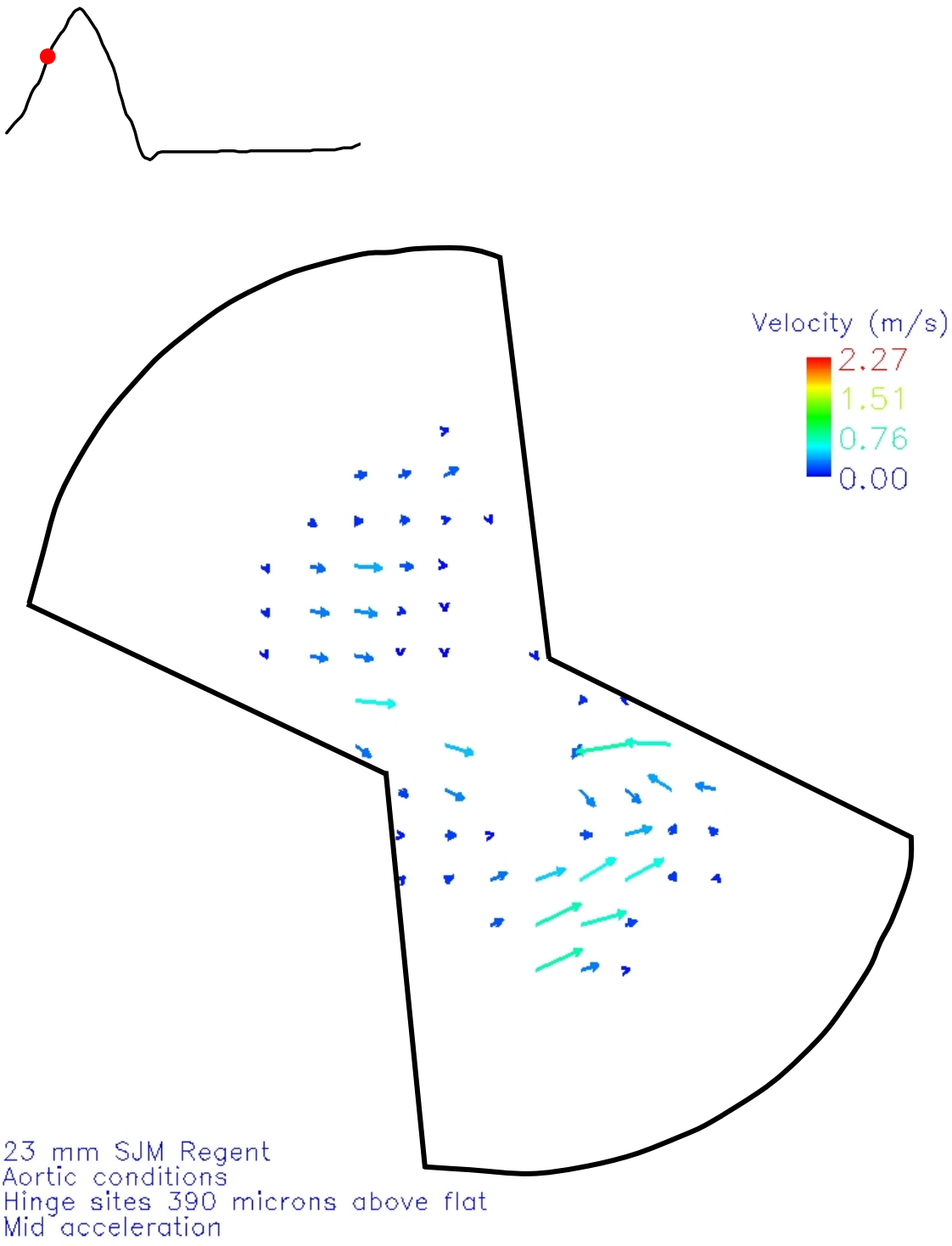

Figure 6.31: 23 mm SJM Regent clear valve hinge flow field
390 μm above the flat at mid acceleration

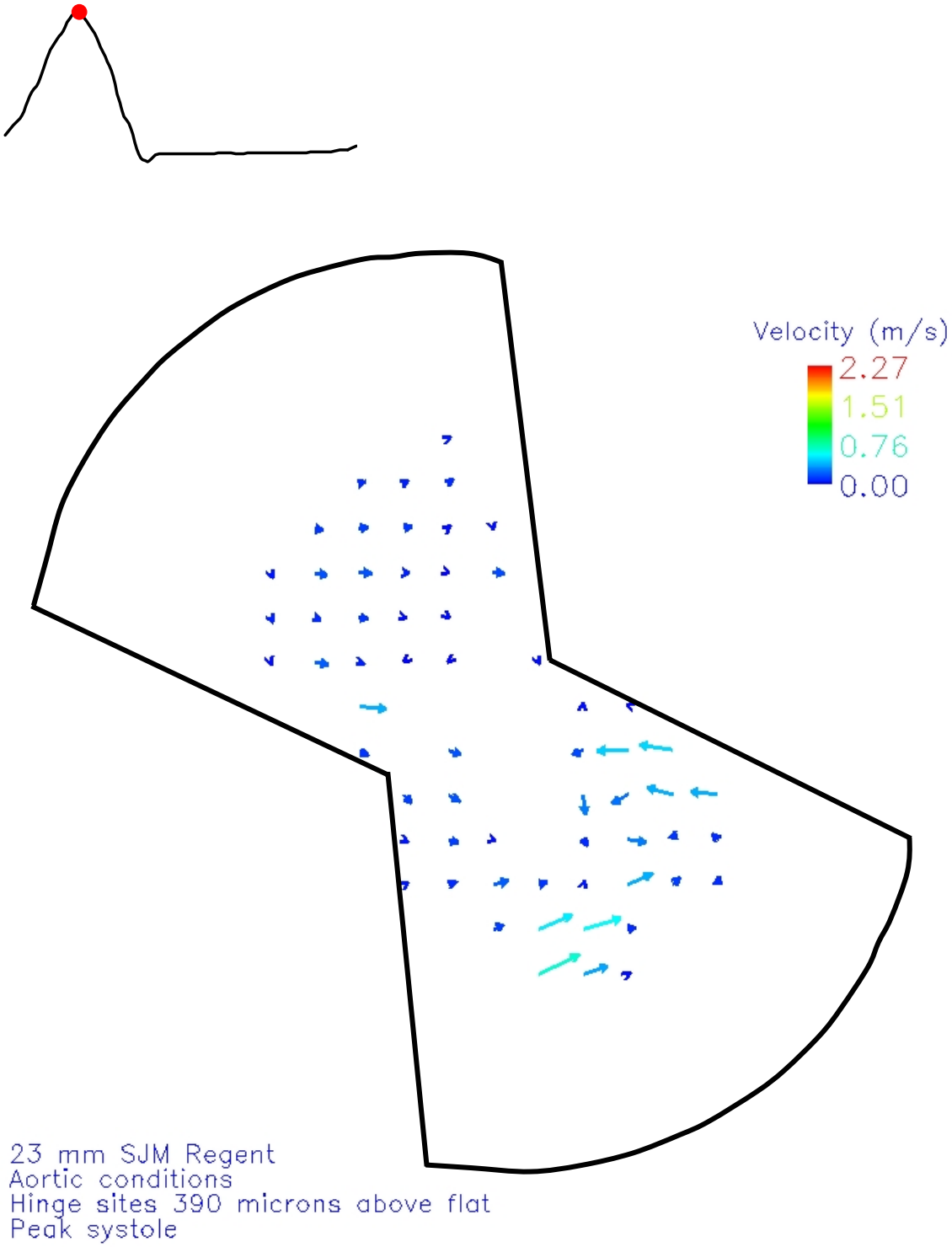

Figure 6.32: 23 mm SJM Regent clear valve hinge flow field
390 μm above the flat at peak systole

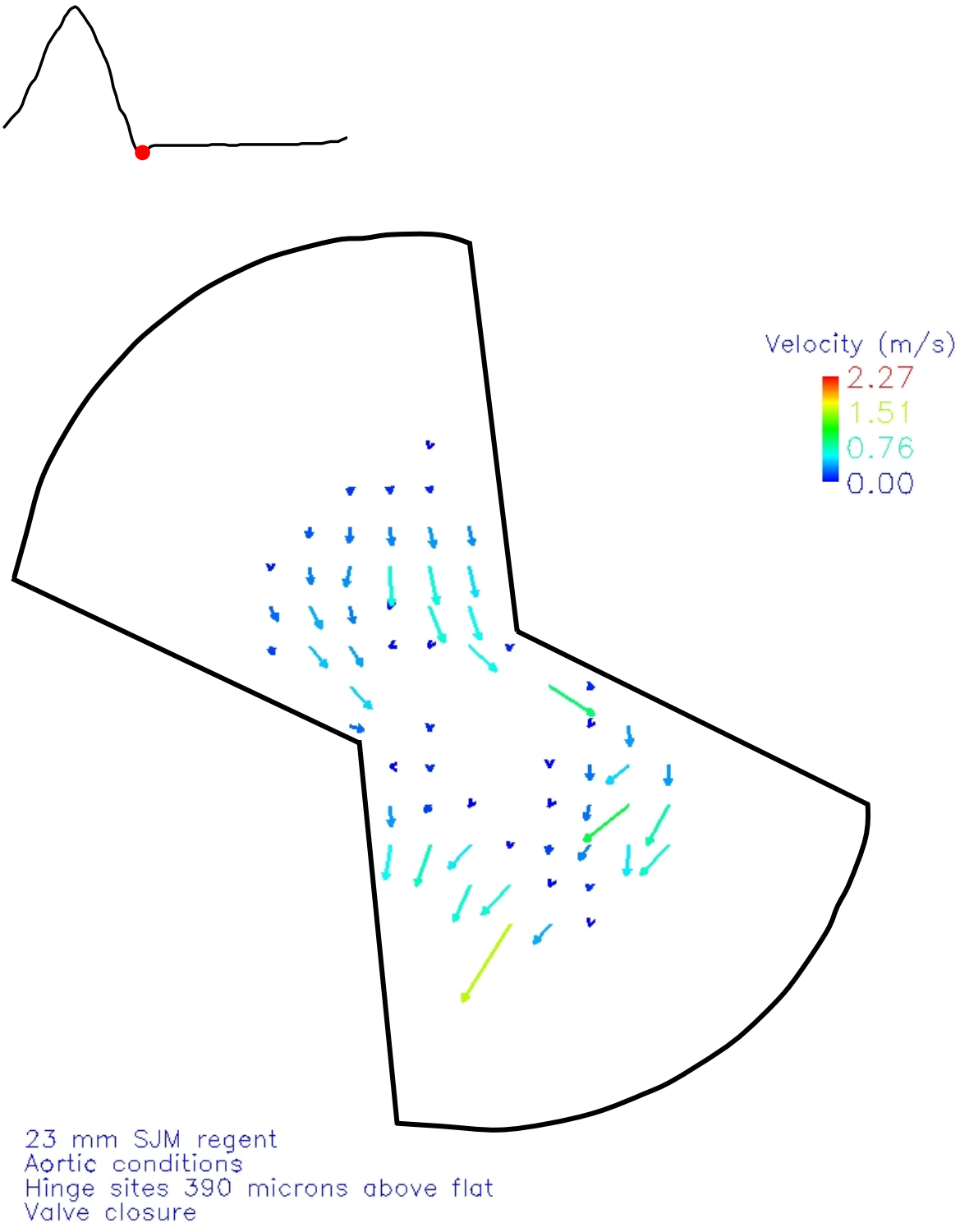

Figure 6.33: 23 mm SJM Regent clear valve hinge flow field
390 μm above the flat at valve closure

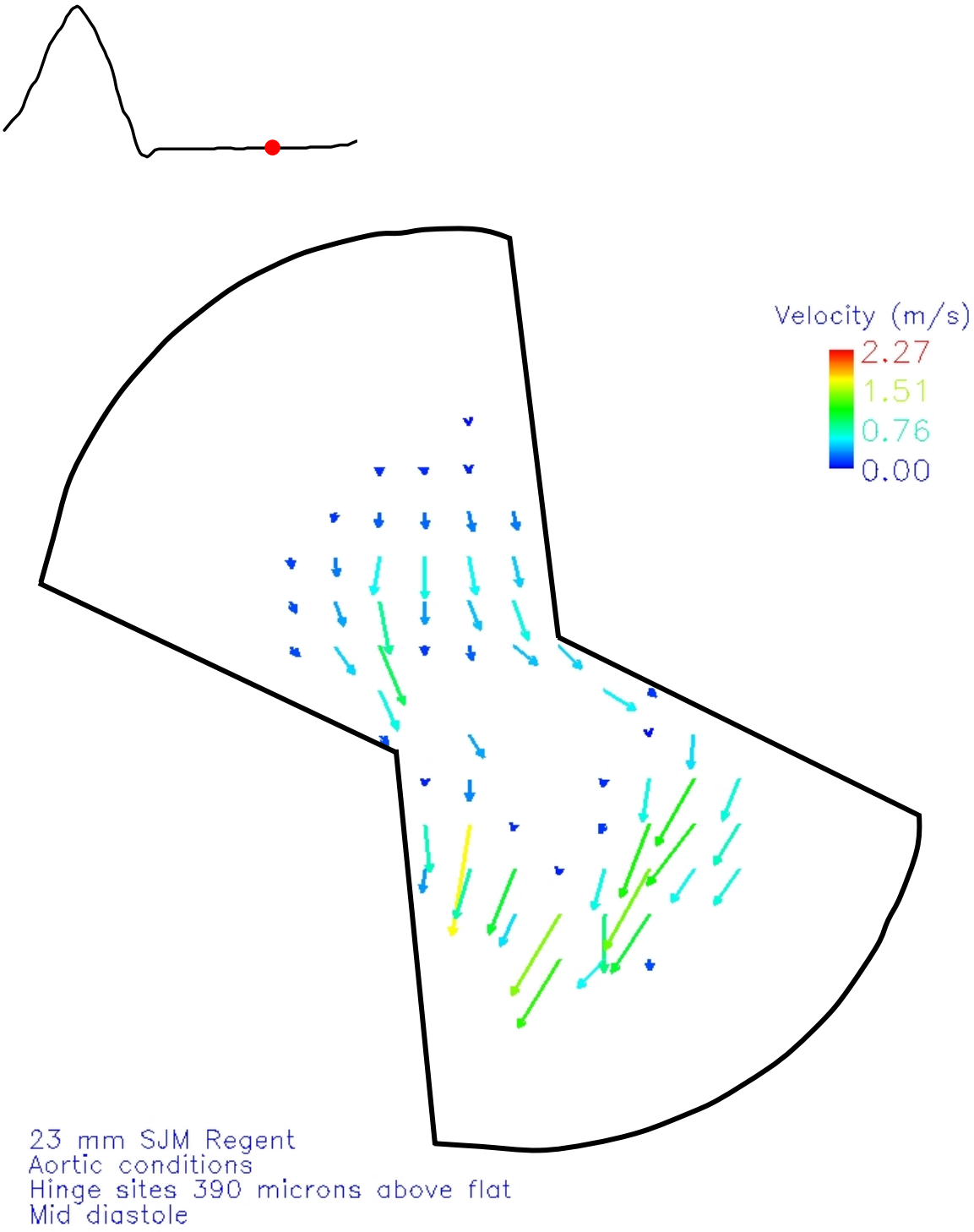

Figure 6.34: 23 mm SJM Regent clear valve hinge flow field
390 μm above the flat at mid diastole

585 μm Above Flat Level

The velocity field at 585 μm above the flat level was similar to those at mid acceleration and peak systole. Velocity magnitudes reached 0.21 m/s and the TSS levels were less than 260 dyn/cm^2. However, during diastole the velocity reached 0.49 m/s and the TSS reached 646 dyn/cm2.

500 μm Below Flat Level

Mid Acceleration

Figure 6.35 shows the velocity field 500 μm below the flat level along the hinge inflow and outflow regions, and within the thumbnail region during mid acceleration. In the hinge region between the leaflets, a central forward jet began to develop. In this region velocity vectors with a strong axial component reached 2.49 m/s. The maximum TSS was 1,065 dyn/cm^2, observed at the right edge of the jet. Low flow was observed on the left side of the jet. In the outflow region, the forward flow jet was slightly slower with a velocity of 2.21 m/s. Lower velocity flow reaching 1.77 m/s was observed at the outside edges of the leaflets.

Within the thumbnail, the forward flow jet velocity decreased to 2.02 m/s due to flow separation and detachment from the thumbnail wall. The diminished forward flow jet had a strong axial component. Adjacent to this jet were two large low flow regions where the velocity magnitudes did not exceed 0.45 m/s. On the right side of the thumbnail region, the low velocity vectors were mainly in the forward direction; while on the left side angulation of the velocity vectors suggested the emergence of a clockwise rotating structure. At the interface between the central jet and the low velocity regions, the highest TSS levels, of up to 1,827 dyn/cm^2 were recorded. Throughout the rest of the

thumbnail region, the TSS levels ranged from 15 to 250 dyn/cm^2. Higher velocity flow reaching 2.15 m/s was seen adjacent to the low flow regions.

Peak Systole

Figure 6.36 shows the velocity field 500 μm below the flat level along the hinge inflow and outflow regions, and within the thumbnail region at peak systole. In the hinge region, between the open leaflets, the central forward flow jet with velocity magnitudes up to 2.06 m/s was slightly slower than at mid acceleration. High speed velocity vectors at the outside edges of the leaflets decreased to 1.59 m/s. In the hinge region, the TSS reached 280 dyn/cm^2 at the left edge of the central jet.

As the forward jet entered the thumbnail, its velocity decreased to 1.82 m/s and the flow pattern within the thumbnail, was asymmetric. The forward jet tended to develop more on the right side of the thumbnail region, but the circumferential velocity vector component was still negligible. On the left side of the jet, a low velocity rotating structure

expanded to fill approximately half of the thumbnail region. At the interface between the jet and the slow rotating structure, TSS levels of up to 913 dyn/cm^2 were recorded. Velocity magnitudes less than 0.30 m/s were observed in this region. At the outside edges of the thumbnail, high speed flow reached 1.95 m/s and the TSS reached 963 dyn/cm^2.

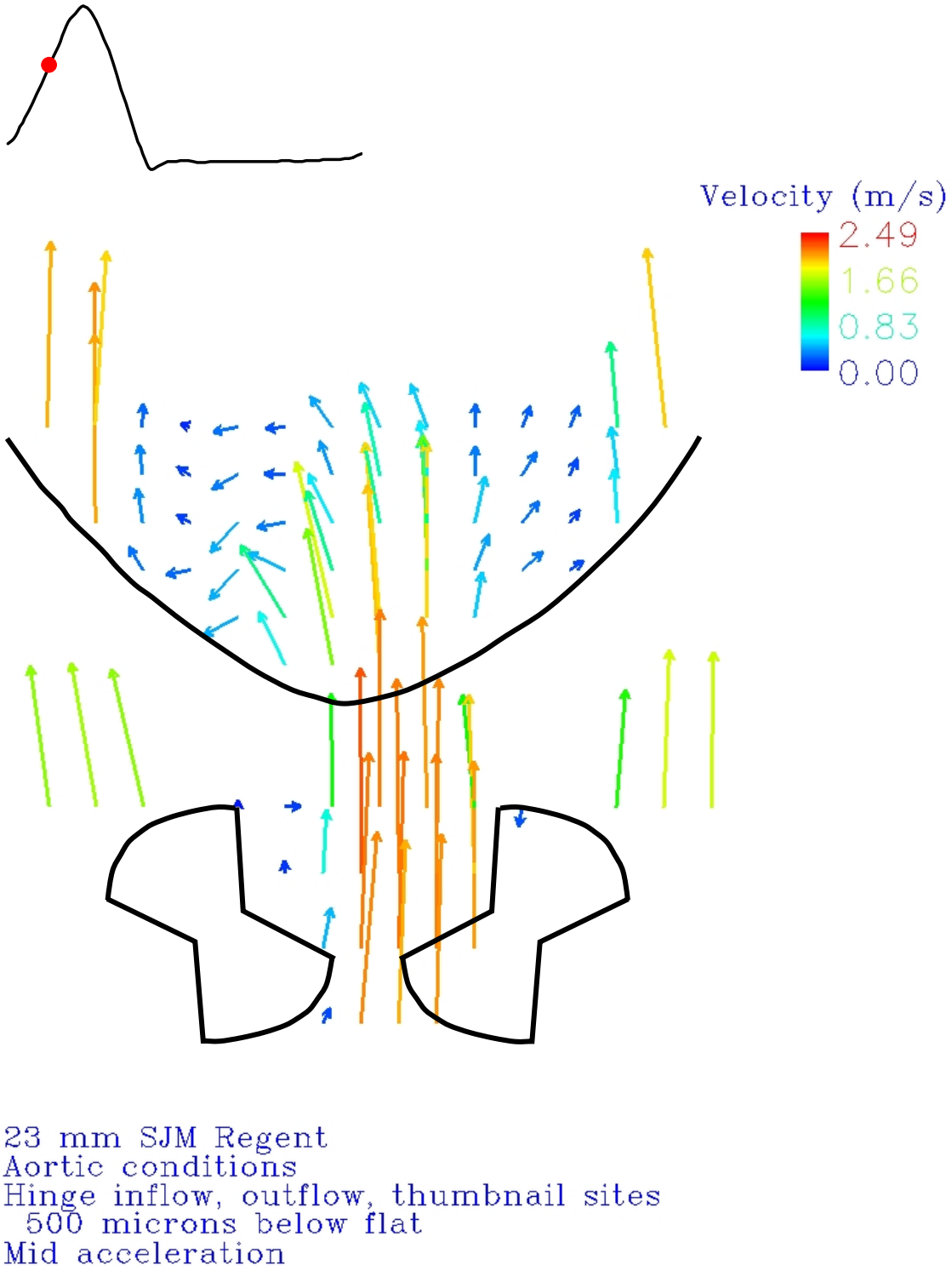

Figure 6.35: 23 mm SJM Regent clear valve hinge inflow, outflow, thumbnail flow field 500 μm below the flat at mid acceleration

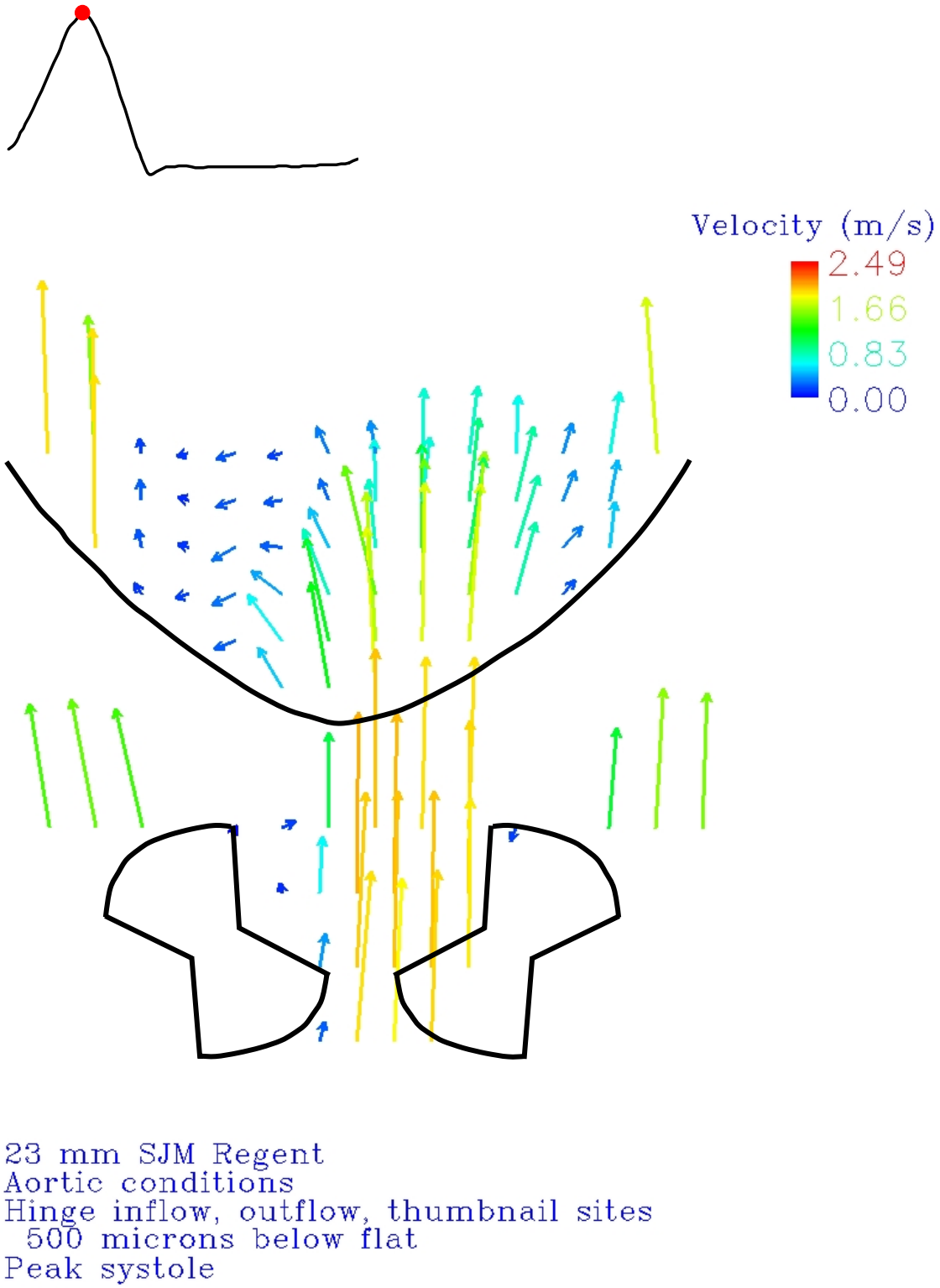

Figure 6.36: 23 mm SJM Regent clear valve hinge inflow, outflow, thumbnail flow field 500 μm below the flat at peak systole

Valve Closure

Figure 6.37 shows the velocity field 500 μm below the flat level along the hinge inflow and outflow regions, and within the thumbnail region at valve closure. Reverse flow was first seen in the thumbnail region 100 ms after peak systole and a peak velocity of 0.34 m/s was recorded in the right side of the thumbnail region. A reverse flow, angulated, towards the B-datum line, was detected between the hinges 40 ms before valve closure. The velocities reached 0.45 m/s in the hinge region, and 0.47 m/s in the thumbnail region. Immediately before valve closure, the flow started to decelerate, and the maximum velocities between the hinges and in the thumbnail region were 0.38 m/s and 0.32 m/s, respectively. Throughout the entire region of interest, the TSS levels were on the order of 60 dyn/cm^2, except between the hinges where a measurement site was associated with a TSS level of 1,236 dyn/cm^2 during 20 ms. At valve closure in the thumbnail region, the velocity magnitude ranged from nearly zero to 0.14 m/s while a peak velocity of 0.2 m/s was recorded in the hinge region. The TSS levels throughout the entire region of interest were less than 60 dyn/cm^2.

Mid Diastole

Figure 6.38 shows the velocity field 500 μm below the flat level along the hinge inflow and outflow regions, and within the thumbnail region during mid diastole. Near zero velocity vectors were observed throughout the hinge and thumbnail regions. Velocity magnitudes did not exceed 0.05 m/s within the thumbnail region. Slightly higher velocities were recorded in the hinge region with velocity magnitudes of up to 0.10 m/s. A closer look at the flow field in the hinge region revealed that as the backflow jet moved towards the inner surface of the closed leaflets, the flow began to converge towards the central seam of the closed leaflets. Near zero TSS levels were recorded throughout the entire region of interest.

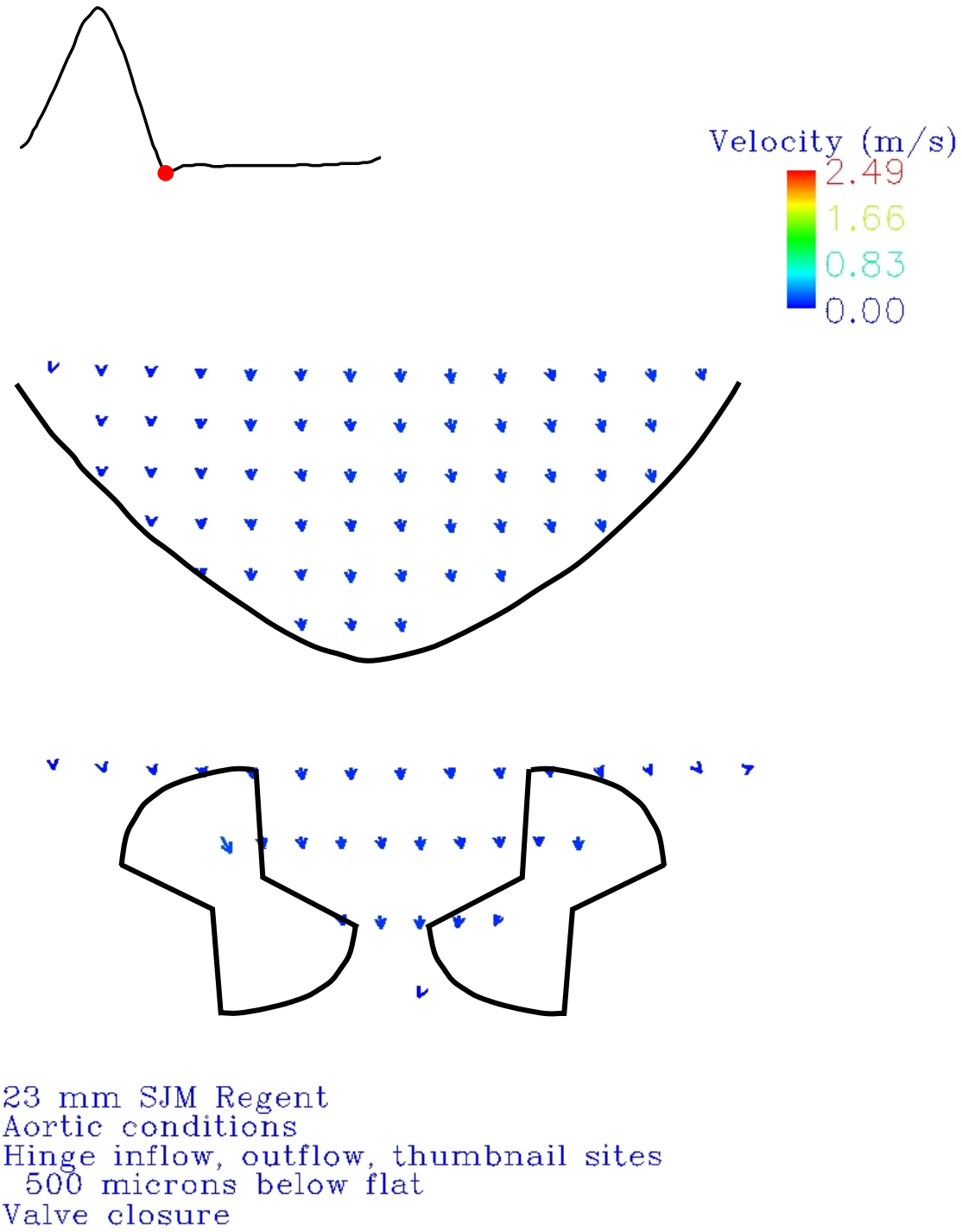

Figure 6.37: 23 mm SJM Regent clear valve hinge inflow, outflow, thumbnail flow field 500 μm below the flat at valve closure

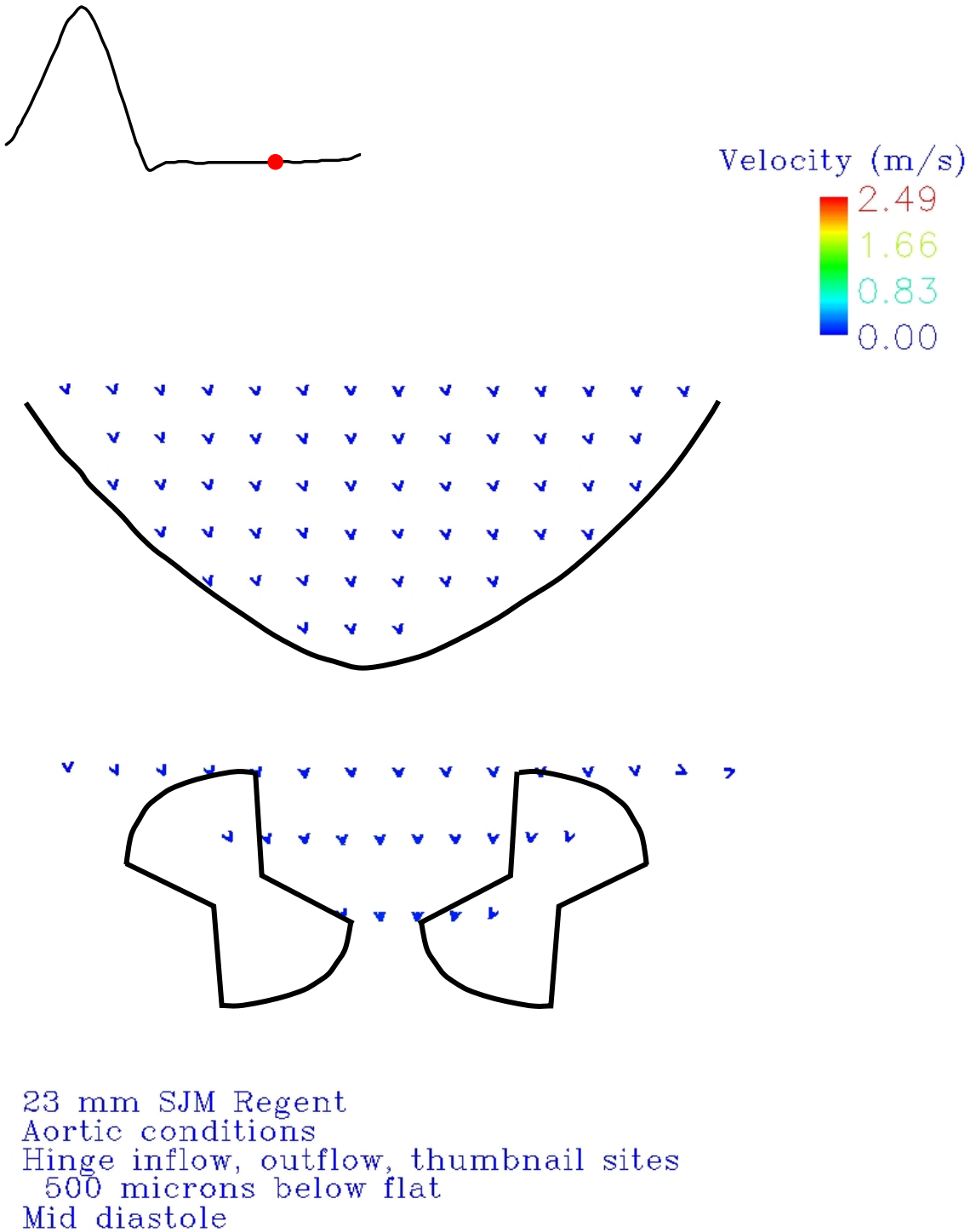

Figure 6.38: 23 mm SJM Regent clear valve hinge inflow, outflow, thumbnail flow field 500 μm below the flat at mid diastole

1 mm Below Flat Level

Mid Acceleration

Figure 6.39 shows the velocity field 1 mm below the flat level along the hinge inflow and outflow regions, and within the thumbnail region during mid acceleration. In the hinge region, between the two open leaflets, velocity magnitudes reached 2.2 m/s as the forward flow jet began to develop between the leaflets. In the outflow region, at the outside edge of the leaflet, lower velocity flow reaching 1.79 m/s was observed. Within the jet, the TSS levels were less than 80 dyn/cm^2, while at the edges of the jet they reached 528 dyn/cm^2.

Within the thumbnail, the forward flow jet velocity decreased due to flow separation and detachment from the thumbnail surface. The peak velocity magnitude within the thumbnail jet was 2.16 m/s. The slightly diminished forward flow jet was also skewed towards the inner surface of the leaflet left of the thumbnail region. The forward flow was delimited by two slow lateral recirculation structures with velocity magnitudes of 0.2 m/s. Higher speed flow reaching 2 m/s was seen adjacent to these rotating flow structures. Throughout the thumbnail, the TSS levels were relatively low with values less than 300 dyn/cm^2 but at the edges of the central thumbnail jet the TSS levels reached 1,830 dyn/cm^2.

Peak Systole

Figure 6.40 shows the velocity field 1 mm below the flat level along the hinge inflow and outflow regions, and within the thumbnail region at peak systole. The flow pattern observed at peak systole was similar to that at mid acceleration. In the hinge region, between the open leaflets, velocity magnitudes within the jet were on the order of 2 m/s with a peak value of 2.07 m/s. The forward flow jet in this region was slightly skewed towards the right leaflet.

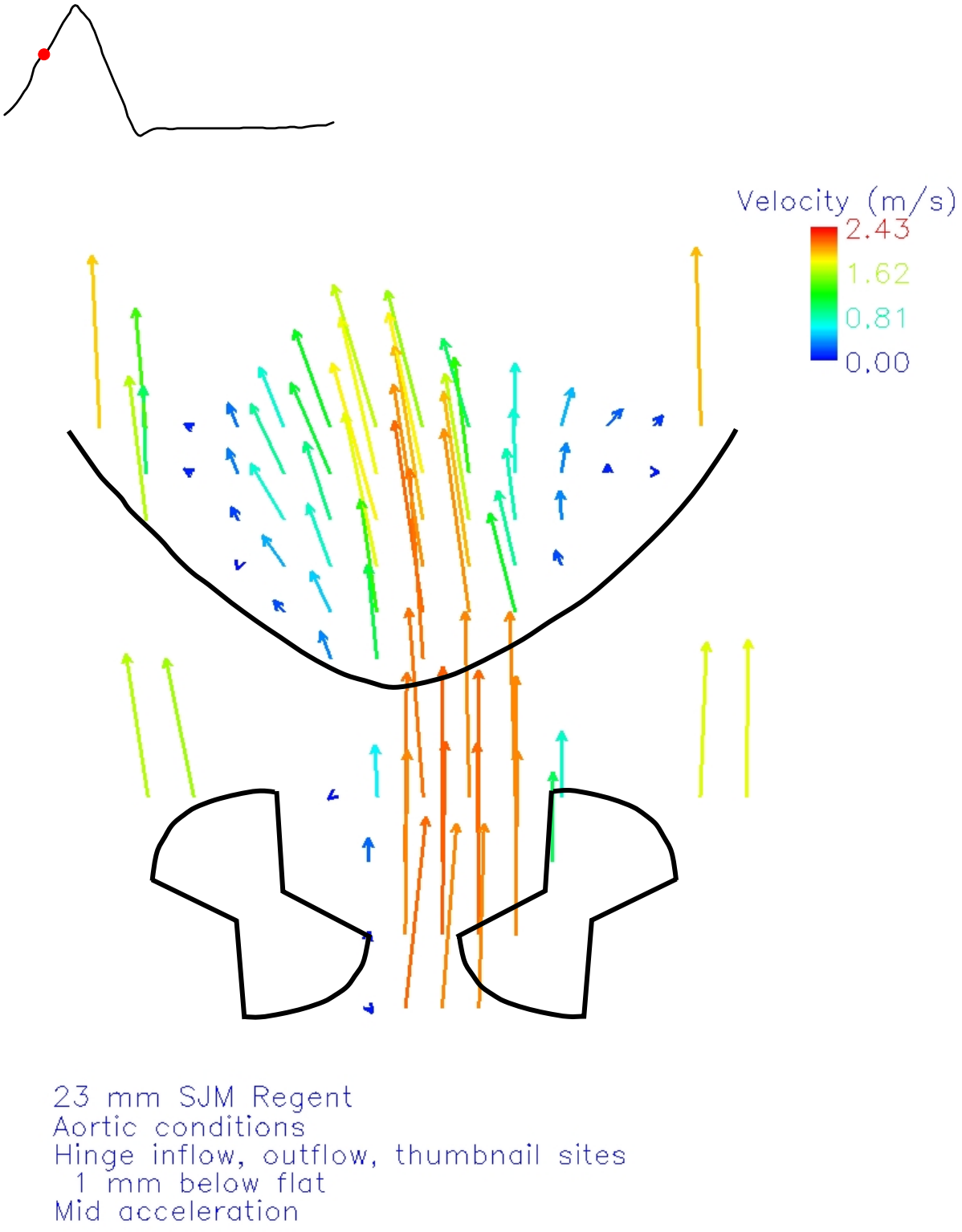

Figure 6.39: 23 mm SJM Regent clear valve hinge inflow, outflow, thumbnail flow field 1 mm below the flat at mid acceleration

In the outflow region, the forward flow velocity vectors had greater axial components. Velocity magnitudes reaching 1.69 m/s were seen at the outside edge of the leaflets, and the TSS did not exceed 100 dyn/cm^2 in the hinge region.

Within the thumbnail the maximum central jet velocity reached 2.04 m/s. The forward jet was skewed towards the inner surface of the left leaflet. However, the forward jet vectors at peak systole were more axial than they were during mid acceleration. The greatest TSS levels were seen at the edges of this jet, reaching levels of 3,192 dyn/cm^2. The rotating structure on the right side of the forward jet vanished, but low velocity vectors were still present. A small low velocity recirculation region was still present to the left of the forward flow jet. High speed flow reaching 1.91 m/s was adjacent to these low velocity regions.

Valve Closure

A forward flow pattern was seen in both hinge and thumbnail regions 80 ms after peak systole. However, 100 ms after peak systole the flow became stagnant except in the right side of the thumbnail region where a reverse flow, with velocity magnitudes up to 0.39 m/s, was observed. Twenty milliseconds later, reverse flow was observed throughout the investigated area. In the hinge region the reverse flow was preferentially skewed towards the B-datum line. The maximum velocity was seen in the inflow hinge region with a peak at 0.5 m/s, while in the thumbnail region the velocities were less than 0. 44 m/s.

Figure 6.41 shows the velocity field 1 mm below the flat level along the hinge inflow and outflow regions, and within the thumbnail region immediately before valve closure. At this instance of the cardiac cycle, the flow pattern was similar to that observed in the CM valve at the same elevation. High velocities up to 0.66 m/s were recorded between the hinges, while the velocity magnitudes throughout the remaining of

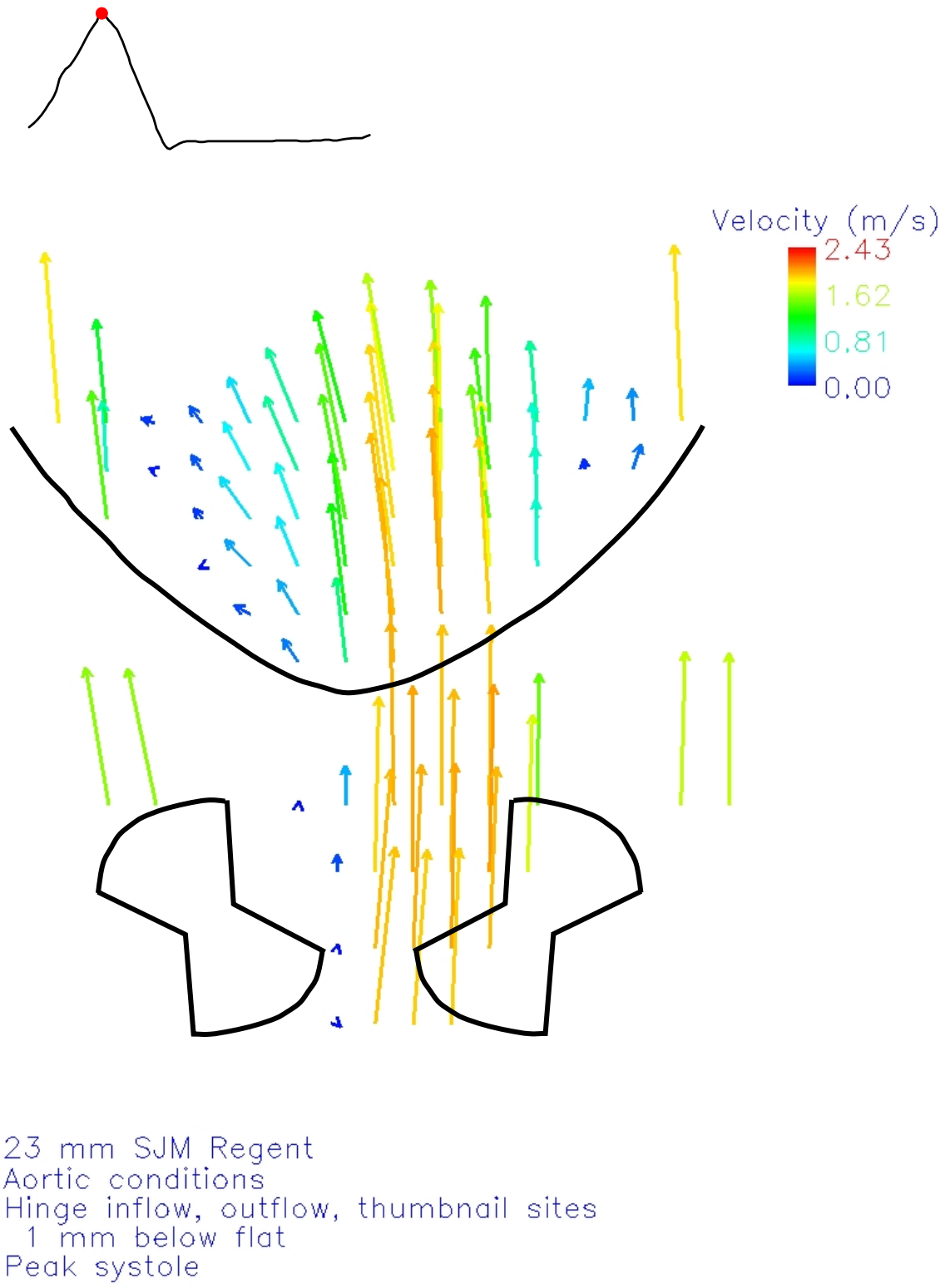

Figure 6.40: 23 mm SJM Regent clear valve hinge inflow, outflow, thumbnail flow field 1 mm below the flat at peak systole

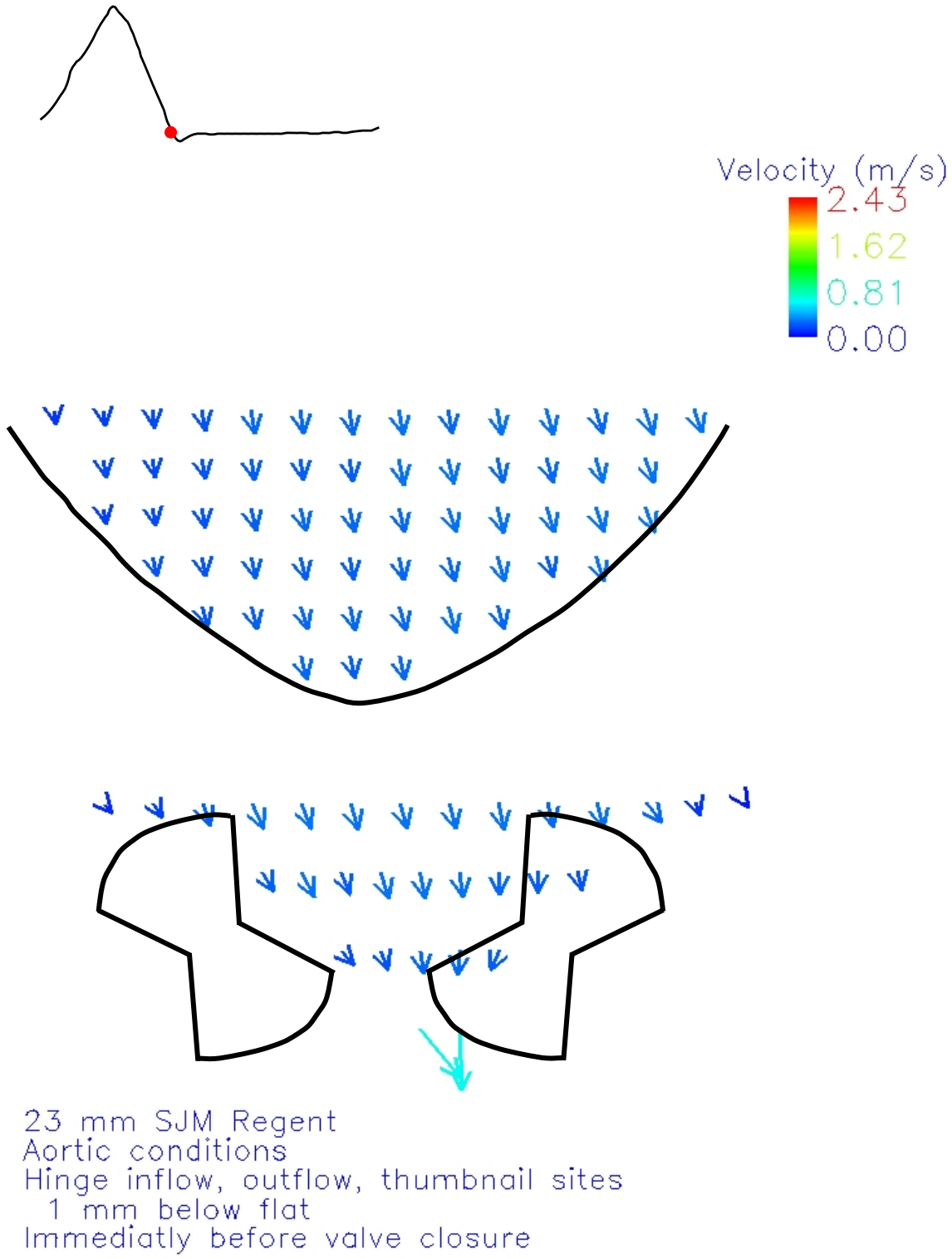

Figure 6.41: 23 mm SJM Regent clear valve hinge inflow, outflow, thumbnail flow field 1 mm below the flat immediately before valve closure

the region of interest were less than 0.3 m/s. The TSS levels were on the order of 60 dyn/cm2, except between the hinges where a peak TSS level of 865 dyn/cm^2 was recorded. At valve closure, near zero TSS levels were recorded throughout the investigated region and the velocity magnitudes did not exceed 0.15 m/s.

Mid Diastole

At 1 mm below the flat level, velocity magnitudes did not exceed 0.05 m/s. As the backflow jet moved towards the inner surfaces of the closed leaflets, the flow began converging towards the central seam of the closed leaflets. Throughout the hinge and thumbnail regions, the TSS levels were near zero. However, during early diastole a peak TSS of 864 dyn/cm^2 was observed during one time bin in the inflow hinge region.

3 mm Below Flat Level

Mid Acceleration

Figure 6.42 shows the velocity field 3 mm below the flat level along the hinge inflow and outflow regions, and within the thumbnail region during mid acceleration. Between the open leaflets, velocity magnitudes reached 2.59 m/s as the forward jet developed between the leaflets. In the outflow region between the two leaflets, the peak forward flow jet velocity magnitude decreased slightly to 2.62 m/s. TSS levels up to 473 dyn/cm^2 were seen at the edges of the forward jet. In the outflow region, at the outside edge of the leaflets, lower velocity flow reaching 1.59 m/s was observed.

Within the thumbnail region the forward flow jet in was slightly skewed towards the inner surface of the left leaflet. The maximum central jet velocity reached 2.20 m/s, and the highest TSS level was seen on the right edge of the jet reaching 1,566 dyn/cm^2.

The central jet was surrounded by two regions of low flow, with the one left of the thumbnail region being larger than the one on the right. In these two regions velocity magnitudes reaching 0.43 m/s and TSS levels up to 400 dyn/cm^2 were observed. However, velocity magnitudes reaching 1.86 m/s were seen at the outside edge of the leaflets and were associated with TSS levels less than 50 dyn/cm^2.

Peak Systole

Figure 6.43 shows the velocity field 3 mm below the flat level along the hinge inflow and outflow regions, and within the thumbnail region at peak systole. In the hinge region between the leaflets, the forward flow jet was slightly skewed towards the right leaflet. Flow in this region reached 2.13 m/s. Low velocity flow of 0.35 m/s was seen to the right side of this forward flow. Velocity magnitudes reached 1.68 m/s at the outside edge of the leaflets. Between the hinge pockets, the TSS levels were less than 200 dyn/cm^2. Within the thumbnail the forward flow jet vectors were more axial than during mid acceleration. Velocity magnitudes reached 2.11 m/s. The velocity vectors left of the jet had a strong axial component towards the central region of the jet. In this region, velocity magnitudes reached 1.29 m/s and the TSS reached 1,241 dyn/cm^2. The low flow region on the right of the thumbnail jet vanished while the one on the left of the jet expanded. Velocity magnitudes up to 0.57 m/s were seen in this low flow region, and high speed flow up to 1.86 m/s was seen at the edge of the thumbnail region.

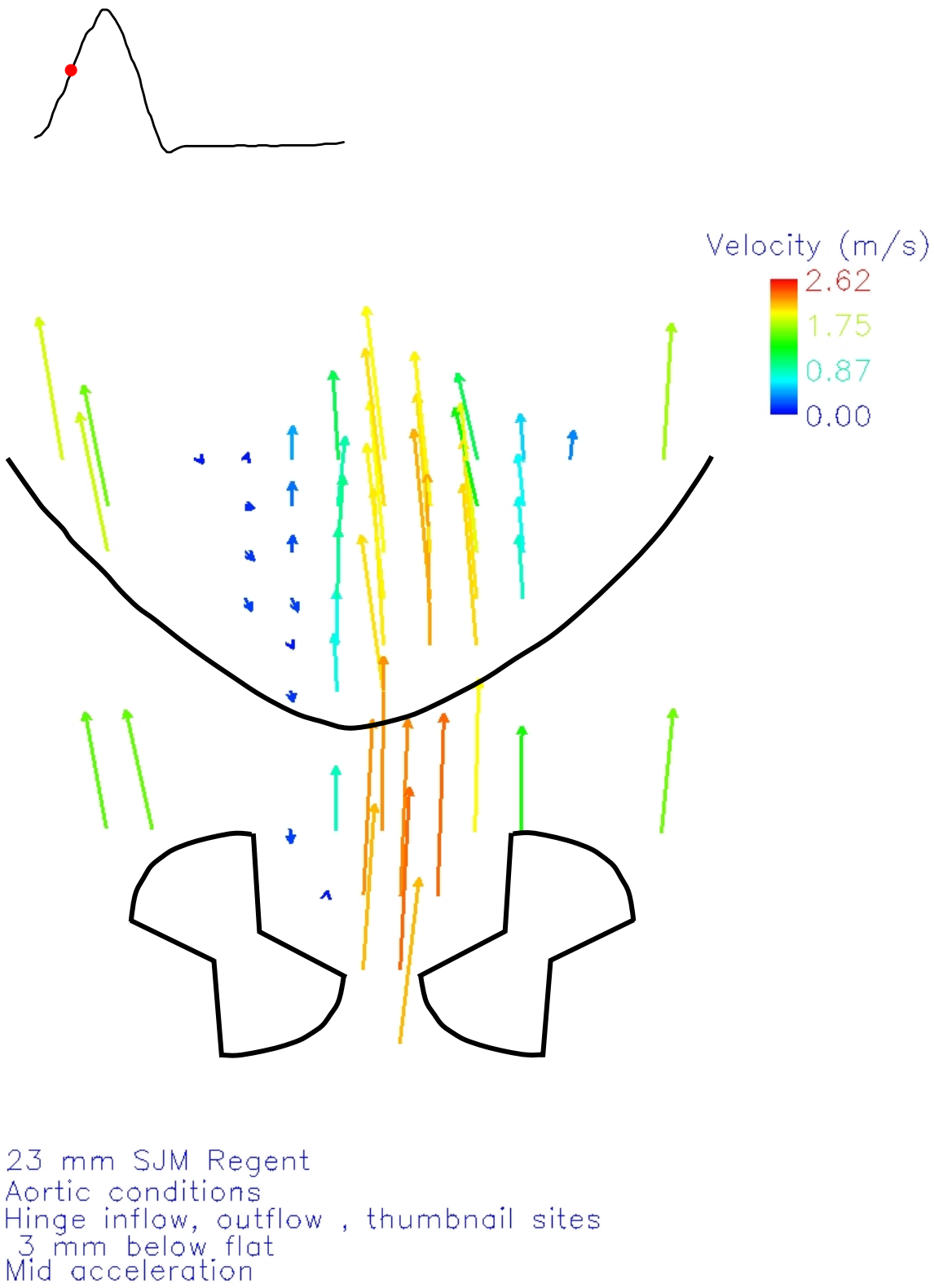

Figure 6.42: 23 mm SJM Regent clear valve hinge inflow, outflow, thumbnail flow field 3 mm below the flat at mid acceleration

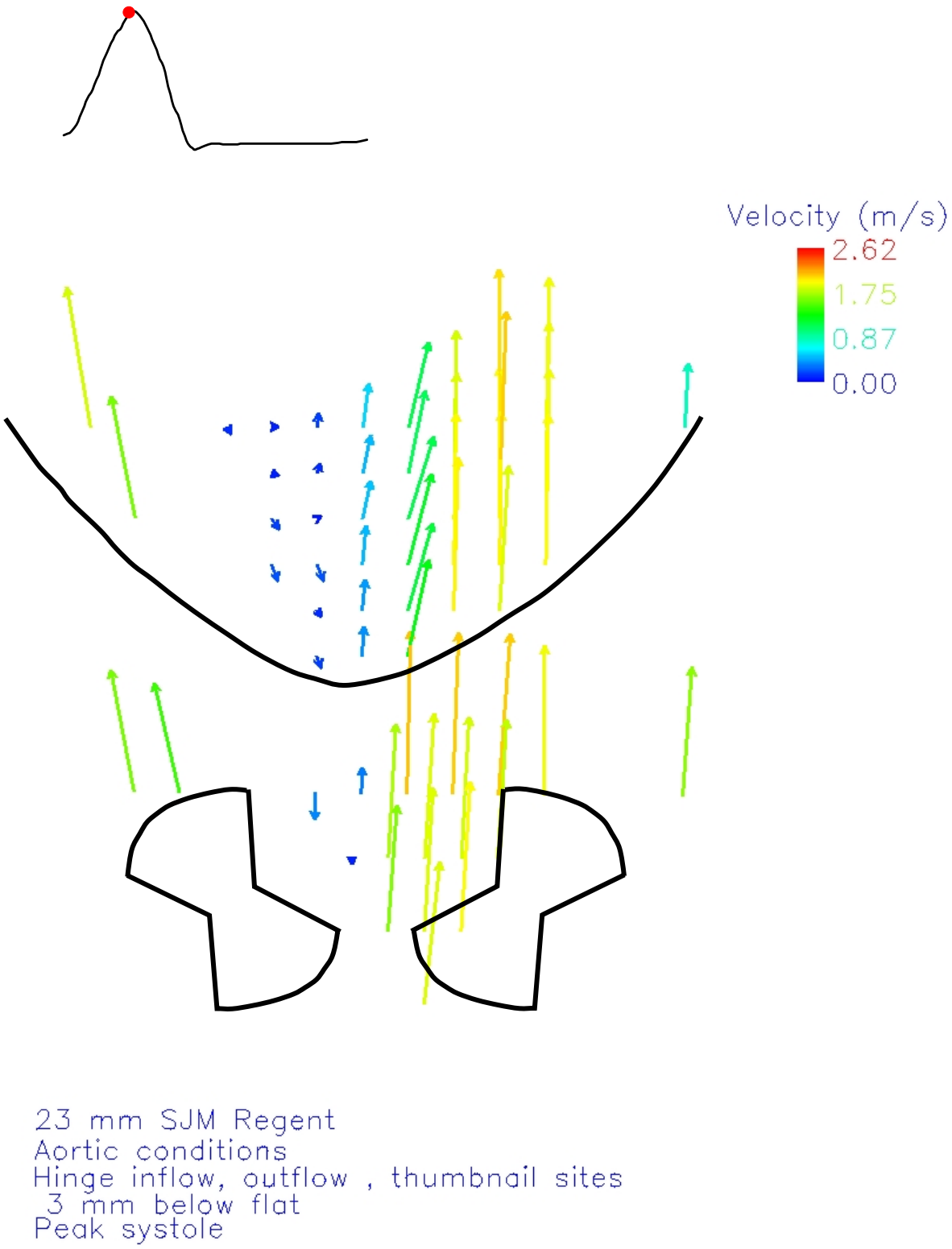

Figure 6.43: 23 mm SJM Regent clear valve hinge inflow, outflow, thumbnail flow field 3 mm below the flat at peak systole

Valve Closure

Figure 6.44 shows the velocity field 3 mm below the flat level along the hinge inflow and outflow regions, and within the thumbnail region at valve closure. The flow pattern at this elevation was similar to those seen 500 μm and 1 mm below the flat level at valve closure. A reverse flow was observed throughout the entire region of interest 40 ms before valve closure, and a peak velocity of 0.45 m/s was recorded in the inflow hinge region. The peak velocity decreased to 0.3 m/s immediately before valve closure, and was observed in the outflow hinge region. The TSS levels were less than 106 dyn/cm^2, except at one measurement site where the TSS reached 335 dyn/cm^2. At valve closure, the velocities were less than 0.2 m/s and the TSS levels less than 93 dyn/cm^2.

Mid Diastole

Velocity magnitudes less than 0.05 m/s were observed throughout the thumbnail region during mid diastole. The flow pattern between the hinge pockets was similar to that seen at 1 mm below the flat level. As the backflow jet moved towards the inner surfaces of the closed leaflets, the flow began to converge towards the central seam of the closed leaflets. Velocity magnitudes reached a peak value of 0.09 m/s at the inflow hinge region. The TSS levels did not exceed 10 dyn/cm^2 throughout the region of interest.

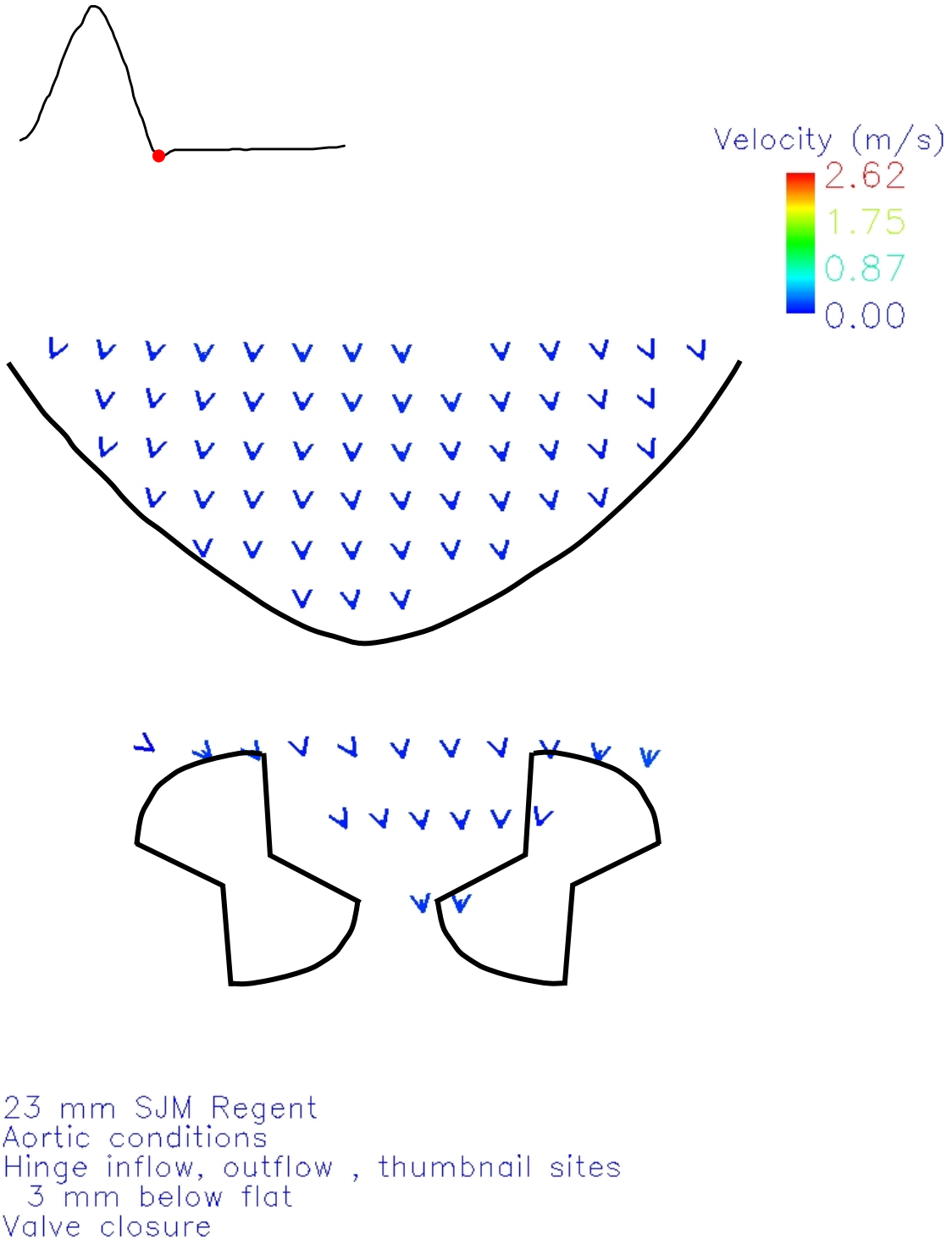

Figure 6.44: 23 mm SJM Regent clear valve hinge inflow, outflow, thumbnail flow field 3 mm below the flat at valve closure

6.3 Leakage Jet Study

Velocity vector fields are presented at pertinent instances during the cardiac cycle to illustrate the development of the aortic leakage jets. The four time bins of interest are late systole, early diastole, mid diastole, and late diastole. In each velocity field image, the arrows point in the direction of the mean velocity vectors and are color-coded by the velocity magnitude (m/s) as given in the figure legends. In each turbulent shear stress (TSS) field image, the arrows point in the direction of the mean velocity vectors and are color-coded by the values of maximum TSS (dyn/cm^2) as calculated in the procedure outlined in the experimental protocol section. A schematic in each color-coded map shows where the leakage jets were observed in relation to the valve structure.

6.3.1 23 mm CarboMedics Valve

6.3.1.1 Flow and Pressure Curves

Figure 6.45 represents aortic flow and aortic pressure waveforms obtained in the vicinity of the 23 mm CM valve. The flow waveform was phase-window averaged according to the procedure outlined in the experimental protocol section. Each open circle denotes a distinct 20 ms time bin. The duration of the sampling interval is shown on the figure. The time bins corresponding to late systole, early diastole, mid diastole, and late diastole are also indicated.

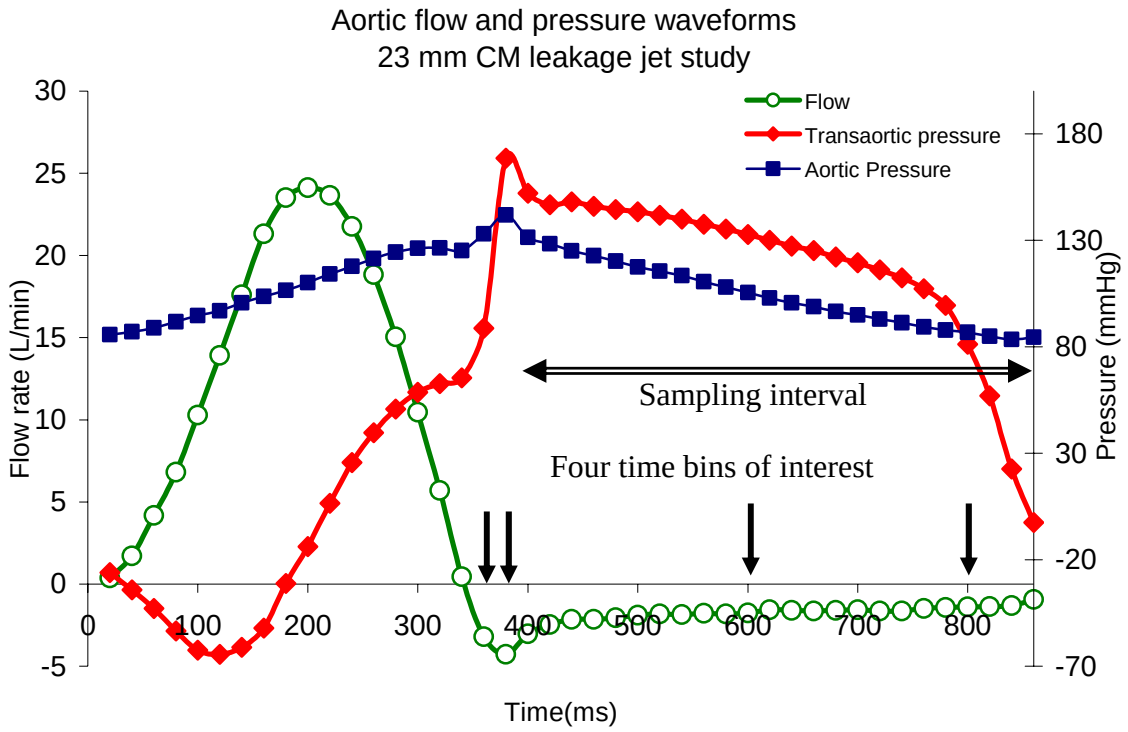

Figure 6.45: Aortic flow and aortic pressure waveforms

6.3.1.2 Overview of the Leakage Jet Results of the 23 mm CM Heart Valve

Animations (AVI and MPG formats) of the upstream velocity flow field of the CM valve are given in appendix B. The upstream flow field was characterized by five leakage jets. A schematic in figure 6.46 shows where these five jets were observed in relation to the valve structure. The two largest jets (jets 1 and 5) were located on each side of the B-datum line. The maximum cross-sectional dimensions were 1.14 x 5.72 mm^2 and 2.67 x 5.33mm^2 for jet 1 and jet 5, respectively. The velocity magnitudes of these two jets were recorded during mid diastole and were relatively low, with a maximum velocity of 0.37 m/s for jet 1, and 0.44 m/s for jet 5. The maximum TSS levels were on the same order of magnitude with a peak TSS of 576 dyn/cm^2 for jet 1 and 553 dyn/cm^2 for jet 5. The velocity vectors within both jets had a weak axial component but dominant radial

and circumferential components. However, the flow within jet 5 was directed towards the B-datum line, while the flow within jet 1 was directed away from the B-datum line.

The three remaining jets were located in the vicinity of the hinge region. The velocity vectors of jet 2 had strong axial and circumferential components but the circumferential component was weaker than that of jet 1. The maximum cross-sectional dimensions were 2.67 x 1.9 mm^2. The maximum velocity was recorded at mid diastole and was slightly higher than that of jet 1, with a peak at 0.41 m/s. The TSS levels reached 625 dyn/cm^2. The highest leakage flow velocities and TSS levels were recorded in jet 3, with a peak velocity of 0.84 m/s and a peak TSS level of 1,284 dyn/cm^2. The velocity vectors had strong radial and axial components, and the maximum cross-sectional dimensions of this jet were 1.9 x 1.71 mm^2. The cross-sectional dimensions of jet 4 were slightly larger with maximum dimensions of 2.29 x 2.48 mm^2. The maximum velocity of jet 4 was recorded during mid diastole and reached 0.68 m/s. The TSS levels reached 940 dyn/cm^2. The spatial and time averaged standard deviation of the velocity magnitude was 0.13 m/s for the CM leakage jet study.

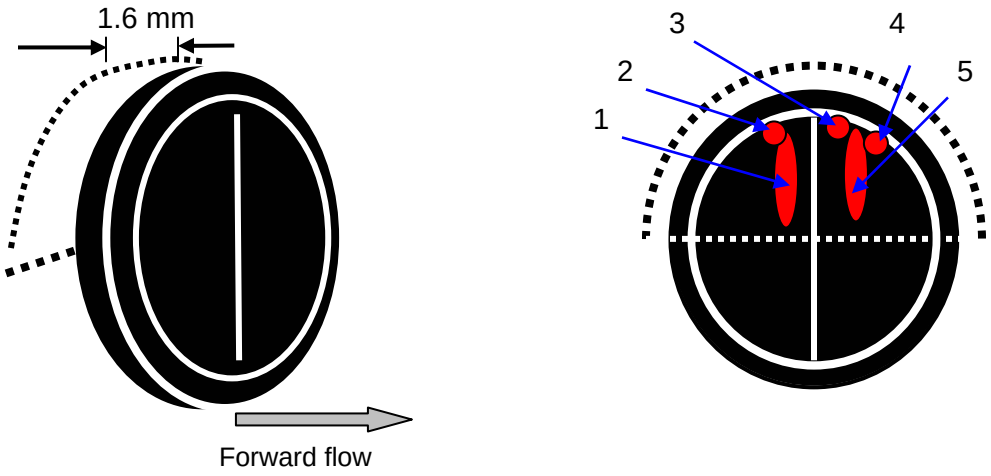

Figure 6.46: Schematic of the region locations in relation to the 23 mm CM valve structure. Each region was associated with a number to facilitate the description of the results.

6.3.1.3 Detailed Description of the Leakage Jets Through the Closed 23mm CM Valve

Measurements were obtained 1.65 mm (0.065 in) upstream of the outermost part of the valve housing, and only the locations where the velocity magnitude was greater than 0.2 m/s during the sampling period were recorded. This velocity magnitude of 0.2 m/s will be referred to the following section as the jet threshold velocity magnitude. Locations associated with velocity magnitudes lower than this threshold were not considered to be part of a jet. In this experiment five different regions were characterized in the area of interest. For ease of reference, each region was numbered in the color-coded velocity and TSS images. A schematic in figure 6.46 shows where these regions were observed in relation to the valve structure.

Late Systole

Figure 6.47 shows the retrograde flow velocity and TSS fields through the 23 mm CM valve at late systole (bin 17), when the leaflets were moving towards the closed position.

There was a long band of reverse flow in region 1, and the velocity magnitudes decreased from 0.24 m/s in the upper part of the region 1 to 0.10 m/s in the lower part. The velocity vectors pointed towards the center of the valve and, therefore, had a strong radial component. The TSS levels were on the order of 130 dyn/cm^2, and the maximum TSS reached 246 dyn/cm^2. The area in which the velocity was greater than the jet velocity magnitude threshold, or jet 1, had cross-sectional dimensions of approximately 0.762 x 0.95 mm^2 (0.030 x 0.0375 in^2).

In region 2 there was a circular zone of reverse flow. The velocity magnitudes in region 2 were slightly greater than those in region 1. Since the velocity magnitudes throughout region 2 were greater than 0.2 m/s the cross-sectional dimensions of jet 2

are similar to that of region 2, and are approximately 2.67 x 1.9 mm^2 (0.105 x 0.075 in^2). The peak velocity magnitude was 0.36 m/s. The vectors directed towards the B-datum line had strong axial and circumferential components. The TSS levels ranged from 40 dyn/cm^2 to 243 dyn/cm^2.

Region 3 was a small circular region located near the valve housing. The maximum velocity magnitude was 0.33 m/s, and was seen in the left side of region 3. Throughout region 3 the velocity magnitudes were on the order of 0.25 m/s. Velocity magnitudes smaller than 0.20 m/s were seen in the upper edge of region 3. Therefore, jet 3 had cross-sectional dimensions of approximately 2.29 x 0.95 mm^2 (0.090 x 0.0375 in^2). Velocity vectors in this region had a strong axial component and a slight circumferential component, as evidenced by the vectors pointing towards the right side of the color-coded map. TSS levels were on the order of 250 dyn/cm^2, and a maximum TSS of 485 dyn/cm^2 was seen in the lower part of region 3.

The highest velocity magnitudes at late systole were seen in the central region of jet 4, where the peak velocity reached 0.4 m/s. Region 4 had an ellipsoidal shape, and the central part was with high velocity magnitudes. This central region was surrounded by regions of lower flow, where the velocity was on the order of 0.3 m/s. Throughout region 4, the velocity magnitudes were greater than 0.2 m/s, therefore jet 4 had cross-sectional dimensions of approximately 2.29 x 2.48 mm^2 (0.090 x 0.0975 in^2). The maximum TSS recorded was 500 dyn/cm^2. The velocity vectors within region 4 had a strong axial component and a non negligible radial component since the velocity vectors pointed upwards.

Region 5 was a long wide band of reverse flow. The lower part of region 5 was characterized by low flow, with velocity magnitudes on the order of 0.10 m/s. In this zone the velocity vectors pointed upwards and were slightly skewed towards the right side of the map. The highest velocity magnitudes were seen in the upper part and the right side

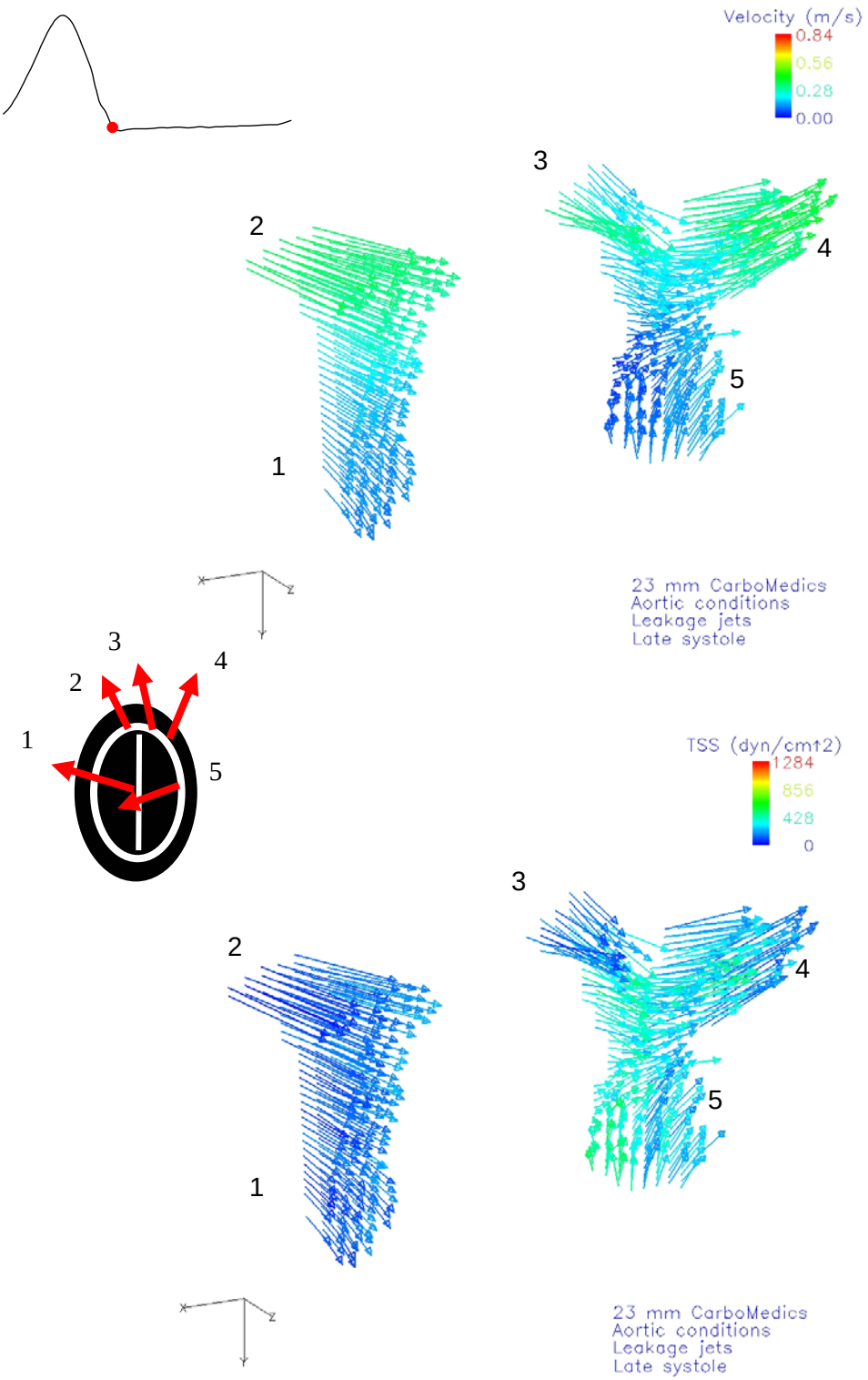

Figure 6.47: 23 mm CarboMedics valve leakage jet velocity field and TSS field at late systole

of region 5. The peak velocity reached 0.25 m/s. Velocity vectors in this region also pointed upwards, but they had a strong circumferential component as the vectors pointed towards region 4. The area that was considered to be jet 5 was located in the upper part of region 5 and had cross-sectional dimensions of approximately 1.9 x 0.76 mm^2 (0.075 x 0.030 in^2). The highest TSS levels at late systole were seen in the lower left part of region 5, with a peak TSS of 553 dyn/cm^2. In the right side of region 5, the TSS levels were on the order of 270 dyn/cm^2.

Comparison of all five jets at late systole revealed that the highest velocity magnitudes were seen in regions 2, 3 and 4, and the maximum velocity was seen in jet 4 with a peak value at 0.40 m/s. Comparison of the TSS color coded map revealed that lower TSS levels were present in regions 1 and 2, while the highest TSS levels occurred in region 5, with a peak value of 553 dyn/cm^2.

Early Diastole

Figure 6.48 shows the retrograde flow velocity and TSS fields at early diastole, 20 ms after late systole. As the driving aortic pressure reached a peak value, and the leaflets were closed, the velocity within the jets slightly increased, and the flow direction changed considerably.

In region 1 the velocity magnitudes were slightly greater than at late systole with velocity magnitudes ranging from 0.37 m/s on the right side to 0.10 m/s at the left edge. The area in this region where the velocity was greater than the jet threshold velocity was considerably larger during early diastole than at late systole. Thus jet 1 had cross-sectional dimensions of approximately 1.14 x 5.72 mm^2 (0.045 x 0.225 in^2). The flow vectors suggested that at this time the fluid moved away from the central region of the valve structure, while at late systole, the vectors were directed towards the B-datum line. The vectors had strong radial and circumferential components and a weak axial

component since the fluid flowed nearly parallel to the measurement plane. The TSS levels were on the order of 350 dyn/cm^2. The highest TSS levels were recorded in the central region with a peak at 576 dyn/cm^2.

In region 2 the flow changed direction during early diastole as it had in region 1. The flow was slightly upwards and directed away from the B-datum line, while at late systole, the vectors pointed towards the B-datum line. Twenty milliseconds after late systole, the velocity vectors had a strong axial component and a circumferential component that was non negligible, but weaker than that of the vectors in region 1. The velocity magnitudes were on the order of 0.30 m/s with a peak velocity at 0.33 m/s, which was slightly lower than in region 1. The velocity magnitudes throughout region 2 were greater than 0.2 m/s; therefore, similar to the results from late systole, region 2 and jet 2 both had cross-sectional dimensions of approximately 2.67 x 1.9 mm^2 (0.105 x 0.075 in^2). The TSS levels were slightly higher than at late systole with a peak TSS of 317 dyn/cm^2 and a minimum TSS level of 109 dyn/cm^2.

The flow direction at early diastole within region 3 was different from the one observed at late systole. The velocity vector distribution suggested that the flow converged and was directed towards the B-datum line. The vectors in this region had a strong circumferential component but a weak radial component. The velocity magnitude ranged from 0.16 m/s to 0.34 m/s. The cross-sectional dimensions of jet 3 were slightly larger than at late systole with dimensions of approximately 1.9 x 1.71 mm^2 (0.075 x 0.0675 in^2). However, the peak velocity magnitude recorded at early diastole was on the same order of magnitude as that recorded at late systole. The TSS levels were on the order of 200 dyn/cm^2, with a maximum TSS of 343 dyn/cm^2 reached in the lower part of region 3.

In region 4 the velocity vectors had a strong axial component and weak radial and circumferential components. Throughout region 4 the vectors were skewed towards

the B-datum line, but the vectors located in the left side of the jet pointed slightly upwards while the vectors located in the right side of the jet pointed slightly downwards. The peak velocity magnitude was 0.49 m/s. High velocity vectors were located in the center of the jet and were surrounded by lower velocity vectors on the order of 0.35 m/s. As seen during late systole, throughout region 4, the velocity magnitudes were greater than 0.2 m/s, therefore, jet 4 had cross-sectional dimensions of approximately 2.29 x 2.48 mm^2 (0.090 x 0.0975 in^2). The highest TSS recorded in this region was 398 dyn/cm^2.

In region 5 the velocity vectors had a strong circumferential component since the fluid was directed towards the B-datum line. However, the axial component of the velocity vectors was weak since the fluid moved nearly parallel to the measurement plane. The flow was directed slightly upwards. The velocity magnitude ranged from 0.07 m/s to 0.39 m/s with the highest velocity magnitudes seen in the center and upper parts of region 5. The cross-sectional dimension of jet 5 where the velocity magnitude was greater than the threshold velocity magnitude, was significantly larger than at late systole. The dimensions were approximately 1.9 x 5.33 mm^2 (0.075 x 0.210 in^2). The TSS levels ranged from 460 dyn/cm^2 to 73 dyn/cm^2.

Comparison of all five jets at early diastole revealed that the highest velocity magnitudes were seen in region 4 with a maximum velocity of 0.49 m/s while the maximum TSS level of 576 dyn/cm^2 was observed in region 1. The jet areas were considerably greater than at late systole.

Mid Diastole

Figure 6.49 shows the retrograde flow velocity and TSS fields through the 23 mm CarboMedics valve at mid diastole, when the leaflets were closed. Figures 6.50 and 6.51 show the jets from different angles.

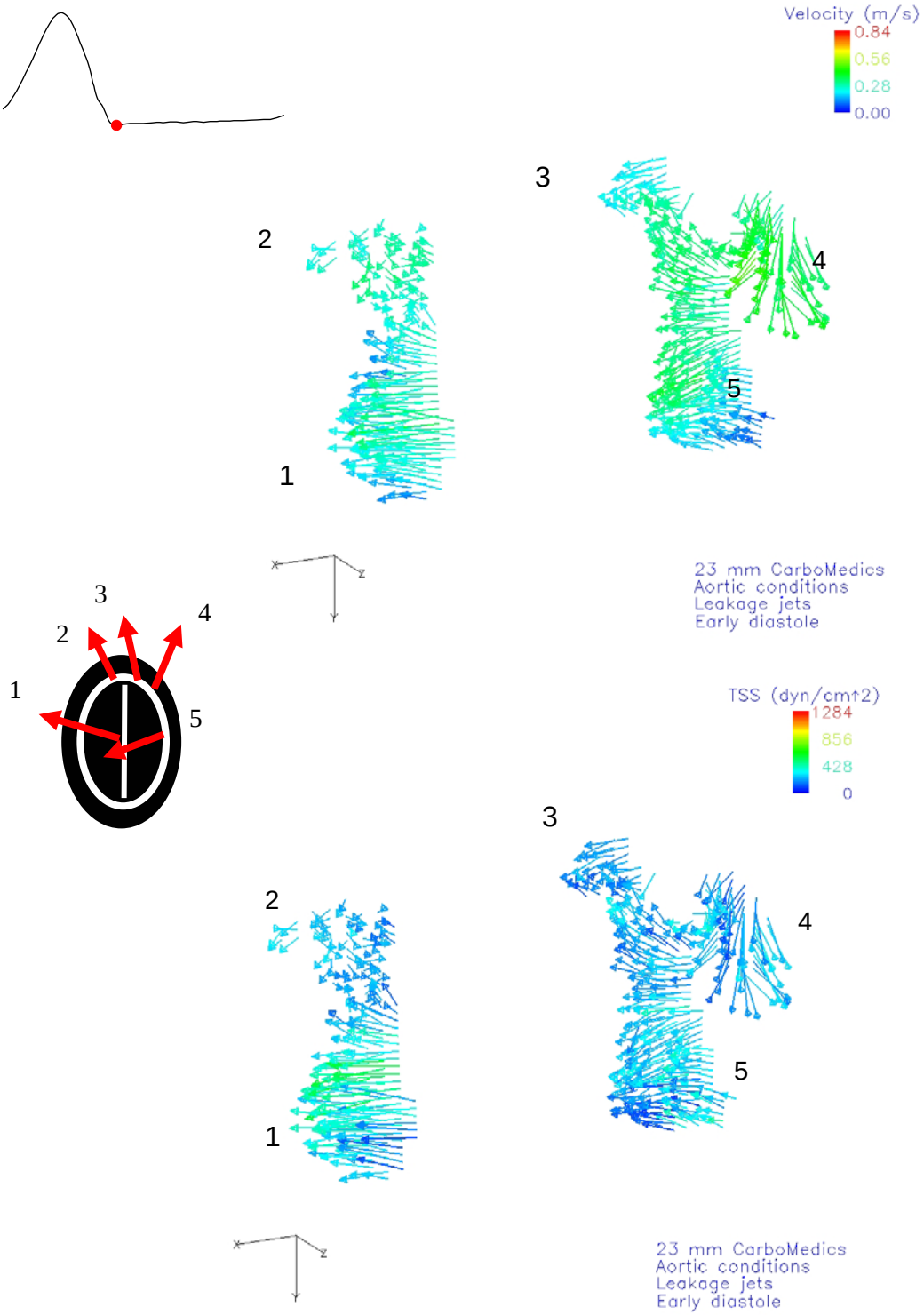

Figure 6.48: 23 mm CarboMedics valve leakage jet velocity field and TSS field at early diastole

In region 1 the maximum velocity decayed to 0.30 m/s, and the velocity magnitudes were on the order of 0.23 m/s. The velocity vector distribution suggested that the fluid flowed downward, away from the B-datum line. The vectors had strong circumferential and radial components. The cross-sectional dimensions of jet 1 were similar to those seen at early diastole with an area of 1.14 x 4.95 mm^2 (0.045 x 0.195 in^2). The TSS levels were higher than at late systole and reached up to 381 dyn/cm^2.

In region 2 the velocity vectors had strong axial and circumferential components, but their circumferential component was weaker than that of the velocity vectors from region 1. The flow vectors suggested the fluid flowed downward, away from the valve housing. The velocity magnitudes reached up to 0.3 m/s. The cross-sectional dimensions of jet 2 were approximately 1.52 x 1.33 mm^2 (0.060 x 0.0525 in^2). The TSS levels were greater in region 2 than in region 1 with a peak value of 610 dyn/cm^2.

In region 3 the velocity vectors had a stronger radial component than during early diastole. The velocity vector distribution clearly suggested that the fluid moved upward, nearly parallel to the main flow direction. The maximum velocity recorded in this jet was 0.76 m/s, and the maximum TSS levels reached 810 dyn/cm^2. The cross-sectional dimensions of jet 3 were slightly smaller than at early diastole with dimensions of approximately 1.9 x 1.33 mm^2 (0.075 x 0.0525 in^2).

In region 4 the velocity vectors were slightly skewed towards region 3. The velocity magnitudes ranged from 0.14 m/s at the edge of region 4 to 0.65 m/s in the center. The peak TSS levels reached 711 dyn/cm^2 in this region. The cross-sectional dimensions of jet 4 were, as seen for jet 3, slightly smaller than during early diastole at 2.1 x 1.52 mm^2 (0.06 x 0.0825 in^2).

In region 5 the flow pattern was similar to that observed at early diastole, but the velocity vectors pointed in a more upward direction. The velocity reached 0.42 m/s in the upper part of region 5 while the peak TSS level at 455 dyn/cm^2 was seen in the lower left

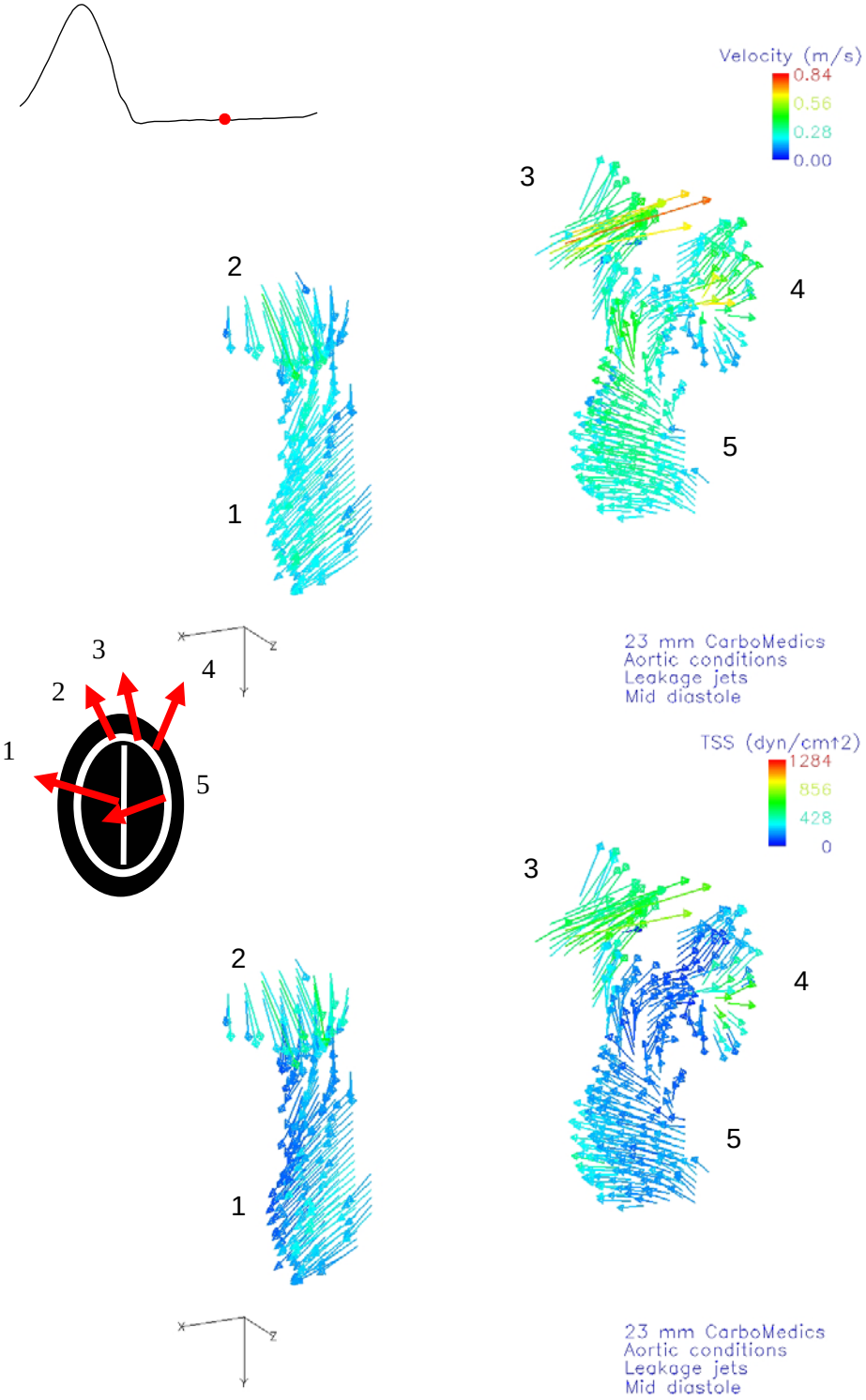

Figure 6.49: 23 mm CarboMedics valve leakage jet velocity field and TSS field at mid diastole

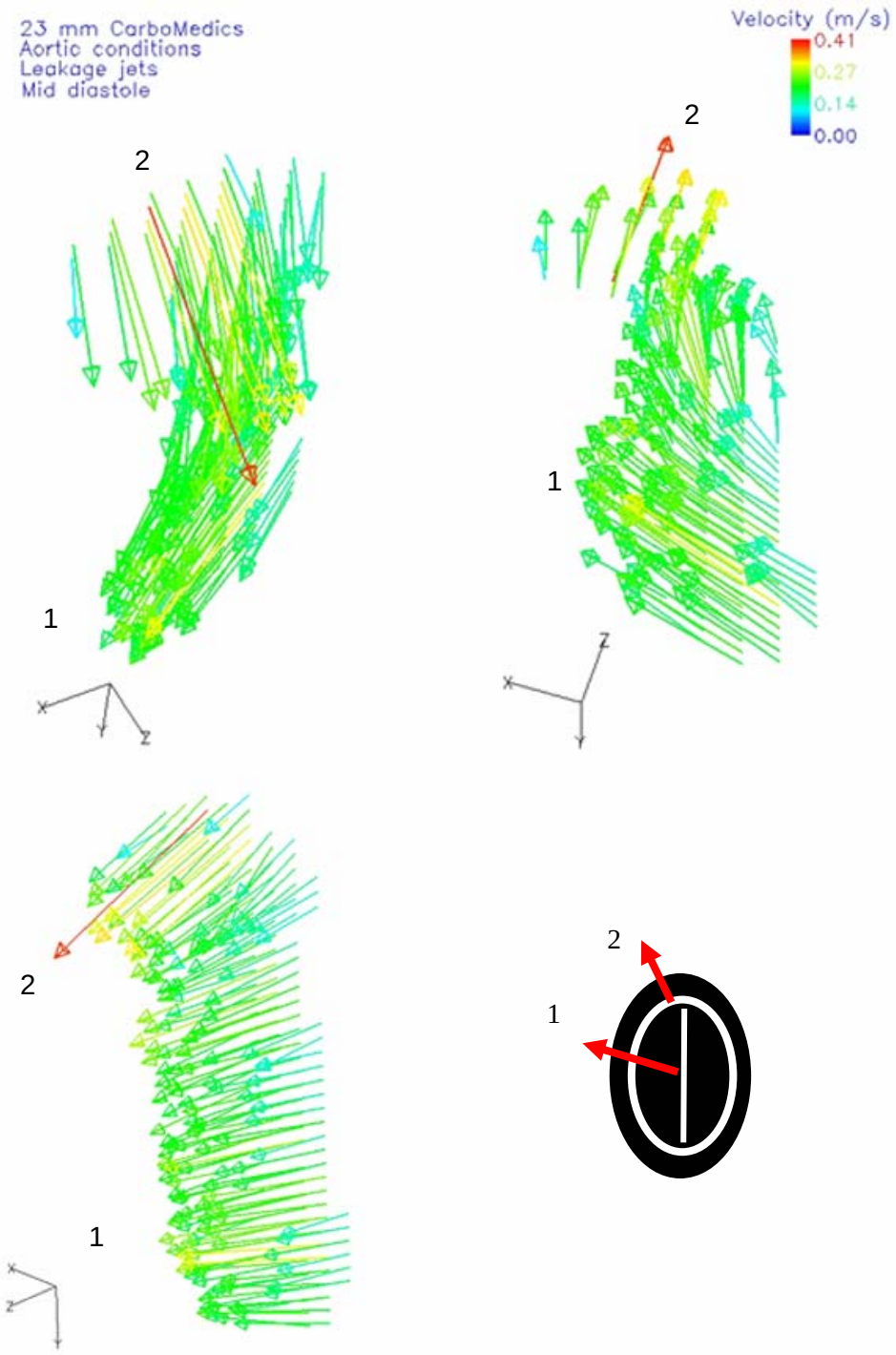

Figure 6.50: Jets 1 and 2 seen from different angles at mid diastole

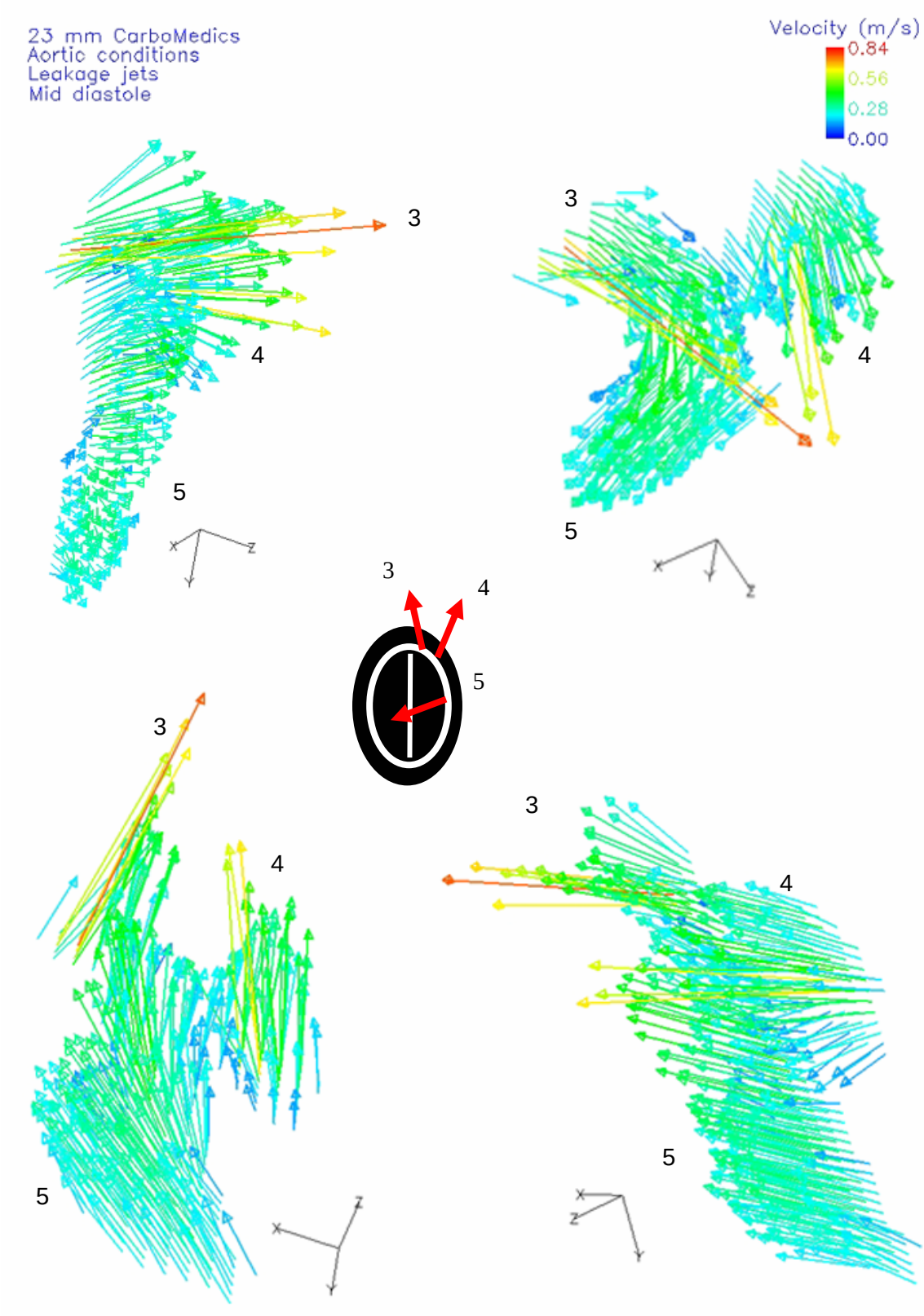

Figure 6.51: Jets 3, 4 and 5 seen from different angles at mid diastole

edge. Throughout region 5 most of the velocity magnitudes were greater than 0.2 m/s. The cross-sectional dimensions of jet 5 were approximately 2.67 x 5.33 mm^2 (0.105 x 0.210 in^2), which was slightly larger than at early diastole.

At mid diastole the highest velocity magnitudes recorded over the measurement area were in regions 3, 4 and in the upper part of region 5. Similarly, the highest TSS levels were recorded in regions 3 and 4.

Late Diastole

Figure 6.52 shows the retrograde flow velocity and TSS fields through the 23 mm CM valve at late systole. Sixty milliseconds before the end of the cardiac cycle (bin 40), velocity magnitudes within regions 1 and 5 were lower than 0.2 m/s. Jets were still present in regions 2, 3 and 4, but had started to dissipate. Forty milliseconds before the end of diastole (bin 41), the flow became almost stagnant as the velocity magnitudes dropped below 0.2 m/s. At time bin 41 the leakage jets had dissipated, and forward flow was visible in region 3 and in the lower left edge of region 5. The velocity magnitudes were lower than 0.7 m/s.

At bin 40 the velocity vectors in region 1 had a magnitude on the order of 0.15 m/s but lower than 0.18 m/s, and were therefore lower than the jet threshold velocity magnitude. As seen during mid diastole, the vectors pointed away from the B-datum line. The TSS levels throughout region 1 did not exceed 100 dyn/cm^2.

A peak velocity of 0.31 m/s was observed in the central area of region 2. The average velocity magnitude throughout region 2 was approximately 0.18 m/s. The cross-sectional dimensions of jet 2 were reduced to 0.76 x 0.57 mm^2 (0.030 x 0.0225 in^2). The TSS levels ranged from 244 dyn/cm^2 to 65 dyn/cm^2. In this region, the vectors pointed downward and had a strong axial component.

Region 3 was divided into two zones. On the left side the velocity magnitudes were lower than 0.06 m/s while on the right side the velocity magnitudes were greater with a peak velocity of 0.23 m/s. The cross-sectional dimensions of jet 3 were 0.76 x 0.38 mm^2 (0.030 x 0.015 in^2). The TSS levels did not exceed 0.89 dyn/cm^2.

The velocity vector magnitudes in region 4 reached a peak value of 0.25 m/s. The flow was mainly parallel to the forward flow direction, but were slightly skewed downward in the lower part of region 4. The cross-sectional dimensions of jet 4 decreased to 0.76 x 2.29 mm^2 (0.030 x 0. 090 in^2). The peak TSS was 0.84 dyn/cm^2.

In region 5 the flow had a similar pattern to that at mid diastole. At late systole jet 5 had dissipated, and the velocity magnitudes did not exceed 0.20 m/s. The highest velocity magnitudes were seen in the right edge of region 5, and nearly zero velocity flow was seen at the left edge of region 5. The highest TSS levels at late diastole were seen in the lower part of region 5 with a peak at 64 dyn/cm^2.

At late diastole, the greatest velocity magnitudes were seen in regions 2, 3 and 4 while the highest TSS levels were recorded in region 2.

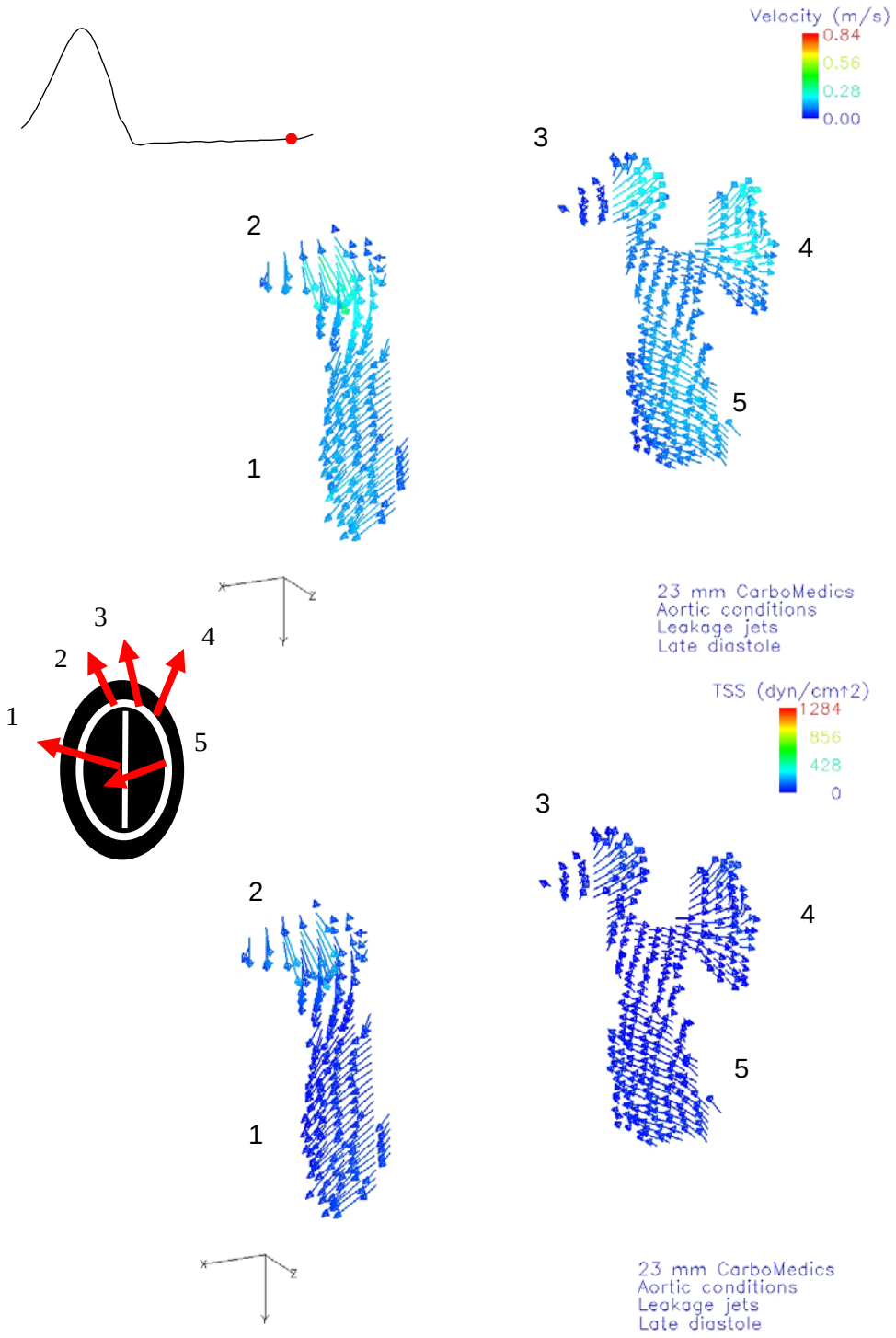

Figure 6.52: 23 mm CarboMedics valve leakage jet velocity field and TSS field at late diastole

6.3.2 23 mm St. Jude Medical Regent Valve

6.3.2.1 Flow and Pressure Curves

Figure 6.53 represents aortic flow and trans-aortic pressure waveforms obtained in the vicinity of the 23 mm St. Jude Medical (SJM) Regent valve. The flow waveform was phase-window averaged according to the procedure outlined in the experimental protocol section. Each open circle denotes a distinct 20 ms time bin. The duration of the sampling interval is shown on the figure. The bins corresponding to late systole, early diastole, mid diastole, and late diastole are also indicated.

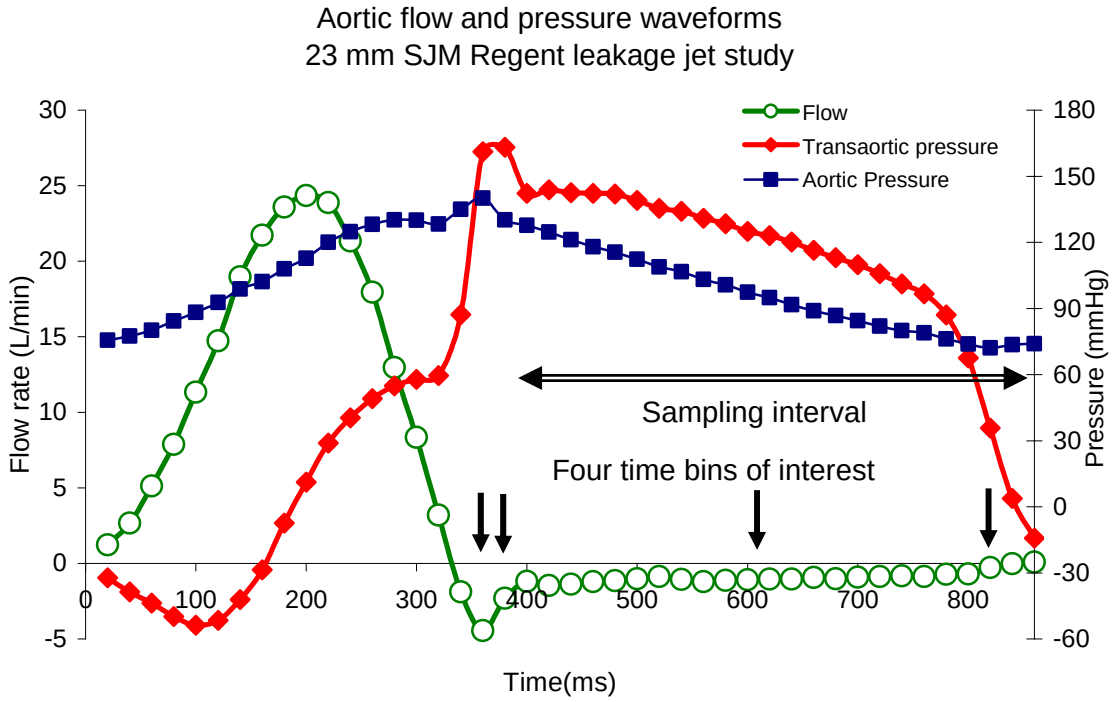

Figure 6.53: Aortic flow and aortic pressure waveforms

6.3.2.2 Overview of the Leakage Jet results of the 23 mm SJM Regent Valve

Animations (AVI and MPG formats) of the upstream velocity flow fields of the SJM regent valve are given in appendix B. The upstream flow field was characterized by two leakage jets. A schematic in figure 6.54 shows where these two jets were observed

in relation to the valve structure. A long, thin region of leakage flow (jet 1) was observed in the vicinity of the valve centerline. The velocity vectors in this central jet had a strong axial component, except at the upper edge where the radial component was dominant. The velocity magnitude distribution was symmetric with respect to the B-datum line axis. A peak velocity magnitude of 2.34 m/s was recorded in the central region of the jet at early diastole. The TSS levels reached 1,687 dyn/cm^2. The maximum cross-sectional dimensions of this jet throughout diastole were 4.95 x 1.40 mm^2.

A second jet (jet 2) was observed in the vicinity of the hinge region. The circumferential vector component was predominant in the upper part of the jet while the flow in the lower part had a strong radial component. The velocity magnitudes were lower than in the central jet (jet 1), with a peak velocity of 0.97 m/s recorded at early diastole. The TSS reached a peak level of 914 dyn/cm^2. The area of this jet was approximately half the size of the central jet, with maximum cross-sectional dimensions of 3.05 x 1.02 mm^2. The spatial and time averaged standard deviation of the velocity magnitude was 0.16 m/s for the SJM leakage jet study.

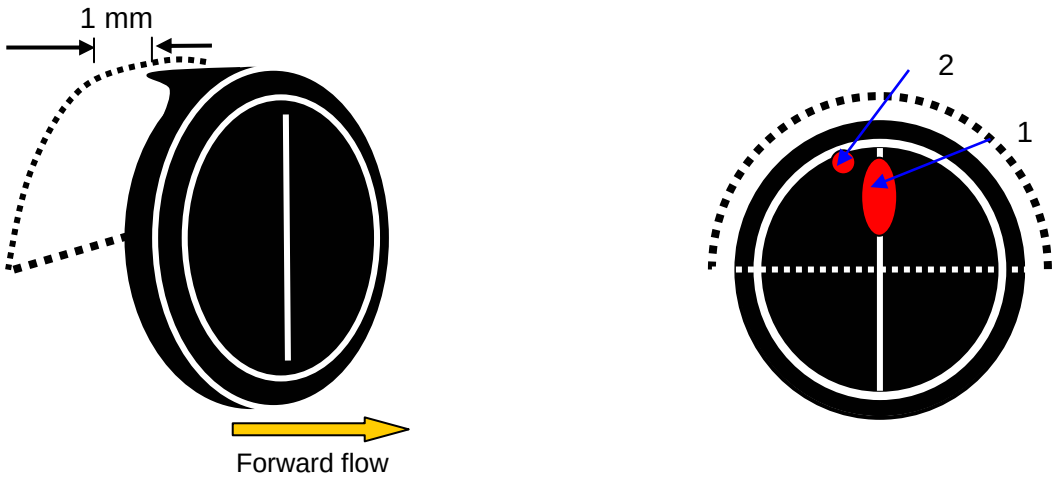

Figure 6.54: Schematic of the region locations in relation to the 23 mm St. Jude Medical Regent valve structure. Each region was associated with a number to facilitate the description of the results.

6.3.2.3 Detailed Description of Leakage Jets Through the Closed 23 mm SJM Regent Valve

Measurements were obtained 1 mm upstream of the pivot guard, and only the locations where the velocity magnitude was greater than 0.2 m/s over the sampling period were recorded. The velocity magnitude of 0.2 m/s will be referred to the following section as the jet threshold velocity magnitude. Locations associated with velocity magnitudes lower than this threshold will not be considered to be part of a jet. In this experiment several regions were characterized over the measurement area. For ease of reference each region was numbered in the color-coded velocity and turbulent shear stress images. In this leakage jet experiment, two regions were characterized over the region of interest. For ease of reference the two regions were numbered 1 and 2 in the color-coded velocity and turbulent shear stress images. A schematic in figure 6.54 shows where these regions were observed in relation to the valve structure. The B-datum line of the SJM valve was horizontal during leakage jet data acquisition. However, to facilitate the comparison with the CM jet results, the color coded maps were rotated so that the B-datum line of the SJM valve was vertical.

Late Systole

Figure 6.55 shows the retrograde flow velocity and TSS fields through the 23 mm SJM Regent valve at late systole (bin 17) when the leaflets were moving towards the closed position.

In region 1 reverse flow was observed in the vicinity of the valve centerline. Region 1 was a long, thin except at the upper edge where a small expansion region was visible. Throughout region 1 the velocity magnitudes were greater than 0.2 m/s, therefore, the cross-sectional dimensions of jet 1 were approximately 4.95 x 1.40 mm^2

(0.195 x 0.055 in^2). The lower edge of the jet was located at the center of the valve implying that this jet may extend symmetrically over the other half of the valve. Velocity vectors within region 1 had a strong axial component. However, in the expansion region velocity vectors pointed slightly towards the left, and were skewed towards the central region of the valve. Within jet 1 the spatial velocity profile was blunted with velocity magnitudes on the order of 0.5 m/s. However, a peak velocity of 0.85 m/s was seen in the lower left side of the strip. The velocity vectors within this jet were almost symmetric, and the central region of the jet, characterized by high speed flow, was surrounded by a region of lower velocity flow. In this region, the TSS levels were on the order of 350 dyn/cm^2. A peak TSS of 544 dyn/cm^2 was seen in the central part of the jet.

In region 2 the velocity vectors pointed towards the left and were slightly slower than in region 1. The velocity magnitudes were on the order of 0.3 m/s, and the peak velocity magnitude reached 0.39 m/s. The flow vectors revealed that the highest velocities were seen in the center of region 2 while the velocity magnitudes on the upper side were lower than the velocity magnitude jet threshold. Therefore, jet 2 had cross-sectional dimensions of approximately 2.29 x 0.89 mm^2 (0.090 x 0.035 in^2), which was smaller than jet 1. Additionally, the velocity vectors on the lower side of the jet had a stronger circumferential component than those on the upper side. The TSS levels gradually decreased from 616 dyn/cm^2 on the upper side of the jet to 81 dyn/cm^2 on the lower side of the jet.

Early Diastole

Figure 6.56 shows the retrograde flow velocity and TSS fields at early diastole (20 ms after late systole). As the driving aortic pressure reached a peak value and the leaflets were closed, the velocity within the jets increased. However, the velocity vectors did not change much.

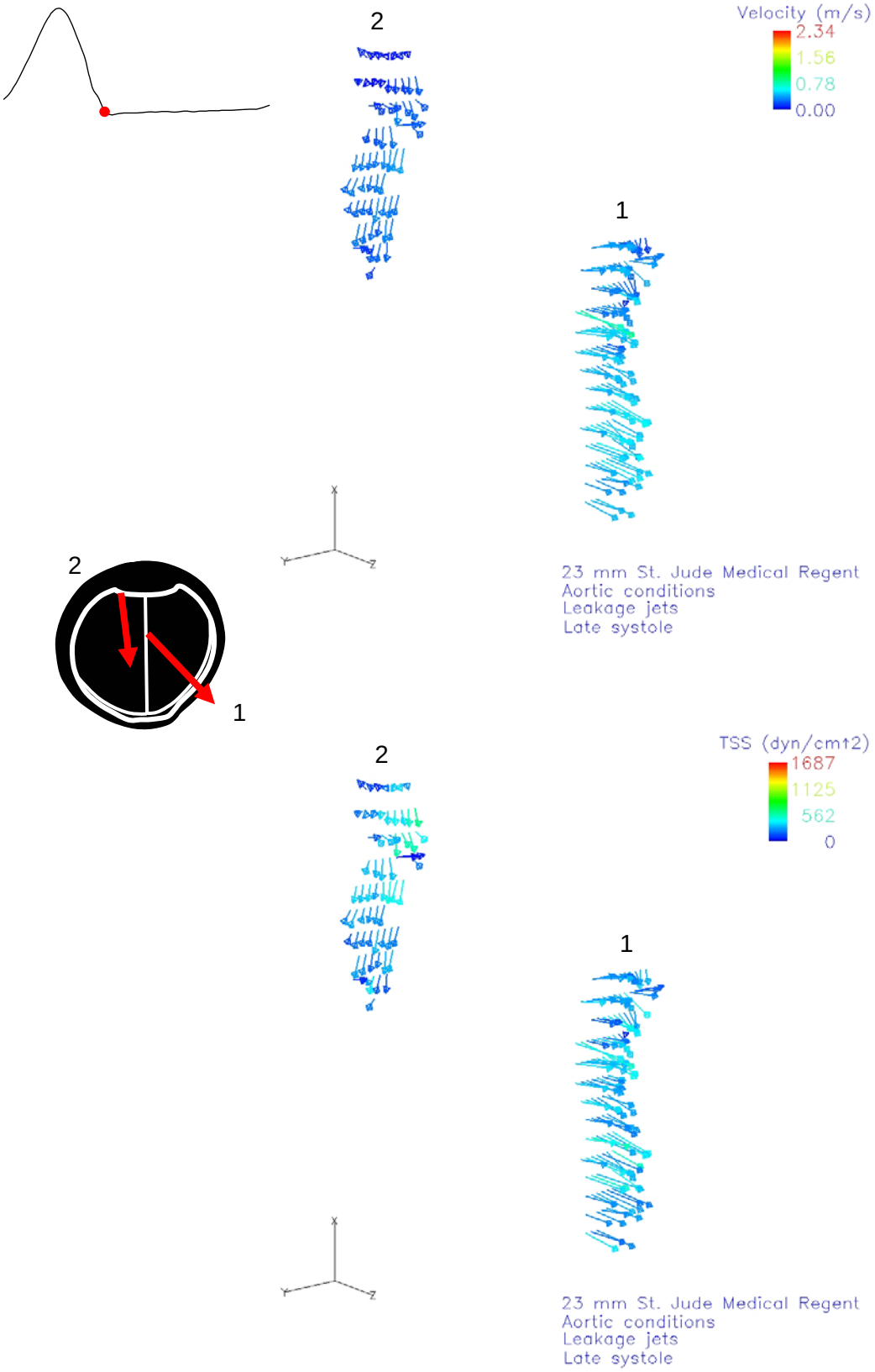

Figure 6.55: 23 mm SJM Regent valve leakage jet velocity field and TSS field at late systole

In region 1, the velocity magnitude was on the order of 0.5 m/s and a peak velocity of 0.86 m/s was recorded. Throughout region 1 the velocity magnitude was greater than 0.2 m/s, except at two locations within the expansion region. The cross-sectional dimensions of jet 1 were therefore similar to those seen in late systole at 4.95 x 1.40 mm^2 (0.195 x 0.055 in^2). Throughout jet 1, the TSS levels were on the order of 400 dyn/cm^2, with a peak TSS of 911 dyn/cm^2. The velocity vectors in the central jet had a strong axial component, except in the expansion region where the velocity vectors had a strong radial component.

The direction of the velocity vectors indicated that the flow on the lower side of region 2 had a strong radial component while on the upper side the circumferential velocity vector component was predominant. On the lower part of the jet the fluid flowed towards the left while on the upper part of the jet, the velocity vector distribution indicated that the fluid was moving away from the valve housing and converging towards the lower part of region 2. The peak velocity magnitude reached 0.52 m/s. Velocity magnitudes lower than 0.2 m/s were seen in the upper left corner of region 2. The cross-sectional dimensions of jet 2 were approximately 2.67 x 0.89 mm^2 (0.105 x 0.035 in^2). The TSS levels gradually decreased from 824 dyn/cm^2 on the upper side to 28 dyn/cm^2 on the lower side of jet 2.

The highest velocity magnitudes and TSS levels throughout diastole were observed at early diastole in both jets. The peak velocity magnitude within region 1 occurred at bin 22 with a velocity magnitude of 2.34 m/s, while in region 2 a peak velocity magnitude of 0.97 m/s was observed at bin 22. The peak TSS level in region 1 occurred at bin 21 and reached 1,687 dyn/cm^2, while in region 2 a peak TSS level of 914 dyn/cm^2 was reached at bin 20.

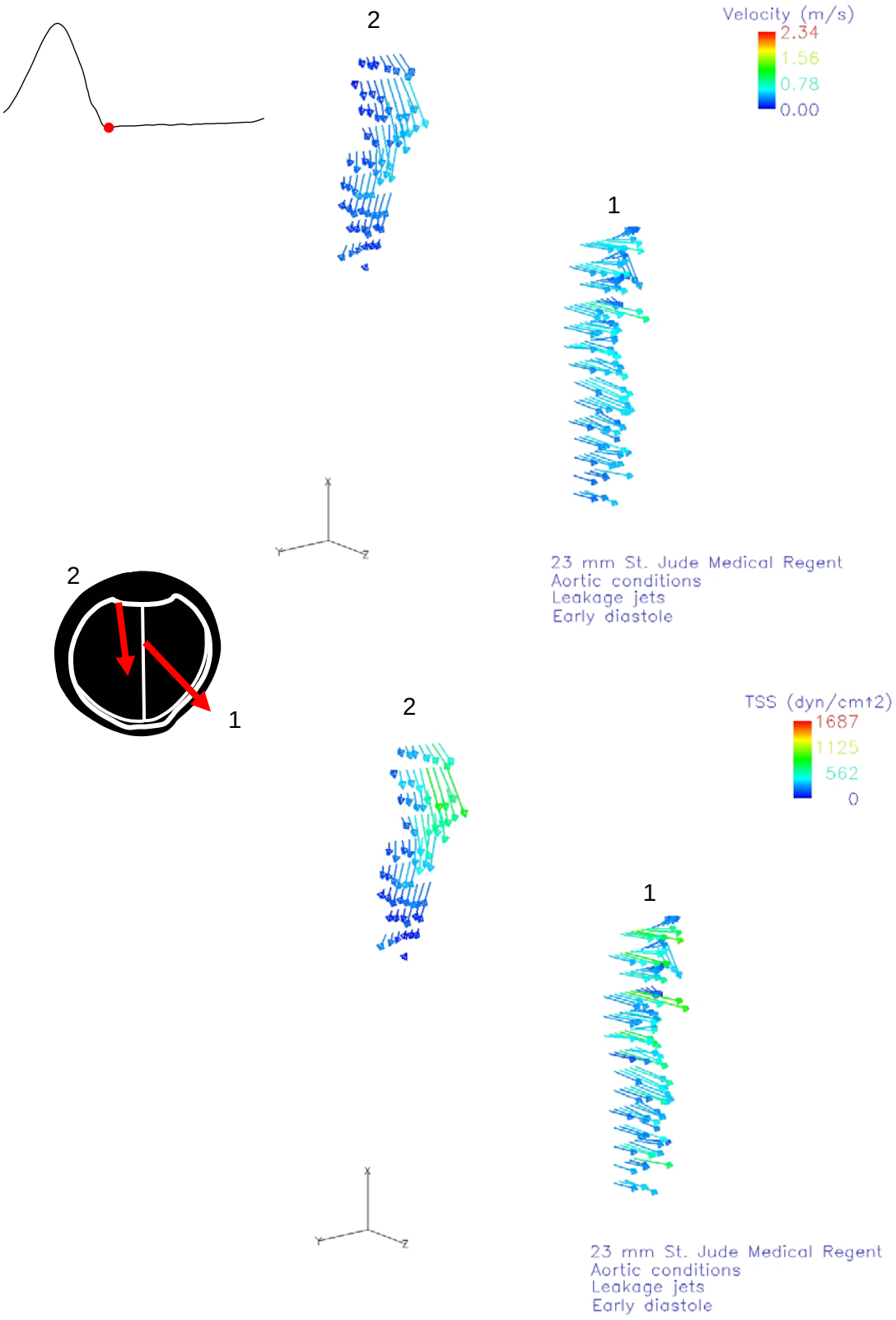

Figure 6.56: 23 mm SJM Regent valve leakage jet velocity field and TSS field at early diastole

Mid Diastole

Figure 6.57 shows the retrograde flow velocity and TSS fields at mid diastole. At mid diastole as the driving aortic pressure decreased, the peak velocity in the central jet decayed to 1.44 m/s while the peak velocity in jet 2 decayed to 0.74 m/s. Figures 6.58 and 6.59 show the jets from different angles.

As seen in late systole, high velocity vectors up to 1.44 m/s, located in the center of region 1, were surrounded by low velocity vectors. Along the edges of region 1, the velocity magnitudes were on the order of 0.4 m/s. Throughout region 1 the velocity magnitude was greater than 0.2 m/s, therefore jet 1 had the same cross-sectional dimensions as it did at early diastole of 4.95 x 1.40 mm^2 (0.195 x 0.055 in^2). The velocity vectors on the lower part of the jet had a strong axial component while in upper part of the jet, within the expansion region, the velocity vector distribution indicated the emergence of a counterclockwise rotating structure. In this expansion region the velocity magnitudes reached up to 0.43 m/s. The peak TSS levels were on the order of 450 dyn/cm^2 with a peak of 905 dyn/cm^2.

Velocity magnitudes ranged from 0.74 m/s on the upper side to 0.18 m/s at the lower edge of region 2. At nearly every location the velocity magnitude was higher than 0.2 m/s, therefore the cross-sectional dimensions of jet 2 were approximately 3.05 x 1.02 mm^2 (0.120 x 0.040 in^2). The TSS levels gradually decreased from 758 dyn/cm^2 on the upper side to 56 dyn/cm^2 on the lower side of region 2. The velocity vectors throughout region 2 had a strong circumferential component, but it was stronger on the upper part of the jet than on the lower part.

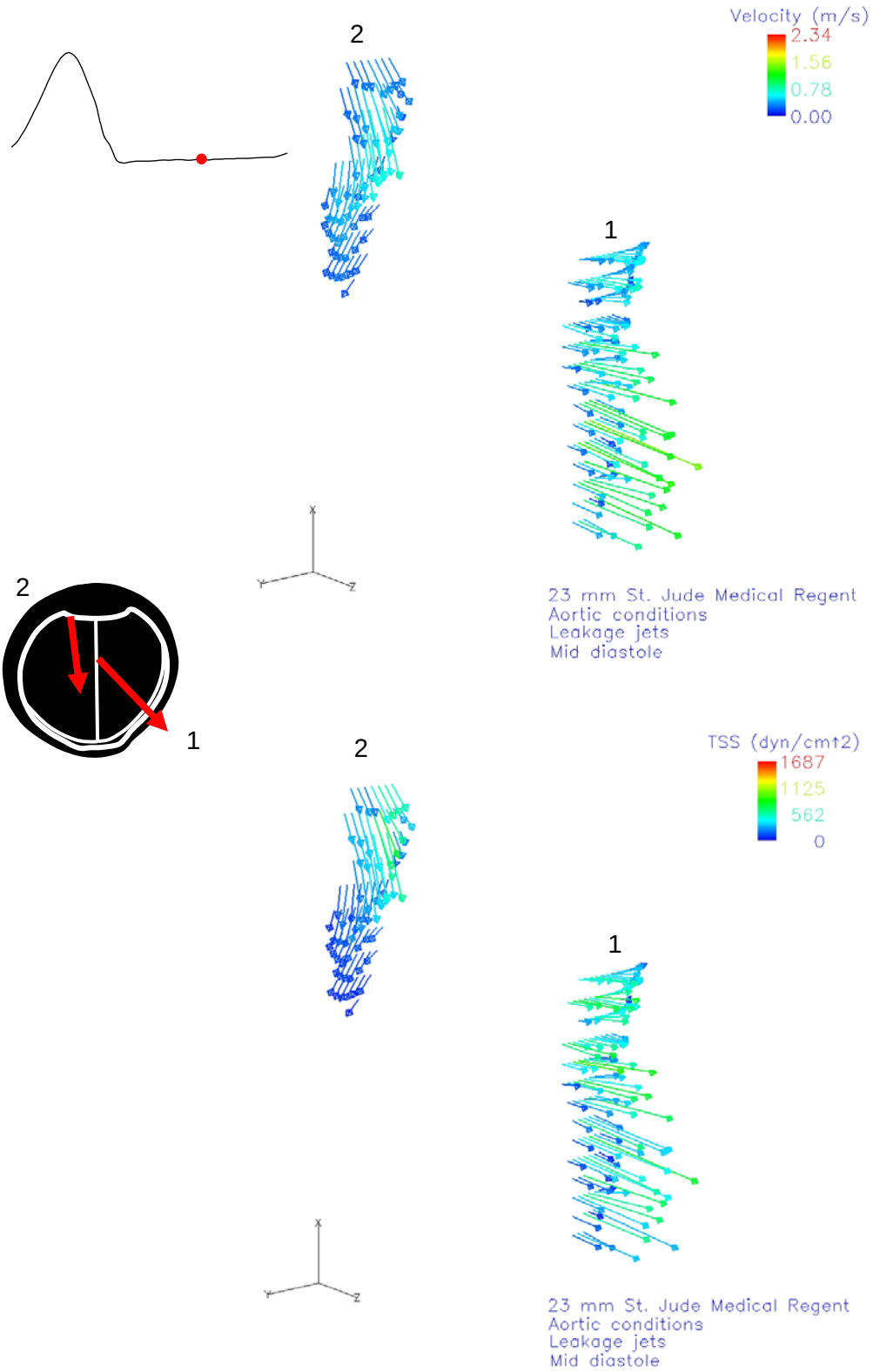

Figure 6.57: 23 mm SJM Regent valve leakage jet velocity field and TSS field at mid diastole

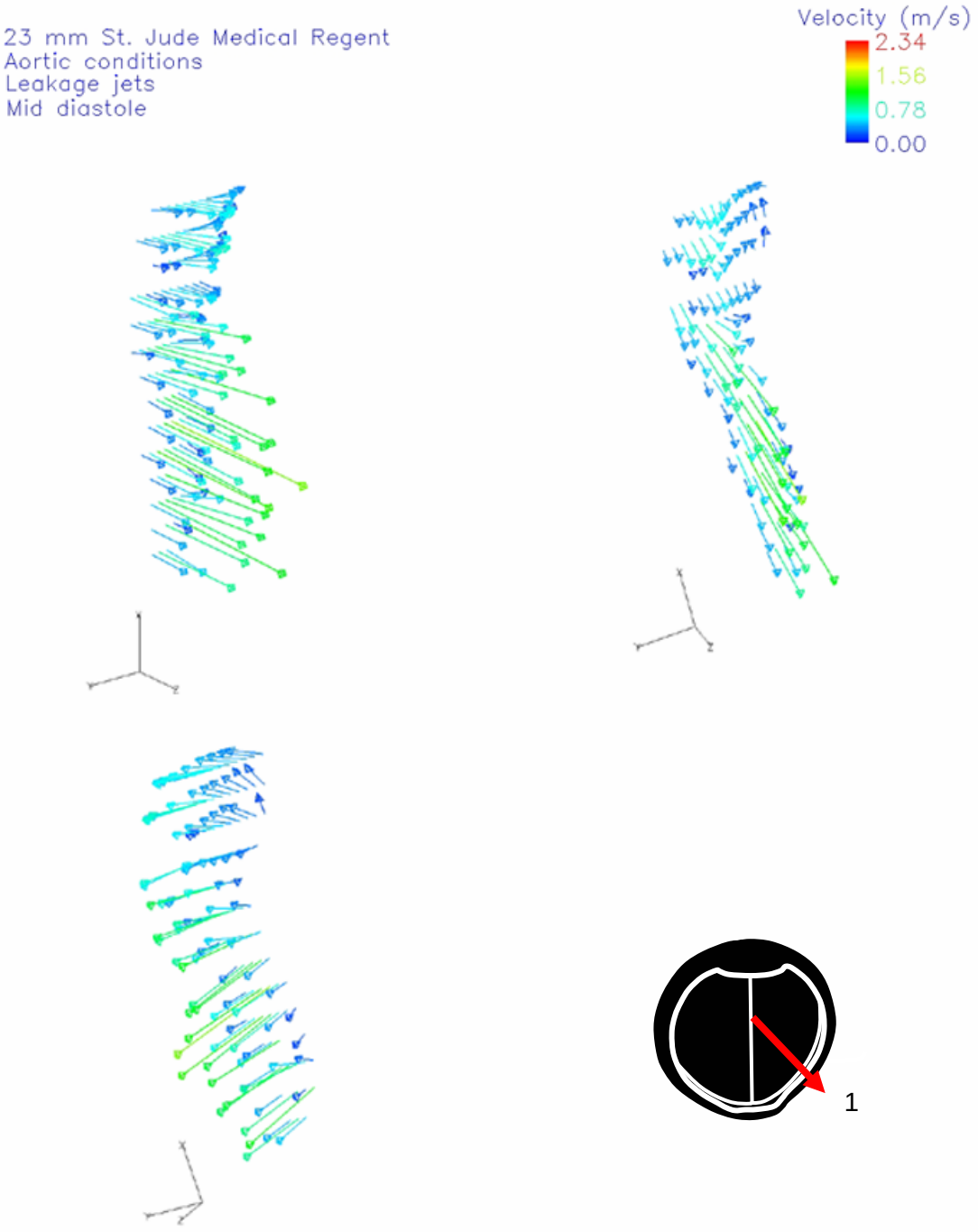

Figure 6.58: Jet 1 seen from different angles at mid diastole

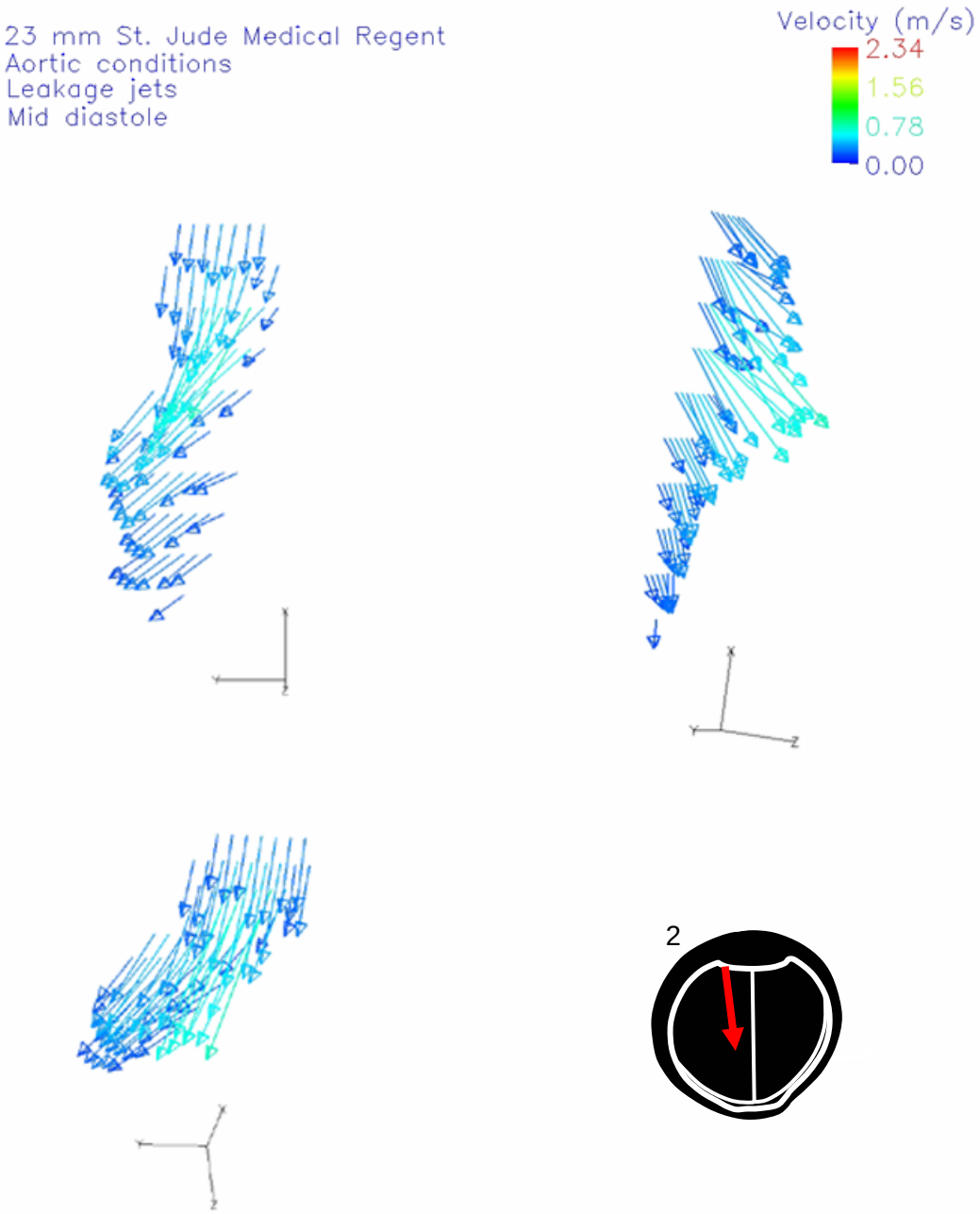

Figure 6.59: Jet 2 seen from different angles at mid diastole

Late Diastole

Figure 6.60 shows the retrograde flow velocity and TSS fields at late diastole. One hundred milliseconds before the end of the cardiac cycle (bin 38), the central and side jets were still present as evidenced by velocity magnitudes higher than 0.2 m/s. However, they had started to dissipate, and at late diastole the flow became almost stagnant. Velocity magnitude dropped below the jet threshold, and at time bin 39 the leakage jet had dissipated.

The flow in region 1 was characterized by a perturbed feature directed mainly in the forward direction. At bin 39 a reverse flow pattern up to 0.14 m/s was present, and the TSS levels were lower than 71 dyn/cm^2. However, at bin 40 the leakage jet vanished, and the flow was mainly forward. The peak velocity and TSS were 0.09 m/s and 32 dyn/cm^2, respectively.

Similarly, in region 2 at bin 39, a slow region of leakage flow was present while at bin 40 most of the flow was already forward. At time bin 39 the maximum velocity was 0.17 m/s and the TSS reached 92 dyn/cm^2. At bin 40 on the lower side of jet 2, the reverse velocity vectors pointed towards the left while on the upper side of the jet, the flow was mainly forward. The peak velocity and TSS were 0.06 m/s and 42 dyn/cm^2, respectively.

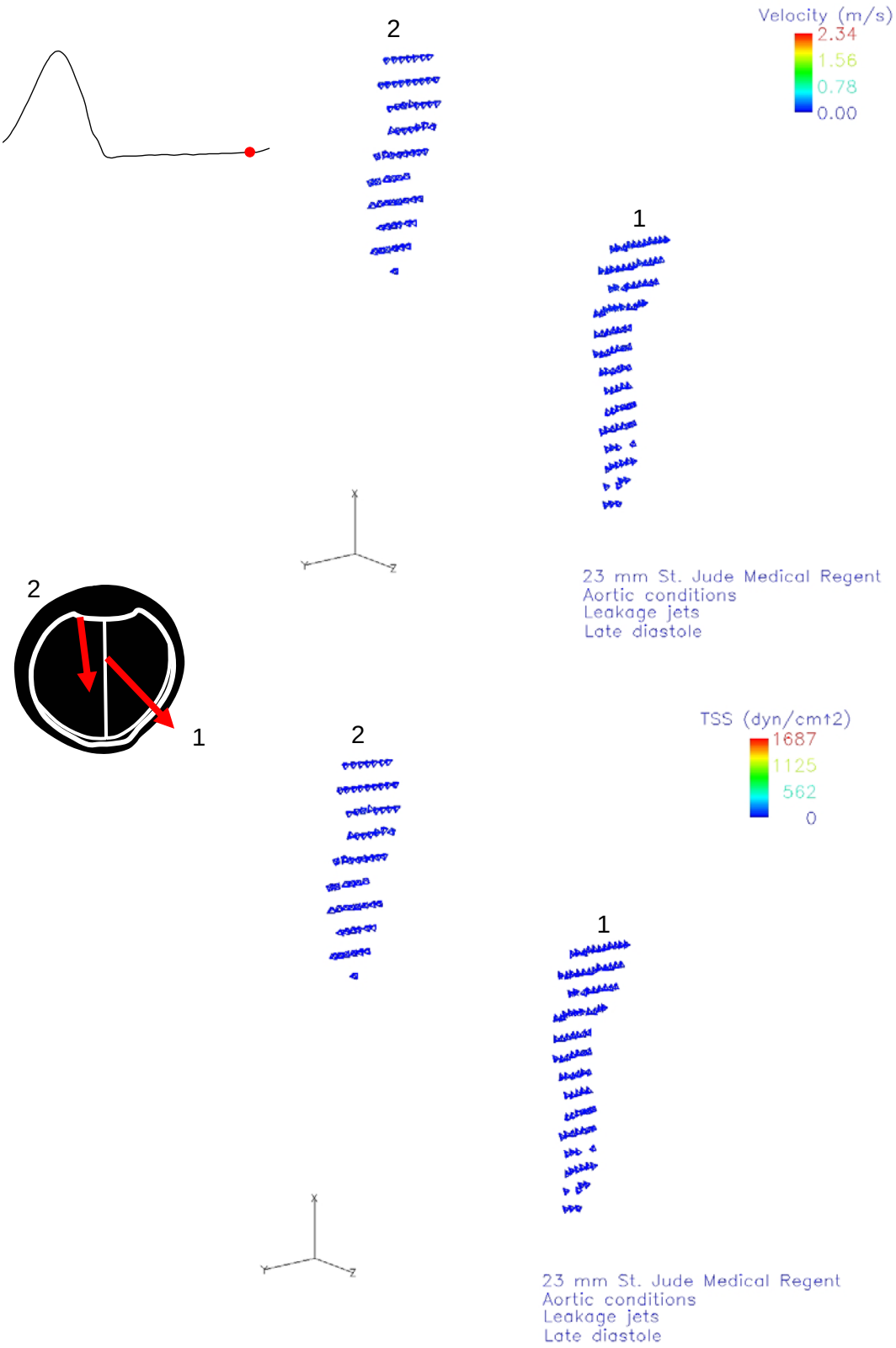

Figure 6.60: 23 mm SJM Regent valve leakage jet velocity field and TSS field at late diastole

6.3.3 Leakage Jet Analysis

The leakage jet study has permitted a detailed characterization of the retrograde jets immediately upstream of each valve. Several parameters were calculated for each jet.

6.3.3.1 Leakage Flow Volume

The blood volume exposed to the leakage flow stimulus during each beat was estimated. Symmetry of the valve was assumed and therefore the sum of the leakage volumes contributed by each studied jet was doubled. The volume contribution of each jet were estimated by the equation 6.1 (Travis, 2001) and are given on Table 6.2.

$$V = 2t\left(\sum_{i=1}^{N} A_i \frac{U\max_i}{2}\right) \qquad \text{Equation 6.1}$$

Where A_i is the cross sectional area of the jet i (m^2)

Umax $_i$ is the maximum velocity magnitude recorded for jet I (m/s)

t is the time of the leakage phase (s)

i is the jet number

N is the maximum number of jets

Table 6.2: Blood volumes per beat expected to experience high Reynolds stresses during the leakage phase

Valve	Jet	Volume (ml)	Total volume (ml)
23 mm CM	1	0.27	4.36
	2	0.11	
	3	0.30	
	4	0.48	
	5	1.01	
23 mm SJM Regent	1	1.87	4.86
	2	0.56	

6.3.3.2 Stokes Layer Reynolds Number

The flow geometry and the Stokes layer Reynolds number characterize turbulence transition in a purely oscillatory flow:

$$\mathrm{Re}_{\delta s} = U\sqrt{\frac{2}{\nu\omega}} \qquad \text{Equation 6.2}$$

Where ν is the kinematic viscosity (m^2/s)

ω is the angular frequency (s^{-1})

U is the average jet velocity (m/s)

In the present study ν was the kinematic viscosity of sodium iodide solution, i.e. 3.5 cSt, and ω corresponded to $2\pi/0.860 = 7.3$ s^{-1}. Stokes layer Reynolds numbers of each jet are given in Table 6.3. Stokes layer Reynolds numbers for the leakage jets are given in table 6.2. For the Stokes layer Reynolds number, the velocity scale is the average velocity during the peak amplitude phase of the oscillatory cycle, and the length scale is the Stoke layer thickness defined as:

$$\delta_s = \sqrt{\frac{2\nu}{\omega}} \qquad \text{Equation 6.3}$$

The average jet velocity was calculated at the time bin when the maximum jet velocity was recorded. Since the leakage gap widths of the two valves of interest, on the order of 100 μm, where much smaller than the Stokes layer thickness, approximately 980 μm, the length scale of the leakage gap width governed the regime of the jets.

Table 6.3: Stokes Layer Reynolds number for each jet

Valve	Jet	U (m/s)	$Re_{\delta s}$
23 mm CM	1	0.26	72
	2	0.25	69
	3	0.39	110
	4	0.32	91
	5	0.27	75
23 mm SJM Regent	1	0.68	190
	2	0.46	130

6.3.3.3 Womersley Number

The Womersley number α is defined as the ratio of inertial to viscous forces (equation 6.4), and was estimated for each jet (Table 6.4)

$$\alpha = \frac{D_e}{2}\sqrt{\frac{\omega}{\nu}} \qquad \text{Equation 6.4}$$

Where ν is the kinematic viscosity (m^2/s)

ω is the angular frequency (s^{-1})

D_e is the equivalent diameter (m) defined as:

$$D_e = 4\frac{(jet\ cross\ sectional\ area)}{(jet\ perimeter)} \qquad \text{Equation 6.5}$$

In the present study ν was the kinematic viscosity of sodium iodide solution, i.e. 3.5 cSt, and ω corresponded to $2\pi/0.860 = 7.3\ s^{-1}$. *The parameter* α can be considered as an "unsteady Reynolds Number since it indicates the relative importance of inertial and viscous forces in determining the motion within the time scale of one period of an oscillation.

Table 6.4: Stokes Layer Reynolds number for each jet

Valve	Jet	Perimeter (mm)	Cross sectional area (mm^2)	De(mm)	α
23 mm CM	1	11.05	2.90	1.05	0.76
	2	6.48	1.09	0.67	0.49
	3	6.29	1.45	0.92	0.67
	4	8.19	2.83	1.38	1.00
	5	18.10	9.22	2.04	1.47
23 mm SJM Regent	1	12.45	3.19	1.03	0.74
	2	8.89	2.32	1.05	0.75

6.3.3.4 Reynolds Number Based on the Equivalent Diameter

Reynolds numbers of the leakage jets were based on the equivalent diameter and the averaged velocity observed in these jets at the time bin when the maximum jet velocity was recorded (Table 6.5).

$$R_e = \frac{D_e U \rho}{\mu} = \frac{D_e U}{\nu}$$ Equation 6.6

Where D_e is the equivalent diameter (m)

ν is the kinematic viscosity (m^2/s)

U is the averaged velocity magnitude (m/s)

Table 6.5: Reynolds number based on equivalent diameter

Valve	Jet	De(mm)	Re
23 mm CM	1	1.05	77
	2	0.67	48
	3	0.92	103
	4	1.38	128
	5	2.04	156
23 mm SJM Regent	1	1.03	200
	2	1.05	138

6.3.3.5 Estimation of the Nozzle Reynolds Number

To calculate the nozzle Reynolds number, the following assumptions were made:

- Submerged jet theory was applied to the leakage jet upstream of the closed mechanical valve. A submerged jet is by definition a jet of fluid into a quiescent reservoir containing the same fluid as the jet. The upstream chamber of the valve was therefore assumed to be quiescent during diastole. This assumption is questionable since the flow in the study of the leakage jets is pulsatile in nature.

- Assuming a uniform pressure field in the absence of any other forces, and a quiescent reservoir, the flux of axial momentum of a jet is conserved even as the jet disperses.

- Once past the nozzle, the jets are assumed to develop free of external applied constraints, and therefore the flows at various axial location are dynamically similar.

- The ratio of the local axial velocity to the centerline axial velocity of the jet was assumed to be only function of the inverse of the distance from the nozzle. Moreover, the distance from the centerline where the axial velocity falls to one half of the centerline velocity, or half width, was assumed to be proportional to the axial distance from the orifice.

- The jets are axysimmetric.

Under these assumptions, one can state that the Reynolds number calculated far from the jet orifice is similar to the nozzle Reynolds number. Therefore, the nozzle Reynolds number was estimated with:

$$\mathrm{Re}_o = \frac{U_c\, b}{\nu} \qquad \text{Equation 6.7}$$

Where ν is the kinematic viscosity (m^2/s)

U_c is the centerline velocity (m/s)

b is the half width (m)

The maximum jet velocity recorded during diastole was chosen as the centerline velocity U_c. The transverse width required for axial flow velocity to decrease to half of the centerline velocity was considered as the half width, b. Due to the complexity of the jet shape, the area of each jet was estimated, and the radius of a circle of same area was calculated. The radius was taken as the half width b. Nozzle Reynolds numbers were estimated for all jets (Table 6.6).

Table 6.6: Reynolds number based on equivalent diameter

Valve	Jet	b(mm)	Nozzle Re
23 mm CM	1	0.97	103
	2	0.64	76
	3	0.36	86
	4	0.53	102
	5	1.70	214
23 mm SJM Regent	1	0.37	249
	2	0.56	154

CHAPTER VII

DISCUSSION

7.1 Hinge Study

The hinge flow studies provide for the first time the detailed flow fields within the hinge region of two bileaflet mechanical heart valves in the aortic position. The following discussion is divided into three sections: features of the CarboMedics (CM) hinge and near-hinge flow fields, features of the St. Jude Medical Regent (SJM) hinge and near hinge flow fields, and influence of geometry on the hinge flow fields. The discussion is based on the animations given in Appendix A.

7.1.1 23 mm CarboMedics valve

The flow field in the 23 mm CM clear housing valve was characterized at selected locations, which, for purposes of comparison, were similar to those used in a previous CM valve hinge study in the mitral position (Leo, 2002).

7.1.1.1 General Features of 23 mm CM Hinge and Near-Hinge Flow Fields under Aortic Conditions

The flow field within the hinge region of the 23 mm CM valve had a dynamic washout flow pattern with minimal formation of vortex structures and stagnation regions. Animations of the hinge and near-hinge velocity flow fields at each elevation are given in Appendix A. Tables 7.1 and 7.2 summarize the peak velocity magnitudes and the corresponding turbulent shear stress (TSS) levels measured in the hinge region of the 23 mm CM clear housing valve in the aortic position at each elevation. Systolic and diastolic spatial-averaged velocity magnitudes were estimated at the time bins when the

peak velocities were recorded. Similarly, systolic and diastolic spatial-averaged TSS levels were estimated at the time bins when the peak TSS levels were recorded. These averaged values obtained during the forward flow and leakage flow phases are given in Tables 7.1 and 7.2.

Table 7.1: Peak phase-averaged velocities and averaged velocities measured within the hinge region of the 23 mm CM valve

Elevation	Peak phase-averaged velocity (m/s)		Averaged velocity (m/s)	
	Forward flow	Leakage flow	Forward flow	Leakage flow
390 μm above flat	0.73	1.37	0.05	0.1
195 μm above flat	1.55	2.57	0.20	0.40
Flat level	2.31	3.08	1.0	0.30
1 mm below flat	2.98	0.82	2.2	0.10

Table 7.2: Peak phase-averaged TSS levels and averaged TSS levels measured within the hinge region of the 23 mm CM valve

Elevation	Peak phase-averaged TSS level (dyn/cm^2)		Averaged TSS level (dyn/cm^2)	
	Forward flow	Leakage flow	Forward flow	Leakage flow
390 μm above flat	4,379	4,339	150	500
195 μm above flat	2,331	6,192	200	300
Flat level	6,902	5,440	200	100
1 mm below flat	5,881	842	100	50

Systole within the Hinge Recess

During systole the peak velocity magnitudes within the hinge recess ranged from 2.31 to 0.4 m/s, with the highest velocity recorded at the flat level. The averaged velocity magnitudes measured at the flat level, at the 195-μm level, and at the 390-μm level were approximately 1 m/s, 0.2 m/s and 0.05 m/s, respectively. A strong forward flow jet was

observed in the outflow lateral corner at the flat level, but was no longer evident at levels above the flat. This is consistent with the fact that the majority of the forward flow was through the opened leaflets, and relatively little fluid was directed towards the hinge recess. A curved forward jet in the adjacent corner was observed at the flat level and at the 195-μm level, but was not evident at the 390-μm level. It is likely that the forward flow in the inflow pocket was being blocked by and directed over the side of the leaflet pivot. Due to the impact of the fluid on the hinge wall, the flow was redirected in a direction nearly perpendicular to the main flow direction (Figure 7.1). Within the hinge recess the flow in the central region of the hinge was characterized by either very low velocities or an absence of measurements due largely to the presence of the leaflet ear

Figure 7.1: Schematic of the flow field during mid acceleration at the flat level

The CM hinge has a butterfly geometry with sharp corners and less streamlined edges than the SJM hinge (Figure 6.5). Consequently, the projections of the leaflets within the recess can not sweep the entire hinge area. Therefore, it is probable that the high velocities in the inflow and outflow pockets during systole contribute to an effective washout of the recess and may keep the hinge region clear of any deposited blood element.

Diastole within the Hinge Recess

During diastole the highest TSS levels and velocity magnitudes were typically found in two isolated regions (Figure 7.2). The first region is the sharp edge of the lateral corner where the fluid appeared to be squeezed between the leaflet ear and the housing, thus generating high velocities and TSS near the housing wall. The second region was the tip of the ventricular inflow corner. The leakage flow within the inflow pocket may have been blocked by and directed over the leaflet ear. This retrograde flow may have been obstructed by the valve housing and redirected out of the hinge region as evidenced by the high velocities of up to 3.08 m/s seen at the tip of the ventricular corner (Figure 7.3). The flow was disturbed at 390 μm above the flat level during the closed phase. It is likely that the confined flow field at this elevation may be three-dimensional in nature because of the complex geometry formed by the mating of the hinge and leaflet. The third velocity component may be predominant as the fluid flows over the leaflet ear, as suggested by the velocity vector distribution along the inner surface of the closed leaflets.

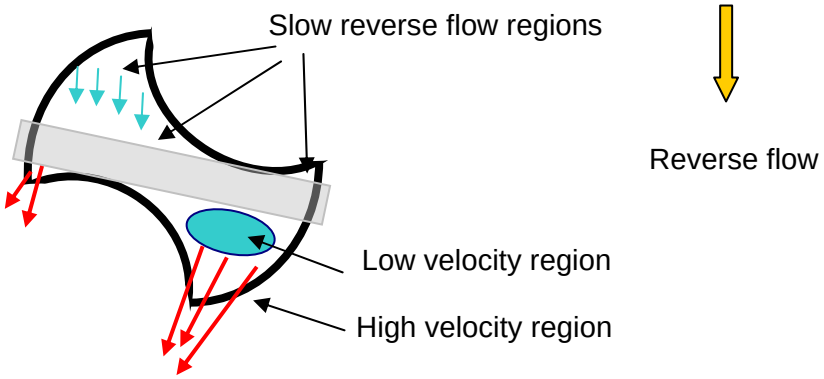

Figure 7.2: Schematic of the flow field at the flat level during mid diastole

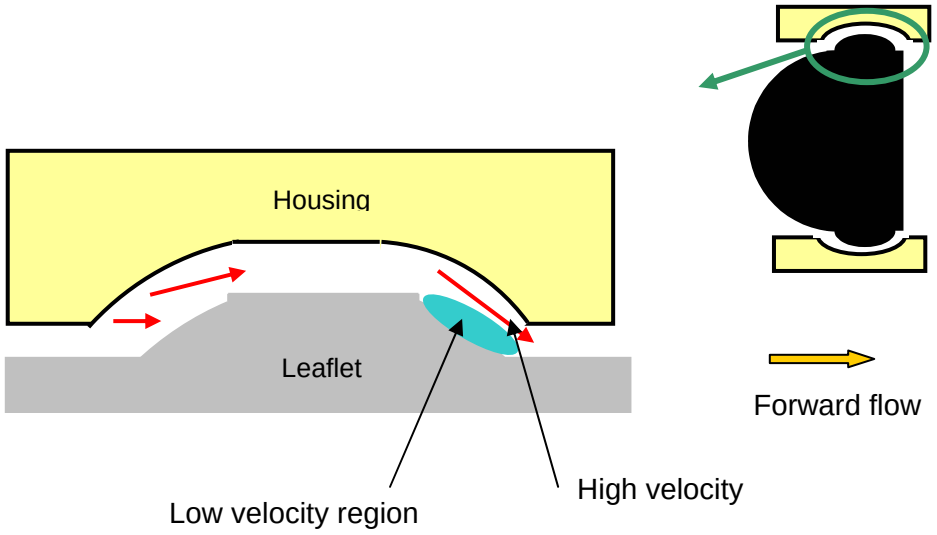

Figure 7.3: Schematic of the flow field within the hinge recess during diastole

Below the Flat Level

Unlike the SJM valve design, the CM valve lacks the thumbnail region, so at 1 mm below the flat level only the flow pattern below the hinge region was measured. At this level the flow was outside the hinge recess. The highest velocities occurred during systole between the open leaflets, with a peak forward flow velocity of 2.98 m/s. The flow arrows suggest that the flow depended primarily on leaflet position and to a lesser degree on hinge location. Regions of high TSS were seen during systole at the edges of the central forward jet where regions of high velocity were adjacent to regions of low velocity. During diastole the flow at 1 mm below the flat level was almost stagnant. The flow was slightly influenced by the proximity of the hinge region since the energy of the leakage jet within the hinge may have already dissipated. A measurement closer to the flat level might reveal a stronger influence of the hinge flow.

7.1.1.2 Comparison of the Aortic and Mitral Positions

The flow field within the hinge region of the 23 mm CM valve was compared to the results obtained with the same valve subjected to mitral conditions (Leo, 2002). Tables 7.3 and 7.4 summarize the peak velocity magnitudes and TSS levels measured in the hinge region in the aortic and mitral positions.

Table 7.3: Peak phase-averaged velocity measured within the hinge region of the 23 mm CM valve under aortic and mitral conditions

Elevation	Peak phase-averaged velocity (m/s)			
	Aortic position		Mitral position	
	Forward flow	Leakage flow	Forward flow	Leakage flow
390 μm above flat	0.73	1.37	0.30	2.52
195 μm above flat	1.55	2.57	0.77	2.91
Flat level	2.31	3.08	0.54	3.17
1 mm below flat	2.98	0.82	1.0	0.5

Table 7.4: Peak phase-averaged TSS levels measured within the hinge region of the 23 mm CM valve under aortic and mitral conditions

Elevation	Peak phase-averaged TSS level (dyn/cm^2)		
	Aortic position		Mitral position
	Forward flow	Leakage flow	
390 μm above flat	4,379	4,339	4,380
195 μm above flat	2,331	6,192	5,640
Flat level	6,902	5,440	5,510
1 mm below flat	5,881	842	4,810

Comparison of the Velocity Field during the Forward Flow Phase

Comparison of the velocity field during the forward flow phase revealed that at all elevations the peak phase-averaged forward flow velocities in the aortic position were higher than in the mitral position (Table 7.3). This observation may be due to the

difference in the cyclic flow rate at these two positions. Typical pressure and flow curves for the aortic and mitral valves are displayed in Figure 7.4. The peak forward flow rate under mitral conditions was 10 L/min, but it was 25 L/min under aortic conditions. Since the valve diameter was the same in both studies, the forward flow velocities were expected to be greater in the aortic position. Additionally, the peak aortic forward flow rate is reached in a shorter period of time than the peak mitral flow rate since systole is twice as short as diastole. Therefore, the fluid through the aortic valve has greater acceleration, leading to greater momentum. Thus, at a given cardiac output flow velocities are higher in the aortic than in the mitral position during the forward flow phase.

At 1 mm below the flat level, the peak phase-averaged forward flow velocity measured under aortic conditions was approximately three times higher than that observed under mitral conditions, with maximum forward flow velocity magnitudes of 2.98 m/s and 1 m/s, respectively. However, the differences in velocity magnitude at the 195-μm and 390-μm levels were smaller than at the flat level and below. Additionally, at the flat level two prominent forward flow jets were present in the lateral and adjacent corners under aortic conditions, while under mitral conditions at the same elevation, only the forward flow in the adjacent corner was observed. Because most of the flow was through the open leaflets and less fluid flowed through the hinge region during the forward flow phase, the difference in peak forward flow rate had less influence on the velocity field at higher measurement levels within the hinge. Therefore, within the hinge recess, the differences in velocity magnitude and flow pattern were not as marked as they were at the flat level and below.

Comparison of the results suggests that the forward flow regions were more dynamic under aortic than under mitral conditions, as evidenced by higher velocity magnitudes measured in the hinge as well as in the near hinge regions in the aortic

position than in the mitral position. The forward flow pattern within and in the vicinity of the hinge was therefore related to the peak forward flow rate as well as the forward flow phase duration. The elevated aortic forward flow rate and the short duration of systole may ensure a better washout of the hinge region during the forward flow phase in the aortic position than in the mitral position.

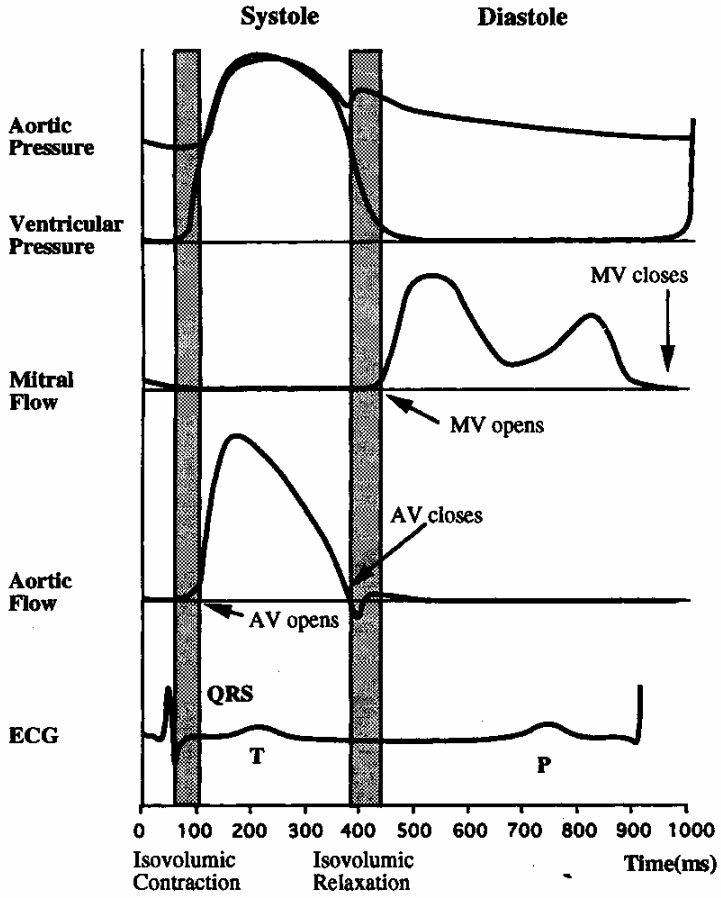

Figure 7.4: Typical pressure and flow curves for the aortic and mitral valve (Yoganathan, 1995)

Comparison of the TSS Levels during the Forward Flow Phase

The TSS levels in the hinge region of a 23 mm CM valve in the aortic position during the forward flow phase were compared to the results obtained with the same valve in the mitral position by Leo et al. (Leo, 2002).

Comparison at the flat level or below revealed that TSS levels were higher in the aortic than in the mitral position. Once again this may be attributed to the difference in peak forward flow rate. Since velocity magnitudes were higher in the aortic position, higher velocity gradient and thus higher TSS levels were expected to be seen under aortic conditions during the forward flow phase. However, the peak TSS calculated in the aortic position at 390 μm above the flat level was similar to that seen in the mitral position, and at 195 μm above the flat level, the peak TSS was lower in the aortic position than in the mitral position. Direct comparison was not possible because the peak TSS levels published for the mitral position were given only during the leakage phase. Nevertheless, because the discrepancy in forward flow velocity magnitudes observed within the hinge recess in both the aortic and the mitral position were not as marked as below the flat level, little difference in TSS levels under aortic and mitral conditions were expected to be seen within the hinge recess.

During the forward flow phase, the peak TSS levels in the aortic position were higher than those in the mitral position at the flat level and below. Nevertheless, the duration of the forward flow phase may play a role in the hinge fluid dynamics. Indeed the forward flow experienced by the mitral valve lasts twice as long as in the aortic valve. Therefore, in the aortic position the leaflet may sweep the hinge region faster causing the closing leaflet motion to be more abrupt than in the mitral position. Because of the higher peak forward flow rate and the shorter duration of systole, flow under aortic conditions during the forward flow phase may be subjected to higher accelerations and,

consequently, to elevated velocities and TSS levels. Two factors are thought to be critical in shear stress-induced blood damage: the TSS levels and the exposure time. Because of the short duration of systole in the aortic position, the exposure time may be too short for the elevated TSS levels to badly damage blood cells. Conversely, under mitral conditions, the longer exposure to lower TSS levels may cause greater damage to blood cells.

Comparison of the Velocity Field during the Closed Phase

In contrast to the forward flow phase, comparison of the velocity field during the closed phase revealed that the peak phase-averaged leakage flow velocities were higher in the mitral position than in the aortic position at all investigated elevations but below the flat level (Table 7.3). At 1 mm below the flat level under aortic conditions, the flow pattern as well as the leakage flow velocities were similar to those observed under mitral conditions. At the flat level and at the 195-μm level, the peak leakage jet velocity measured under aortic conditions was slightly smaller than under mitral conditions; while at the 390-μm level, the peak velocity magnitudes obtained during the closed phase in the mitral position (2.52 m/s) were approximately twice as high as those seen in the aortic position (1.37 m/s). The difference in peak leakage velocity magnitudes may be due to a difference in the transvalvular pressure gradient (Figure 7.4). Since the pressure gradient across the valve was higher under mitral conditions than under aortic conditions during the leakage phase, the velocities associated with the leakage flow through the hinge region were higher in the mitral position than in the aortic position.

Comparison of the TSS Levels during the Closed Phase

This study showed that the calculated TSS levels in the hinge region during the closed phase were lower in the aortic position than those measured previously (Leo, 2002) in the mitral position (Table 7.4). At all elevations but the 195-μm level, the peak TSS levels calculated in the aortic position were lower than in the mitral position. At the 195-μm level a peak TSS of 6192 dyn/cm^2 was observed for approximately 20 ms in the aortic position. However, during the duration of the closed phase the TSS levels throughout the rest of the hinge did not exceed 4633 dyn/cm^2, which was lower than the peak TSS of 5640 dyn/cm^2 seen in the mitral position. Consequently, the TSS levels recorded at all elevations in the aortic position were smaller than those seen in the mitral position, which was consistent with the conclusion drawn from the forward phase results.

7.1.2 23 mm St. Jude Medical Regent Valve

The flow field in the 23 mm SJM Regent clear housing valve was characterized at selected locations, which, for purposes of comparison, were similar to those used in a previous SJM valve hinge study performed under mitral conditions (Ellis, 2000) and to those used in a CM valve study performed by Leo et al. (Leo, 2002).

7.1.2.1 General Features of 23 mm SJM Regent Hinge and Near Hinge Flow Fields in the Aortic Position

The flow within the hinge region of the 23 mm SJM Regent valve was dynamic with leaflet sweeping action within the SJM hinge recess creating a washout flow pattern, which restricted the persistence of separated flow and stagnation zones. Animations of the hinge and near-hinge velocity flow fields at each elevation are given in Appendix A. Tables 7.5 and 7.6 summarize the peak velocity magnitudes and the

corresponding TSS levels measured in the hinge region of the 23 mm SJM Regent clear housing valve at each elevation under aortic conditions. Systolic and diastolic spatial-averaged velocity magnitudes were estimated at the time bins when the peak velocities were recorded. Similarly, systolic and diastolic spatial-averaged TSS levels were estimated at the time bins when the peak TSS levels were recorded. These averaged values obtained during the forward flow and leakage flow phases are given in Tables 7.5 and 7.6.

Table 7.5: Peak phase-averaged velocities and averaged velocities measured within the hinge region of the 23 mm SJM Regent valve

Elevation	**Peak phase-averaged velocity (m/s)**		**Averaged velocity (m/s)**	
	Forward flow	**Leakage flow**	**Forward flow**	**Leakage flow**
585 μm above flat	0.32	0.49	0.2	0.3
390 μm above flat	1.07	2.27	0.2	0.4
195 μm above flat	1.06	1.96	0.15	0.4
Flat level	1.75	1.64	0.2	0.1
500 μm below flat	2.49	0.14	1.0	0.06
1 mm below flat	2.43	0.15	1.0	0.06
3 mm below flat	2.62	0.15	1.0	0.07

Table 7.6: Peak phase-averaged TSS levels and averaged TSS levels measured within the hinge region of the 23 mm SJM Regent valve

Elevation	**Peak phase-averaged TSS level (dyn/cm^2)**		**Averaged TSS level (dyn/cm^2)**	
	Forward flow	**Leakage flow**	**Forward flow**	**Leakage flow**
585 μm above flat	260	647	40	200
390 μm above flat	779	7,903	100	1,000
195 μm above flat	936	5,460	40	500
Flat level	1,327	2,657	50	~0
500 μm below flat	3,189	1,236	200	~10
1 mm below flat	3,192	864	400	~0
3 mm below flat	4,544	48	150	~0

Systole

Animations of the velocity flow fields obtained within the hinge recess of the SJM valve are given in Appendix A. During the forward flow phase, two prominent flow features were observed at the flat level (Figure 7.5). A strong jet of approximately 1.75 m/s was observed in the lateral corner. A slow counterclockwise rotating structure was observed in the adjacent corner and may have been due to the confining effect of the leaflet ear upon the entering flow. Some flows from the rotating structure may have been squeezed against the hinge wall creating a region of high velocity flow of approximately 1.23 m/s. The forward flow pattern was no longer evident at the levels above flat because most of the forward flow was through the opened leaflets with less fluid being directed towards the hinge recess. The central region of the hinge was characterized by a very low flow field or an absence of measurement that may be due largely to the presence of the leaflet ear. However, because the leaflet pivot dimension decreased within the hinge, the region of near zero flow field decreased in size as the measurement plane was raised within the hinge recess.

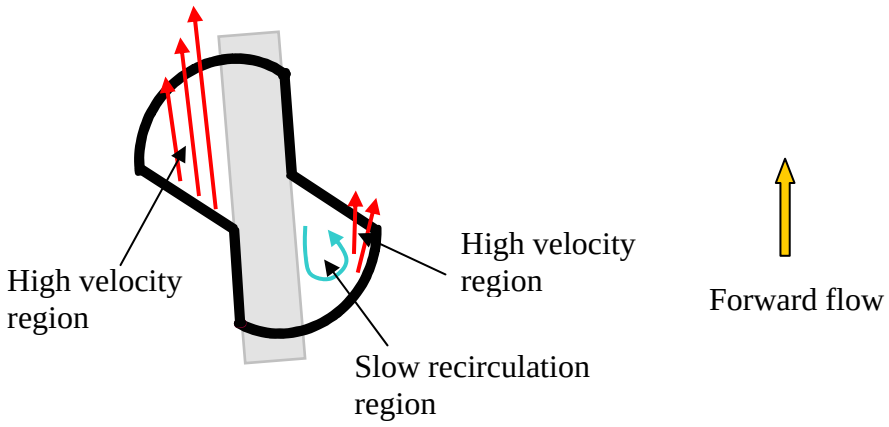

Figure 7.5: Schematic of the velocity field at the flat level during systole

Animations of the velocity flow fields obtained at each elevation below the flat level of the SJM valve are given in Appendix A. Similar flow features were seen at all elevations below the flat during the forward flow phase. The central systolic jet was skewed as it entered the thumbnail region and detached from the thumbnail, resulting in the formation of two recirculation regions (Figure 7.6). The region of separated flow persisted in the thumbnail at all elevations below the flat.

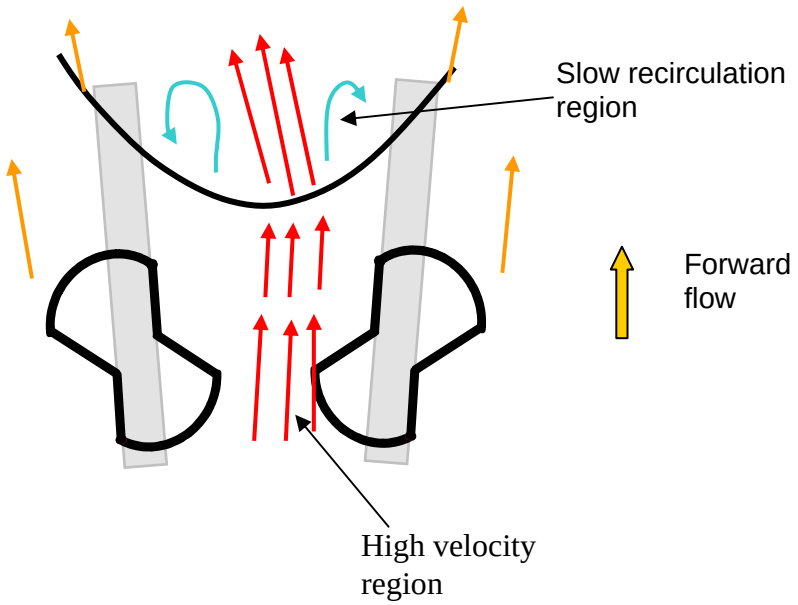

Figure 7.6: Schematic of the flow field below flat level during systole

Diastole

Animations of the velocity flow fields obtained at each elevation are given in Appendix A. Due to the strong washout of the hinge region, the rotating structure that persisted in the inflow pocket during systole was no longer evident during diastole. High velocity leakage jets occurred in the ventricular inflow and the outflow lateral corners. Maximum velocity magnitudes and TSS levels were observed near the housing wall,

where the leaflet impacted the hinge wall during valve closure. At the flat level, the reverse jet occurred when the reverse flow was squeezed between the leaflet ear and the housing. At levels above the flat, the reverse jet in the inflow pocket flowed over the side of the leaflet ear and expanded to the ventricular corner. This leaflet action may keep the hinge region cleared of any deposited blood elements under *in vivo* conditions. The active motion of the leaflet throughout the hinge region may therefore be a contributing factor to the long-term clinical success of the SJM Regent valve.

7.1.2.2 Comparison of the Mitral and Aortic Positions

The flow field within the hinge region of the 23 mm SJM Regent valve was compared to the results obtained with the same valve placed under mitral conditions. Tables 7.7 and 7.8 summarize the peak velocity magnitudes and the corresponding TSS levels measured in the hinge region of the 23 mm SJM Regent valve under mitral and aortic conditions. The velocity and the turbulent shear stress flow fields in the mitral and the aortic positions were qualitatively similar, but some quantitative discrepancies were observed.

Table 7.7: Peak phase-averaged velocity measured within the hinge region of the 23 mm SJM Regent valve under aortic and mitral conditions

Elevation	**Peak phase-averaged velocity (m/s)**			
	Aortic position		**Mitral position**	
	Forward flow	**Leakage flow**	**Forward flow**	**Leakage flow**
585 μm above flat	0.32	0.49	0.08	0.60
390 μm above flat	1.07	2.27	0.20	1.52
195 μm above flat	1.06	1.96	0.15	0.95
Flat level	1.75	1.64	0.13	0.72
500 μm below flat	2.49	0.14	0.85	0.40
1 mm below flat	2.43	0.15	1.18	0.40
3 mm below flat	2.62	0.15	1.10	0.20

Table 7.8: Peak phase-averaged TSS levels measured within the hinge region of the 23 mm SJM Regent valve under aortic and mitral conditions

Elevation	Peak phase-averaged TSS levels (dyn/cm^2)		
	Aortic position		Mitral position
	Forward flow	Leakage flow	
585 μm above flat	260	647	2,600
390 μm above flat	779	7,903	1,000
195 μm above flat	936	5,460	700
Flat level	1,327	2,657	700
500 μm below flat	3,189	1,236	400
1 mm below flat	3,192	864	600
3 mm below flat	4,544	48	450

Comparison of the velocity Field during the Forward Flow Phase

Comparison of the velocity field during the forward flow phase revealed that the peak phase-averaged forward flow velocity was higher in the aortic than in the mitral position. At all elevations within the hinge recess, the flow pattern was similar in both the aortic and the mitral positions, but the velocity magnitudes were different as shown in table 7.7. At the flat level the two dominant forward flow features seen in the aortic position were also present in the mitral position. However, the rotating structure was flowing slightly faster (0.3 m/s) in the aortic than in the mitral position (0.1 m/s), and the forward flow in the outflow region was five times faster in the aortic position (1.45 m/s) than in mitral position (0.3 m/s). Similarly, at all elevations below the flat the difference in velocity magnitude was also noticeable as the forward flow velocity magnitude remained higher in the aortic than in the mitral position (Table 7.7). However, the flow features remained similar, as studies under aortic and mitral conditions revealed the same flow pattern with the preferential skewing of the jet and the regions of separated flow, which persisted in the thumbnail region.

These findings were comparable to those observed in the CM hinge and could also be attributed to the difference in cyclic flow rate. The peak forward flow rate was about twice as high in this study than in the study performed by Ellis et al. (Ellis, 2000), and, consequently, since the valve diameters were the same the forward flow velocities were greater in the aortic position than in the mitral position (Table 7.7). The previous results suggest that the forward flow regions were more dynamic under aortic than under mitral conditions, as evidenced by higher velocity magnitudes measured in the hinge as well as in the thumbnail region in the aortic position.

Comparison of the Velocity Field during the Closed Flow Phase

During the closed phase the flow pattern was qualitatively similar under both aortic and mitral conditions, but with higher velocities in the aortic position (Table 7.7). At the flat level the rotating structure that developed during the forward flow phase was no longer present during the closed phase in both the mitral and the aortic positions, but the leakage velocity in the inflow pocket was approximately twice as high in the aortic than in the mitral position. Similarly, at the 195-μm and 390-μm levels, the velocities magnitudes in the aortic position were larger than those recorded in the mitral position. These results do not agree with those obtained with the CM valve, where the leakage velocity magnitudes were higher in the mitral than in the aortic position. This discrepancy may be due to differences in the measurement grid resolution. The measurement grid is an important parameter in fluid dynamics investigation, especially in a narrow region like the hinge geometry, which contains complex flow structures associated with high velocity gradients. The spatial resolution should be able to provide a detailed and accurate representation of the fluid profile. At the flat level and above, only 30 locations were investigated by Ellis et al. (Ellis, 2000). Due to the complexity of the flow, the chosen grid may not have been fine enough to accurately capture the flow pattern; therefore the high

velocity flow may have been missed. This would explain why the peak leakage velocity within the hinge recess was higher in the aortic than in the mitral position.

However, at any elevation below the flat, the highest velocity magnitudes during the closed phase were seen in the mitral position and not in the aortic position (table 7.7) At these elevations, the flow was outside the restricted region of the hinge and was therefore less complex with smaller velocity gradients than in the hinge recess. Moreover, the measurement grids in the present study and in the work of Ellis et al. (Ellis, 2000) were similar at levels below the flat. The results suggest that the severe mitral conditions created higher velocity magnitude than the aortic conditions, which is in agreement with the CM results.

Comparison of the TSS Levels during the Cardiac Cycle

At all elevations, TSS levels were higher in the aortic position than in the mitral position during both the forward flow and closed phases (Table 7.8). High shear stress levels were expected at the interface between regions of high velocity and regions of low velocity. Since the velocities within the hinge recess in the aortic position were higher than those in the mitral position, higher shear stress levels were expected in the aortic position during the forward flow phase. However, the order of magnitude of the TSS levels was approximately ten times higher in the aortic position than in the mitral position; therefore, the issue of the measurement grid may also question the TSS levels obtained within the hinge in the mitral position (Ellis, 2000). Indeed, the turbulent shear stress levels were calculated from the velocity gradient over space. Thus, if high velocities were not recorded, TSS calculations did not lead to peak TSS values.

During the closed phase, high velocity may have been missed in the mitral position due to a coarse measurement grid. Therefore, direct comparison of the TSS levels may not be appropriate.

7.1.3 Influence of Geometry on Hinge Flow Fields in Different Designs

Investigation of a 23 mm SJM Regent valve and a 23 mm CM valves revealed a qualitatively similar flow pattern within the hinge in both the mitral and the aortic positions. Due to higher forward flow velocities, the regions of forward flow were more dynamic under aortic than under mitral conditions. During the closed phase, due to the higher transmitral pressure, leakage flow velocity magnitudes were higher in the mitral than in the aortic position.

Influence of the geometry on hinge flow fields was investigated intensively (Leo, 2002; Ellis, 2000; Ellis, 1996; Saxena, 2003). Leo showed that in the mitral position, the velocity magnitudes of the flow in the CM valve design was somewhere between those of the SJM and the Medtronic Parallel valve designs (Leo, 2002). This comparison was performed for the mitral position, and no study of the micro flow fields of bileaflet mechanical heart valves in the aortic position had been carried out. The results of the present study give a new insight to the influence of the hinge geometry on valve hemodynamic performance in the aortic position.

Peak phase-averaged velocity magnitudes measured under aortic conditions were higher in the CM design than in the SJM design, except at the 390-μm level where the velocities where higher in the SJM design. Similarly, comparison of the TSS levels during the leakage phase revealed higher levels within the CM valve than within the SJM valves, except at the 390-μm level during the leakage phase where the TSS levels where higher in the SJM design. These findings suggest that the SJM design caused less blood damage than the CM valve design, and therefore agree with Leo's conclusions (Leo, 2002). The hinge geometry might be a predominant parameter in the clinical success of a bileaflet mechanical heart valve.

The SJM design provides a streamlined hinge profile, with a gradual change in geometry (Figure 6.18). The leakage jet flowing through the hinge is likely to follow the smooth inside surface of the hinge, thus reducing the propensity for flow separation and turbulence. The CM hinge also has a butterfly hinge geometry but has sharper corners and less streamlined edges than the SJM hinge (Figure 6.5). Consequently, the projections of the leaflets within the recess cannot sweep the entire hinge area. Therefore the gap space between the leaflet and the housing is wider than in the SJM hinge. This may allow more flow through the hinge and may therefore lead to higher velocity magnitudes and TSS levels. Additionally, the SJM hinge has a smooth recess while the CM hinge has an angulated recess, which may also disrupt the flow and favor elevated TSS levels. Consequently, the smooth streamlined SJM hinge geometry seemed to be a more favorable design than the sharp corners of the CM hinge design.

During clinical trials, the Medtronic Parallel (MP) valves exhibited unacceptably high thrombogenic rate. Since thrombi were mainly noted within and upstream of the hinge region, Ellis hypothesized that the flow fields within the hinge may have contributed to the thrombus formation (Ellis, 1996). Experimental investigations under mitral conditions of the hinge flow revealed elevated turbulent shear stress (8,000 dyn/cm^2) near the top of the inflow channel and a large persistent vortical structure in the inflow channel. These results suggested that the complex MP hinge design significantly affects the washout capacity and the thrombogenic potential of the valve. Furthermore, Leo et al. showed that the MP valve design has a greater blood damage potential than the SJM and CM valve design in the mitral position (Leo 2002). Since, the present results agree with Leo's findings, it is conceivable that the sudden expansion and contraction zones of the MP hinge would also lead to high velocity magnitudes and elevated turbulent shear stresses in the aortic position. Hence, it is likely that the MP

valve design has a greater thromboembolic potential than the SJM and CM valve design in the aortic position as well.

Saxena showed that the hinge flow fields of a 29 mm Medtronic Advantage and a 29 mm SJM Standard valves under mitral conditions exhibited similar features (Saxena, 2003). However, the flow was more dynamic during the forward flow phase in the Advantage valve and slightly greater velocities were recorded in the SJM Standard valve during the leakage flow phase. Since the Medtronic Advantage valve design has a butterfly hinge design similar to the SJM valves, Saxena concluded that the bi-level flat design feature characteristic of the Advantage valve may reduce flow resistance and thus the potential for stagnation zones. It is therefore likely that data acquired within the Advantage hinge in the aortic position would reveal an enhanced forward flow pattern during systole, probably with higher velocities than those recorded in the SJM hinge under aortic conditions. Additionally, results in the mitral position suggest that the hinge leakage flow field in the aortic position would be similar to that of a SJM valve, but probably with lower velocities than in the hinge leakage flow field of the SJM valve. Nevertheless, the full understanding of the hinge and near hinge flow field of the Advantage valve design in the aortic position can only be achieved with an in-vitro study; but it is likely that the valuable influence of the bi-level flat design feature on the hinge washout may also be observed under aortic conditions.

7.2 Leakage Jet Study

These studies have permitted a detailed characterization of the leakage jets immediately upstream of each valve. The following discussion is divided into three sections: features of the CM leakage jets, features of the SJM leakage jets, and influence of the valve design on leakage flow fields. The discussion is based on the animations given in Appendix B.

The results suggest that the formation, persistence and dissipation of the jets were dependent upon both time and valve design. Even though the jets were driven by similar transaortic pressure at valve closure, the leakage jets appeared to be strongly reliant on design factors such as hinge geometry and leakage gap width since the upstream leakage flow fields were different for both valves.

7.2.1 23 mm CarboMedics valve

7.2.1.1 General Features of the Leakage Jets

A pulsatile leakage jet study was performed with a 23 mm CM valve under aortic conditions. Several jets were observed within the measurement area emanating from different gaps within the valve structure (Figure 7.7).

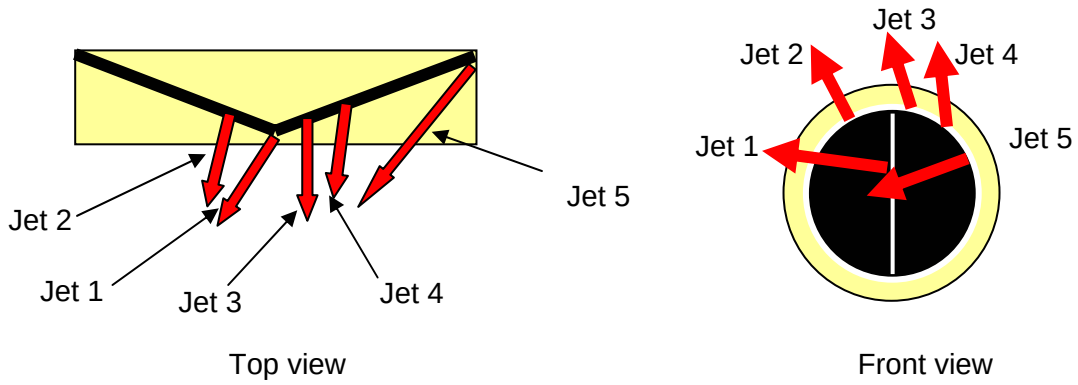

Figure 7.7: Leakage jet locations upstream of the CM valve

Table 7.9 gives the maximum velocity magnitudes, the peak TSS levels, and the maximum cross-sectional dimensions observed during diastole for each jet. The horizontal and vertical distances, which contained the maximum number of grid points, where the velocity magnitude was greater than 0.2 m/s, were considered as the maximum cross-sectional dimensions.

Table 7.9: Peak velocity magnitudes, peak TSS levels, and maximum cross-sectional dimensions recorded throughout diastole for each CM leakage jet

Jet	Peak velocity magnitude (m/s)	Peak TSS level (dyn/cm^2)	Maximum cross-sectional dimensions (mm^2)
1	0.37	576	1.14 x 5.72
2	0.41	625	2.67 x 1.9
3	0.84	1,284	1.9 x 1.71
4	0.68	940	2.29 x 2.48
5	0.44	553	2.67 x 5.33

The largest regions, regions 1 and 5, were located along each side of the B-datum line, i.e. the dividing line between the two leaflets, but the flow arrows suggest that they did not emanate from the same gap. The velocity vector distribution within jet 1 shows that the fluid moved away from the B-datum line, i.e. the dividing line between the two leaflets. Therefore, it is likely that the large skewed flow emanated from the gap between the leaflets. The cross-sectional dimensions of the jet changed throughout diastole reaching a maximum value at early diastole of 1.14 x 5.72 mm^2. On the other side of the B-datum line, velocity vectors within region 5 pointed towards the B-datum line suggesting that the jet emerged from a gap between the leaflet and the housing. This jet was the largest jet observed. The maximum cross-sectional dimensions for this jet of 2.67 x 5.33 mm^2 were observed during mid diastole. The peak velocity was slightly higher in jet 5 than in jet 1 (Table 7.9). The peak TSS levels were on the same order of magnitude with a maximum of 576 dyn/cm^2 in jet 1 and 553 dyn/cm^2 in jet 5. Throughout

diastole the TSS levels were on the order of 200 dyn/cm^2 over jet 1 and 250 dyn/cm^2 over jet 5. Studies have shown that, in turbulent flow such as blood flow through a mechanical heart valve, platelet activation can occur in response to applied shear stresses of 100-500 dyn/cm^2 and that hemolysis occurs in the presence of shear stress of 4,000 dyn/cm^2 (Sutera, 1972; Sallam, 1984). Consequently, the TSS levels seen in regions 1 and 5 are sufficient to lead to blood damage.

Three regions of elevated velocity were found near the flat hinge region. Velocity vector distributions within region 2 and 4 suggest that the flow emanated from the outflow pocket of the hinge areas. Peak velocity magnitudes and TSS levels were higher in region 4 than in region 2. The third jet (jet 3) located near the valve housing is believed to have emanated from the inflow pocket of the hinge. The flow within this jet had a strong radial component. The velocity magnitudes and TSS levels recorded in jet 3 were higher than in jets 2 and 4 (Table 7.9). The TSS levels recorded in all three jets emanating from the hinge areas were high enough to damage blood elements. Comparison of the cross-sectional dimensions of these three jets shows that jets 2 and 4 were wider than jet 3 (Table 7.9).

Typically, retrograde flow is classified into two primary events. One is the squeeze flow that occurs because of the onset of an adverse pressure difference. The second retrograde flow, or leakage jet, occurs because of the large transvalvular pressure when the valve is fully closed. Ellis et al. characterized the retrograde flow fields of the 27 mm SJM and the 27 mm Medtronic Parallel heart valves and recorded higher velocity magnitudes and TSS levels in the sustained retrograde flow than in the squeeze flow (Ellis, 1996). Similarly, the present study revealed higher velocities in the sustained retrograde flow than in the squeeze flow and, therefore, the results of the 23 mm CM in the aortic position agree with the findings of Ellis et al.

Higher velocity magnitudes and TSS levels were expected to occur closer to the plane of the valve housing. However, limits to the optical access allowed the closest measurements to be taken along a plane located 1.65 mm upstream of the outermost part of the valve. Therefore, along the measurement grid the fluid may have already lost most of its energy since the jet had nearly vanished.

The blood volumes per beat that were expected to experience high Reynolds stresses during diastole were presented in table 6.2. The total volume of blood exposed to high stress was 4.36 ml and was mainly due to the leakage flow between the housing and the leaflet (jet 5). Velocities in jet 5 were twofold lower than those observed in jet 3, but the cross-sectional dimensions of jet 5 were the largest of all the jets.

Table 7.10 lists the pertinent parameters for the 23 mm CM jets. The nozzle Reynolds number range that defines the laminar regime for a free submerged jet is greatly dependent upon the jet shape. Laminar jets emanating from a long narrow orifice, plane laminar jets, are very sensitive to small disturbances, and turbulence instabilities become appreciable beyond a nozzle Reynolds number of 30. However, an axisymmetric jet remains laminar up to a Reynolds number of 1,000 and is fully turbulent for a Reynolds number greater than 3,000 (Blevins, 1984). Since the planar free jet model was the most appropriate model for jets 1 and 5, these two jets were considered in the transitional regime between laminar flow and fully turbulent flow. The three jets emanating from the hinge region could be modeled by a round free jet theory. Therefore, since their nozzle Reynolds numbers were lower than 1,000, the jets were considered to be in the laminar regime. Nevertheless, the upper and lower limits of the aforementioned regimes have to be taken with caution since all the assumptions associated with these jet theories are not fulfilled. Furthermore, Travis showed that Reynolds shear stress generated by transitional planar jets could be much greater than the viscous stresses present within these jets, and concluded that free round jet may cause less blood

damage than free planar jets (Travis, 2001). Therefore, it is probable that jets 1 and 5 may induce more platelet and red blood cell disruption than the three remaining jets.

The Stokes layer Reynolds numbers of the jets are presented in Table 7.10. Studies have shown that Stokes layer Reynolds numbers above 550 create turbulence in purely oscillatory pipe flow (Hino, 1983). Based on this criterion, all five leakage jets were in the laminar regime.

The values obtained for Womersley numbers were lower than typical values of α in blood vessels at normal heart rate, except at the level of terminal arteries where α tends to be one (Caro, 1978). Womersley numbers for jets 1, 2 and 3 were less than unity, implying that the flow was quasi-steady, the flow profile was parabolic at all time and the magnitude of the flow-rate was determined by the instantaneous pressure gradient. For jets 1, 2 and 3, the viscous forces dominate the flow and the oscillatory inertia forces can be neglected. However, Womersley numbers of jets 3 and 4 were equal or greater than unity. Therefore, the instantaneous velocity profile was not parabolic but somewhat distorted since the inertial forces began to influence the flow, and the flow will begin to lag behind the applied pressure gradient. Nevertheless, inertial forces begin to dominate significantly the flow α greater than 4.

Table 7.10: Pertinent parameters for the jets in the pulsatile leakage flow LDV experiment

Jet	De (mm)	α	Re	Nozzle Re	$Re_{\delta s}$
1	1.051	0.76	77	103	72
2	0.672	0.49	48	76	69
3	0.924	0.67	103	86	110
4	1.382	1.00	128	102	91
5	2.037	1.47	156	214	75

7.2.1.2 Comparison with Previous Studies

Comparison of the Mitral and Aortic Positions

The present study of the leakage jets through a closed 23 mm CM valve was performed under aortic pulsatile conditions. Similar leakage jets emanating from hinge regions were also observed under mitral conditions (Steegers, 1999; Meyer, 2001). However, Steegers did not find any additional jets between rings and leaflets or at the B-datum line of the closed valve while Meyer observed a strong regurgitant jet emanating from the gap between the ring and the leaflet and a small regurgitant jet near the B-datum line. From these findings, it appears that, under both mitral and aortic conditions, the hinge regions is the principal sites of regurgitation.

Steegers et al. reported a maximum leakage velocity of 1.7 m/s and maximum TSS of 800 dyn/cm^2 (Steegers, 1999). Meyer et al., in a similar study, recorded axial velocities as high as 2.2 m/s in the jet coming from the gap between the ring and the leaflets and axial velocities up to 1.3 m/s in the jet coming from the hinge region (Meyer, 2001). The highest TSS observed was 3,628 dyn/cm^2. Under aortic conditions the maximum TSS levels recorded in the retrograde flow field of the CM valve was 1,284 dyn/cm^2, and the peak velocity magnitude was 0.84 m/s. Therefore, in the aortic position the peak velocity magnitude was smaller than in the mitral position. Because the mitral conditions are more severe than the aortic conditions, such a difference in velocity magnitude was expected. However, no final conclusion could be drawn from the TSS field since the maximum TSS obtained under aortic conditions was slightly greater than that calculated from Steegers, but significantly smaller than that recorded by Meyer. Because the valve size was not stated in the two aforementioned publications, direct comparison may not be conclusive since the leakage gap width may change with valve size. Nevertheless, because of the severe mitral conditions leading to elevated leakage velocities, higher TSS levels were expected in the mitral than in the aortic position.

7.2.2 23 mm St. Jude Medical Regent valve

7.2.2.1 General Features of the Leakage Jets

A pulsatile leakage jet study was performed with a 23 mm SJM Regent valve under aortic conditions. Two regions of high velocity magnitude were detected within the measurement area (Figure 7.8). Table 7.11 gives the maximum velocity magnitude, the peak TSS levels, and the maximum cross-sectional area observed during diastole for each jet.

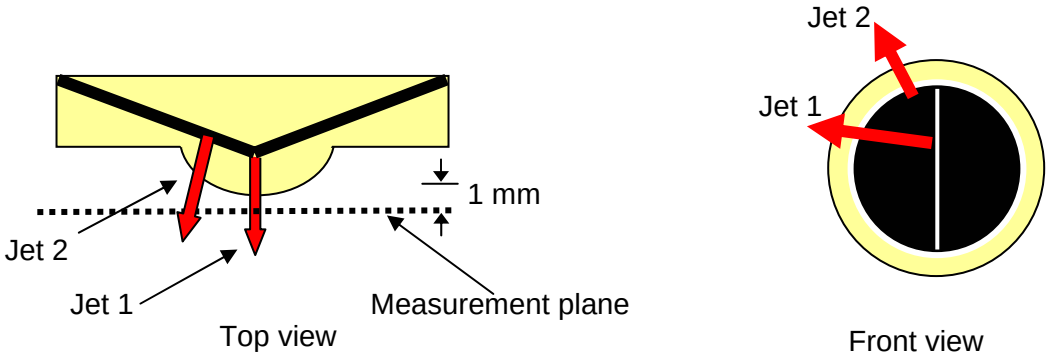

Figure 7.8: Leakage jet location upstream of the SJM Regent valve

Table 7.11: Peak velocity magnitude, peak TSS levels, and maximum cross-sectional dimensions observed during diastole for each SJM leakage jet

Jet	Peak velocity magnitude (m/s)	Peak TSS level (dyn/cm^2)	Maximum cross-sectional dimensions (mm^2)
1	2.34	1,687	4.95 x 1.40
2	0.97	914	3.05 x 1.02

Jet 2 was located proximal to the valve occluder perimeter and may have emanated from the hinge region. The cross-sectional dimensions of this jet changed slightly over time and reached a maximum during mid diastole of 3.05 x 1.02 mm^2. A maximum velocity magnitude and TSS of 0.97 m/s and 914 dyn/cm^2, respectively, were recorded at early diastole. Therefore, since the average TSS level throughout diastole was approximately 300 dyn/cm^2 over the entire jet area, the TSS levels were high enough to damage blood elements (Sutera, 1972; Sallam, 1984).

A large ellipsoidal jet (jet 1) was observed upstream of the valve's B-datum line. The cross-sectional dimensions of this jet were approximately 4.95 x 1.40 mm^2 during all of diastole. Measurements were taken in only one half of the valve area, with the assumption that the flows in the valve were symmetrical. Since high leakage velocity magnitudes were seen in the center of the valve, and since a leakage jet over the complete B-datum line was observed in the static leakage conditions (Figure 6.2), it is likely that the central jet may extend over the other half of the valve area. Throughout the closed phase the peak TSS levels and velocity magnitudes reached 1,687 dyn/cm^2 and 2.34 m/s, respectively. This localized peak velocity magnitude was observed at early diastole and sustained for only 40 ms. Throughout the rest of the investigated area the maximum velocity did not exceed 1.6 m/s. The average TSS level over the leakage phase was approximately 400 dyn/cm^2 throughout the jet area. Since the elevated velocity magnitudes and TSS levels persisted throughout diastole, the TSS levels were large enough to cause blood damage.

Detailed investigation of the measurement area located upstream of the second hinge did not reveal any jet flow. Since the measurement were taken 1 mm upstream of the outermost part of the valve (Figure 7.8), it may be that the jet had already dissipated 1 mm upstream of the pivot guard as no velocity magnitude greater than 0.2 m/s was detected during diastole. This assumption agrees with the static leakage results.

Pictures of the leakage flow through the closed 23 mm CM SJM regent clear housing valve under a 120 mmHg static water column revealed jets emanating from both hinge regions. However, the hinge jets angulated sharply and impinged the pivot guard or the chamber wall immediately upstream of the pivot guard. Thus, the measurement plane may be too far from the hinge to detect all of the hinge jets.

For both jets the highest velocity magnitudes and TSS levels were recorded at early diastole, 80 ms after valve closure (Table 7.11). At mid diastole, the velocity magnitudes decreased to 1.44 m/s in jet 1 and to 0.74 m/s in jet 2. Ellis et al. showed that, in the leakage flow fields of the 27 mm SJM and the 27 Medtronic parallel valve, higher velocity magnitude and TSS levels were seen in the sustained retrograde flow than in the squeeze flow (Ellis, 1996). In the present study, the maximum leakage velocities were therefore recorded earlier in the cardiac cycle than in the CM study as well as in Ellis' study. These early peak velocities may be caused by the impact, and subsequent rebound of the leaflet against the valve housing, the rigidity of the valve chamber or pressure wave reflection in the flow loop.

The blood volume per beat through a 23 mm SJM Regent valve expected to experience high Reynolds stresses during diastole were presented in table 6.2. The total volume of blood exposed to high stress was 4.86 ml and was mainly due to the leakage flow between the two leaflets through the B-datum line (jet 1).

Table 7.12 lists the pertinent characteristics of the 23 mm SJM Regent leakage jets. The regime associated with the nozzle Reynolds number have been shown to be greatly dependent upon the jet shape. Free planar jets have been shown to transition to turbulence at much lower Reynolds number than axisymmetric free jets (Blevins, 1984). The planar free jet model was the most appropriate model for the jet through the B-datum line (jet 1). This jet was considered to be in the transitional regime between laminar flow and fully turbulent flow. The jet emanating from the hinge region was also

long and thin in shape and therefore could also be modeled by a planar free jet. Since the Reynolds number exceeded 30, the jet was considered to be transitional. Once again, these findings have to be taken with caution as all the assumptions associated with these jet theories are not fulfilled due to the complexity of the flow through the valve geometry.

The Stokes layer Reynolds numbers of the jets, presented in table 7.12, were lower than 550 and, therefore, suggest that both jets were in the laminar regime. The values obtained for Womersley numbers were lower than unity (Table 7.12). Viscous forces dominate over oscillatory inertia forces. Womersley numbers in this range have been shown to create parabolic flow profile (Caro, 1978).

Table 7.12: Pertinent parameters for the jets in pulsatile leakage flow LDV experiment

Jet	De (mm)	Wo	Re	Nozzle Re	$Re_{\delta s}$
1	**1.026**	**0.74**	200	249	190
2	**1.045**	**0.75**	138	154	130

7.2.2.2 Comparison with Previous Studies

Aortic Position

Ellis et al. characterized the retrograde flow of a 27 mm SJM Standard valve under aortic conditions and observed a large region of squeeze flow in the vicinity of the centerline and a leakage flow from the hinge (Ellis, 1996). The retrograde flow through the B-datum line was observed mainly at late systole and early diastole while the leakage flow from the hinge occurred at mid diastole. A similar flow pattern was observed in the upstream flow field of the 23 mm SJM Regent valve under aortic

conditions, but both jets were sustained over the entire duration of diastole. Therefore, the results of the 23mm SJM Regent in the aortic position agreed with the findings of Ellis et al.

Travis investigated the retrograde flow field of the 27 mm SJM Standard valve and the 17 mm SJM Regent valve (Travis, 2001). The jets were mainly coming from the hinge regions, and no significant jet emanating from the B-datum line was recorded. The maximum leakage jet velocity magnitudes were 0.57 m/s in the Standard valve and 0.59 m/s in the Regent valve design, which is much lower than in the present study. Therefore, the flow pattern was notably different, except for the hinge jets that were present in both studies. The main difference is the jet through the B-datum line that led to very high leakage velocities in the 23 mm SJM Regent valve. This B-datum line jet may be a specific feature of the investigated clear housing valve.

Under aortic conditions the blood volume per beat expected to sustain high stress during diastole was 1.1 cm^3 for the 27 mm SJM Standard valve and 2.3 cm^3 for the 17 mm SJM Regent (Travis, 2001). However, the leakage flow volumes obtained in the present study were more than twofold higher than those obtained by Travis, with 4.36 cm^3 per beat for the 23 mm CM valve and 4.86 cm^3 per beat for the 23 mm SJM Regent valve (Table 7.13). Calculations of the blood volume exposed to the leakage flow stimulus during each beat were based on the maximum cross-sectional area as well as the peak velocity of each jet throughout diastole (Table 6.2). Comparison of the aforementioned leakage flow volumes with the leakage flow rate obtained under static conditions reveals that the static leakage flow rates do not reflect appropriately and accurately the pulsatile leakage jet results (Table 7.13).

Regurgitant volumes are typically divided into closing volume and leakage volume. Closing volume corresponds to the reverse flow created during valve closure whereas the leakage volume corresponds to the reverse flow once valve is closed.

While pulsatile leakage jets were characterized throughout diastole, static leakage results could not take into account the closing volume, and thus corresponded only to the leakage volume. Since the closing volume differs from one mechanical valve to another (Yoganathan, 1995), the static leakage flow rate cannot be used to estimate the blood volume expected to sustain high stress during diastole.

Additionally, studies used to detect and quantify mitral regurgitation showed that jet volume and regurgitant volume are not equal but can be correlated (Helmcke, 1987). Theoretical work done by Cape and al. showed that regurgitation through mechanical valves can be estimated noninvasively in vivo by applying turbulence jet theory to Doppler ultrasound data (Cape, 1993). Direct correlation between jet volume and regurgitant volume is limited because jet volume is the sum of regurgitant volume and fluid entrained by the jets. In the present study, the leakage jets while flowing back into the quasi-quiescent ventricular fluid entrained the surrounding fluid. Therefore there is supposedly a higher volume of reverse flow that is subjected to high stress upstream of the valve than directly at the nozzle of the jets. Static leakage flow rates are hence non-representative of the volume of leakage flow subjected to high shear stress during diastole.

Table 7.13: Static leakage flow rates and leakage flow volume par beat of four different bileaflet mechanical valves

Valve	Type	Static leakage flow rate (L/min)	Leakage volume per beat (cm^3)
17 mm SJM Regent (Travis, 2001)	Clinical valve	0.136 ± 0.011	2.3
27 mm SJM Standard (Travis, 2001)	Clinical valve	0.423 ± 0.034	1.1
23 mm SJM Regent	Clear housing valve	0.430 ± 0.026	4.86
23 mm CM	Clinical valve	0.327 ± 0.022	4.36

Comparison of the Aortic and Mitral Positions

In the upstream flow field of a SJM valve under mitral conditions, Meyer observed significant reverse flow in the hinge region but did not find any leakage flow along the B-datum line or the valve circumference (Meyer, 2001). Echo-Doppler studies performed by Steegers showed a similar leakage flow pattern near the hinge area to that seen by Meyer. However, Laser Doppler Velocimetry results revealed that the leakage jets did not emerge directly from the hinge area, but from the gap between the housing ring and the leaflet and from the B-datum line (Steegers, 1999). Under aortic conditions the leakage jets were generated upstream of the B-datum line and the hinge region. From these findings it appears that, under both mitral and aortic conditions, the hinge is a region where leakage flow is very likely to be observed.

Meyer found that, under mitral conditions, the peak axial velocity was about 0.7 m/s at valve closure but quickly decayed to a sustained level of 0.1 m/s (Meyer, 2001). He observed a closure spike as high as 1,800 dyn/cm^2 but not a large velocity spike. The TSS levels throughout diastole were on the order of 450 dyn/cm^2. Steegers' results showed a maximum leakage velocity of 1 m/s and a maximum TSS level of 500 dyn/cm^2. However, under aortic conditions the leakage jet study of the SJM Regent valve revealed that the peak velocity magnitudes were 2.34 m/s in region 1 and 0.97 m/s in region 2 while the peak TSS levels were 1,687 dyn/cm^2 in region 1 and 914 dyn/cm^2 in region 2. The peak velocity in the flow that emerged from the hinge region was on the same order of magnitude as that observed under mitral conditions while the peak velocity in region 1 was two to three times greater than that observed by Steegers and Meyer. Because the leakage flow is driven through the valve by the transvalvular pressure, smaller velocities were expected to be seen in the aortic position since the mitral conditions are more severe. The presence of the jet through the B-datum line may

not be a characteristic of the 23 mm SJM Regent clinical valve but may be a feature specific to the investigated clear housing valve.

7.2.3 Influence of the Valve Design on Leakage Flow Fields

7.2.3.1 Valve Position

In the SJM leakage jet study, the B-datum line of the valve was positioned horizontally, but the B-datum line of the CM valve was positioned vertically due to optical limitations. However, Travis et al. showed that valve orientation did not affect leakage jet results, since the jets were similar in shape and location upon rotation of 180° of the valve chamber (Travis, 2001). Moreover, the static leakage experiments showed that the orientation of the valve did not affect the jet location. Therefore, the orientation of the B-datum line should not impact leakage jet results, and valves with vertical or horizontal B-datum line should generate similar leakage jets.

7.2.3.2 Leakage Flow Volume

The difference between the CM and SJM Regent valves in blood volumes expected to experience high stress during diastole was approximately 11.5% (Table 7.13). The highest leakage volume was obtained for the SJM Regent valve, because of the main leakage jet through the B-datum line. Nevertheless, most of the areas of the leakage jets were not turbulent, and the turbulence generated in the jets was expected to dissipate quickly as the jets were in the laminar to transitional regime. Therefore, it is believed that equation 6.1 overestimates the volume of blood expected to be exposed to high stress during diastole.

7.2.3.3 Flow Field

Although the bileaflet mechanical valves were assumed to be symmetric in shape, the leakage jets observed on opposing sides of the symmetry plane were not equivalent in both studies. These differences in leakage jet shape, velocity and TSS on opposing side of the symmetry plane have been observed by Steegers et al. (Steegers, 1999; Travis, 2001). The differences probably result from micro scale differences that are in the leakage gap dimensions, within the manufacturing tolerances. These differences could have a large impact on velocity magnitudes and TSS levels. The leakage flow patterns were different in the CM and SJM studies, but similar features were observed, such as flow through the B-datum line and, particularly, the hinge region.

Higher velocity magnitudes were recorded in the upstream leakage flow field of the SJM valve than in that of the CM valve. However, higher velocities are commonly seen in the retrograde flow field of the CM than in the SJM valve (Meyer, 2001; Steegers, 1999). One reason for this difference in velocity magnitude may be the location of the measurement plane with respect to the valve housing. The study of the SJM leakage jets was performed with a clear housing valve, and the measurement grid was located only 1 mm from the outermost part of the valve while the measurement plane for the CM leakage jet study was located 1.65 mm from the valve housing because of optical limitations. At 1.65 mm from the housing, the energy of the jet had already started to dissipate, and smaller velocity magnitudes were therefore recorded. Additionally, the highest velocity magnitudes were not observed at the same instance during the cardiac cycle. The peak velocity magnitude in the upstream flow field of the SJM Regent valve was due to the presence of a squeeze flow at early diastole while the peak velocity in the CM leakage jets was observed at mid diastole.

Both jet results reveal that the leakage flow patterns during diastole were dependent upon valve design. Even though the valves were placed under similar

conditions, discrepancies were seen in the jet shapes and locations. Therefore, the results show that the valve design, such as gap width and hinge design may have a strong impact on the leakage jets. Thus since the leakage rates vary among individual valves of the same type due to variations in gap widths associated with manufacturing tolerances, comparison of the leakage flow pattern obtained from a single valve design may not be conclusive, and results should be used only to reveal order of magnitude measurements and flow patterns.

CHAPTER VIII

LIMITATIONS

Clinical quality clear housing replicas of carbon valves were used to gain optical access to the hinge regions. During the hinge study wear of the housing was noticed in the hinge regions of the CM clear housing valve. The point of contact of the leaflet ear with the housing may have been subjected to a high stress, thus creating elevated material load and wear. The housing wear enlarged the hinge recess, modifying the leaflet motion, and thus generating small fluctuations in the physiological waveforms. It is therefore possible that the abnormal leaflet motion may have slightly influenced the hinge flow field. Static leakage experiments revealed that the material wear affected the sealing of the valve. As a matter of fact, the leakage flow rate was 0.66 $\pm$ 0.01 L/min before starting the pulsatile experiments, but reached 1.20 $\pm$ 0.05 L/min after the pulsatile experiments as a major leak from the B-datum line was observed. The choice of a wear resistant material to manufacture the clear housing valve appears to be essential. Nevertheless, the wear was only seen at the hinge mechanisms of one leaflet, and the investigated hinge maintained its integrity for the entire duration of data acquisition.

Investigations of the flow fields in the vicinity of the SJM valve were entirely performed with a clear housing valve to be able subsequently to correlate the results of the hinge study with those of the leakage jet study. However, due to the wear of the clear housing CM valve, the valve used in the hinge study could not be used for the leakage jet investigation. Therefore, a clinical CM valve was mounted in the flow loop and used for the leakage jet experiments.

Another limitation of this study was the number of valves investigated. The performance of one single valve for each design was characterized. However, leakage rates vary among individual valves due to small variations in gap width associated with manufacturing tolerances.

A primary experimental limitation that prevented more detailed interrogations of the hinge regions was the complex geometry of the hinge. Due to the proximity of the hinges to the outer surface of the valve chamber and to the motion of the leaflets within the hinge region, the three-component LDV technique could not be used, thus, measurements were collected using the two-component backscattering LDV technique. However, due the complex geometry of the hinge, it is believed that the flow within the recess is three-dimensional. Another limitation that prevented more detailed characterization of the pulsatile leakage jets was the valve geometry and material. The measurements were taken as close as possible to the valve housing but this distances was still a few millimeters upstream of the housing, and therefore far from the jet nozzles.

Additionally, LDV measurements were only conducted at selected locations, thus, the flow fields were not completely defined. The choice of the measurement grid resolution was mainly based upon the probe volume dimensions, the time required to acquire data over the entire measurement grid, and the expected flow field. A coarse grid may limit the accuracy of the flow field characterization since major but localized flow features may not be captured. Therefore, grid resolution appears to be an important parameter in LDV experiments.

Another limitation involved the accuracy of the probe volume translation through the hinge and leakage jet regions. The traversing mechanism had an accuracy of one thousandth of an inch and it is conceivable that spatial error on the order of 0.1 thousandth of an inch may have been introduced. Furthermore, approximately forty

points were located at the edge of the hinge and interpolation between the points was used to determine the hinge edge. Even though the mapping was not continuous but performed at discrete locations, the visual mapping technique gave a good estimate of the hinge geometry. However, even if the valve chamber was firmly tightened to the table, it may have vibrated due to the proximity of the compressor contributing to the introduction of error.

CHAPTER XI

CONCLUSIONS

The specific aims of this study were structured to gain a better understanding of the clinical performances of the bileaflet mechanical heart valves implanted in the aortic position compared to those in the mitral position. The first two objectives were to characterize the hinge and near-hinge flow fields as well as the upstream leakage flow fields of one 23 mm St. Jude Medical Regent (SJM) and one 23 mm CarboMedics (CM) bileaflet mechanical heart valve placed under aortic conditions. The final objective was to compare the results of the two aforementioned valves in the aortic position with findings previously published for the mitral position.

The LDV hinge studies provided an understanding of the flow structures within and in the vicinity of the hinge regions of these two valves placed under physiological aortic conditions. This study revealed a complex and unsteady flow field within the restricted hinge geometry. During systole the hinge flow field in both valves was dominated by a strong forward flow pattern with a peak velocity of 2.31 m/s in the CM hinge recess and 1.75 m/s in the SJM hinge recess. This forward flow probably ensures an effective washout of the hinge regions and limits the accumulation of blood elements. Throughout the cardiac cycle, higher velocities as well as higher turbulent shear stress levels were recorded in the CM than in the SJM valve design. The sharper corners of the CM valve enlarge the gap offered for leakage flow leading to greater velocities, and thus higher turbulent shear stress levels. Additionally the CM's angulated recess disrupts the flow favoring elevated regions of high turbulent shear stress. In contrast, in the SJM valve design, the active motion of the leaflet that sweeps the complete hinge area as well as the smooth streamlined hinge geometry reduce the propensity for flow separation

and turbulence. These findings suggest that the SJM valve design in the aortic position has a more favorable hemodynamic performance than the CM valve, thus reducing the thromboembolic potential of the valve.

The LDV leakage jet study characterized the upstream leakage flow fields of two different bileaflet mechanical heart valve designs under physiological aortic conditions. This study showed that the leakage flow field was strongly dependent upon valve design since the upstream flow patterns of both valves differed; more jets were observed in the CM valve but were associated with lower velocities than in the SJM valve design. The peak velocity in the SJM valve was 2.34 m/s and only 0.84 m/s for the CM valve. However, the presence of the jet through the B-datum line, associated with elevated velocities, may not be characteristic of the 23 mm SJM Regent clinical valve but may be a feature specific to the investigated valve. Nevertheless, the blood volumes per beat expected to experience high stress were similar for both valves. Furthermore, the peak turbulent shear stress levels in the leakage flow fields of the CM valve design and the SJM valve design reached 1,284 dyn/cm^2 and 1,687 dyn/cm^2, respectively. Therefore, the turbulent shear stress levels were greater than the threshold for blood cells damage. In both valve designs, the jets emanated mainly from the hinge regions and the B-datum line but their shapes were different. The shape of the leakage jet may affect greatly the likelihood of turbulence since free planar jets fall into the transitional regime for a lower Reynolds number than free round jets, and therefore may lead to higher turbulent shear stresses. Thus, valve design should favor free round jets to free planar jets.

Flow field characteristics obtained in the aortic position were compared with results previously published under mitral conditions. The forward flow pattern seen in the hinge region in the aortic position was not observed in the mitral position. This flow contributes to washing out the hinge region of any deposited blood elements and, therefore, may constitute one factor that explains the good performances of the valves

implanted in the aortic position. Nonetheless, higher turbulent shear stress levels were recorded in the aortic position during the forward flow phase than in the mitral position. However, because of the short duration of systole, the exposure time may be too short for the elevated TSS levels seen in the aortic position to badly damage blood cells, whereas under mitral conditions, the longer exposure time to lower TSS levels during the forward flow phase may cause greater damage to blood cells. The leakage flow pattern in the hinge region was similar under both conditions but the velocities were lower in the aortic position than in the mitral position. Comparison of the upstream leakage flow revealed that the hinge is one of the principal sites of regurgitation. In addition the turbulent shear stress levels during the leakage phase were greater in the mitral position and were applied for a longer time during the cardiac cycle than in the aortic position, thus increasing the blood damage potential of the valve. Therefore, the severe mitral conditions generate elevated velocities and turbulent shear stress levels that enhance the thrombogenic potential of the valve and diminish the valve's clinical performance in the mitral position. In contrast, the strong forward flow pattern in the hinge region as well as the lower turbulent shear stresses during diastole in the aortic position contribute to the clinical success of valves implanted in the aortic position.

CHAPTER X

RECOMMENDATIONS

A major area of improvement is the use of LDV to characterize the hinge flow field. Since LDV measurements are conducted at selected locations only, fine resolution grids should be used to ensure detailed and accurate characterization of the flow field. Thus, previous results obtained with a coarse grid must be considered with caution and probably have to be checked to verify the validity of the work. However, experimentally obtaining a detailed velocity flow field is time-consuming. An improvement to this study would be the use of Particle Image Velocimetry (PIV) as a complementary technique. Investigation of the hinge region and the upstream leakage flow field could be done with micro-PIV and stereo 3D PIV, respectively. The PIV technique, triggered using the pulsatile waveforms, could be used to capture more efficiently the general flow field features at specific instances of the cardiac cycle. The LDV technique could be used subsequently to characterize in detail selected regions of the flow field. In addition, Computational Fluid Dynamics could be a very useful tool and could be used in parallel with experimental work to gain a better understanding of the complex hemodynamic characteristics of prosthetic heart valves.

Moreover, LDV provides quantitative data, such as velocity and turbulent shear stress information at discrete points, and therefore this Eulerian technique does not allow the visualization of the full flow field. Flow visualization, using hydrogen bubble or dye injection, combined with LDV technique would give a better understanding of the spatial and temporal stress applied to a blood cell flowing through the hinge region. The use of a scale-up model to visualize the flow fields could help elucidating fine features of

the flow pattern recorded with LDV technique, particularly within the restricted regions of the hinges.

The leakage jets under pulsatile conditions were defined with three-component LDV. Future work could include two-component LDV data acquired along a plane parallel to the closed leaflet. This would enable a complete characterization of the retrograde flow field since measurements would be located closer to the leakage gaps, and thus the jet nozzles. It is likely that the three dimensional measurements taken upstream of the valve did not reveal the small energy jets since they may have already dissipated. Therefore these jets could be captured with 2D LDV measurements taken in the vicinity of the leaflet surface.

Another improvement of this study would be to modify the flow loop setup in order to isolate the valve chamber from the rest of the flow loop. In the current setup, transceivers and receiver are mounted to an isolated sturdy frame that allows accurate positioning of the probe volume within the investigated area and also limits the influence of vibrations. In contrast, the valve chamber is mounted to a frailer table where the remaining of the flow loop lays. Thus, the valve chamber vibrates slightly with the pneumatic pulsatile pump. Ideally, the valve chamber would still be connected to the flow loop only to the inflow and outflow tubes, and could be tighten to an isolated sturdy frame to minimize the influence of all types of vibrations, specifically the vibrations generated by the air compressor.

Future data analysis may have to take into account instantaneous velocities. Elevated instantaneous velocities were found in the raw data of the hinge study. These peak values were recorded at valve closure and were sustained only for a brief period of time. During data processing, the raw data was sorted into time bins. If all the high values don’t fall into the same time window, they would be averaged later with lower velocities and thus the phase-averaged data would not present the same profile as the

instantaneous velocity data. This particular flow behavior at valve closure may have to be taken into account to determine accurately the thromboembolic potential of a valve design since high velocity gradient and thus elevated shear stress, even though applied for a short duration, may damage the blood elements.

Additionally, the leakage jet and hinge experiments were performed under physiological conditions at rest. Another improvement to this work would be to perform a similar set of experiment but under more severe conditions such as exercise.

The present study compared the results of two bileaflet mechanical heart valves in the aortic position with the previously published findings in the mitral position obtained with valves of identical design and size. However, the aortic valve is usually smaller than the mitral valve, therefore, comparison of valves with identical design but with different diameters implanted in different positions may have to be pursued to fully understand the clinical performances of bileaflet mechanical heart valves implanted in the aortic and mitral positions. Furthermore, to complete the study, the Medtronic Parallel and the Medtronic Advantage valves should also be investigated to determine the influence of the hinge geometry in the aortic position.

APPENDIX A

ANIMATIONS OF THE HINGE AND NEAR HINGE FLOW FIELDS

The following appendix contains the file naming protocol for the hinge flow field animation files. The animations of the hinge and near hinge velocity flow fields throughout the cardiac cycle for the experiments in specific aim 1 are QuickTime movies. The files have the following naming convention: “hinge_valve_level.mov”

- “Hinge” refers to the hinge and near hinge flow field study.

- “Valve” describes the bileaflet mechanical heart valve used in the experiment: “cm” 23 mm CarboMedics valve and “sjm” 23 mm St. Jude Medical Regent valve.

- “Level” denotes the level where measurements were acquired.

Table A.1 gives the name and a brief description of the hinge flow field animation files.

The protocol followed to generate QuickTime movies from FieldView data is depicted in a detailed fashion by Venugopalan (Venugopalan, 2001). An abbreviated description of the method is provided below.

Each flow field image was exported as a JPG file from FieldView and was then imported to PowerPoint. The position in the cardiac cycle was displayed by adding an Excel graph of the flow curve on each slide. A macro was recorded and used to make all the slides exactly the same. The PowerPoint presentation was saved as a sequence of PNG files. MacroMedia Flash 5 was then used to generate AVI movies. First, 43 keyframes, one per time bin, were inserted. Then, the PNG files were imported as a sequence and were finally exported as an AVI movie. All AVI movies were subsequently converted into QuickTime movies.

Table A.1: Description of the hinge animation files

"Valve"	**"Level"**	**File description**
cm	flatlevel	23 mm CM clear housing valve hinge flow field at the flat level
	195micronslevel	23 mm CM clear housing valve hinge flow field 195 μm above the flat level
	390micronslevel	23 mm CM clear housing valve hinge flow field 390 μm above the flat level
	1mmlevel	23 mm CM clear housing valve hinge inflow, outflow flow field 1 mm below the flat level
sjm	flatlevel	23 mm SJM Regent clear housing valve hinge flow field at the flat level
	195micronslevel	23 mm SJM Regent clear housing valve hinge flow field 195 μm above the flat level
	390micronslevel	23 mm SJM Regent clear housing valve hinge flow field 390 μm above the flat level
	500micronslevel	23 mm SJM Regent clear housing valve hinge inflow, outflow, thumbnail flow field 500 μm below the flat level
	1mmlevel	23 mm SJM Regent clear housing valve hinge inflow, outflow, thumbnail flow field 1 mm below the flat level
	3mmlevel	23 mm SJM Regent clear housing valve hinge inflow, outflow, thumbnail flow field 3 mm below the flat level

APPENDIX B

ANIMATIONS OF THE UPSTREAM LEAKAGE FLOW FIELDS

The following appendix contains the file naming protocol for the upstream leakage jet flow field animation files for the experiments in specific aim 2. The files have the following naming convention “leakagejets_valve_type.ext”:

-- “leakagejets” refers to the upstream leakage flow field study.

- “valve” describes the bileaflet mechanical heart valve used in the experiment: “cm” 23 mm CarboMedics valve and “sjm” 23 mm St. Jude Medical Regent valve.

- “type” denotes the animation type: “time” refers to the evolution of the flow field throughout the cardiac cycle while “space” refers to the animation in space of the flow field at mid diastole.

- “ext” denotes the file format: “mpg” or “mov”

Table B.1 gives the name and a brief description of the leakage jet animation files.

Table B.1: Description of the leakage jet animation files

“Valve”	**“Type”**	**“Ext”**	**File description**
cm	time	mov	Evolution of the 23 mm CM leakage jet velocity field throughout the cardiac cycle
	space	mpg	Animation in space of the 23 mm CM leakage jet velocity field at mid diastole
sjm	time	mov	Evolution of the 23 mm SJM Regent leakage jet velocity field throughout the cardiac cycle
	space	mpg	Animation in space of the 23 mm SJM Regent leakage jet velocity field at mid diastole

The QuickTime movies were generated according to the protocol described in Appendix A. The MPEG movies were generated with the Keyframe Animation Tool of FieldView software. The protocol to create a moving view of the flow fields is briefly depicted below. A detailed description of the Keyframe Animation Tool of FieldView can be found in FieldView Reference Manual (FieldView, 2001).

The Keyframe Animation tool can be accessed through the Keyframe Animation Controls, on the Control Panels pull-down from the Main Menu of FieldView. To create a moving view of the flow field, the steps are as follows:

1. Press the “Animation create” button
2. Select the “Data Set #1” Track
3. Set the current frame to 1
4. Press the “Keyframe Create” button
5. Turn on the “Transformation” button to set up the initial view
6. Change the current Frame to 20
7. Press the “Keyframe Create” button
8. Move the model to the desired position using the mouse controls.

The last step will turn the transformation button ON and define the position at frame 20. It is also possible to move the model by inputting parameters such as angle of rotation, visibility, spin…When the Keyframe Animation is played, FieldView will smoothly interpolate between the initial view and the view at frame 20.

To animate the flow field over the cardiac cycle, the steps are:

1. Select “Comp dataset” Track (Selecting “World” or “ DataSet” as Track does not allow to animate the flow field over the cardiac cycle.)
2. Set the current frame 1
3. Press the “Keyframe create” button

4. Select the “UP” current sweep value

Thus, Keyframe Animation will sweep the flow field starting at frame 1, and will continue until the current sweep value is changed to OFF by setting another keyframe. Each frame will correspond to one time bin.

Track can be changed at any time, and therefore, animations in both space and time are possible. Once the animation has been created, press the “Build Flipbook” button. The active Fieldview Graphic Window becomes a “playback” window. Range of the frames as well as frame rates can be modified. Pressing the “Save” button in the Flipbook Control Panel will bring up a browser with two format options, MPEG and MIFF. MIFF files will be higher quality than MPEG Files, but can only be played with ImageMagick, while MPEG can be played on standard MPEG players.

APPENDIX C

STANDARD DEVIATION CALCULATIONS

The following appendix presents the Visual Basic macros used to calculate, at each measurement location and within each time bin, the standard deviation of the velocity magnitude from the standard deviations of each velocity component. The first macro OrganizeData was used with Microsoft Word, while the last two, MacroStandardDeviation_2D and MacroStandardDeviation_3D were run in Microsoft Excel.

Sub OrganizeData()

```
'The ouput files of the fortran code"phaseavg.f" displays the data in a series of
‘paragraph. This macro formats the files so that the data are displayed in column.

'Find all white spaces
    Selection.Find.ClearFormatting
    Selection.Find.Replacement.ClearFormatting
    With Selection.Find
        .Text = "^w"
        .Replacement.Text = "^t"
        .Forward = True
        .Wrap = wdFindContinue
        .Format = False
        .MatchCase = False
        .MatchWholeWord = False
        .MatchWildcards = False
        .MatchSoundsLike = False
        .MatchAllWordForms = False
    End With
'Replace all white spaces by a tab character
    Selection.Find.Execute Replace:=wdReplaceAll
 'Find all paragraph mark
    With Selection.Find
        .Text = "^p"
        .Replacement.Text = "^t"
        .Forward = True
        .Wrap = wdFindContinue
        .Format = False
        .MatchCase = False
        .MatchWholeWord = False
```

```
        .MatchWildcards = False
        .MatchSoundsLike = False
        .MatchAllWordForms = False
    End With
'Replace all paragraph mark by a tab character
    Selection.Find.Execute Replace:=wdReplaceAll
 'Find all white space mark
    With Selection.Find
        .Text = "^w"
        .Replacement.Text = "^p"
        .Forward = True
        .Wrap = wdFindContinue
        .Format = False
        .MatchCase = False
        .MatchWholeWord = False
        .MatchWildcards = False
        .MatchSoundsLike = False
        .MatchAllWordForms = False
    End With
  'Replace all white space mark by a paragraph mark
    Selection.Find.Execute Replace:=wdReplaceAll
    Selection.Delete Unit:=wdCharacter, Count:=1
    Selection.Find.ClearFormatting
    Selection.Find.Replacement.ClearFormatting
    With Selection.Find
        .Text = "^w"
        .Replacement.Text = "^p"
        .Forward = True
        .Wrap = wdFindContinue
        .Format = False
        .MatchCase = False
        .MatchWholeWord = False
        .MatchWildcards = False
        .MatchSoundsLike = False
        .MatchAllWordForms = False
    End With
End Sub
```

Sub MacroStandardDeviation_2D()

```
'This macro calculates the standard deviation of the velocity magnitude at each location
‘and each time bin from 2D output data files of Fortran Code "Phaseavg"
‘(V1m, V2m, SD1, SD2) and estimates the average of all standard deviations.

'Data from XXX.v1m have to be copied-pasted in column A
'Data from XXX.v2m have to be copied-pasted in column B
'Data from XXX.sd1 have to be copied-pasted in column C
'Data from XXX.sd2 have to be copied-pasted in column D
'The number of locations investigated has to be given in cell E1
'The macro "organizeData" should be run in each file before copy-pasting the data in
‘excel. The number of locations investigated has to be given in cell E1

'Read the number of location
   PointMax = Range("E1")
'Initialize Counter and councolumn
   Bin = 43
   Counter = Bin + 1
   countcolumn = 1
'Remove the first 5 headers(number of bin, cycle time, time bin width, X-position, Y-
‘position) of each column.
   Range("A1:A5").Select
   Range("A1:A5").Activate
   Selection.Delete Shift:=xlUp
   Range("B1:B5").Select
   Range("B1:B5").Activate
   Selection.Delete Shift:=xlUp
   Range("D1:D5").Select
   Range("D1:D5").Activate
   Selection.Delete Shift:=xlUp
   Range("C1:C5").Select
   Range("C1:C5").Activate
   Selection.Delete Shift:=xlUp

'Remove throughout each column the headers(time bin width, X-position, Y-position)
   For countcolumn = 1 To 4
   Column = countcolumn
      Worksheets("Sheet1").Cells(Counter, Column).Select
      Worksheets("Sheet1").Cells(Counter, Column).Activate
      Selection.Delete Shift:=xlUp

      Worksheets("Sheet1").Cells(Counter, Column).Select
      Worksheets("Sheet1").Cells(Counter, Column).Activate
      Selection.Delete Shift:=xlUp

      Worksheets("Sheet1").Cells(Counter, Column).Select
      Worksheets("Sheet1").Cells(Counter, Column).Activate
      Selection.Delete Shift:=xlUp

    Maxcount = Bin * PointMax
    Counterraw = Counter
```

```
        For Counterraw = Counter To Maxcount
        Counter = Counter + Bin
        Worksheets("Sheet1").Cells(Counter, Column).Select
        Worksheets("Sheet1").Cells(Counter, Column).Activate
        Selection.Delete Shift:=xlUp

        Worksheets("Sheet1").Cells(Counter, Column).Select
       Worksheets("Sheet1").Cells(Counter, Column).Activate
        Selection.Delete Shift:=xlUp

        Worksheets("Sheet1").Cells(Counter, Column).Select
        Worksheets("Sheet1").Cells(Counter, Column).Activate
        Selection.Delete Shift:=xlUp

        Counterraw = Counter
        Next
        countercolumn = countercolumn + 1
        Worksheets("Sheet1").Cells(1, Column).Select
        Selection.Insert Shift:=xlDown
        Counter = Bin + 1
        Next
'Insert the legend of each column
        Range("A1").Select
        ActiveCell.FormulaR1C1 = "Velocity 1"
        Range("B1").Select
        ActiveCell.FormulaR1C1 = "Velocity 2"
        Range("C1").Select
        ActiveCell.FormulaR1C1 = "Standard Dev 1"
        Range("D1").Select
        ActiveCell.FormulaR1C1 = "Standard Dev 2"


'Calculate the standard Deviation of Vmag from the standard deviation of each velocity
‘component at each location and at each time bin
    Maxcount = Maxcount + 1

    Range("F1").Select
    ActiveCell.FormulaR1C1    =    "=SQRT(RC[-5]^2/(RC[-5]^2+RC[-4]^2)*RC[-3]^2+RC[-
4]^2/(RC[-5]^2+RC[-4]^2)*RC[-2]^2)"
    Selection.Copy
    Worksheets("Sheet1").Cells(Maxcount, 6).Select
    Range(Selection, Selection.End(xlUp)).Select
    ActiveSheet.Paste
    Range("F1").Select
    ActiveCell.FormulaR1C1 = "STD_mag"

'When all velocity components are zero at a particular location and time bin, the standard
‘deviation can not be estimated and excel displays #DIV 0.
'So the #DIV 0 are replaced by 0
    Range("G1").Select
    ActiveCell.FormulaR1C1 = "=IF(RC[-6]=0,IF(RC[-5]=0,0,RC[-1]),RC[-1])"
```

```
    Selection.Copy
    Worksheets("Sheet1").Cells(Maxcount, 7).Select
    Range(Selection, Selection.End(xlUp)).Select
    ActiveSheet.Paste
    Range("G1").Select
    ActiveCell.FormulaR1C1 = "STD corrected"

'Calculate the average of all the standard deviations
    Range("H1").Select
    ActiveCell.FormulaR1C1 = "STD averaged"
    Range("H2").Select
    ActiveCell.FormulaR1C1 = "=AVERAGE(RC[-1]:R[-10]C[-1])"

End Sub
```

Sub MacroStandardDeviation_3D()

```
' This macro calculates the standard deviation of the velocity magnitude at each location
‘and each time bin from 3D output data files of Fortran Code "Phaseavg"
‘(V1m, V2m,V3m, SD1, SD2,SD3) and estimates the average of all standard deviations.

'Data from XXX.v1m have to be copied-pasted in column A
'Data from XXX.v2m have to be copied-pasted in column B
'Data from XXX.v3m have to be copied-pasted in column C
'Data from XXX.sd1 have to be copied-pasted in column D
'Data from XXX.sd2 have to be copied-pasted in column E
'Data from XXX.sd3 have to be copied-pasted in column F
'The macro "organizeData" should be run in each file before copy-pasting the data in
‘excel. The number of locations investigated has to be given in cell G1

'Read the number of location
PointMax = Range("G1")

'Initialize Counter and councolumn
   Bin = 43
   Counter = Bin + 1
   countcolumn = 1

'Remove the first 5 headers(number of bin, cycle time, time bin width, X-position, Y-
‘position) of each column.
   Range("A1:A5").Select
   Range("A1:A5").Activate
   Selection.Delete Shift:=xlUp
   Range("B1:B5").Select
   Range("B1:B5").Activate
   Selection.Delete Shift:=xlUp
   Range("C1:C5").Select
   Range("C1:C5").Activate
   Selection.Delete Shift:=xlUp
   Range("D1:D5").Select
   Range("D1:D5").Activate
   Selection.Delete Shift:=xlUp
   Range("E1:E5").Select
   Range("E1:E5").Activate
   Selection.Delete Shift:=xlUp
   Range("F1:F5").Select
   Range("F1:F5").Activate
   Selection.Delete Shift:=xlUp

'Remove throughout each column the headers(time bin width, X-position, Y-position)
   For countcolumn = 1 To 6
   Column = countcolumn
      Worksheets("Sheet1").Cells(Counter, Column).Select
      Worksheets("Sheet1").Cells(Counter, Column).Activate
      Selection.Delete Shift:=xlUp

      Worksheets("Sheet1").Cells(Counter, Column).Select
```

```
        Worksheets("Sheet1").Cells(Counter, Column).Activate
        Selection.Delete Shift:=xlUp

        Worksheets("Sheet1").Cells(Counter, Column).Select
        Worksheets("Sheet1").Cells(Counter, Column).Activate
        Selection.Delete Shift:=xlUp

      Maxcount = Bin * PointMax
      Counterraw = Counter
        For Counterraw = Counter To Maxcount
        Counter = Counter + Bin
        Worksheets("Sheet1").Cells(Counter, Column).Select
        Worksheets("Sheet1").Cells(Counter, Column).Activate
        Selection.Delete Shift:=xlUp

        Worksheets("Sheet1").Cells(Counter, Column).Select
       Worksheets("Sheet1").Cells(Counter, Column).Activate
        Selection.Delete Shift:=xlUp

        Worksheets("Sheet1").Cells(Counter, Column).Select
        Worksheets("Sheet1").Cells(Counter, Column).Activate
        Selection.Delete Shift:=xlUp

        Counterraw = Counter
        Next
        countercolumn = countercolumn + 1
        Worksheets("Sheet1").Cells(1, Column).Select
        Selection.Insert Shift:=xlDown
        Counter = Bin + 1
        Next
  'Insert the legend of each column
        Range("A1").Select
        ActiveCell.FormulaR1C1 = "Velocity 1"
        Range("B1").Select
        ActiveCell.FormulaR1C1 = "Velocity 2"
        Range("C1").Select
        ActiveCell.FormulaR1C1 = "Velocity 3"
        Range("D1").Select
        ActiveCell.FormulaR1C1 = "Standard Dev 1"
        Range("E1").Select
        ActiveCell.FormulaR1C1 = "Standard Dev 2"
        Range("F1").Select
        ActiveCell.FormulaR1C1 = "Standard Dev 3"


'Calculate the standard Deviation of Vmag from the standard deviation of each velocity
‘component at each location and at each time bin
     Maxcount = Maxcount + 1

     Range("H1").Select
```

```
    ActiveCell.FormulaR1C1 = "=SQRT(RC[-7]^2/(RC[-7]^2+RC[-6]^2+RC[-5]^2)*RC[-
4]^2+RC[-6]^2/(RC[-7]^2+RC[-6]^2+RC[-5]^2)*RC[-3]^2+RC[-5]^2/(RC[-7]^2+RC[-
6]^2+RC[-5]^2)*RC[-2]^2)"
    Selection.Copy
    Worksheets("Sheet1").Cells(Maxcount, 8).Select
    Range(Selection, Selection.End(xlUp)).Select
    ActiveSheet.Paste
    Range("H1").Select
    ActiveCell.FormulaR1C1 = "STD_mag"

'When all velocity components are zero at a particular location and time bin, the standard
‘deviation can not be estimated and excel displays #DIV 0.
'So the #DIV 0 are replaced by 0
   Range("I1").Select
    ActiveCell.FormulaR1C1 = "=IF(RC[-8]=0,IF(RC[-7]=0,IF(RC[-6]=0,0,RC[-1]),RC[-
1]),RC[-1])"
    Selection.Copy
    Worksheets("Sheet1").Cells(Maxcount, 9).Select
    Range(Selection, Selection.End(xlUp)).Select
    ActiveSheet.Paste
    Range("I1").Select
    ActiveCell.FormulaR1C1 = "STD corrected"

'Calculate the average of all the standard deviations
    Range("J1").Select
    ActiveCell.FormulaR1C1 = "STD averaged"
    Range("J2").Select
    ActiveCell.FormulaR1C1 = "=AVERAGE(RC[-1]:R[-10]C[-1])"

End Sub
```

REFERENCES

Aagaard,J., Tingleff, J., Andersen, P.V., Hansen, C.N. (2003) “Fourteen Years’ Experience with the CarboMedics Valve in young Adults with Aortic Valve Disease.” The journal of Heart Valve Disease 12(1):81-86

Anderson, G. H, Hellums, J.D., Moake, J.L., Alfrey, C.P. (1978) “Platelet Lysis and Aggregation in Shear Fields” Blood Cells 4(3): 499-511

Akins, C.W. (1995) “Results With Mechanical Cardiac Valvular Prostheses.” Annals of Thoracic Surgery 60:1836-1844

Bernstein, E.F., Marzec, U., Johnston, G.G. (1977) “Structural Correlates of Platelet Functional Damage by Physical Forces” Trans. Am. Soc. Artif. Intern. Organs, 23: 617-625

Black, M.M., Drury, P.J. (1994) “Mechanical and Other Problems of Artificial Valves.” Current Topics in Pathology , Springer-Verlag Berlin Heidelberg 86:127-159

Blackshear, P.L.(1972) “Mechanical Hemolysis in Flowing Blood” Biomechanics, its Foundations and Objectives by Fung, Englewood Cliffs, NJ: Prentice Hall, 501-528

Blevins, R.D. (1984) Applied Fluid Dynamics Handbook Van Norstrand Reinhold Company Inc. 229-278

Born (1962) “Aggregation of Blood Platelets by Adenosine Diphosphate and its Reversal” Nature 194:927

Brown, C. H. , Leverett L.B., Lewis, C.W., Alfrey,C.P.,Hellums,J.D. (1975) “Morphological, Biochemical, and Functional Changes in Human Platelets Subjected to Shear Stress” J. Lab. Clin. Med. sept 86(3):462-471

Carbomedics Inc. 2003
http://www.carbomedics.com/professional_surgeon_pressure.asp

Cape, E.G., Nanda, N.C., Yoganathan, A.P. (1993) “Quantification of Regurgitant Flow Through Bileaflet Heart Valve Prostheses: Theoretical and In Vitro Studies.” Ultrasound in Medicine and Biology 19(6):461-468

Caro, C. G., Pedley, T.J., Schroter, R.C., Seed, W.A. (1978) The Mechanics of the Circulation Oxford University Press

Chang, B.C., Lim, S.H. Kim, D.K., Seo, J.Y., Cho, S.Y., Shim, W.H., Chung, N., Kim, S.S., Cho. B.K. (2001) “Long-Term Results with St. Jude Medical and CarboMedics Prosthetic Heart Valves.” The Journal of Heart Valve Disease 10(2):185-194

Chien, S. (1977) “Red Cell Membrane and Hemolysis” Cardiovascular Flow Dynamics and Measurements edited by Hwang, N.H.C. and Normann, N.A 757-793

Cape, E.G., Nanda, N.C., Yoganathan, A.P. (1993) “Quantification of Regurgitant Flow Through Bileaflet Heart Valve Prostheses: Theoretical and In Vitro Studies” Ultrasound in Medicine and Biology 19(6):461-468

Dalrymple-Hay, M.J., Pearce, R. K., Dwkins, S., Alexiou, C., Haw, M.P., Livesey, S.A., Monro, J.L. (2000) “Mid-Term Results with 1,503 CarboMedics Mechanical Valve Implants.” The Journal of Heart Valve Disease 9(3):389-395

Ellis, J.T., Healy, T.M., Fontaine, A.A., Saxena, R., Yoganathan, A.P. (1996) “Velocity Measurements and Flow Pattern within the Hinge Region of a Medtronic Parallel Bileaflet Mechanical Heart Valve with Clear Housing.” The Journal of Heart Valve Disease 5(6):591-599

Ellis, J.T., Healy, T.M., Fontaine, A.A., Weston, M.W., Jarret, C.A., Saxena, R., Yoganathan A.P. (1996) “An In Vitro Investigation of the Retrograde Flow Fields of Two Bileaflet Mechanical Heart Valves” The Journal of Heart Valve Disease 5(6):600-606

Ellis, J.T. (1999) “An In Vitro Investigation of the Leakage and Hinge Flow Fields through Bileaflet Mechanical Heart Valves and their Relevance to Thrombogenesis”, PhD Thesis, Georgia Institute of Technology

Ellis, J.T., Travis, B.R., Yoganathan, A.P. (2000) “An In Vitro Study of the Hinge and Near-Field Forward Flow Dynamics of the St Jude Medical Regent Bileaflet Mechanical Heart Valve “. Annals of Biomedical Engineering 28:524-532

Ellis, J.T., Yoganathan, A.P. (2000)” A Comparison of the Hinge and Near-Hinge Flow Fields of St Jude Medical Hemodynamic Plus and Regent Bileaflet Mechanical Heart Valve.” The Journal of Thoracic and Cardiovascular Surgery 119(1):83-93

FieldView Reference Manual (2001), Chapter 8, Software release 8.0, Intelligent Light, Lyndhurst, NJ

Gao, Z. B., Hosein, N., Dai, F.F., Hwang, N.H. (1999) “Pressure and Flow Fields in the Hinge Region of Bileaflet Mechanical Heart Valves.” The Journal of Heart Valve Disease 8(2):197-205

Graf, T., Fisher, H., Reul, H., Rau, G. (1991) “Cavitation Potential of Mechanical Heart Valve Prostheses” The International Journal of Artificial Organs 14(3):169-174

Gross, J.M., Shu, M.C., Dai, F.F., Ellis, J., Yoganathan, A.P. (1996) ”A Microstructural Flow Analysis Within a Bileaflet Mechanical Heart Valve Hinge.” The Journal of Heart Valve Disease 5(6):581-590

Grunkemeier, G.L., Anderson, W.N. Jr. (1998) “Clinical Evaluation and Analysis of Heart Valve Substitutes.” The Journal of Heart Valve Disease 7(2):163-169

Hellums, J.D., Brown, C.H. (1977) “Blood Cell Damage by Mechanical Forces” Cardiovascular Flow Dynamics and Measurements edited by Hwang , N.H.C. and Normann, N.A. 799-823

Helmcke, F., Nanda, N.C., Hsiung, M.C., Soto, B., Adey, C.K., Goyal, R.G., Gatewood, R.P. (1987) “Color Doppler Assessment of Mitral Regurgitation with Orthogonal Planes” Circulation 75(1):175-183

Hino, M., Kashiwayanagi, M., Nakayama, A., Hara, T. (1983) “Experiments on the Turbulence Statistics and the Structure of a Reciprocating Oscillatory Flow.” Journal of Fluid Mechanics 131:363-400

Jamieson, W.R., Fradet, G.J., Miyagishima, R.T., Henderson ,C., Brownlee, R.T., Zhang, J., Germann, E. (2000) “CarboMedics Mechanical Prosthesis: Performance at Eight Years.” The Journal of Heart Valve Disease 9(5): 678-687

Krautzberger, W., Clevert, D., Keilbach, H., Kleine, H.O., Grosse-Siestrup, C., Affeld, K., Henning, E., Klass, H., Unger, V., Bücherl, E.S. (1978) “Cardiac Output and Right Atrial Pressure in Long Surviving Animals after Total Heart Replacement.” ESAO Proc. 4:294-302

Leo, H.W., He, Z., Ellis, J.T., Yoganathan, A.P. (2002) “Microflow Fields in the Hinge Region of the CarboMedics Bileaflet Mechanical Heart Valve Design.” The Journal of Thoracic and Cardiovascular Surgery 124(3):561-574

Leverett, L.B., Hellums, J.D., Alfrey, C.P., Lynch, E.C. (1972) “Red Blood Cell Damage by Shear Stress.” Biophysical Journal 12(3):257-273

Lu, P.C., Lai H.C, Liu, J.S. (2001) “A Reevaluation and discussion on the Threshold Limit for Hemolysis in a Turbulent Shear Flow.” J. Biomech. oct 34(10):1361-1364

Martini, F.H., Ober, W.C., Garrison, C.W. (2000) Fundamentals of Anatomy and physiology fifth edition Prenctice Hall, 474-496

McLaughlin, D.K., Tiederman, W.G. (1973) “Biasing Correction for Individual Realization of Laser Anemometer Measurements in Turbulent Flows.” The Physics of Fluids 16(12):2082-2088

Meyer, R.S., Deutsch, S., Maymir, J.C., Geselowitz, D.B., Tarbell, J.M. (1997) “Three-component Laser Doppler Velocimetry Measurements in the Regurgitant Flow Region of a Bjork-Shiley Monostrut Mitral Valve.” Annals of Biomedical Engineering 25:1081-1091

Meyer, R.S., Deutsch,S., Bachmann, C.B., Tarbell, J.M. (2001) “Laser Doppler Velocimetry and Flow Visualization Studies in the Regurgitant Leakage Flow Region of Three Mechanical Mitral Valves” Artificial Organs 25(4):292-299

Minakata, K., Wu, Y.X., Zerr, K.J., Grunkemeier, G.L., Handy, J.R. Jr, Ahmad, A., Starr, A., Furnary, A.P. (2002) “Clinical Evaluation of the CarboMedics Prosthesis: Experience at Providence Health System in Portland” The Journal of Heart Valve Disease 11(6):844-850

Nevaril, C.G., Lynch, E.C., Alfrey, C.P., Hellums, J.D. (1968) “Erythrocyte Damage and Destruction Induced by Shearing Stress” J. Lab. Clin. Med. 71: 784

Perin, E.C., Jin, B.S., De Castro, C.M., Ferguson, J.J., Hall, R.J. (1991) “Doppler Echocardiography in 180 Normally Functioning St. Jude Medical Aortic Valve Prostheses. Early and Late Postoperative Assessments.” Chest 100(4):988-990

Piehler, H.R. (2000) “The Future of Medicine: Biomaterial” Material Research Society Bulletin August:67-70

Sallam, A.M., Hwang, N.H.C. (1984) “Human Red Blood Cell Hemolysis in a Turbulent Shear Flow: Contribution of Reynolds Shear Stresses” Biorheology 21:783-797

Saxena, R., Lemmon, J., Ellis, J., Yoganathan, A.P. (2003) “An in vitro Assessment by Means of Laser Doppler Velocimetry of the Medtronic Advantage Bileaflet Mechanical Heart Valve Hinge Flow” The Journal of Thoracic and Cardiovascular Surgery 126(1):90-98

Shipkowtiz,T., Ambrus, J., Kurk, J., Wickramasinghe, K. (2002) “Evaluation Technique for Bileaflet Mechanical Valves.” The Journal of Heart Valve Disease 11(2):275-282

Skoularigis, J., Essop, M.R., Skudicky, D., Middlemost, S.J., Sareli, P. (1993) “Frequency and Severity of Intravascular Hemolysis after Left-Sided Cardiac Valve Replacement with Medtronic Hall and St. Jude Medical Prostheses and Influence of Prosthetic Type, Position, Size, and Number “ American Journal of Cardiology 71:587-591

Steegers, A., Paul, R. Reul, H., Rau, G. (1999) “Leakage Flow At Mechanical Heart Valve Prostheses: Improved Wahout or Increased Blood Damage?” The Journal of Heart Valve Disease 8(3):312-323

Sung, H.W., Cape, E.G., Yoganathan, A.P. (1994) “In Vitro Fluid Dynamic Evaluation of the CarboMedics Bileaflet Heart Valve Prosthesis in the Aortic and Mitral position.” The Journal of Heart Valve Disease 3(6): 673-683

Sutera, S.P., Mehrjardi, M.H. (1975) “Deformation and Fragmentation of Human Red Blood Cells in Turbulent Shear Flow” Biophysical J. 15: 1-10

Sutera S.P, Croce P., Mehrjardi M.H. (1972) “Hemolysis and Subhemolytic Alterations of Human RBC Induced by Turbulent Shear Flow” ASAIO Transactions 18:335-341

Travis, B.R., Marzec, U.M., Leo, H.L., Momin, T., Sanders, C., Hanson, S.R., Yoganathan, A.P. (2001) “Bileaflet Aortic Valve Prosthesis Pivot Geometry Influences Platelet Secretion and Anionic Phospholipid Exposure.” Annals of Biomedical Engineering 29:657-664

Travis, B. (2001) “The Effects of Bileaflet Prosthesis Pivot Geometry on Turbulence and Blood Damage Potential”, PhD Thesis, Georgia Institute of Technology

Travis, B.R., Leo, H.L., Shah, P.A., Frakes, D.H., Yoganathan, A.P. (2002) “An Analysis of Turbulent Shear Stress In Leakage Flow Through a Bileaflet Mechanical Prostheses.” Journal of Biomechanical Engineering April (124):155-165

Vallana, F., Rinaldi, S., Galleti, P.M., Nguyen, A., Piwnica, A. (1992) “Pivot Design in Bileaflet Valves.” ASAIO Journal 38:M600-M606

Venugopalan, P. (2001) “LDV Hinge Flow Study of CM (SJM) 23 mm Bileaflet Mechanical Heart Valve”, Cardiovascular Fluid Mechanics Lab Report, Georgia Institute of Technology

Walker, P., Yoganathan, A. (1992). “In vitro Pulsatile Flow Hemodynamics of Five mechanical Aortic Heart Valve Prostheses.” European Journal of Cardiothoracic Surgery 6 (Suppl):S113-S123

Walker, D.K., Brendzel, A.M., Scotten, L.N. (1999) “The New St. Jude Medical Regent Mechanical Heart Valve: Laboratory Measurements of Hydrodynamic Performance.” The Journal of Heart Valve Disease 8(6):687-696

Zellner, J.L., Kratz, J.M., Crumbley, A.J., Stroud, M.R., Bradley, S.M., Sade, R.M., Crawford, F.A. Jr (1999) “Long term Experience with the St Jude Medical Valve Prothesis.” Annals of Thoracic Surgery 68:1210-1218

Yoganathan, A.P. (1995) “Cardiac Valve Prostheses.” The Biomedical Engineering Handbook, J. Bronzino Boca Ranton, FL CRC Press:1847-1870, Chapter 127